

AD-A124 044

CORROSION CONTROL THROUGH A BETTER UNDERSTANDING OF THE
METALLIC SUBSTRAT. (U) LEHIGH UNIV BETHLEHEM PA CENTER
FOR SURFACE AND COATINGS RESE. H LEIDHEISER ET AL.

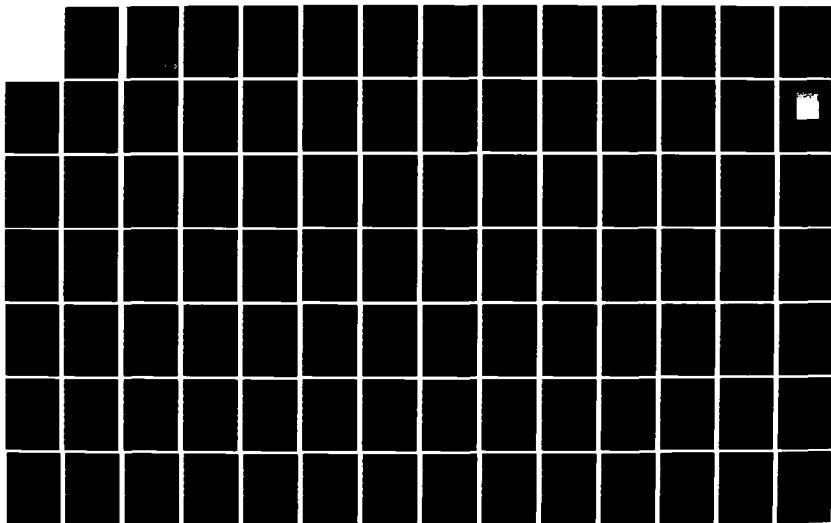
1/3

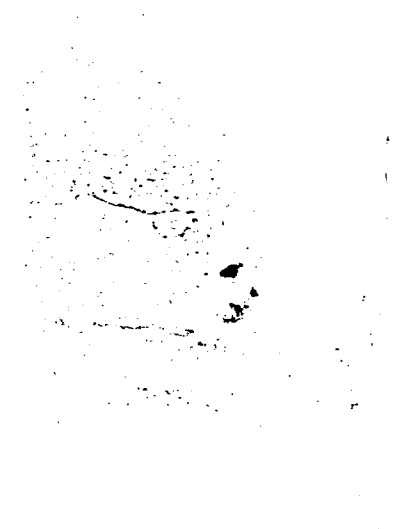
UNCLASSIFIED

01 DEC 82 N00014-79-C-0731

F/G 11/6

NL





(1)

**CORROSION CONTROL THROUGH A BETTER UNDERSTANDING
OF THE METALLIC SUBSTRATE/ORGANIC COATING/INTERFACE**

ADA 124044

Agreement No. N00014-79-C-0731

Third Annual Report

Covering the Period,

September 1, 1981-August 31, 1982

Sponsor: Office of Naval Research

Washington, D.C.

Principal Investigator: Henry Leidheiser, Jr.

Co-Investigators: Eugene M. Allen
Mohamed S. El-Aasser
Frederick M. Fowkes
John A. Manson
Fortunato J. Micale
David A. Thomas
Gary W. Simmons
John W. Vanderhoff

Center for Surface and Coatings Research
Lehigh University
Bethlehem, Pa. 18015

December 1, 1982

DTIC
ELECTE
S FEB 1 1983 D
B

DISTRIBUTION STATEMENT A

Approved for public release
Distribution Unlimited

83

01

02

044

DTIC FILE COPY

TABLE OF CONTENTS

	<u>Page</u>
Foreword	1
Section 1 - A List of Public Disclosures of the Research during the Period, September 1, 1981 - August 31, 1982	2
• Published Papers	2
• Papers Accepted for Publication.	4
Section 2 - The Titles of the Component Programs Summarized Herein and the Participants.	5
• Programs Concerned with Corrosion at the Interface.	5
• Programs Concerned with the Chemistry of the Metal/Coating Interface.	5
• Programs Concerned with the Properties of the Coating	6
• Programs Related to the Surface Properties of Iron Oxides from the Standpoint of Their Presence at the Steel/Organic Coating Interface and Their Use as Pigments	7
• Active Programs Not Summarized in the Present Report	9
Section 3 - A Summary of the Experimental Results Obtained during the Period, September 1, 1981 - August 31, 1982	10
Section 4 - Individual Programs.	17
Program #1. Improved Corrosion Resistance of Steel in Mild Media after Abrasive Blasting with Alumina.	17
Program #2. A Two-Step Anodization Process for Inhibition of the Oxygen Reduction Reaction on Iron.	35
Program #3. The Application of Emission Mössbauer Spectroscopy to the Chemistry of the Coating/Substrate Interface.	59

CONTENTS Cont'd.

	<u>Page</u>
Program #4 - Determination of the Acidity of Iron Oxide Surfaces.	71
Program #5 - Ion Exchange Properties of Iron Sur- faces	81
Program #6 - Investigation of Phosphated Steel Sur- faces by Laser Raman Spectroscopy . . .	91
Program #7 - Detection of Aggregated Water in Polymer Coatings.	101
Program #8 - Radiochemical and Electrochemical Mea- surements of Diffusion in Organic Coatings.	111
Program #9 - Drying and Curing of Epoxy Films. . . .	137
Program #10 - Cathodic Electrodeposition of Polymer Latexes	155
Program #11 - Application of Laser Raman Spectroscopy to the Analysis of Electrodeposited Epoxy Resin	177
Program #12 - Pigment/Binder Interactions and Corro- sion Protection	189
Program #13 - Characterization of the Surface Proper- ties of Iron Oxides	203
Program #14 - An Understanding of the Principles Re- lated to the Application of Paints to Rusted Steel Surfaces with Little or No Surface Preparation	229



Accession For	
NTIS GRA&I	<input checked="" type="checkbox"/>
DTIC TAB	<input type="checkbox"/>
Unannounced	<input type="checkbox"/>
Justification	
PER LETTER	
By	
Distribution/	
Availability Codes	
Dist	Avail and/or Special
A	

FOREWORD

This report represents the third annual summary of research carried out under Office of Naval Research Contract No. N00014-79-0731. The objective of this research is to obtain a better understanding of the metallic substrate/organic coating/interface system so that improvements may be made in corrosion control of metals by painting. The report this year includes a summary of progress made in 14 different components of the program. These activities are divided for convenience into those primarily concerned with (a) corrosion at the interface, (b) the chemistry of the metal/coating interface, (c) the properties of the coating, and (d) the surface properties of iron oxides from the standpoint of their presence at the steel/organic coating interface and their use as pigments. Each of the 14 sections has been authored by the program component director and there is thus a difference in the style of presentation in many of the sections.

It is recognized that readers of this report will be interested in the contents for different purposes. In an effort to accommodate to these diverse interests, the report is presented in the following format.

- (1) A list of public disclosures of the research. The references may be useful to those who wish to explore the research results in greater detail.
- (2) A list of the titles of the 14 component programs keyed to the experimental summaries in Section 4 and the names of the participants.
- (3) A condensation of the total program. This summary is aimed at those who wish to obtain an overview of the program.
- (4) A more detailed outline of the results generated in the component programs during the period, September 1, 1981 - August 31, 1982.

SECTION 1

A List of Public Disclosures of the Research during the Period,
September 1, 1981 - August 31, 1982

Published Papers

"Kinetics and Film Growth by Cathodic Electrodeposition of Epoxy Latexes," M. S. El-Aasser, C. C. Ho, A. Humayun, and J. W. Vanderhoff in Proceedings of 2nd World Congress of Chemical Engineering, Vol. 3 (1981), pp.211-220.

"Some Aspects of Cathodic Electrodeposition of Epoxy Latexes and Corrosion Resistant Coatings," C. C. Ho, A. Humayun, M. S. El-Aasser, and J. W. Vanderhoff, in Corrosion Control by Organic Coatings, Henry Leidheiser, Jr., Editor, National Association of Corrosion Engineers, Houston, Texas, 111-121 (1981).

"Acid-Base Interaction by Polymeric Vehicles with the Corrosion Products of Iron," J. W. Vanderhoff, L. M. Bennetch, M. J. Cantow, K. A. Earhart, M. S. El-Aasser, T. C. Huang, M. H. Kang, J. A. Manson, F. J. Micale, O. L. Shaffer, and D. W. Timmons, Preprints, Org. Coatings Plastics Chem. 46, 12-16 (1982).

"Kinetics and Mechanism of Cathodic Electrodeposition of Epoxy Latexes," M.S. Thesis, Chemical Engineering, June 1982, by Arif Humayun.

"Enhancing Polymer Adhesion to Iron Surfaces by Acid-Base Interaction," F. M. Fowkes, C.-Y. Sun, and S. T. Joslin, in Corrosion Control by Organic Coatings, Henry Leidheiser, Jr., Editor, National Association of Corrosion Engineers, Houston, Texas, 1-3 (1981).

"Acid-Base Interactions in Polymer Adhesion," F. M. Fowkes, in Microscopic Aspects of Adhesion and Lubrication, Proceedings of the 34th International Meeting of the Societe de Chimie Physique, Paris, Sept. 1981, J. M. Georges, Editor, Elsevier, Amsterdam (1982), pp.119-37.

"Acid-Base Interactions in Polymer Adhesion," F. M. Fowkes, in Aspects of Polymer Surfaces, K. Mittal, Editor, Plenum, New York (1982).

"Surface Treatments for Enhanced Bonding Between Inorganic Surfaces and Polymers," F. M. Fowkes, in Surface Treatments for Improved Performance and Properties, Sagamore Army Materials Research Conference Proceedings 26, J. J. Burke and V. Weiss, Editors, Plenum, New York (1982), pp.75-86.

" ^{57}Fe Mössbauer Spectroscopic Study of the Thermal Decomposition of $\text{Fe}/\text{IO}_3/3$," S. Music, G. W. Simmons, H. Leidheiser, Jr., Radiochem. Radioanal. Letters 48/3-4, 227-33 (1981).

" ^{57}Fe Mössbauer Spectroscopic Study of the Thermal Decomposition of Basic Iron(III) Sulfate," S. Music, A. Vértes, G. W. Simmons, I. Czako-Nagy, and H. Leidheiser, Jr., Radiochem. Radioanal. Letters 49, No. 5, 315-22 (1981).

BOOK: Corrosion Control by Organic Coatings, Henry Leidheiser, Jr., Editor, National Association of Corrosion Engineers, Houston, Texas, 1981, 300 pp.

"Properties and Behavior of Corrosion Protective Organic Coatings as Determined by Electrical Impedance Measurements," J. V. Standish and H. Leidheiser, Jr., in Corrosion Control by Organic Coatings, Henry Leidheiser, Jr., Editor, National Association of Corrosion Engineers, Houston, Texas, 38-44 (1981).

"An AC Impedance Probe as an Indicator of Corrosion and Defects in Polymer/Metal Substrate Systems," M. C. Hughes and J. M. Parks, in Corrosion Control by Organic Coatings, Henry Leidheiser, Jr., Editor, National Association of Corrosion Engineers, Houston, Texas, 45-50 (1981).

"Rate Controlling Steps in the Cathodic Delamination of 10 to 40 μm Thick Polybutadiene and Epoxy Polyamide Coatings from Metallic Substrates," H. Leidheiser, Jr., and W. Wang, in Corrosion Control by Organic Coatings, Henry Leidheiser, Jr., Editor, National Association of Corrosion Engineers, Houston, Texas, 70-77 (1981).

"Mössbauer Spectroscopic Study of the Formation of Fe(III) Oxyhydroxides and Oxides by Hydrolysis of Aqueous Fe(III) Salt Solutions," S. Music, A. Vértes, G. W. Simmons, I. Czako-Nagy, and H. Leidheiser, Jr., J. Colloid Interface Sci. 85, 256-66 (1982).

"Technical Note: Inhibition of the Cathodic Reaction on Zinc in Aerated 3% NaCl Solution," H. Leidheiser, Jr., Y. Momose, and R. D. Granata, Corrosion 38, 178-9 (1982).

"The Metal Organic Coating Interface as Studied by Emission Mössbauer Spectroscopy," Henry Leidheiser, Jr., Svetozar Music, and Gary W. Simmons, Nature 297, No. 5868, 667-9 (1982); June 24-30, 1982 issue.

"Corrosion of Painted Metals—A Review," Henry Leidheiser, Jr., Corrosion 38, 374-83 (1982).

"Mössbauer Spectroscopic Study of the Corrosion Inhibition of Zinc by Cobalt Ions," Henry Leidheiser, Jr., Gary W. Simmons, Sandor Nagy, and Svetozar Music, J. Electrochem. Soc. 129, 1658-62 (1982).

"Some Effects of Acid-Base Interaction in Polymer Composites and Coatings," J. A. Manson, J.-S. Lin, and A. Tiburcio, Organic Coatings and Plastics Chemistry 46, 121 (1982).

"Surface Polarity of High-Temperature and Silane-Treated Iron Oxides by Water Adsorption," F. J. Micale and C.-C. Yu, Preprints, Org. Coatings Plastics Chem. 46, 7-11 (1982).

"Surface Polarity of High-Temperature and Silane-Treated Iron Oxides by Water Adsorption," M.S. Thesis, Chemical Engineering June 1982, by C.-C. Yu.

"Characterization of Electron Beam Cross-Linked Poly(Styrene-Block-Ethylene-Co-Butylene-Block-Styrene)," M.S. Thesis, Chemical Engineering, June 1982, by D. E. Zurawski.

"Electron Optical Methods and the Study of Corrosion," M.S. Thesis, Polymer Science & Engineering, October 1981, by Y. West.

"Preparation and Polymer Interaction of Colloidal Iron Corrosion Products," M.S. Report, Polymer Science & Engineering, June 1982, M.-H. Kang.

Papers Accepted for Publication

"Characterization of Solid Surfaces by Wet Chemical Techniques," F. M. Fowkes, in Industrial Applications of Surface Analysis, L. A. Casper and C. J. Powell, Editors, ACS Symposium Series, in press.

"The Atmospheric Corrosion of Iron as Studied by Mössbauer Spectroscopy," H. Leidheiser, Jr., and S. Music, Corrosion Science, in press.

"Fundamental Aspects of Corrosion Protection," H. Leidheiser, Jr., P. A. Clarkin, and E. McCafferty, Naval Research Review, in press.

"A Two-Step Anodization Process for Inhibition of the Oxygen Reduction Reaction on Iron," H. Leidheiser, Jr., and H. Konno, J. Electrochem. Soc., in press.

"New Studies of the De-Adhesion of Coatings from Metal Substrates in Aqueous Media—Interpretation of Cathodic Delamination in Terms of Cathodic Polarization Curves," Henry Leidheiser, Jr., Lars Igetoft, Wendy Wang, and Keith Weber, Proc. 7th Intl. Conf. in Org. Coatings Sci., in press.

SECTION 2

The Titles of the Component Programs Summarized Herein and the Participants

Programs Concerned with Corrosion at the Interface

- (1) Improved Corrosion Resistance of Steel in Mild Media
after Abrasive Blasting with Alumina

Principal Investigator: Henry Leidheiser, Jr.
Professor of Chemistry

Associate: John F. McIntyre
Research Associate

- (2) A Two-Step Anodization Process for Inhibition of the
Oxygen Reduction Reaction

Principal Investigator: Henry Leidheiser, Jr.
Professor of Chemistry

Associates: Hidetaka Konno
Visiting Scientist
Richard D. Granata
Research Scientist

Programs Concerned with the Chemistry of the Metal/Coating Inter- face

- (3) The Application of Emission Mössbauer Spectroscopy to
the Chemistry of the Coating/Substrate Bond

Principal Investigator: Henry Leidheiser, Jr.
Professor of Chemistry

Associate: Svetozar Music
Visiting Scientist

- (4) Determination of the Acidity of Iron Oxide Surfaces

Principal Investigator: Frederick M. Fowkes
Professor of Chemistry

Associate: Sara Joslin
Graduate Student

Programs Concerned with the Chemistry of the Metal/Coating Interface Cont'd.

(5) Ion Exchange Properties of Iron Surfaces

Principal Investigator: Gary W. Simmons
Professor of Chemistry

Associate: Bruce Beard
Graduate Student

(6) Investigation of Phosphated Steel Surfaces by Laser Raman Spectroscopy

Principal Investigator: Henry Leidheiser, Jr.
Professor of Chemistry

Associate: Andre' Sommer
Graduate Student

Programs Concerned with the Properties of the Coating

(7) Detection of Aggregated Water in Polymer Coatings

Principal Investigator: Henry Leidheiser, Jr.
Professor of Chemistry

Associate: Douglas Eadline
Graduate Student

(8) Radiochemical and Electrochemical Measurements of Diffusion in Organic Coatings

Principal Investigator: Henry Leidheiser, Jr.
Professor of Chemistry

Associate: Jeffrey Parks
Graduate Student

(9) Drying and Curing of Epoxy Films

Principal Investigator: Mohamed S. El-Aasser
Professor of Chemical Engineering

Programs Concerned with the Properties of the Coating Cont'd.

(9) Drying and Curing of Epoxy Films Cont'd.

Associates:

Cesar Silebi
Assistant Professor of Chem. Engrg.
John W. Vanderhoff
Professor of Chemistry
Kenneth Earhart, Staff
Olga Shaffer, Staff
Arif Humayun, Graduate Student
Ata-Ur Rahman, Graduate Student

(10) Cathodic Electrodeposition of Polymer Latexes

Principal Investigator: Mohamed S. El-Aasser
Professor of Chemical Engineering

Associates:

John W. Vanderhoff
Professor of Chemistry
Kenneth Earhart, Staff
Olga Shaffer, Staff
Ata-Ur Rahman, Graduate Student
J. Andrew Hadley, Graduate Student

(11) Application of Laser Raman Spectroscopy to the Analysis of Electrodeposited Epoxy Resin

Principal Investigator: Eugene M. Allen
Professor of Chemistry

(12) Pigment/Binder Interactions and Corrosion Protection

Principal Investigator: John Manson
Professor of Chemistry

Associate:

Astrophel Tiburcio
Graduate Student

Programs Related to the Surface Properties of Iron Oxides from the Standpoint of Their Presence at the Steel/Organic Coating Interface and Their Use as Pigments

(13) Characterization of the Surface Properties of Iron Oxides

Principal Investigator: Fortunato J. Micale
Associate Professor of Chemistry

Programs Related to the Surface Properties of Iron Oxides from
the Standpoint of Their Presence at the Steel/Organic Coating
Interface and Their Use as Pigments Cont'd.

- (13) Characterization of the Surface Properties of Iron Oxides
Cont'd.

Associates:

C.-C. Yu, Graduate Student
Dennis J. Kiernan, Graduate
Student

- (14) An Understanding of the Principles Related to the Appli-
cation of Paints to Rusted Steel Surfaces with Little or
No Surface Preparation

Principal Investigator: John W. Vanderhoff
Professor of Chemistry

Associates:

Mohamed S. El-Aasser
Professor of Chemical Engineering
John A. Manson
Professor of Chemistry
Fortunato J. Micale
Associate Professor of Chemistry
Leonard M. Bennetch, Consultant
Kenneth A. Earhart, Staff
Olga Shaffer, Staff
T-C. Huang, Graduate Student
M.-H. Kang, Graduate Student
Donna Visioli, Graduate Student

Active Programs Not Summarized in the Present Report

Optical Studies of Corrosion under Organic Coatings

Principal Investigator: David A. Thomas
Prof. of Metallurgy and Materials
Engineering

Associate: Dale Zurawski, Graduate Student

The Mechanism for the Cathodic Delamination of Coatings
from a Metal Surface

Principal Investigator: Henry Leidheiser, Jr.
Professor of Chemistry

Associate: Wendy Wang, Graduate Student

The Mechanism of the Oxygen Reduction Reaction

Principal Investigator: Richard D. Granata
Research Scientist

SECTION 3

A Summary of the Experimental Results Obtained during the Period, September 1, 1981 - August 31, 1982

A summary is given herein of the total research program, the components of which are directed by 9 Lehigh faculty members and a research scientist.

The corrosion process which occurs beneath an organic coating is electrochemical in nature with readily identifiable anodic and cathodic regions. These regions are being studied under the microscope using time lapse motion picture photography in the case of transparent coatings. The behavior of the separate anodic and cathodic regions, the merging of these regions, and the onset of new regions of activity are being studied. These efforts will be complemented during the next year with electrical and microscopic studies of the coating/substrate interface as viewed through a thin transparent metal deposited onto glass. The latter method will permit quantitative studies of the corrosion and will permit the study of pigmented opaque coatings.

The development of cathodic areas beneath the coating leads to breakdown of the coating/substrate bond and the accumulation of an aqueous phase in contact with the metal. The phenomenon is known as "cathodic delamination" or "cathodic disbondment" and has been the subject of past studies. The parameters governing the rate of growth of the cathodic area have been extensively studied previously. Work during the present report period has concentrated on a quantitative interpretation of the diffusion processes which occur through the coating and laterally through the aqueous phase in the interfacial region. The species which appear to play the major role in the rate controlling process are oxygen and cations. The critical issue is to determine which species is involved in the rate controlling step under specific conditions.

It is well known that the service behavior of an organic coating is critically dependent on the treatment which the metal received prior to the application of the coating. The effect of abrasive blasting with alumina has been singled out for special examination after it was noted that the rate of cathodic delamination was decreased after such treatment relative to other forms of surface abrasion. Corrosion potential measurements, polarization resistance studies and additional cathodic delamination studies provided evidence that steel abrasively blasted with alumina exhibits a lower initial rate of corrosion in mild media than similar steels blasted with steel grit or abraded with silicon carbide paper. Auger spectroscopy and electron microprobe analysis revealed the presence of significant amounts of aluminum

species on the surface, largely in the form of embedded alumina particles but possibly also as a constituent of the oxide film on the steel. Non-metallic abrasive blasting may have application in the chemical modification of metal surfaces.

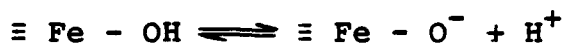
A critical issue in understanding better the protective performance of organic coatings is the chemical nature of the organic coating/metal interface. Mössbauer emission spectroscopy was applied to this problem in the case of a model system, cobalt/polybutadiene. Radiotracer cobalt in the interfacial region provided the gamma-ray source which was analyzed. The following conclusions were drawn about the interfacial region: (1) The contact between the cobalt metal and the polybutadiene is through an oxide or hydrous oxide at the interface. (2) No major changes occurred at the cobalt surface developed after application of the coating and before thermal treatment. (3) The oxide on cobalt did not thicken during the thermal curing of the polybutadiene. (4) Thermal treatment at 200°C caused a significant amount of conversion of trivalent species to divalent species at the oxide/coating interface. (5) The reduction process was not a consequence of the reaction, $2\text{Co}^{3+} + \text{Co} = 3\text{Co}^{2+}$, during baking of the coating because the relative amount of unoxidized metal remained approximately constant before and after thermal curing.

In a related study of a metal substrate/metal coating interface the Mössbauer technique was applied to a coating of flame-sprayed aluminum on a cobalt substrate. The oxide film on cobalt remained constant in amount before and after flame spraying indicating that the aluminum did not reduce the oxide film on cobalt and the oxide film did not thicken. There was no evidence of a change in the chemical nature of the cobalt oxide at the interface. These results are added support for the viewpoint that the bonding between flame sprayed aluminum and another metal is largely mechanical in nature.

The adhesion of organic coatings to inorganic oxides, such as those which normally exist on a steel surface, result from acid/base interactions between the polymer and the oxide. Quantitative studies of polymer/oxide interactions based on the acid/base concept have been made using flow microcalorimetry. The adsorption of pyridine and poly-2-vinyl pyridine on $\alpha\text{-Fe}_2\text{O}_3$ powders and the desorption of the adsorbed species have been determined. These results indicate that the microcalorimetry technique is satisfactory for studying the kinetics of the adsorption of polymers on high area metal oxides and that it may be useful in studying the competitive adsorption between water and an organic polymer. Such information may be useful in understanding better the loss of adhesion of some coatings when exposed to aqueous environments at room or elevated temperature.

Metals exposed to the atmosphere readily form a surface oxide. This oxide interacts with moisture in the air or with aqueous phase water to form an hydroxylated surface. It is with such a surface that a coating interacts. A better understanding of this surface

oxide is required. Auger spectroscopy and X-ray photoelectron spectroscopy are being utilized to characterize the oxide surface. Steel, surfaced in a standard way, is immersed in a medium, the pH of which is closely controlled, and the amount of a constituent in the medium which is present on the metal surface after immersion is determined. Complications arising from surface contamination have been minimized by the use of ultrapure chemicals, prior thermal treatment in a hydrogen atmosphere in a quartz furnace, and the use of highly purified distilled water. The acid/base properties of an iron surface have been appraised in terms of the pick-up of potassium by the surface as a function of pH. The results, albeit with considerable scatter in the data, were interpreted in terms of the two equilibria:



Preliminary experiments have been carried out to explore the possibility of studying the substrate/organic coating interface or conversion coatings at the interface in a non-destructive way using laser Raman spectroscopy. The technique has been found capable of fingerprinting different phosphates and different iron oxides. Good spectra of the phosphate can be obtained through an organic coating provided the coating does not fluoresce under the incident laser radiation. Representative spectra of phosphate coatings on steel and a manganese-based phosphate beneath a polyester-melamine coating are given.

Corrosion beneath an organic coating is dependent on the presence of an aqueous phase at the interface. Without an aqueous phase the electrochemical corrosion process does not occur. Capacitance measurements have proven to be a useful method to detect the amount of water taken up by a coating exposed either to a humid environment or to an electrolyte. However, these measurements do not distinguish between water that is dispersed throughout the coating in a gas-like form from water that has aggregated to form a condensed phase. A technique which appears to have the capability to distinguish between these two forms of water is based on dielectric measurements at 10^9 Hz using a technique known as time domain spectroscopy. Equipment to make such measurements has been constructed, the computer programs have been developed, and the data handling methods have been tested. Tests with Teflon and with polyvinyl acetate yield dielectric values in agreement with quoted values in the literature. The dielectric values changed appreciably upon exposure of polyvinyl acetate coatings to steam, a method known to introduce water into a coating. The major problem encountered to date is the undesired reflections which occur in the microwave cavity. The method looks promising as a means for detecting aggregated water in a coating.

Radiotracer measurements have been adopted as a means for quantitatively determining the rate of migration of anions and cations through a coating. Such information is critically important in a quantitative description of cathodic delamination and in a quantitative description of the aging process of coatings exposed to an aggressive environment. The following steady-state values for the diffusion coefficients of Na^+ , Cl^- , and H_2O through an alkyd coating, 28-51 μm in thickness, were obtained: $7.0 \times 10^{-8} \text{ cm}^2/\text{hr}$, $2.3 \times 10^{-8} \text{ cm}^2/\text{hr}$, and $3.8 \times 10^{-8} \text{ cm}^2/\text{hr}$, respectively. These values are the average of duplicate measurements made on 12 different coatings. The diffusion of water differed from that of Na^+ and Cl^- in that the rate of diffusion of water was very rapid during the first 3 hours. During this period, the diffusion coefficient for water was $1.25 \times 10^{-6} \text{ cm}^2/\text{hr}$. The diffusion coefficients are of the same magnitude as those reported by other investigators for free films.

The properties of an organic coating are importantly dependent upon drying conditions. Important parameters include temperature, air velocity, and relative humidity. Drying curves were obtained for 4 different aqueous-based epoxy systems and one organic solvent-based epoxy system in a homemade wind tunnel under various drying conditions: temperature 77 - 104°F, air velocity 1 - 76 cm/sec, and relative humidity 10-52%. The drying curves of the aqueous-based latex system, and to a lesser extent the aqueous-solubilized formulations, showed that the initial low and constant flux rate is followed by a sudden increase in flux which may or may not drop again at the advanced stages of drying. This phenomenon was taken as an indication of "skin" formation at the surface of the coating. This effect did not exist in the drying of films cast from organic solvents. Drying curves for the same 5 epoxy systems were generated under milder drying conditions. Increasing the relative humidity, at constant temperature and air velocity, resulted in increasing the time at which the upswing in the flux curves took place during the advanced stages of drying. Morphological studies of the dry films showed that rapid drying leads to rough surfaces and cracks, whereas mild drying conditions yielded smoother films and a lesser number of cracks. The relative corrosion protection performance of films dried under different conditions will be studied.

Studies are being carried out to determine the corrosion protection properties of coatings prepared in different ways. Epoxy coatings prepared from aqueous and organic solvent systems and dried under different conditions were described above. A third technique for preparing the coating is based on cathodic electrodeposition from aqueous dispersions. The kinetics of film growth were studied during the cathodic electrodeposition of single-component Epon 1001 latex and a mixture of two-component Epon 1001-amine curing agent latex systems. The current-time curves generated at constant voltage were analyzed to calculate the mass of deposited film vs. time relationship and the coulombic efficiency of deposition from these latex systems was high, 60-98 mg/coulomb; 3-8 times higher than the reported

coulombic efficiency of polymer solubilized systems. A linear relationship was established between the mass of deposited film and deposition time, indicating that the presence of the film does not affect continued film growth. A mechanism was proposed for the cathodic electrodeposition of latex particles, which involved nonionic accumulation of the particles at the cathode followed by coalescence of the particles under the effect of the electrical pressure.

A polyurethane-modified acrylic graft copolymer cationic latex system was prepared by a 3-step process involving solution polymerization, emulsification and emulsion polymerization. Studies of the cathodic electrodeposition behavior of this latex have been initiated. The kinetics of the electrodeposited film growth at constant applied voltage were determined. Current-time curves at constant applied voltages have been generated over a voltage range of 50-225 v., and the coulombic efficiency for deposition was calculated. Much better coating films were produced with this polyurethane latex system compared to the epoxy latex. The well-behaved polyurethane latex system lends itself to a more quantitative analysis of important electrodeposition process parameters such as, percent solids in the bath, surface charge density of the particles, pH and agitation.

Laser Raman spectroscopy has been applied to the determination of the epoxy/amine ratio on a localized basis in a coating on steel. Two Raman lines, one at 1609 cm^{-1} characteristic of the epoxy and the other at 1450 cm^{-1} characteristic of the amine, were selected as candidates for determining the epoxy/amine ratio. The peak ratio method showed promise but much more work remains to be done before the method can be accepted.

The permeabilities of zinc and glass-bead-filled epoxy films, a model system for studying water transport, are sensitive to the interfacial adhesion and hence to the extent of the acid/base interaction. The tighter the interface, the lower the permeability. As predicted by theory, the permeability of the composite may exceed that of the matrix alone if the filler and the matrix are not well bonded. With zinc-filled films, poor initial interfacial adhesion permits the generation of corrosion products that quickly fill up the pores and reduce the permeability to that of a well bonded composite. The permeability is also lower, the more rigorous the curing condition.

Studies of iron oxides were performed with the hope that a better knowledge of the surface character of iron oxides might be helpful in improving the adherence of organic coatings to a steel surface and might be helpful in designing systems for use in painting slightly oxidized or rusted steel. Commercial materials and colloidal sols were used.

The surface properties of four iron oxides, Fe_3O_4 , $\alpha\text{-Fe}_2\text{O}_3$, $\alpha\text{-FeOOH}$ and $\beta\text{-FeOOH}$ were appraised using argon gas adsorption, water adsorption, silane treatment, and calorimetric measurements

of heats of adsorption. α -FeOOH surfaces were strongly hydrophilic and this hydrophilicity was maintained after heating at 200°. Hydrophilicity of α -Fe₂O₃ and Fe₃O₄ was increased by heating. The hydrophilic nature of the surface is considered to be a consequence of the presence of hydroxyls at the surface.

Eight compounds, identified by others as corrosion products of iron, were prepared in the form of colloidal sols: Fe₃O₄, α -Fe₂O₃, γ -Fe₂O₃, α -FeOOH, β -FeOOH, γ -FeOOH, δ -FeOOH, and FeCO₃. Methods used in the preparation of these materials are outlined. The compounds were characterized by means of X-ray diffraction, Mössbauer spectroscopy, and by electron microscopy. Typical surface areas ranged from 16 to over 200 m²/g. Adsorptions of polymethyl methacrylate, acidic chlorinated polyvinyl chloride, Epon 1001F epoxy resin, and Emerez 1511 curing agent were determined on 4 iron oxides from organic solvents. The amounts of polymer adsorption as measured in mg polymer/m² surface area for the 4 polymers, respectively, were: α -Fe₂O₃ 90, 22, 20.5, 17; γ -Fe₂O₃ 315, 2, 9, 13; Fe₃O₄ 140, 15, 2, 11; α -FeOOH 590, 4.5, 19, 11.5. These values, however, were a function of the method used in the preparation of the oxide dispersion. Two methods gave adsorption values far in excess of those expected for monolayer adsorption.

SECTION 4

Program #1. Improved Corrosion Resistance of Steel in Mild Media after Abrasive Blasting with Alumina

ABSTRACT

Corrosion potential measurements, polarization resistance studies and cathodic delamination studies provide evidence that steel abrasively blasted with alumina exhibits a lower initial rate of corrosion in mild media than similar steels blasted with steel grit or abraded with silicon carbide paper. Auger spectroscopy and electron microprobe analysis revealed the presence of significant aluminum on the surface, largely in the form of embedded particles but possibly also as a constituent of the oxide film. Non-metallic abrasive blasting may have application in the chemical modification of metal surfaces.

INTRODUCTION

Many miscellaneous observations of our own and of others during the past few years have made us aware of the important role that surface condition plays in the superficial corrosion of metals. More recently we have noted a very effective inhibition of corrosion of steel which had been subjected to abrasive blast cleaning with alumina. This observation heightened our interest because it had previously been found that the oxygen reduction reaction occurs much less readily on an aluminum surface than on a steel surface [1,2]. Since the rate at which the oxygen reduction reaction occurs is critically important in the cathodic disbonding of an organic coating from a metal substrate under many experimental conditions [3], it appeared worthwhile to explore further the effect of abrasive blasting with alumina on the superficial corrosion of steel. The results of this work may be valuable to workers with practical corrosion problems involving coated metals.

There is much interest at the present time in modifying the surface composition of steels in order to develop superior corrosion resistant behavior. Techniques such as ion implantation, laser surface alloying, and surface diffusion processes are being explored intensively. It appears that another candidate method for modifying the surface composition is non-metallic abrasive blasting. The

term, "non-metallic abrasive blasting", is used because there are proprietary processes that utilize metallic-coated abrasives that leave significant amounts of the metallic component on the substrate.

RESULTS

The experimental data from which the conclusions were drawn are based on corrosion potential measurements, polarization resistance measurements, gravimetric corrosion studies, cathodic delamination studies, Auger spectroscopy and electron microprobe analyses of blasted surfaces, and Mössbauer spectroscopy of corrosion products. The results from each of these techniques will be reported.

Corrosion Potential Measurements. All measurements reported here were carried out with 1010 steel in distilled water at room temperature. Representative corrosion potential measurements for various types of surface treatments are summarized in Table I. It will be noted that in all sets of experiments the corrosion potential moved in the active direction as a function of time and that panels abraded with alumina had more positive potentials.

A second set of experiments was carried out in which the samples, surface treated in various ways, were oxidized in air at 220°C for 1-1/2 - 2 hr before immersion in the distilled water and measurement of the corrosion potential. These data are summarized in Table II. Again, the corrosion potential of the samples blasted with alumina exhibited more noble potentials after short immersion times.

Polarization Resistance Measurements. This technique was adopted as the prime method for comparing corrosion behavior since it was desired to make corrosion measurements at short times in the situation where the metal corrosion loss was minimal. It was also desired to make corrosion measurements as a function of time without removing the samples from the solution. Polarization resistance measurements appeared to meet the required needs.

Measurements were made in each experiment at 20, 50, and 80 minutes after the sample was immersed in distilled water. It will be noted from the data summarized in Table I that samples surfaced by blasting with either pumice or alumina resulted in a lower corrosion rate during the 80-minute duration of the experiment. The corrosion rate increased as a function of time in the cases of the as-received materials, those abraded with silicon carbide, and those abrasively cleaned with steel grit, whereas the corrosion rate decreased as a function of time for the panels abrasively cleaned with glass beads, pumice, or alumina.

Table I

Calculated Corrosion Rates from Polarization Resistance
Measurements of Steel in Distilled Water after
Surfacing in Various Ways

<u>Surface Treatment</u>	<u>Time of Immersion in Min.</u>	<u>Calc. Corrosion Rate in mpy</u>	<u>Corrosion Potential vs. SCE</u>
As received	20	0.83	-0.603 v.
	50	0.91	-0.659
	80	1.00	-0.667
Abraded with 600 grit silicon carbide paper	20	0.57	-0.464
	50	0.74	-0.526
	80	0.74	-0.610
Blasted with G-80 steel grit	20	0.38	-0.416
	50	0.53	-0.462
	80	0.67	-0.554
Blasted with glass beads	20	1.47	-0.644
	50	0.84	-0.660
	80	0.76	-0.670
Blasted with pumice	20	0.43	-0.505
	50	0.30	-0.569
	80	0.27	-0.601
Blasted with alumina (54 lbs pressure)	20	0.12	-0.343
	50	0.09	-0.410
	80	0.09	-0.489
Blasted with alumina (40 lbs pressure)	20	0.32	-0.238
	50	0.22	-0.370
	80	0.25	-0.420

Table II

Calculated Corrosion Rates for Polarization Resistance
Measurements of Steel in Distilled Water after
Various Surface Treatments Followed by
Oxidation in Air at 220°C

<u>Surface Treatment</u>	<u>Time of Oxidation in Hrs.</u>	<u>Time of Immersion in Min.</u>	<u>Calculated Corrosion Rate in MPY</u>	<u>Corrosion Potential vs. SCE</u>
As received	2	3	61	-0.586 v.
		28	0.51	-0.672
		48	0.61	-0.674
As received	1.5	5	16.5	-0.592
		30	3.6	-0.674
		50	2.6	-0.696
Blasted with alumina	2	3	1.8	-0.250
		28	0.21	-0.522
		48	0.21	-0.526
Blasted with alumina	1.5	5	4.5	-0.350
		30	1.0	-0.594
		50	0.84	-0.622
Blasted with G-80 steel grit	2	3	46.5	-0.448
		28	1.1	-0.556
		48	0.89	-0.550
Abraded with 600 grit silicon carbide paper	2	5	5.5	-0.430
		25	0.72	-0.540
		50	0.78	-0.552

The relationship between the corrosion rate and the corrosion potential for all the data summarized in Table I is given in Figure 1. The data obtained for the panels abrasively cleaned with either alumina or pumice are outlined in the rectangular boxes.

Data for the calculated corrosion rates of panels surface treated in various ways and then oxidized in air at 220° for 1-1/2-2 hr are summarized in Table II. The corrosion rate measured after 3-5 min exposure to the distilled water was much lower in the case of the alumina-blasted panels than any of the other panels surface treated in other ways. No conclusions could be drawn about the effect of surface treatment plus oxidation after immersion in distilled water for 30 min.

Gravimetric Corrosion Studies. Weight loss measurements over a 16-day period indicated very little difference in the rate of corrosion of samples abraded with silicon carbide and those blasted with alumina. The weight losses per cm² after 3, 7, and 16 days' exposure to distilled water were 0.35 mg, 0.78 mg, and 1.28 mg for the abraded steel and 0.42 mg, 0.84 mg, and 1.58 mg for the alumina-blasted steel. These measurements indicate that the lower corrosion rate after alumina blasting applies only to the very first stages of the corrosion.

Cathodic Delamination. Steel panels, approximately 6 mm in thickness, with a composition typical of a pipeline steel were coated with a commercial epoxy powder coating according to the specifications of the manufacturer. The panels were heated in an oven to 450°F and were spray coated with the epoxy powder to yield a coating 0.25 - 0.55 mm thick. A 3.1 mm diameter hole was drilled through the coating and it was then made the cathode at a potential of -1.5 v vs. SCE in 0.5M NaCl solution. The panel was removed at intervals and the area delaminated radially from the hole was determined by cutting the coating with a knife and measuring the boundary of the non-adherent region. Data typical of panels abrasively cleaned with steel grit and those abrasively cleaned with alumina are given in Figure 2. Each point in Figure 2 represents a separate experiment on panels that were prepared at the same time. Although the absolute values of the delamination rate varied with the type of epoxy powder, the alumina blasted panels yielded a lower rate of delamination than the steel-grit-blasted panels.

Chemical Analysis of the Surface. Auger spectroscopy yielded evidence that aluminum was a constituent of the surface and was present in concentrations greater than 1%.

SEM studies of the surface indicated that many particles of alumina were visible as shown, for example, in Figure 3. X-ray fluorescence analysis of the individual particles yielded a very strong signal for aluminum and a minor signal for iron. A significant signal for aluminum was obtained over much of the surface, along with the expected very large signal for iron, in areas in which there were no readily identifiable particles of alumina. The

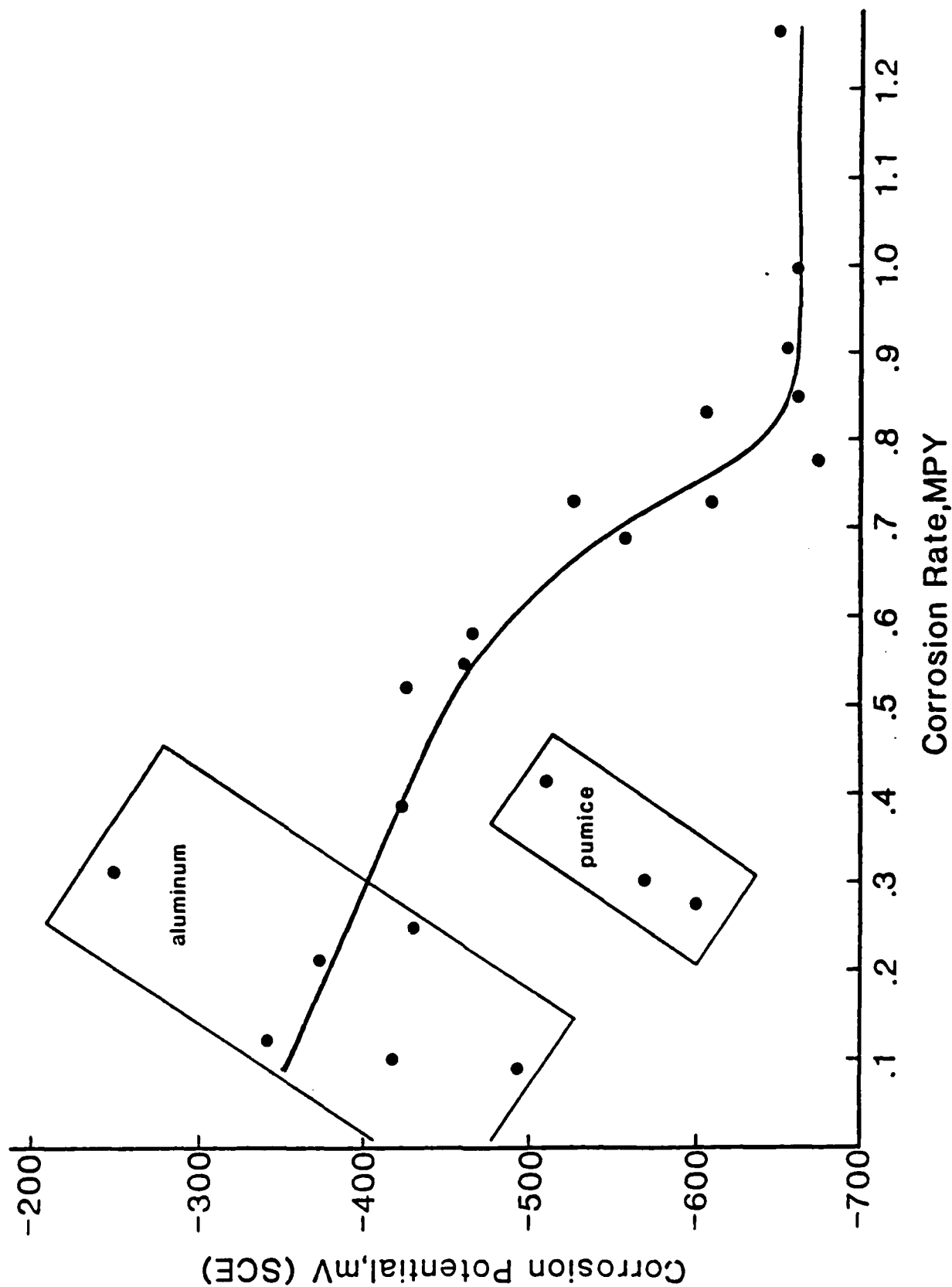


Figure 1. Plot of corrosion potential against corrosion rate.
Data taken from R_p studies in distilled water.

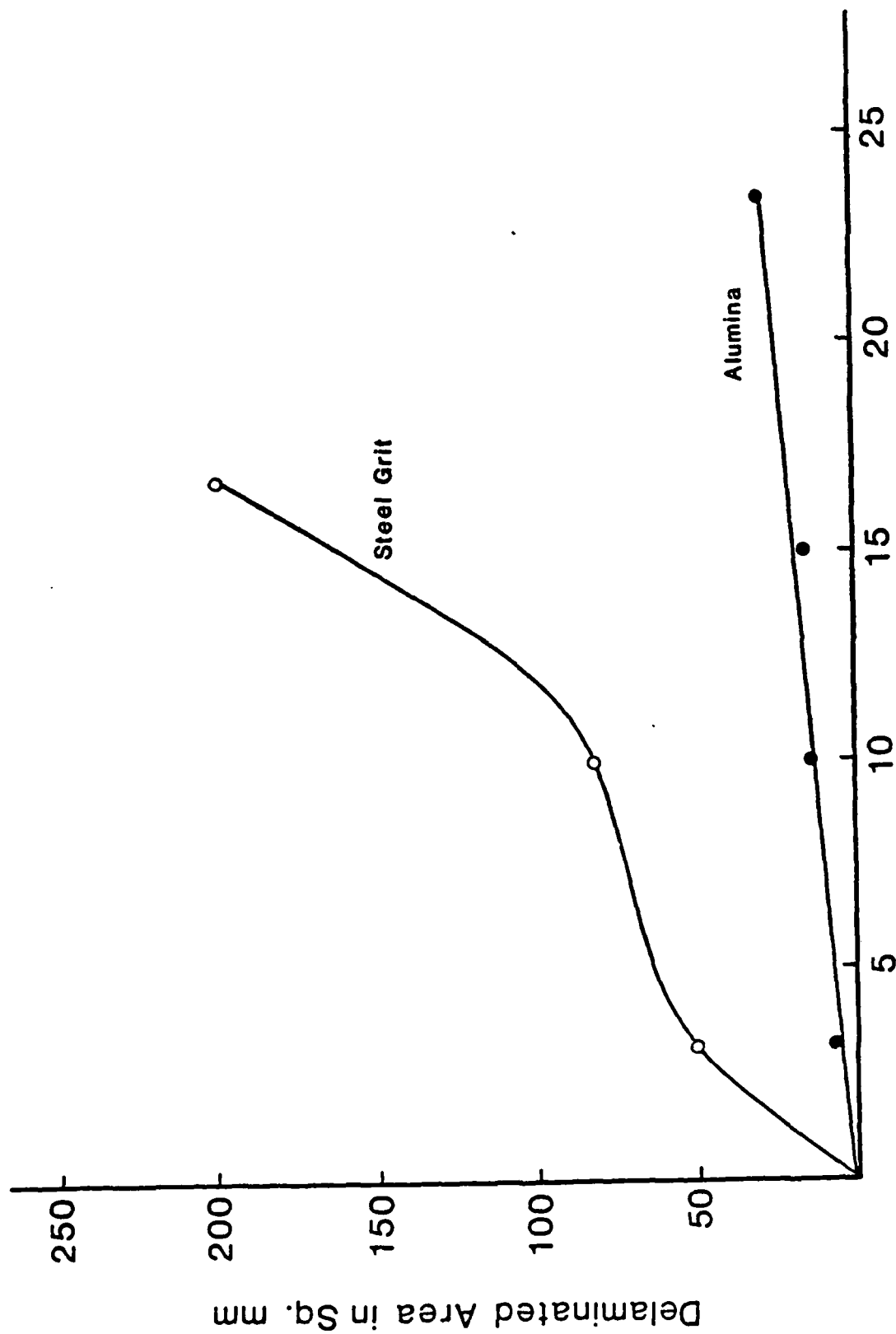


Figure 2. Plot of delaminated area against time for cathodic delamination studies of epoxy-powder coated steel surfaced by abrasive blasting with steel grit and alumina.

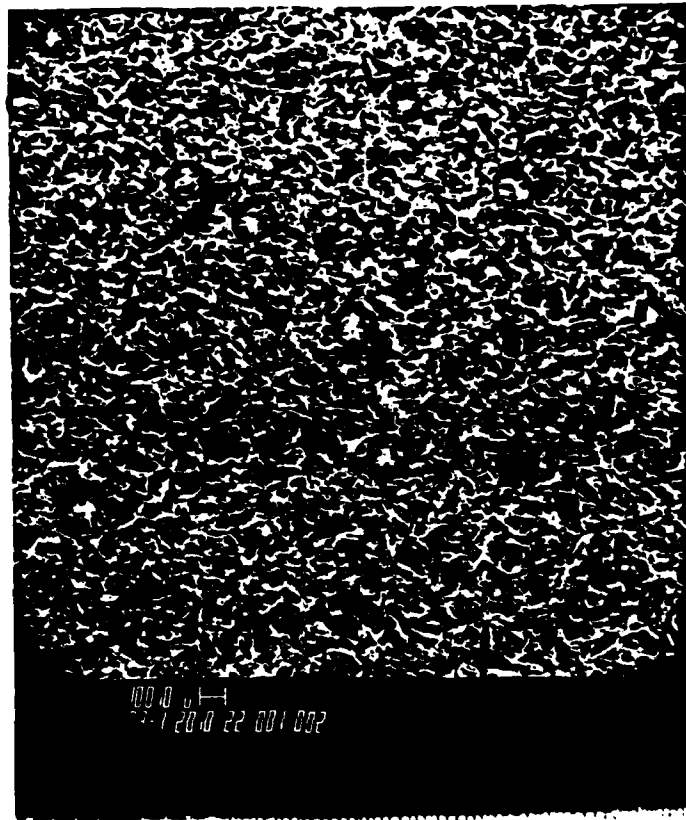


Figure 3. SEM photograph of alumina blasted steel. White particles indicate embedded alumina as determined by X-ray fluorescence analysis. 30X.

X-ray studies gave the impression that the aluminum was present in low concentration over the entire surface along with individual particles of alumina.

Mössbauer Spectroscopy. It was noted that the appearance of the surface was very different when alumina-blasted steel was corroded in water at room temperature or at 90°C in comparison with steel-grit-blasted steel under the same conditions. The alumina-blasted surface was dark in color whereas the steel-grit-blasted surface had the typical orange-brown color of rusted steel. This difference in surface appearance was maintained during corrosion for times as long as 20 days.

The adherent corrosion product was scraped from the surface of the steel and transmission Mössbauer spectra were obtained. The chief distinguishing feature of the spectra is the presence of Fe_3O_4 on the surface of the alumina-blasted steel and the presence of $\gamma\text{-Fe}_2\text{O}_3$ on the surface of the steel-grit-blasted steel. This difference is readily visible in the two sharp peaks on the left of the spectrum in Figures 4 and 5 which are characteristic of Fe_3O_4 and the much lower intensity of the inner peak of the outer pair on the left in Figures 6 and 7 which indicates that the stoichiometry of Fe_3O_4 is approaching that of $\gamma\text{-Fe}_2\text{O}_3$. A tabulation of the Mössbauer parameters of the constituents giving rise to the spectral components is given in Table III.

It is well known that abrasive grit blasting leads to the incorporation of the grit in the surface of the softer metal being subjected to the abrasive treatment. An interesting example of this phenomenon is cited here. A steel panel was blasted with steel grit. Examination of the surface under the optical microscope and the scanning electron microscope suggested the incorporation of a small amount of the steel grit in the surface but it was very difficult to discriminate between the substrate and the grit because of the similar composition. The steel was then oxidized in air at 275°C for 2 hours and, after cooling, the surface was masked with adhesive tape. The tape was removed and it was noted that a large quantity of fine powder was attached to the tape. Mössbauer spectroscopic analysis indicated that the particles were elemental iron with Mössbauer parameters characteristic of the steel grit. The slight oxidation of the surface was sufficient to break the loose adhesion between the grit and the steel surface.

DISCUSSION

Data from measurements of corrosion potential, polarization resistance, and cathodic delamination studies indicate that abrasive treatment of steel with alumina powder leads to a surface which is less active relative to steel not subject to abrasive treatment.

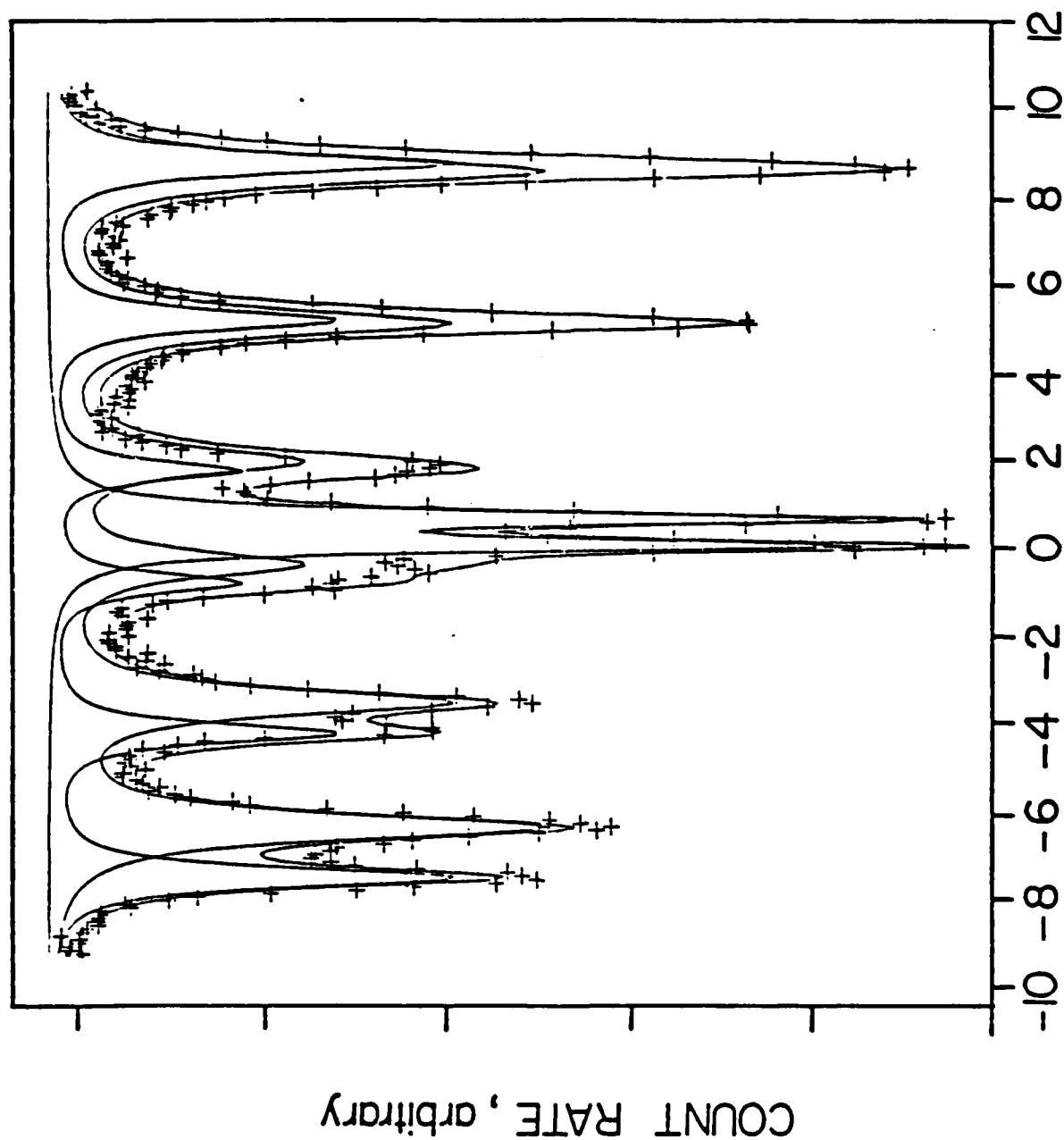


Figure 4. Mössbauer spectrum of adherent corrosion products from alumina blasted sample. Specimen was immersed in distilled water at room temperature for twenty days.

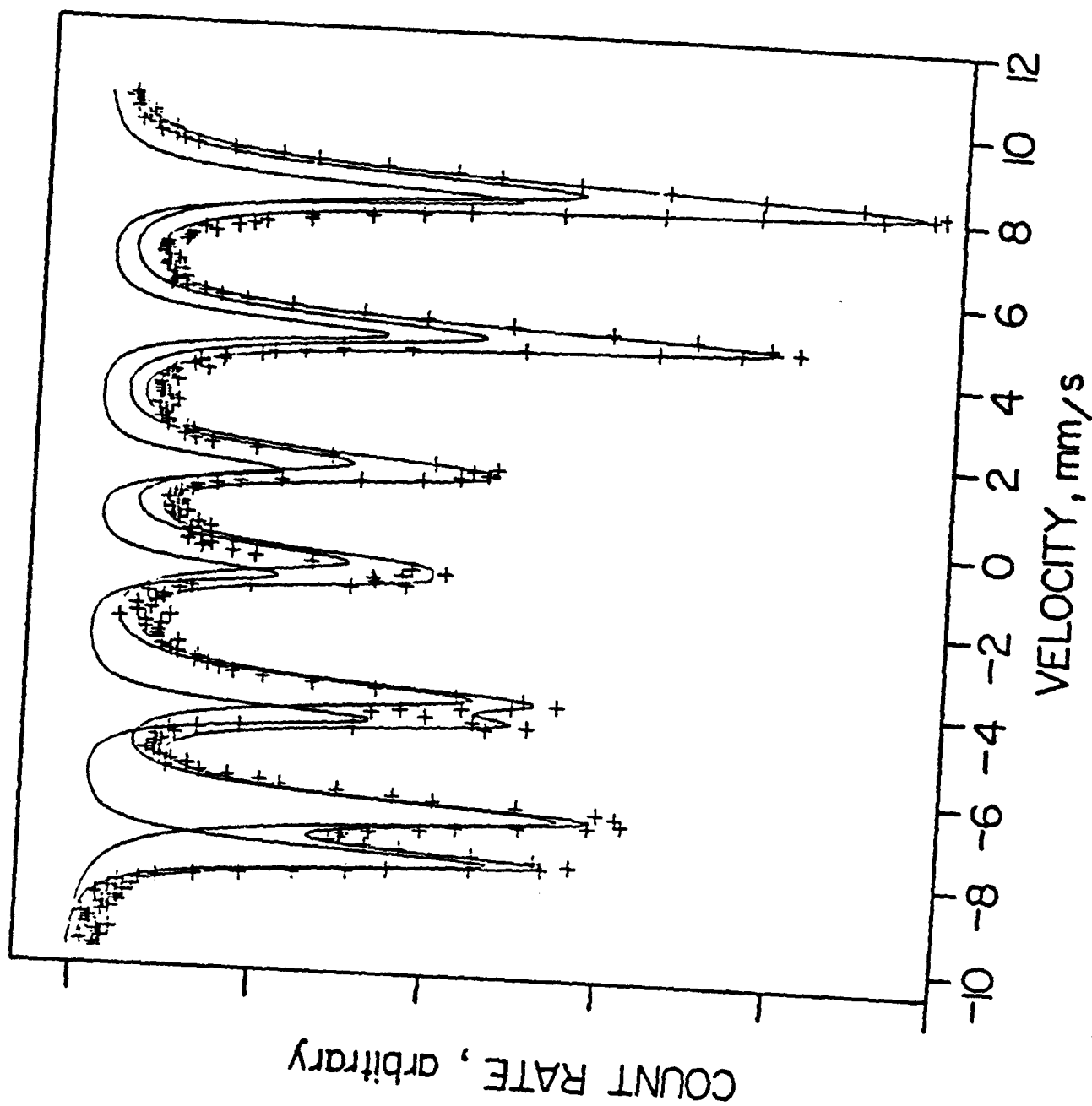


Figure 5. Mössbauer spectrum of adherent corrosion products from alumina blasted sample. Specimen was immersed in distilled water at 90°C for twenty days.

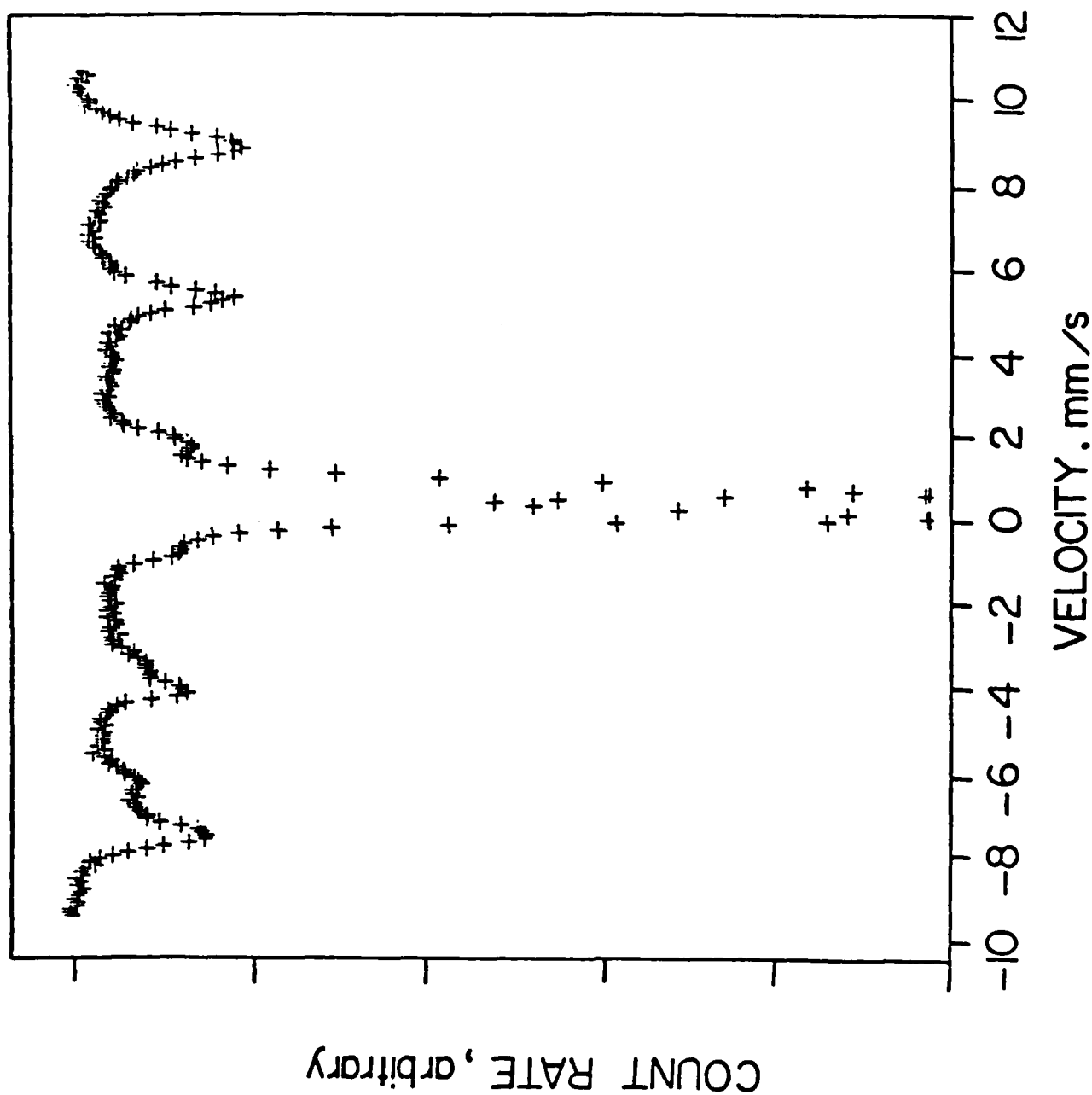


Figure 6. Mössbauer spectrum of adherent corrosion products from steel grit blasted sample. Specimen was immersed in distilled water at room temperature for twenty days.

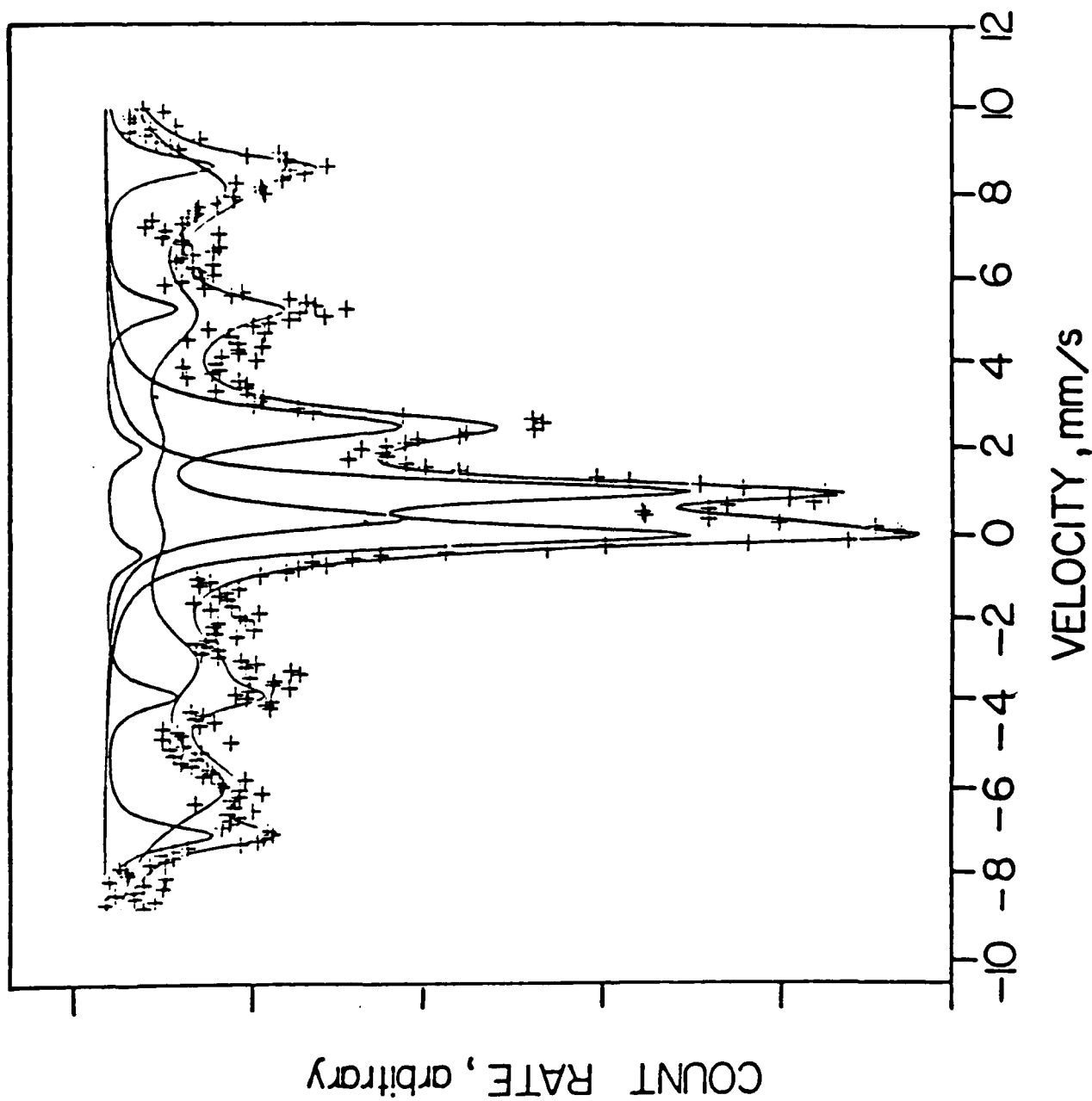


Figure 7. Mössbauer spectrum of adherent corrosion products from steel grit blasted sample. Specimen was immersed in distilled water at 90°C for twenty days.

Table III

Summary of the Mössbauer Parameters Giving Rise to the Spectra in Figures 4-7.

Figure No.	Component	Chemical Shift (mm/sec)	Quadrupole Splitting (mm/sec)	Magnetic Hyperfine Splitting kOe	Relative Area	Compound
4	Doublet	0.238	0.610		17%	γ -FeOOH
	6-line	0.474		508	31%	Fe_3O_4
	6-line	0.885		467	52%	Fe_3O_4
5	6-line	0.305		499	37.5%	Fe_3O_4
	6-line	0.811		470	62.5%	Fe_3O_4
6	Doublet	0.210	0.621		40%	γ -FeOOH
	6-line	0.482		507	41%	Mixture of γ - Fe_2O_3 and Fe_3O_4
	6-line	0.901		463	19%	
7	Doublet	0.231	1.040		27%	γ -FeOOH
	Doublet	1.107	2.168		21%	$\text{Fe}(\text{OH})_2$
	6-line	0.370		492	39%	Mixture of γ - Fe_2O_3 and Fe_3O_4
	6-line	0.662		441	13%	

Supporting evidence that the alumina treatment affects the activity of the surface came from the Mössbauer studies of the product formed during corrosion in distilled water and from surface analysis which indicated the presence of aluminum. Although we are reluctant to say that the data contained herein conclusively prove that abrasive blasting of steel with alumina leads to a less active steel surface, this evidence along with information on the reduced activity of steel surfaces implanted with aluminum [4] suggests that superficial corrosion of steel may be reduced by proper abrasive treatment with alumina.

The corrosion potential of the alumina-blasted steel in distilled water was significantly more noble than steel blasted with steel grit, abraded with silicon carbide or used in the as-received condition. This difference in behavior of the corrosion potential was maintained for at least 80 min at room temperature showing that the difference was real and was not based on a very short term transient effect. This more noble potential combined with the lower corrosion rate proves that the main effect is on the anodic corrosion reaction and that the anodic/cathodic surface area ratio is less on the alumina-blasted panels than on the steel panels blasted with steel grit or polished with silicon carbide. However, the cathodic delamination studies indicate that the surface was also inactivated for the oxygen reduction reaction. It thus appears that the blasting with alumina results in a surface which is inhibited for both the anodic and cathodic half reaction, but the anodic inhibition occurs to a greater extent than the cathodic inhibition.

The low corrosion rate and more noble potential of the alumina-blasted steel in distilled water after oxidation at 220°C indicate that effects of alumina blasting are not readily dissipated. These experimental results also have significance to epoxy powder coating since the steel is heated in air before the application of the dry powder.

The Mössbauer data are surprising because the effects are observed over a 20-day period in which the panel was maintained at room temperature or at 90°C in the distilled water. The effects are real because they were repeated several times. The sharp twelve-line hyperfine splitting spectrum is characteristic of Fe_3O_4 and the relative intensities of the two six-line spectra allow one to calculate the stoichiometry of the Fe_3O_4 [5]. In the case of the spectra shown in Figures 4 and 5, the Fe_3O_4 approaches the stoichiometric composition. The product formed on the steel-grit blasted surface is shown in Figures 6 and 7 for samples prepared at room temperature and at 90°. In both cases it is apparent that the spectra are very different from those obtained on the alumina-blasted surfaces. The product is highly non-stoichiometric Fe_3O_4 and appears to be best described as a mixture of Fe_3O_4 and $\gamma\text{-Fe}_2\text{O}_3$.

The most important question raised by this work is "How does the alumina blasting reduce the surface activity of the steel?"

Both the Auger surface analysis and the electron microprobe analysis showed that the element aluminum was present on the surface after abrasive treatment. However, neither measurement gives conclusive evidence regarding the chemical state of the aluminum. It is likely that the majority is present as finely divided alumina which is embedded in the steel. The local hot spots generated by the impinging alumina particles and the high activity of the abraded steel surface towards oxygen in the air suggests that some aluminum is incorporated in the surface oxide during blasting and that some portion of this aluminum becomes incorporated in the steel at levels below the surface. It is thus proposed that the abrasive blasting of the steel surface with alumina leads to doping of the steel surface with aluminum and that some portion of this aluminum eventually becomes incorporated in the corrosion product at the surface. Under relatively mild corrosion conditions, such as during the early stages of exposure to distilled water at room temperature, much of the aluminum remains at the surface and the surface film becomes enriched in aluminum. The resulting iron aluminum oxide is assumed to have a lower activity for both the anodic and cathodic reactions because of the greater thermodynamic stability of aluminum oxide relative to iron oxides and the lower activity of oxidized aluminum surfaces for the oxygen reduction reaction [1,2].

Several examples have been found in the literature in which abrasive blasting of a surface altered greatly the corrosion or surface properties of a metal. Such references are difficult to locate because they generally are peripheral to the major purpose of the paper and they are not usually found as index entries.

The most significant article is that by Andziak and Bokszczanin [6] in which it was noted that the anticorrosion properties of powder epoxy coatings on steel were improved when the steel was abrasively blasted with aluminum oxide in the form of corundum.

Calabrese and Allen [7] have characterized the surface of atmospherically corroded and blast-cleaned steel. A typical test procedure was to expose a steel panel to an industrial environment for 1 - 1½ years, abrasively clean the metal to an SP-5 finish, and then expose the panel to 50% relative humidity for 720 hours or to 100% relative humidity for 42 hours. Although the objective of their experiments was to understand better the surface structure and surface chemistry of steel after prior corrosion and refinishing of the surface, they did observe differences dependent upon the abrasive material used. Panels that were polished with 600-grit polishing abrasive exhibited no macroscopic or microscopic visible corrosion whereas those that were abrasively blasted with a silicon oxide or a silicon-aluminum-iron oxide abrasive resulted in substantial macroscopic and microscopic detectable corrosion.

Berry [8] reported that the corrosion rate of Inconel 600 in an alkaline borate buffer at 316°C was 10 times greater for grit-blasted specimens than for those that were pickled.

An outstanding example of the effect of different abrasives on corrosion behavior is shown in the work of van Rooyen, Copson and Berry [9] in experiments carried out with Inconel 600 in borated water at 600°F. They observed that panels grit-blasted with alumina exhibited corrosion rates of the order of 50-70 mg/dm² whereas panels grit-blasted with ferrochrome corroded at the rate of 30 mg/dm². Although the authors did not carry out experiments to understand the unusual behavior of the panels abraded with ferrochrome, they did conjecture that the ferrochrome grit-blasting increased the chromium content of the surface.

Schwab and Drisko [10] have studied the dry adherence of six different types of organic coatings to steel that was abrasively finished to white metal (NACE 1) as a function of different abrasives. They noted a 0.999 level of significance between the bonding strength and the type of adhesive. Although the profile after abrasion appeared to be an important variable, they also noted that "abrasives may have been deposited on surfaces or may have reacted chemically with them."

The wettability of gold surfaces by water has been shown to be a function of the type of abrasive used in polishing the surface. White and Drobek [11] have shown that polishing gold with alumina or smoothing the surfaces by compression between aluminum, stainless steel or mica led to contact angles of water on the gold of 34-56°. Electron diffraction studies yielded evidence for the presence of alumina, iron oxide, and muscovite, respectively, on these surfaces. Gold surfaces prepared by vacuum evaporation on silica substrates or by polishing with diamond abrasive followed by firing in oxygen at 1000°C yielded surfaces with contact angles of 55-65°. Electron diffraction studies showed no contaminating oxide material.

The following represents an hypothesis to account for the effects of abrasive blasting with alumina in the experiments reported herein. It is proposed that much of the alumina that ends up on the surface is present as embedded particles that impact the surface and plastically deform it. These particles increase the surface roughness and act as foreign matter, but they have little influence on the chemical behavior of the steel. They are very poor electrical conductors and do not play a role in the anodic/cathodic surface area ratio. They behave as neutral inclusions in steel. However, a small fraction of the total aluminum present in the surface is presumed to be incorporated in the oxide film on an atomic scale. The noble corrosion potentials of the alumina-blasted panels in distilled water, both before and after oxidation in air, are supportive of the concept that aluminum is incorporated in the oxide film on iron. It is suggested that the very small asperities on the alumina particles are fractured during impact. The number of atoms in an asperity is small, the energy released locally during impact is high, and some of the aluminum ions or aluminum-oxygen complex, enter the iron oxide during its formation as the aluminum oxide particle impacts the surface. The consequence of this interaction is the formation of an iron oxide that is doped

with, or enriched in, aluminum. This oxide is assumed to be a poorer catalyst for the oxygen reduction reaction and more resistant to anodic attack. The oxide is thus more protective and the surface is more resistant to corrosion. Proof of this hypothesis requires an analytical method to be used to show that aluminum is present in the iron oxide as a component of the oxide on an atomic scale and not as part of an occluded particle of aluminum oxide. No analytical method appears suitable to discriminate, on the scale required, between aluminum dissolved in the oxide and aluminum in a particle of aluminum oxide.

REFERENCES

- [1] H. Leidheiser, Jr., Corrosion 38, 374 (1982).
- [2] D. R. Gabe and M. Shirkhanzadeh, Br. Corrosion J. 15, 216 (1980).
- [3] H. Leidheiser, Jr., Ind. Eng. Chem. Prod. Res. Dev. 20, 547 (1981).
- [4] B. D. Sartell, quoted by V. Ashworth, W. A. Grant, and R. P. M. Procter, "Treatise on Materials Science and Technology," J. K. Hirvonen, Editor, Academic Press, New York, 1980, pp. 175-256.
- [5] G. W. Simmons, E. Kellerman, and H. Leidheiser, Jr., Corrosion 29, 227 (1973).
- [6] J. Andziak and W. Bokszczanin, Powloki Ochr. 7, No. 2, 2 (1979).
- [7] C. Calabrese and J. R. Allen, Corrosion 34, 331 (1978).
- [8] W. E. Berry, "Corrosion in Nuclear Applications," John Wiley and Sons, New York, 1971, p.185.
- [9] D. van Rooyen, H. R. Copson, and W. E. Berry, Corrosion 25, 194 (1969).
- [10] L. K. Schwab and R. W. Drisko, Materials Performance 20, No. 5, 32 (1981).
- [11] M. L. White and J. Drobek, J. Phys. Chem. 70, 3432 (1966).

Program #2. A Two-Step Anodization Process for Inhibition of the Oxygen Reduction Reaction on Iron

ABSTRACT

Anodization of iron by a two-step procedure, first in a borate solution and, second, in a borate solution containing 8-hydroxyquinoline, results in a surface which is inactive for the oxygen reduction reaction and which has good corrosion resistance in chloride media. The anodized surface also exhibits good resistance to the disbondment of an organic coating under an applied cathodic potential. It is conjectured that the anodized surface consists of a very small amount of surface oxide, possibly a layer of a ferric complex of 8-hydroxyquinoline, and an outer layer of unreacted 8-hydroxyquinoline.

INTRODUCTION

The cathodic half reaction during the corrosion of iron and steel in near neutral aqueous environments is the oxygen reduction reaction, $\text{H}_2\text{O} + 1/2\text{O}_2 + 2\text{e}^- = 2\text{OH}^-$. Under many conditions this reaction is the rate controlling step. Many methods are available for inhibiting the anodic half reaction but relatively few methods are available for inhibiting the oxygen reduction reaction. Previous work in this laboratory has shown that this reaction may be inhibited on zinc by doping the oxide on the surface with small amounts of cobalt or nickel [1,2]. It has also been shown that cathodic treatment of a chromated surface on zinc leads to a surface which has low activity for the oxygen reduction reaction [3].

We report herein a novel method for inhibition of the cathodic half reaction on iron. This method consists of anodizing iron in a borate buffer followed by a second anodization step in a solution containing an organic compound. This procedure leads to a surface which is inactive for the oxygen reduction reaction and which has a low rate of corrosion in a mildly corrosive medium.

EXPERIMENTAL PROCEDURE

All measurements in this study were made on cold-rolled SAE 1010 steel panels, 0.5 mm thick, obtained from the Q-Panel Co. The as-received panels were cut in the form of a rectangle, 1 cm wide and 7.5 cm long, with an indentation at the waterline as shown in Figure 1. They were immersed in the electrolyte to a depth such that the exposed area was 10 cm². Samples were used either in the electropolished condition or after abrasion with No. 240 emery paper. Electropolishing was carried out in a 4:1 mixture of glacial acetic acid and perchloric acid. All potentials described in the test are with reference to the saturated calomel electrode.

The steel was anodized in a vigorously stirred 0.15M sodium borate solution (pH 8.4) open to the air in a two-step process.

Step I: Anodization at a potential (E_{a1}) between -0.4 V and +2.2 V in the borate solution for 2-10 min.

Step II: Anodization at a potential (E_{a2}) between +0.5 V and +2.0 V for 2-10 min in the borate buffer solution to which an organic compound was added.

Cathodic polarization curves and corrosion rate measurements were made in a 250 cm³ volume of 0.5M NaCl - 0.15M borate at pH 7 in the cell shown in Figure 1. The solution was aerated during the measurements by passing air through the solution at a rate of 600 cm³/min or was deaerated with purified argon gas. The measurements were performed using a Princeton Applied Research Model 350 Corrosion Measurement Console featuring microprocessors and a data storage system. Unless otherwise mentioned, polarization curves were determined using a scanning technique. Measurements were initiated after the sample had been exposed to the medium for 10 min and the scanning rate was 0.3 mV/sec. Cyclic voltammograms were obtained using a similar procedure with the exception that the scan rate was 1 mV/sec. Corrosion rates determined by the polarization resistance (R_p) method and corrosion potential measurements were made every 30 min during a 16-hour period. R_p values were obtained from the slope of the polarization curve in the potential range of ± 5 mV from the corrosion potential.

Gravimetric measurements of the corrosion rate were made in 400 cm³ of solution maintained in a 600 cm³ beaker. Weighed specimens were immersed in either aerated or deaerated solutions for 4-16 hr and the loss in weight was determined. Corrosion products were removed from the specimen surface using a nylon test tube brush under running distilled water.

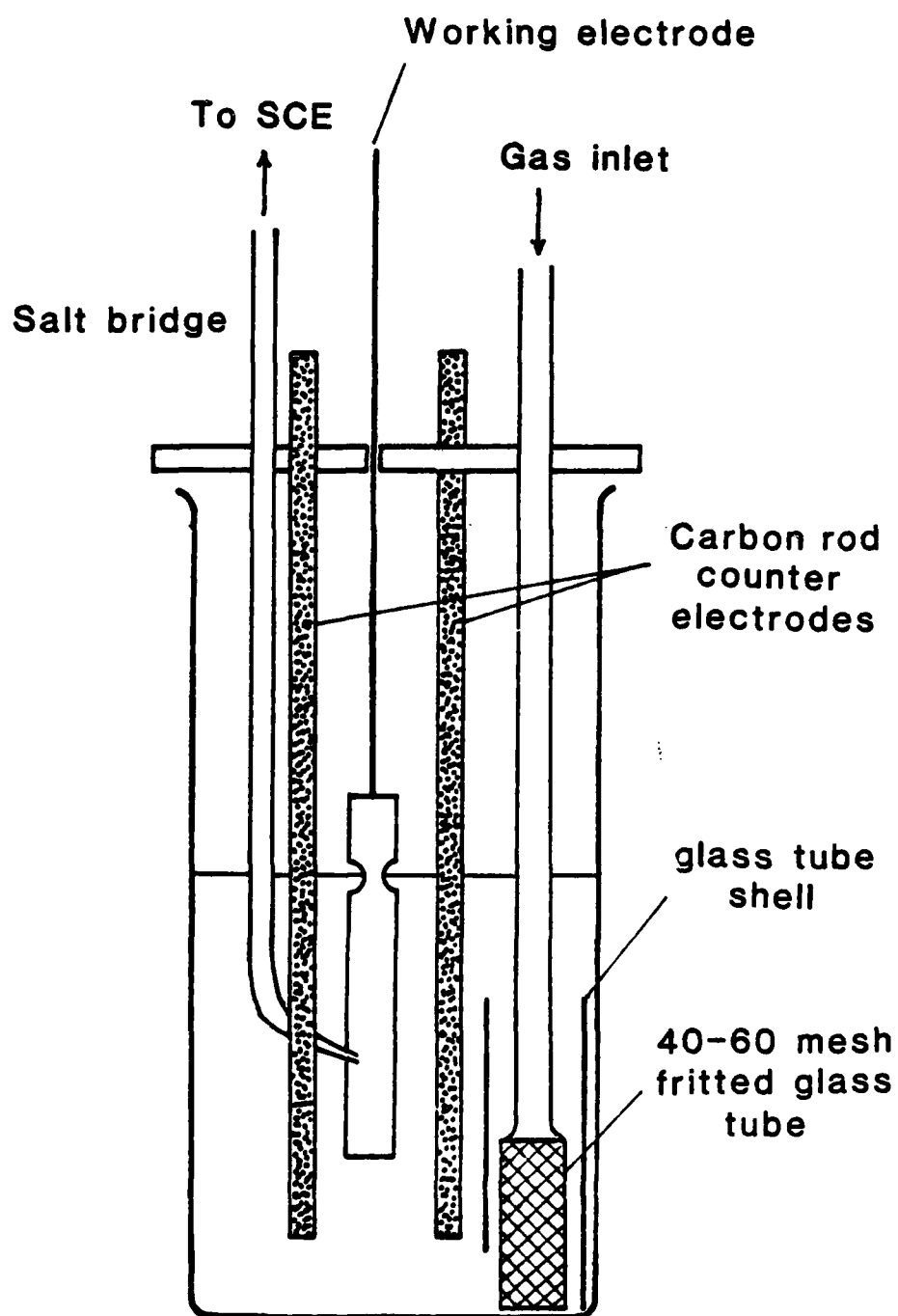


Figure 1. Schematic diagram of cell used for electrochemical measurements.

Impedance measurements were made by cementing a cylinder to the steel surface and using mercury as the counterelectrode. The means for making the measurements have been described previously [4].

Cathodic delamination tests were performed using the method previously described [5]. Panels were coated with a commercial product [Rust-Oleum primer 7773 and Rust-Oleum topcoat 7791] using two primer coats and three topcoats to yield a coating of thickness 93 μm . A small defect was made in the coating and the specimen was made the cathode while immersed in 0.5M NaCl solution open to the air. In all cases the cathode potential was potentiostatically maintained at -0.8 V.

X-Ray photoelectric spectroscopy measurements were made using a Physical Electronics Model 548 electron spectrometer. Samples were irradiated with the K_{α} radiation of magnesium in a vacuum of $2.5\text{--}4.5 \times 10^{-7}$ Pa. The analyzer energy was set at 25 eV which yielded a resolution of 1.22 eV for the Au $4f_{7/2}$ peak for the full width at half maximum. In order to compensate for a small charging shift, the electron binding energy, E_B , was corrected by assigning a value of 285.0 eV to the aromatic carbon or hydrocarbon C 1s peak [6].

EXPERIMENTAL RESULTS

During the earliest phases of this study, it was observed that the addition of several types of organic compounds to a borate anodizing bath caused a marked reduction in the current at a fixed potential. This observation suggested that the anodized procedure was leading to a steel surface with a lower activity. Determinations of the cathodic polarization curve, measurements of the corrosion rate, and general observations of the metal surface while it was exposed to a corrosive medium confirmed that the steel surface had been inactivated by the anodization treatment. As a first step in a study of this phenomenon, a survey was made of a large number of organic compounds that we felt might be suitable candidates for an intensive study. Table I summarizes the organic compounds that yielded positive results, the conditions of anodization, the effect on the current during anodization, the corrosion potential, the effect on the cathodic polarization curve, and the corrosion rate in a borate medium as determined by gravimetric measurements.

The results summarized in Table I indicated that one of the more interesting and effective compounds was 8-hydroxyquinoline (HQ). The decision was then made to confine the work reported herein to observations with this compound. The optimum experimental conditions for maximum corrosion inhibition were determined by varying E_{a_1} in the borate solution and E_{a_2} in the borate-HQ

Table I. Results of an Exploratory Study of the Effect of Organic Compounds on the Electrochemical Properties of Steel during Anodization

Organic Compound	Conc. mol/l	i_a at E_{a_2} A/m ²	Corrosion Potential E_{corr} V vs. SCE	Effect on Cathodic Polarization Curve		Corrosion Rate r_{ave} g/m ² hr
				i_c at -0.5v	i_c at -0.8v	
N-benzoyl-N-phenyl- hydroxylamine	0.004	0.3	-0.434	0.22	1.68	0.48
Cupferron	0.01	1.3	-0.553	--	1.88	0.39
Diphenylguanidine	0.004	4.2	-0.448	0.22	1.42	0.23
8-Hydroxyquinoline	0.004	0.3	-0.422	0.02	1.01	0.10
1-Nitroso-2-naphthol	0.002	0.9	-0.463	0.24	1.70	0.25
Phenylthiourea	0.004	1.9	-0.454	0.03	2.15	0.34
Salicylamide	0.01	8.2	-0.425	0.26	1.12	0.21
Salicylanilide	0.002	2.8	-0.549	--	1.31	0.28
Blank	--	25	-0.389*	0.25*	2.03*	0.74

All samples anodized at $E_{a_1} = 1.0$ V and $E_{a_2} = 1.4$ V in a 0.15M borate solution (pH 8.4) for 10 minutes at each potential.

*Electropolished specimen.

solution at various pH values and for different anodizing times. The criterion used to identify the optimum condition was the degree of inhibition as determined by the cathodic polarization curve as measured in aerated 0.5M NaCl-0.15M borate solution. Optimum conditions were $E_{a1} = 0.9 - 1.8$ V in a borate solution, $E_{a2} = 1.0 - 1.7$ V in a 0.004M HQ-borate solution, pH 7-10, and anodizing time of 10 min at each potential. It was observed that a suitable value for E_{a1} was in the transpassive region of the anodic polarization curve for steel in the borate buffer and a suitable value for E_{a2} was in the passive region of the anodic polarization curve for steel in the borate-HQ solution. See Figure 2. At pH's lower than 7, a large number of small dark spots was formed on the surface during the anodization and a uniform layer was not obtained. At pH's higher than 10, the dissolution rate of the steel in Step I was greater than desired.

Typical cathodic polarization curves for HQ-treated and panels anodized in the absence of HQ (blank) are shown in Figure 3 for electropolished specimens and in Figure 4 for abraded specimens. Unless otherwise mentioned, experiments were carried out on specimens anodized at $E_{a1} = 1.0$ V, $E_{a2} = 1.4$ V, and pH 8.4. In the case of the abraded specimens the anodic oxide was reduced during the cathodic polarization but the oxide on the electropolished specimen was stable under mildly cathodic conditions. Under both sets of conditions the HQ-treated panels exhibited similar cathodic polarization characteristics. The cathodic current density for the HQ-treated panels was approximately 0.1 of that of the blank at -0.45 V and approximately 0.5 of that of the blank at -0.8 V. In order to obtain a clearer picture of the polarization characteristics in the vicinity of the corrosion potential, anodic and cathodic polarization curves are plotted for unanodized iron, anodized iron, and the HQ-treated iron in Figure 5. It will be noted that the HQ-treated panels show substantial inhibition of the cathodic reaction and significant inhibition of the anodic reaction.

The two likely cathodic reactions on the anodized samples are (a) oxygen reduction and (b) reduction of the oxide film on the surface. Both these reactions appear to be suppressed on the HQ-treated samples as shown by potentiostatic polarization at -0.8 V and cyclic voltammetry measurements. Potentiostatic polarization at -0.8 V yielded a short-term, steady-state current value of approximately 0.9 A/m² for the HQ-treated panel and approximately 1.8 A/m² for the blank. These values became 0.73 A/m² and 1.87 A/m², respectively, after 1 hr. These latter values are assumed to represent the oxygen reduction current and are confirming evidence that the oxygen reduction reaction is inhibited on the HQ-treated sample.

Cyclic voltammograms for the HQ-treated sample (Figure 6) demonstrated anodic and cathodic scans that were very similar in both directions, whereas the voltammogram for the blank (Figure 7) suggested that reduction of the oxide occurred during the scan in the cathodic direction.

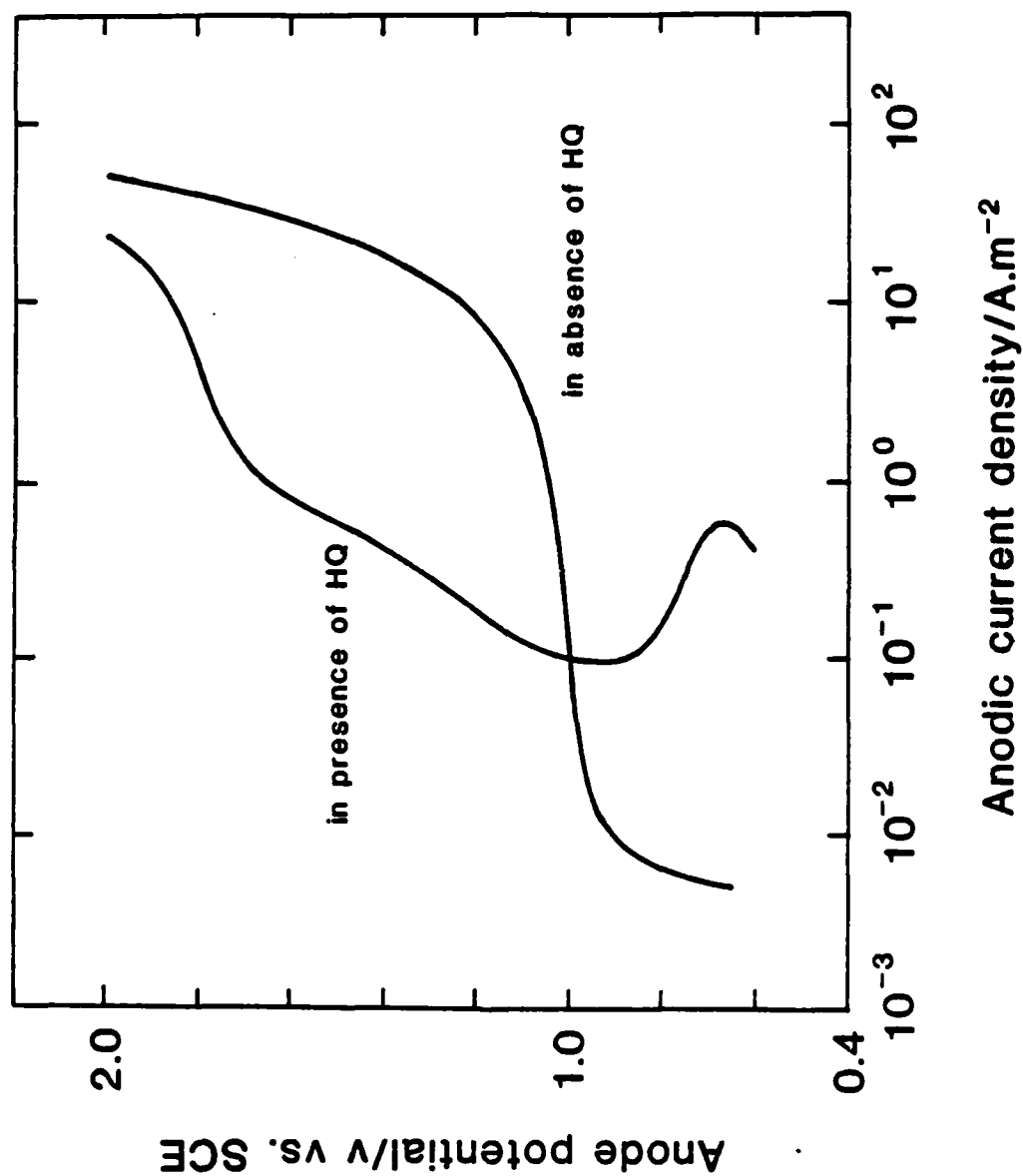


Figure 2. Anodic polarization curves for steel as determined in 0.15M borate solution (pH 8.4) with and without 0.004M 8-hydroxyquinoline. Curves determined at a scan rate of 1 mV/sec.

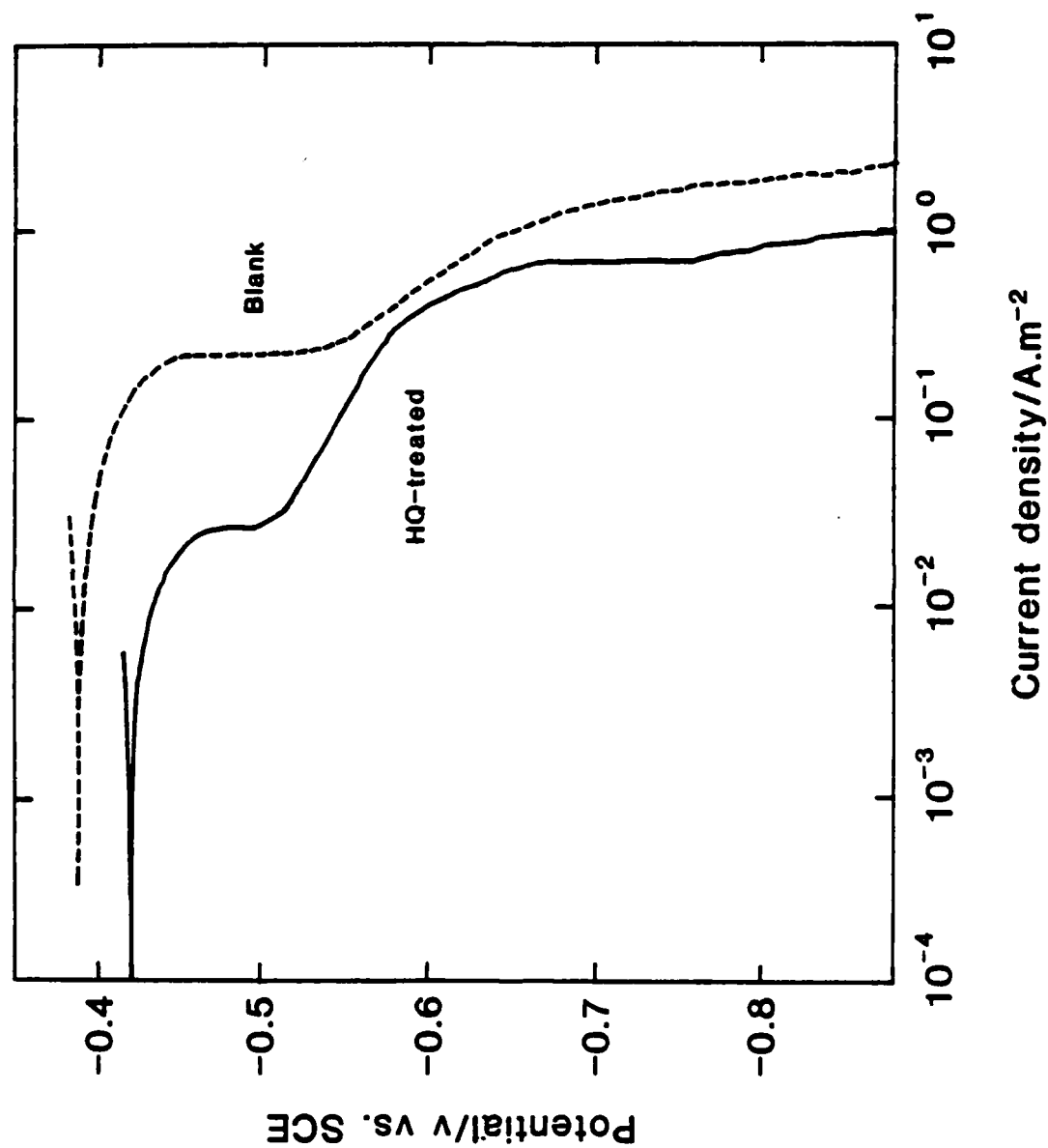


Figure 3. Cathodic polarization curves for electropolished steel specimens in aerated 0.5M NaCl - 0.15M borate solution. Both specimens were anodized in 0.15M borate solution, one in the presence of 8-hydroxyquinoline and the other in its absence.

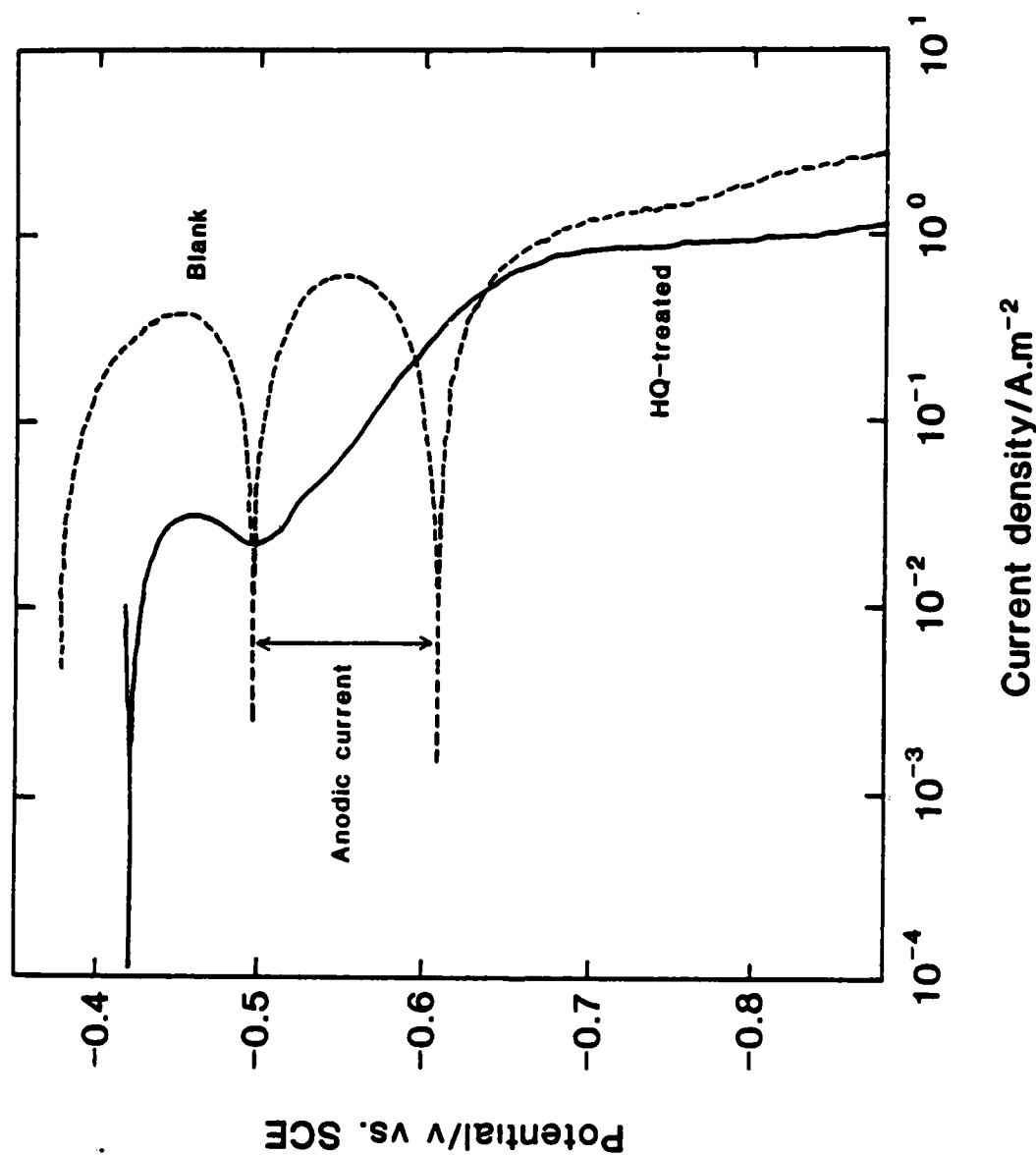


Figure 4. Cathodic polarization curves for abraded steel specimens in aerated 0.5M NaCl - 0.15M borate solution. Both specimens were anodized in 0.15M borate solution, one in the presence of 8-hydroxyquinoline and the other in its absence.

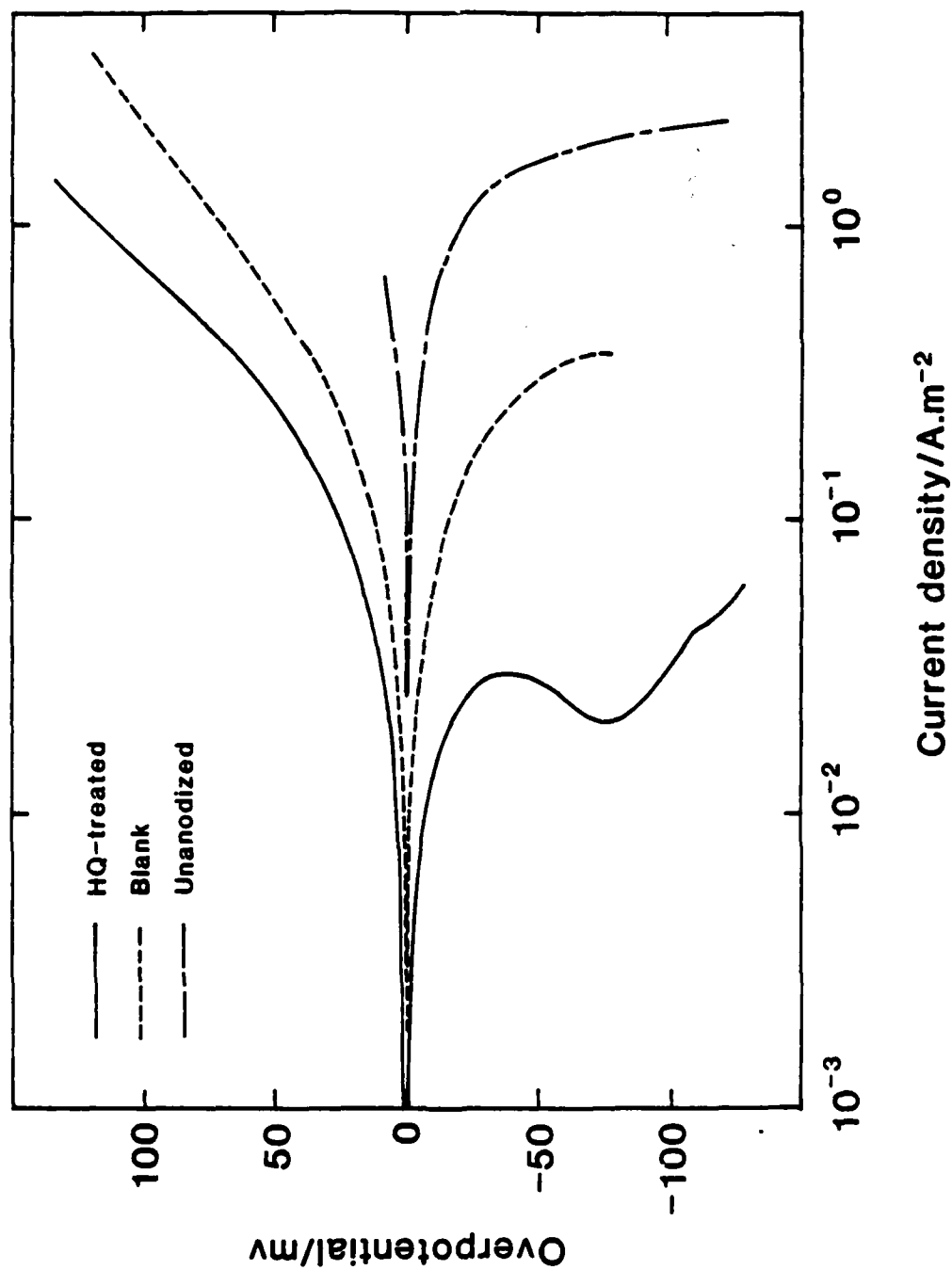


Figure 5. Polarization behavior in the vicinity of the corrosion potential. The potential axis is normalized with respect to the corrosion potential.

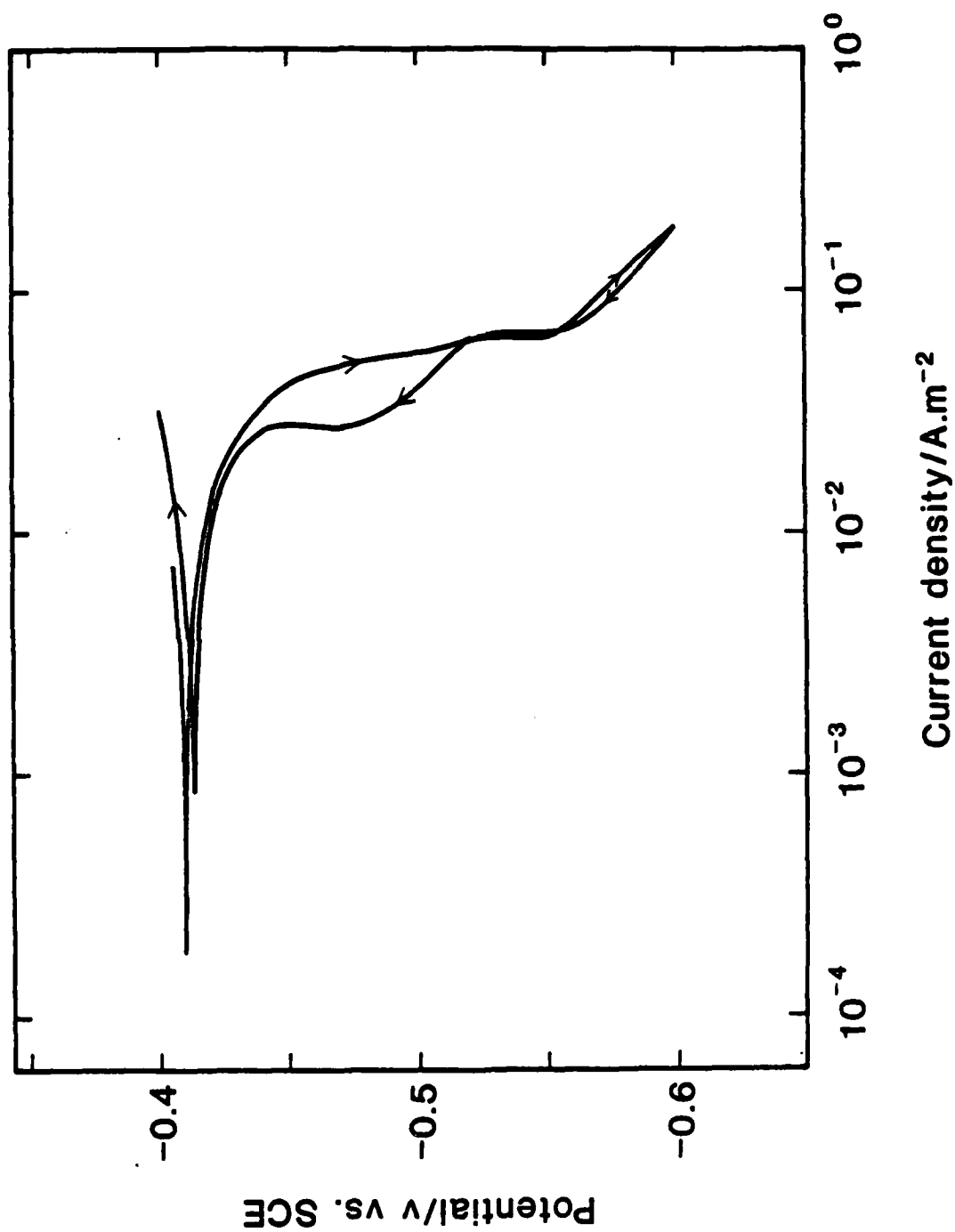


Figure 6. Cyclic voltammogram in 0.5M NaCl - 0.15M borate solution for a specimen anodized in the presence of 8-hydroxyquinoline.

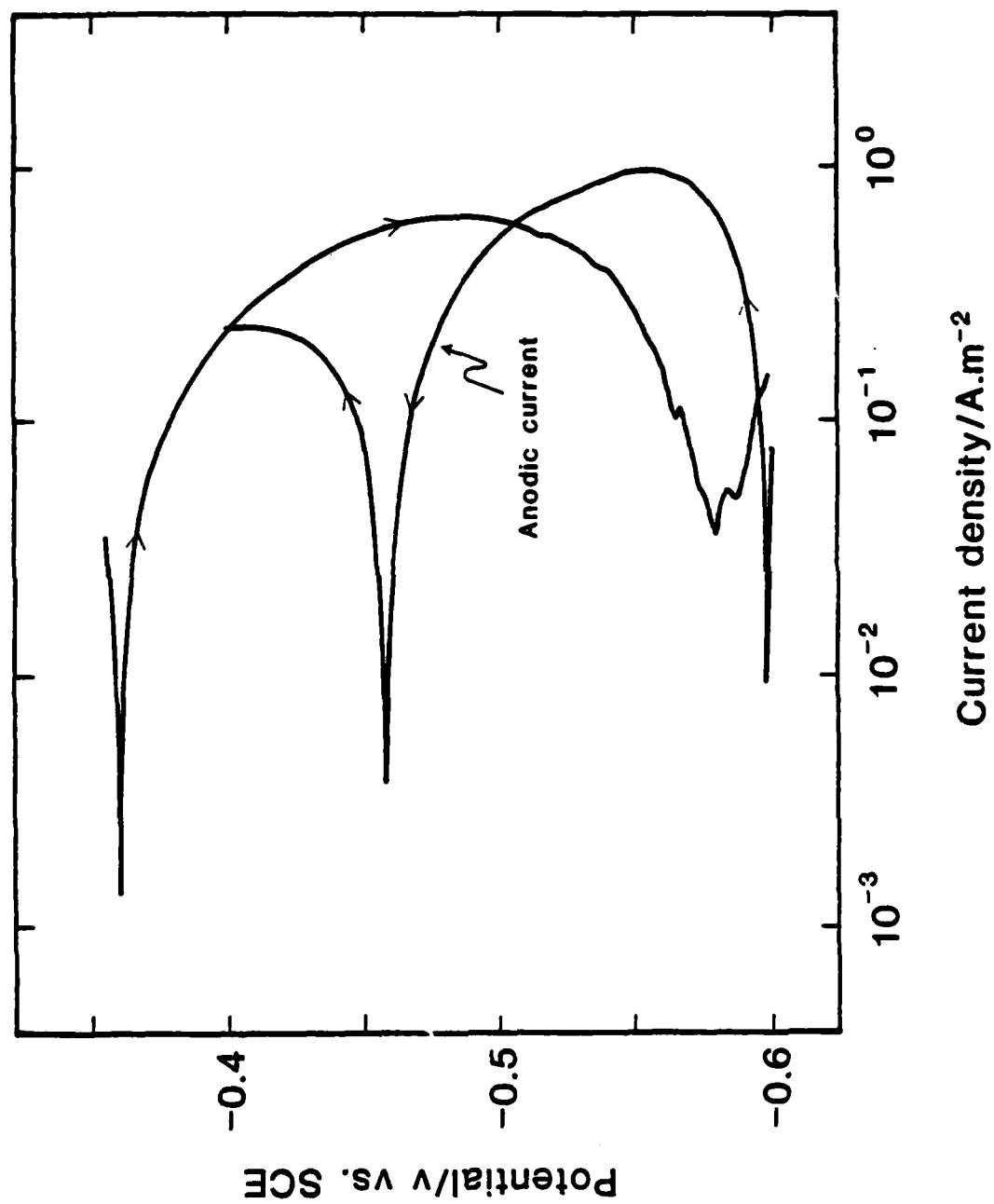


Figure 7. Cyclic voltammogram in 0.5M NaCl - 0.15M borate solution for an anodized specimen, a so-called blank.

Cathodic polarization measurements in deaerated chloride-borate solution indicated that the hydrogen evolution reaction is also inhibited on the HQ-treated samples. Representative curves are shown in Figure 8 in which it will be noted that the cathodic current density on the treated specimen is less than 1/3 that of the blank in the potential region between -0.8 and -1.1 V.

Impedance measurements at 100, 1,000, and 10,000 Hz are summarized in Table II. It will be noted from these data that the impedance of the HQ-treated sample is significantly greater than that of the blank.

Table II

Impedance Measurements on HQ-treated and Blank Samples

Frequency (Hz)	Total Impedance (ohms)		Calc. Resistive Component (ohms)	
	HQ-Treated	Blank	HQ-Treated	Blank
100	3.30	0.18	3.29	0.16
1,000	3.64	0.97	3.51	0.22
10,000	10.6	9.60	4.52	0.99

The cathodic polarization curves and the anodic polarization curves suggested that the rate of corrosion of the HQ-treated panels would be significantly less than that of an anodized blank. This conclusion was confirmed by polarization resistance, R_p , and gravimetric measurements. The variation of the R_p value with time is shown in Figure 9 in the case of aerated chloride-borate solution and in Figure 10 in the case of deaerated chloride-borate buffer solution. In the aerated medium the R_p values were erratic during the first few hours and were occasionally very high. These values are probably of limited meaning because the polarization curve was not linear and the lack of linearity was maintained with change in scan rate or scan direction. The R_p for the HQ-treated panel in aerated media achieved a steady state value of approximately 3,300 ohms·cm² after 8 hr whereas the R_p for the blank was less than 1,000 ohms·cm² after 2 hr. In deaerated solution the R_p value of the HQ-treated panel is higher than that for the blank over the entire time period, but the differences are much less than those observed in the aerated solution.

Gravimetric measurements are summarized in Table III. These results are in good support of the R_p measurements. The rates of corrosion of the anodized samples (blanks) were much greater in aerated solution than the HQ-treated samples and were slightly greater during corrosion in deaerated solutions.

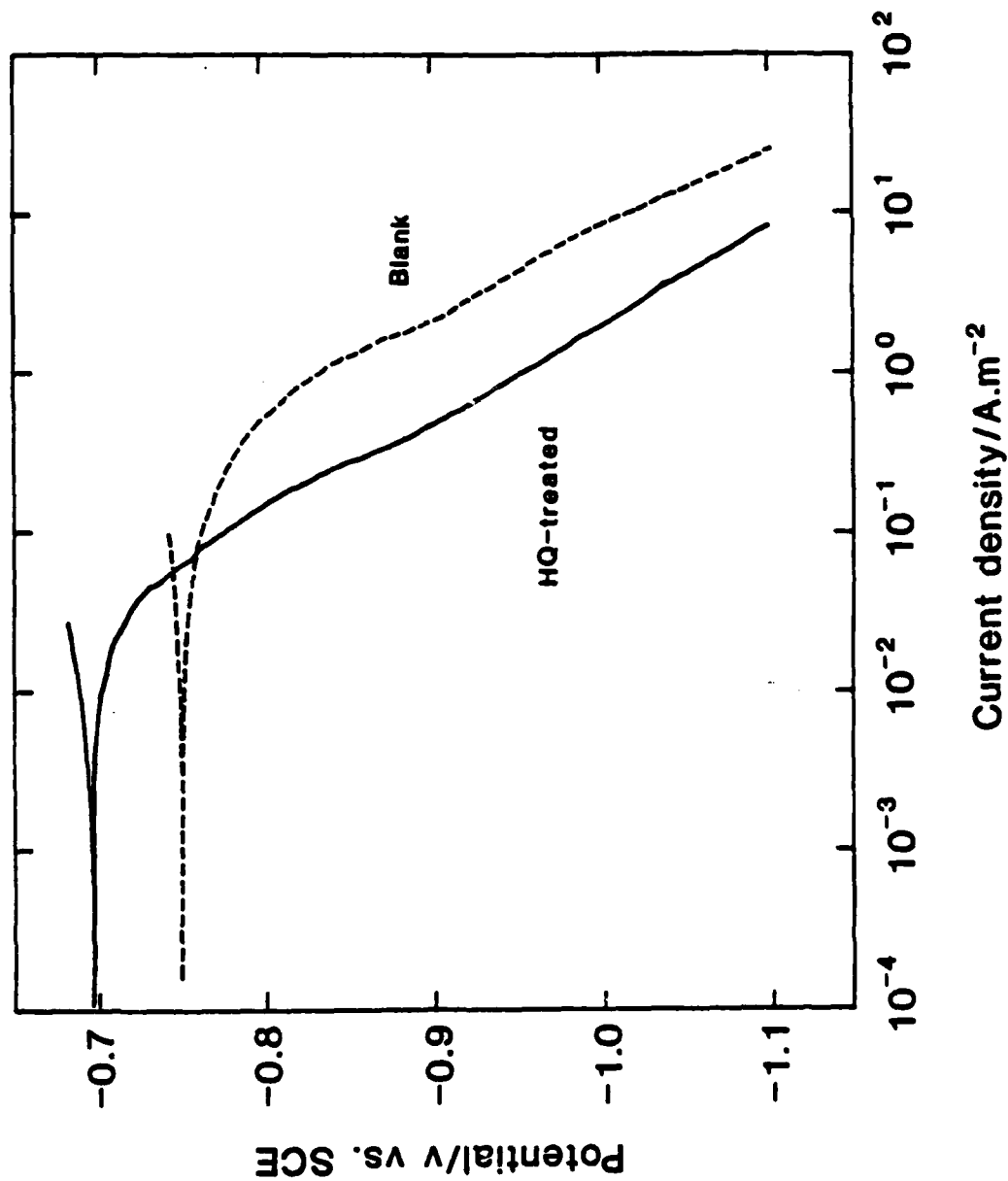


Figure 8. Cathodic polarization curves for abraded steel specimens in deaerated 0.5M NaCl - 0.15M borate solution. Both specimens were anodized in 0.15M borate solution, one in the presence of 8-hydroxyquinoline and the other in its absence.

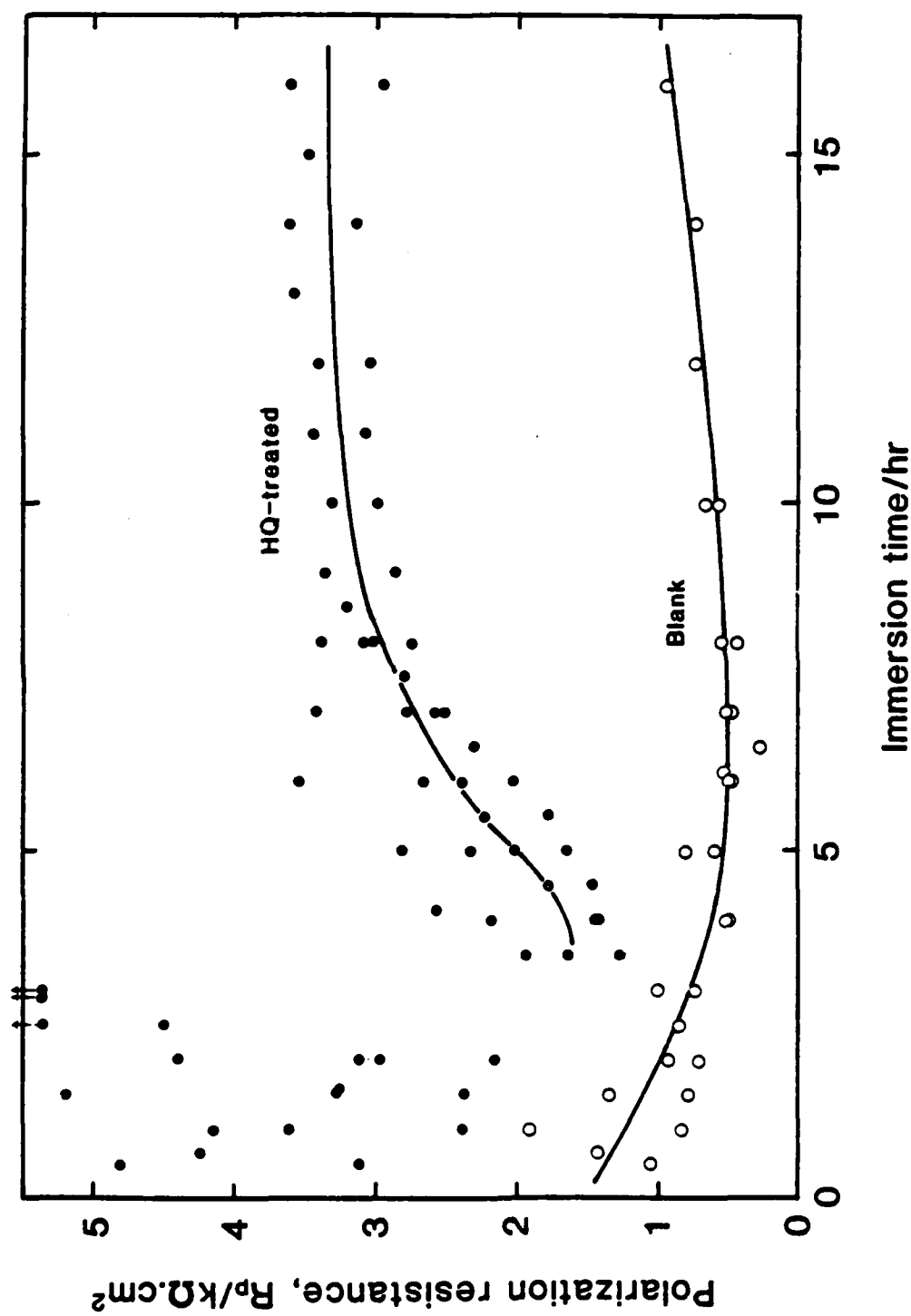


Figure 9. Polarization resistance (R_p) values as a function of time in aerated 0.5M NaCl ± 0.15M borate solution. Both specimens were anodized in 0.15M borate solution, one in the presence of 8-hydroxyquinoline and the other in its absence.

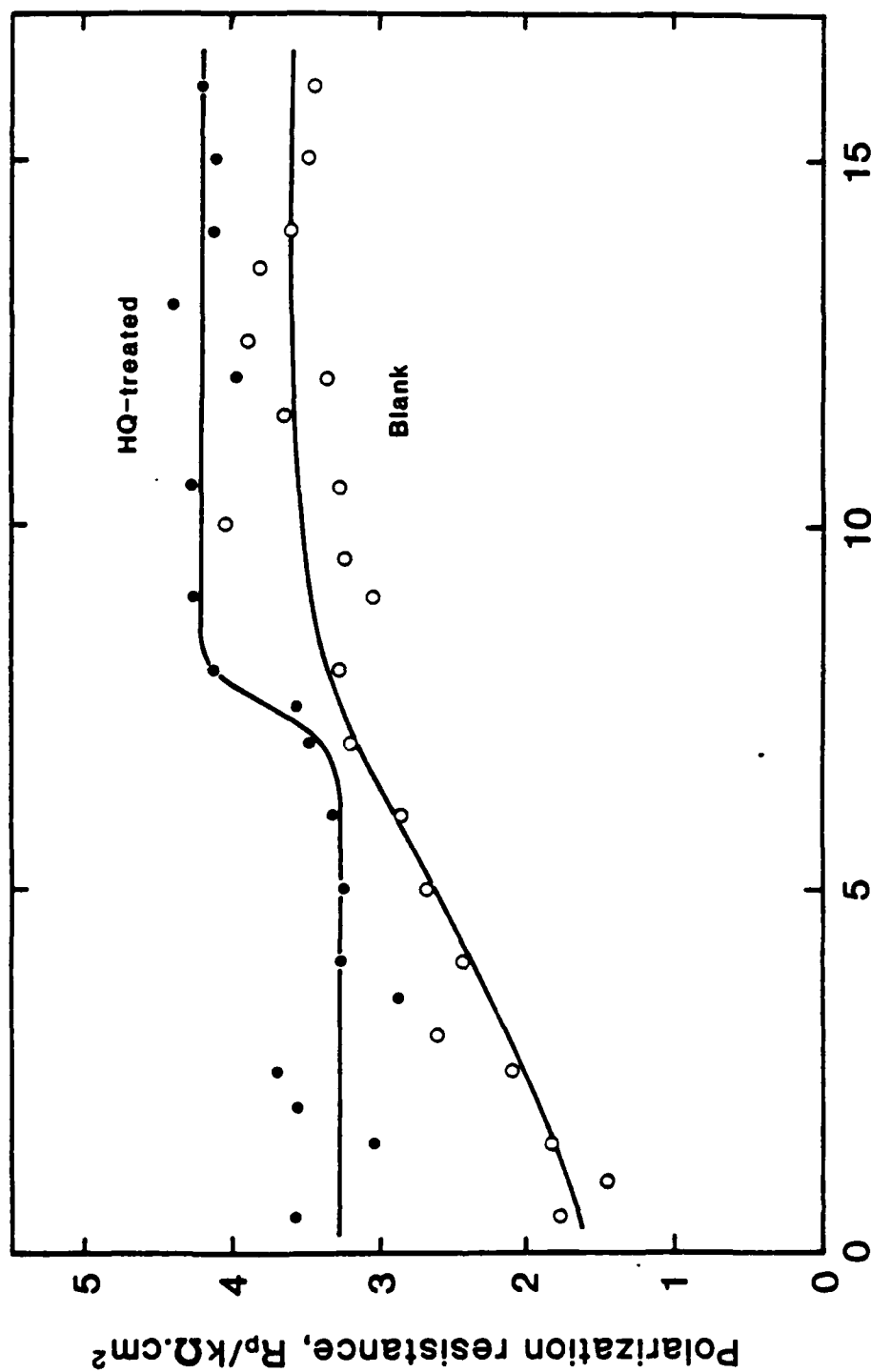


Figure 10. Polarization resistance (R_p) values as a function of time in deaerated 0.5M NaCl - 0.15M borate solution. Both specimens were anodized in 0.15M borate solution, one in the presence of 8-hydroxyquinoline and the other in its absence.

Table III

Average Corrosion Rate during 16-Hour Period of
Immersion in 0.5M NaCl - 0.15M Borate (pH = 7)

Sample No.	Anodization Conditions			Corrosion Medium	Corrosion Rate (g/m ² ·hr)	
	E _{a1} (V)	E _{a2} (V)	pH		HQ-Treated	Blank
3,4	1.0	1.4	8.4	Deaerated	0.060	0.094
1,2	1.0	1.4	8.4	Aerated	0.10	0.74
5	1.0	1.4	7.0	Aerated	0.14	
6	1.0	1.4	10.0	Aerated	0.10	
7,8	1.8	1.1	8.4	Aerated	0.14	0.95
9	---	1.4	8.4	Aerated	0.27	
10*,11*	1.0	1.4	8.4	Aerated	0.22	0.99
12**	1.0	1.4	8.4	Aerated	0.18	
13	abraded only			Aerated		0.91

Note: All specimens were abraded with No. 240 emery paper before anodizing.

* Heated at 200°C for 20 min after anodization.

** Dipped into methanol for 10 min after anodization.

Figure 11 shows that the corrosion rates of both the blank and the HQ-treated material occur linearly with time, at least over the 16-hour period of the experiment.

Changes in the corrosion potential as a function of time of exposure to the chloride-borate medium are shown in Figure 12 for the HQ-treated samples and the blanks under both aerated and de-aerated conditions. The value of E_{corr} for the HQ-treated panel dropped abruptly after about 3 hr and achieved a steady-state value of -0.69 V. This behavior as shown in Figure 12 parallels the R_p behavior as shown in Figure 9.

Cathodic delamination occurred much more slowly in the case of the HQ-treated samples as compared to the blank or abraded steel. The rate of delamination of the HQ-treated panels in 0.5M NaCl open to the air at a potential of -0.8 V was $0.004\text{ cm}^2/\text{hr}$ whereas the abraded panels yielded values in the range of 0.015 to $0.023\text{ cm}^2/\text{hr}$. The rate of delamination of the blank was so high that no quantitative value was obtained.

XPS studies (Table IV) revealed that the surface of the HQ-treated specimen was covered with organic material which yielded a spectrum identical to the spectrum obtained from a sample of 8-hydroxyquinoline powder. The electron binding energy of the N 1s electron in the HQ-treated sample was identical to that obtained with the hydroxyquinoline powder but was slightly different from the binding energy for a powder of the ferric complex of 8-hydroxyquinoline. Also, the Fe 2p peaks in the HQ-treated sample were very weak whereas they were strong in the ferric complex. After a 16-hr immersion in the aerated corrosion medium, the N 1s peak changed in value to that characteristic of the ferric complex. As judged from the intensities of the C 1s and N 1s peaks, significant amounts of the organic compound remained on the surface after a 16-hr exposure to the corrosion medium. The data are consistent with the view that the outermost part of the surface layer of the HQ-treated sample consists of 8-hydroxyquinoline with very little chemical reaction to form the ferric complex.

DISCUSSION

The experiments reported herein show conclusively that it is possible to inhibit the oxygen reduction reaction on steel using an organic compound. It is interesting to point out that under similar experimental conditions in which good inhibition was observed in this study on the HQ-treated panels, only insignificant corrosion inhibition was observed when 8-hydroxyquinoline was present in the corrosion medium and was absent during the anodization procedure. Weisstuch, Carter and Nathan [8] observed corrosion inhibition of iron by 8-hydroxyquinoline in an aerated,

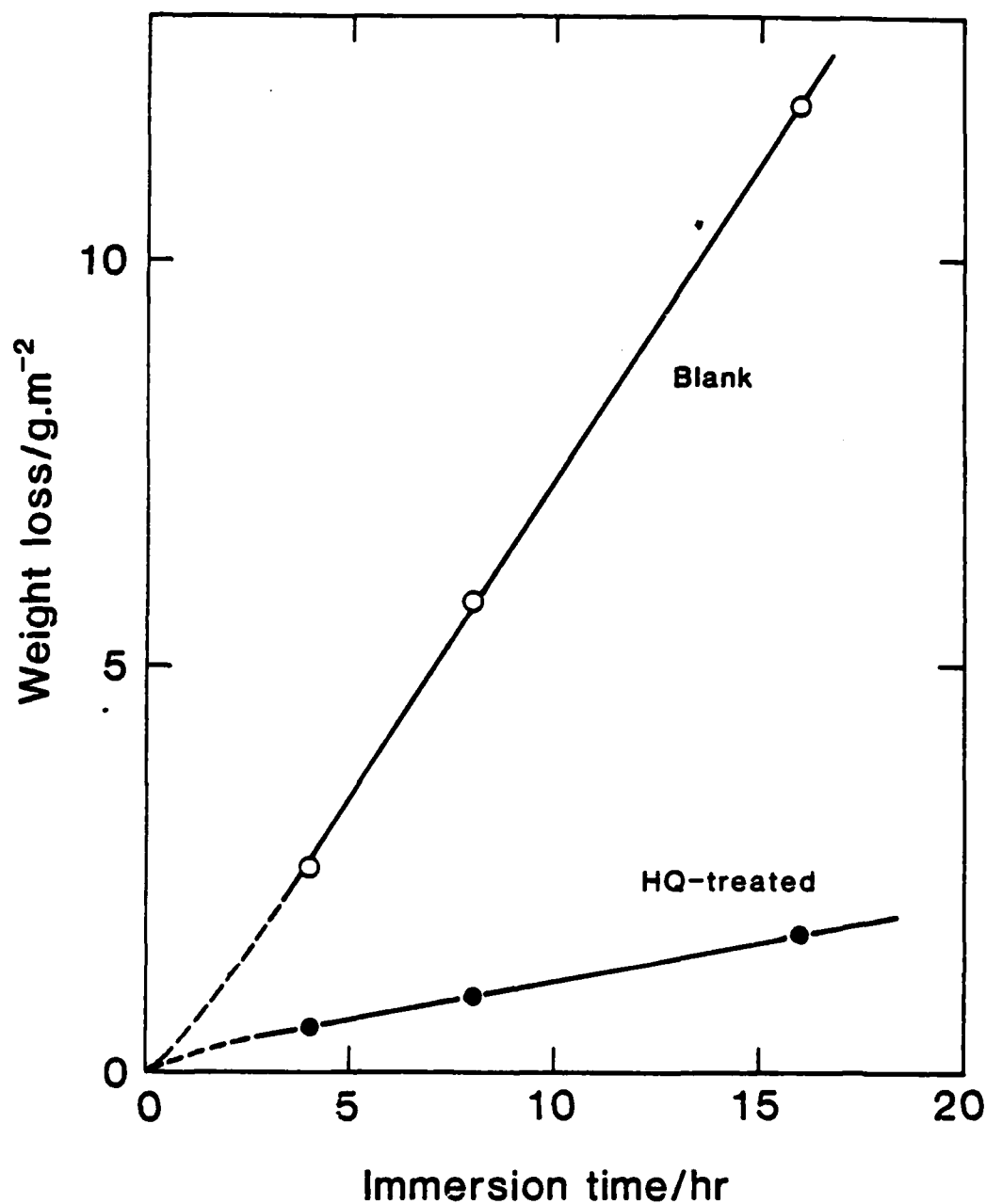


Figure 11. Corrosion rate as a function of time as determined gravimetrically. Both specimens were anodized in 0.15M borate solution, one in the presence of 8-hydroxyquinoline and the other in its absence.

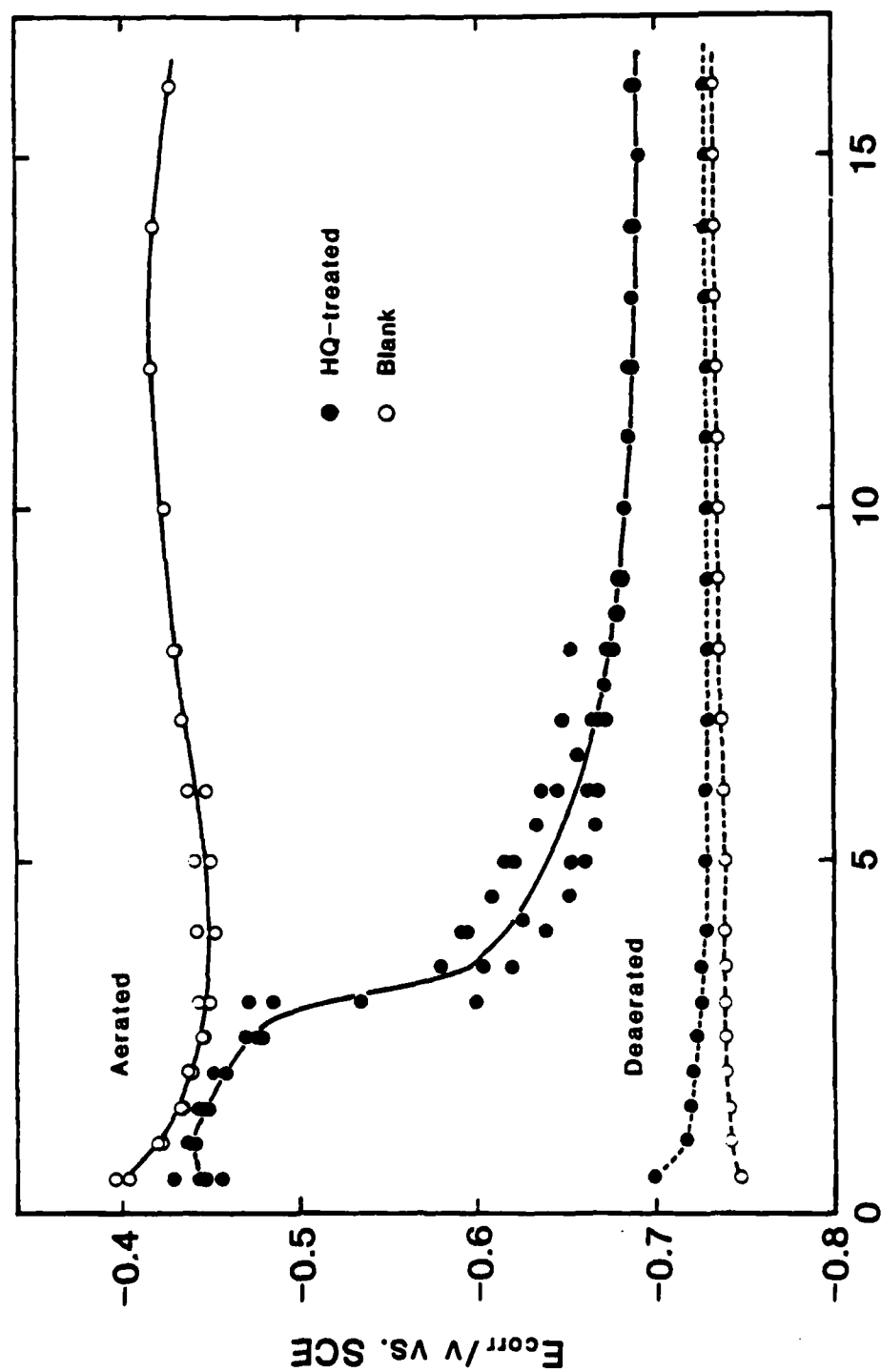


Figure 12. Corrosion potential measurements as a function of immersion time as measured in aerated and deaerated 0.5M NaCl - 0.15M borate solution.

Table IV

Results of XPS Measurements for Specimens and Standard Samples

<u>Sample</u>	Electron Binding Energy, E_B /eV			
	<u>C 1s</u>	<u>N 1s</u>	<u>O 1s</u>	<u>Fe 2p_{3/2}</u>
HQ-treated	285.0	399.5	533.1 max ca. 531 sh	trace
Blank	285.0	--	530.3 max ca. 532.5 sh	711.3
HQ-treated and immersed*	285.0 287.9	399.0	530.2 max ca. 532 sh	711.3
Electropolished steel	285.0	--	530.3 max ca. 532 sh	711.2 707.0
8-Hydroxyquinoline (HQ), powder	285.0	399.5	531.5	--
Fe(III)-8-hydroxy- quinolate, powder	285.0	399.1	531.5	711.2

max : maximum , sh : shoulder

*Specimen immersed in an aerated 0.5M NaCl - 0.15M borate solution (pH 7.0) for 16 hours.

simulated cooling water environment at pH 7 but they also observed the formation of an insoluble, non-adherent film. All the evidence generated to date indicates that anodization in the presence of 8-hydroxyquinoline is essential in order to obtain good corrosion inhibition. So far as we are aware a two-step anodization process, the second step of which is carried out in a medium to which an organic compound is added, is a novel method for developing a corrosion resistant surface on steel. It is our expectation that the procedure can be optimized to obtain metal surfaces with a high degree of corrosion resistance under service conditions.

The polarization curves shown in Figures 3, 4, and 5 indicate that the HQ-treatment yields a surface which is less active for both the anodic and cathodic half-reactions, although the effect is much greater on the cathodic half-reaction. On the basis of the cathodic polarization curves in Figure 3, it can be estimated that the corrosion rate of the blank should be approximately 9 times that of the HQ-treated material. The gravimetric measurements for samples 1 and 2 in Table III indicate that the rate is 7.4 times that of the HQ-treated material for corrosion measurements made over a 16-hr period. The two types of experiments, along with the R_p data in Figure 9, conclusively show the large degree of corrosion inhibition which results from the anodization in solutions containing 8-hydroxyquinoline.

The mechanism by which this corrosion inhibition occurs is probably by the development at the iron surface of an organic layer, of unknown thickness at the present time, which impedes the flow of electrons which are a necessary reactant in the oxygen reduction reaction, $H_2O + 1/2O_2 + 2e^- = 2OH^-$. The data shown in Table II prove that the HQ-treated samples exhibit a much higher impedance than samples anodized in the absence of HQ. The data also suggest that the major contribution to the impedance is a resistive component since over 96% of the impedance value can be attributed to the resistive component at measurement frequencies of 100 and 1000 Hz under the assumption that the equivalent circuit consists of a resistance and a capacitor in series.

The most interesting question raised by this study is "What is the chemical nature of the steel surface after the two-step anodization process?" This question is being addressed in studies now underway but the data already available allow certain conclusions to be drawn. The XPS studies summarized in Table IV show that the outer surface appears to be 8-hydroxyquinoline immediately after anodization but that the outer surface approaches a form equivalent to a ferric complex of 8-hydroxyquinoline after exposure to the corrosive medium. It is impossible from the present data, and it could not be determined from spectra taken after sputtering, to ascertain whether the surface after anodization consists of an inner ferric complex of 8-hydroxyquinoline and an outer 8-hydroxyquinoline, or whether exposure to the corrosion medium caused the conversion of the 8-hydroxyquinoline to a ferric complex. It is well known that the ferric complex of 8-hydroxyquinoline is very insoluble.

The anodic film formed in borate solution is readily reduced as shown by the cathodic polarization curve in Figure 4 and the voltammogram for the blank in Figure 7 whereas there was minimal reduction in the case of the HQ-treated sample as shown in Figure 6. These behaviors can be interpreted in either of two ways. First, the oxide present on the HQ-treated sample is reduced with great difficulty or, second, there is no appreciable amount of oxide on the HQ-treated sample. We are conjecturing at the present time, on the basis of very preliminary spectra obtained after sputtering, that the amount of surface oxide on the HQ-treated panel is very small. Infrared reflectance studies, laser Raman studies, and additional electrolytic reduction experiments must be performed before a definite conclusion can be reached.

It has been shown previously [7] in the case of galvanized steel that a surface treatment which leads to inhibition of the cathodic half reaction improves the performance of a coated metal in a cathodic delamination experiment. In the present studies the rate of cathodic delamination of an alkyd coating from the HQ-treated surface occurred at significantly lower rate than from either an abraded surface or one that had simply been anodized in the absence of 8-hydroxyquinoline. These data thus provide additional support for the concept that inhibition of a metal surface for the oxygen reduction reaction will increase the resistance of the metal to cathodic delamination. The procedure outlined in this paper holds promise for the development of a surface treatment method that will reduce the tendency of a coating to disbond from a metal either during corrosion or during cathodic treatment.

REFERENCES

- [1] H. Leidheiser, Jr., and I. Suzuki, J. Electrochem. Soc. 128, 242 (1981).
- [2] H. Leidheiser, Jr., G. W. Simmons, S. Nagy, and S. Music, J. Electrochem. Soc. 129, 1658 (1982).
- [3] H. Leidheiser, Jr., Y. Momose, and R. D. Granata, Corrosion 38, 178 (1982).
- [4] M. C. Hughes and J. M. Parks, "Corrosion Control by Organic Coatings," H. Leidheiser, Jr., Editor, Natl. Assoc. Corrosion Engrs., Houston, Texas, p. 45 (1981).
- [5] H. Leidheiser, Jr., and W. Wang, J. Coatings Technol. 53, No. 672, 77 (1981).

- [6] U. Gelius, P. F. Heden, J. Hedman, B. J. Lindberg, R. Manne, R. Nordberg, C. Nordling, and K. Siegbahn, Phys. Scripta 2, 13 (1970).
- [7] H. Leidheiser, Jr., and W. Wang, "Corrosion Control by Organic Coatings," H. Leidheiser, Jr., Editor, Natl. Assoc. Corrosion Engrs., Houston, Texas, p. 70 (1981).
- [8] A. Weisstuch, D. A. Carter, and C. C. Nathan, Mater. Prot. Perf. 10, No. 4, 11 (1971).

Program #3. The Application of Emission Mössbauer Spectroscopy to the Chemistry of the Coating/Substrate Interface

Two studies have been carried out during the past year that relate to the application of emission Mössbauer spectroscopy to studies of the interface between a coating and the metal substrate. The first study is concerned with an organic coating and the second is concerned with a metallic coating. These will be presented separately.

Part A. The Metal/Organic Coating Interface

A major unknown in an understanding of the interface between an organic coating and a metal substrate is the chemical nature of the interfacial region. This is specially important in understanding the phenomena that control "wet adhesion" [1], the ability of coated metals to withstand long exposure to high humidity conditions, and the disbonding of light-sensitive polymers used in lithographic plates and photoresists. We report here how ^{57}Co emission Mössbauer spectroscopy can be used to study the chemistry of the interfacial region in a model system consisting of cobalt metal and a commercial polybutadiene coating.

A previous study showed that the Mössbauer technique was suitable for studying corrosion beneath a coating [2]. Cobalt is selected here as the substrate metal because the isotope ^{57}Co is Mössbauer-active and can be concentrated at the metal surface using electrodeposition. Polybutadiene is selected as the coating because of our previous work with this material [3] and the utilization of polybutadiene by Dickie and co-workers [4] and by Castle and Watts [5] in corrosion studies.

Emission Mössbauer spectroscopy is based on the 14.4 keV γ ray that is emitted from ^{57}Fe as a consequence of the electron capture decay of ^{57}Co . Although the Mössbauer spectra obtained with this method are of ^{57}Fe , it is likely that it will be possible to obtain information about the chemical state of the initial ^{57}Co isotope. Indeed, in many cases emission spectra of cobalt compounds give hyperfine parameters expected on the basis of known oxidation state, structure and magnetic properties. It is also commonly observed that a fraction of the oxidation states of ^{57}Fe is atypical of the original oxidation state of ^{57}Co . These atypical oxidation states are produced as a consequence of the Auger cascade that follows the electron capture decay of ^{57}Co [6-8]. The fraction of these states that are stabilized is a function of chemical environment. For example, no atypical

^{57}Fe oxidation states are found in metallic environments, whereas in other compounds, such as hydrated cobaltous salts, a significant fraction of Fe^{3+} is found. Our interpretation of the emission Mössbauer data is based on extensive emission studies of the oxides, hydroxides and hydroxyoxides of cobalt that may be present at a cobalt metal-polymer interface [9-11]. The reported changes in the emission spectra of cobalt at this interface represent either direct changes in the chemical state of cobalt or changes in the environment of cobalt that in turn affects the stabilization of atypical ^{57}Fe charge states.

Cobalt, doped with ^{57}Co , was electrodeposited at room temperature on a cobalt substrate at a current density of 0.1 A cm^{-2} for 5-20 s while the metal was immersed in a bath containing $0.31 \text{ g l}^{-1} \text{ CoSO}_4 \cdot 7\text{H}_2\text{O}$, $100 \text{ g l}^{-1} \text{ MgSO}_4 \cdot 7\text{H}_2\text{O}$, and $30 \text{ g l}^{-1} \text{ H}_3\text{BO}_3$, $\text{pH} = 4.0$. The calculated thickness of the deposit was 20-120 nm assuming a current efficiency of 100%, but the actual thickness was considerably less. The Mössbauer spectrum of a thin deposit is shown in Figure 1 in which the metallic component (six-line spectrum) was ~24% and the ionic component was ~76%. These values are calculated on the basis of the area under the curve for each component and assume that the recoilless fraction is the same for all components. The ionic component presumably results from superficial oxidation of the metallic surface on exposure to air. The ratio of the metallic to the ionic component increased as the thickness of the electrodeposit was increased. Maximum sensitivity in the experiments to be described was obtained with deposits which yielded a spectrum similar to that in Figure 1. The major doublet is at a position characteristic of Fe^{3+} and only a small amount of Fe^{2+} (4%) is revealed by computer curve fitting. On the basis of the studies of Barr [12] and of Rice et al. [13], it is likely that the outer layer of cobalt exposed to the atmosphere has a composition equivalent to CoOOH . Identification of the surface composition by Mössbauer techniques alone does not appear practical as $\text{Co}(\text{OH})_2$ exhibits spectra showing different amounts of Fe^{2+} and Fe^{3+} depending on the method of preparation [1].

The cobalt surface was then coated with a commercial polybutadiene coating (Budium RK-662, DuPont) to a thickness of ~15 μm and the emission spectrum was again obtained without baking the coating. The spectrum was very similar to that shown in Figure 1. The Mössbauer parameters are given in Table 1. The coated metal was cured by baking at 200°C in air for 30 min and a spectrum was again obtained. As shown in Figure 2 and in Table 1, the Fe^{2+} doublet is now a substantial part of the total spectrum. Two possible changes at the interface could account for the increase in the Fe^{2+} component. First, an interaction between the cobalt oxide and the polymer may have reduced Co^{3+} in the surface oxide to Co^{2+} . Second, the treatment may have led to the dehydration of a Co^{2+} oxide with the result of destabilization of Fe^{3+} . (Stabilization of Fe^{3+} in the presence of water is thought to be the result of oxidation of Fe^{2+} to Fe^{3+} by OH radicals produced

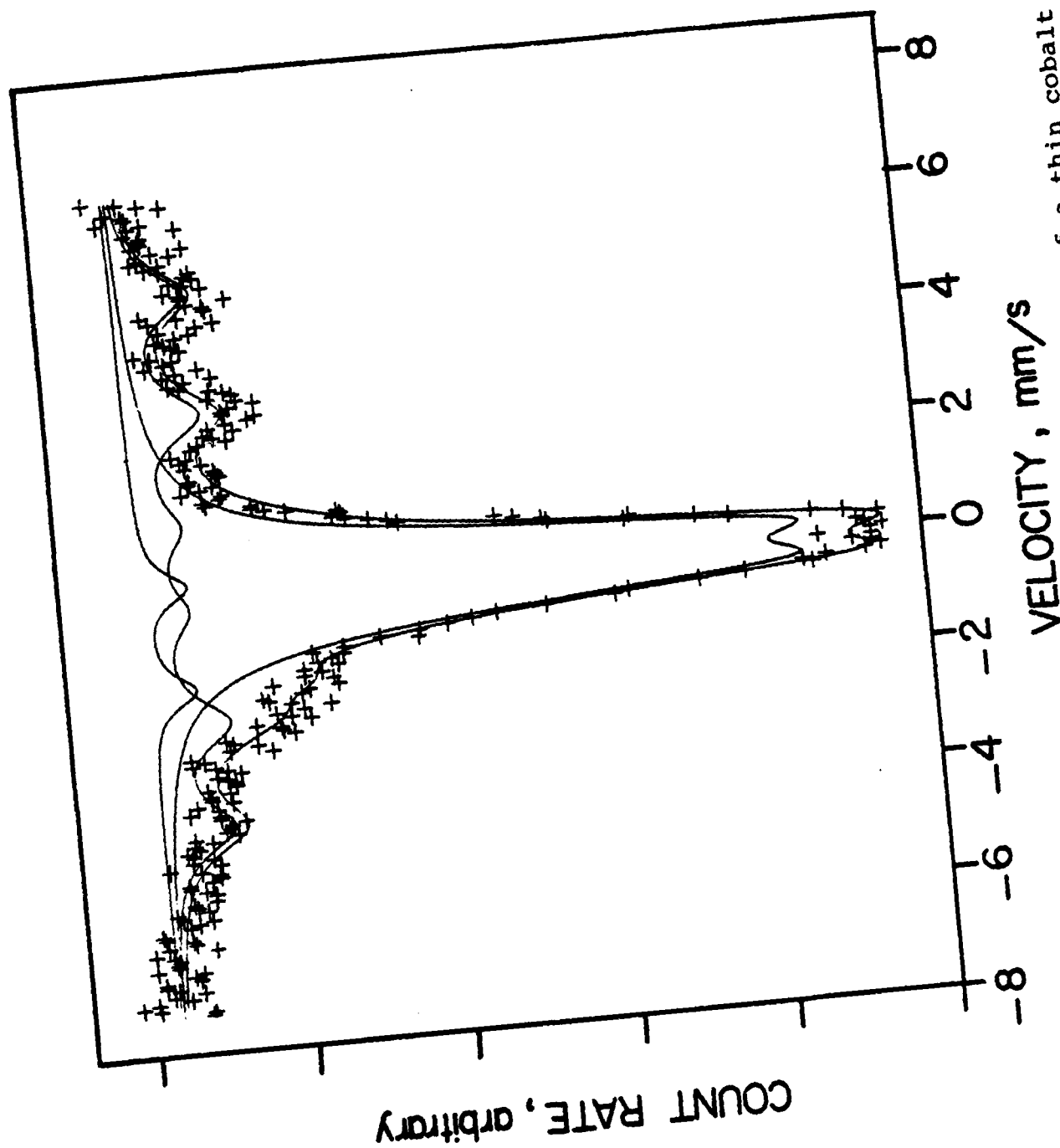


Figure 1. ^{57}Co Mössbauer emission spectrum of a thin cobalt electrodeposit used as the starting point in this experiment described in the text.

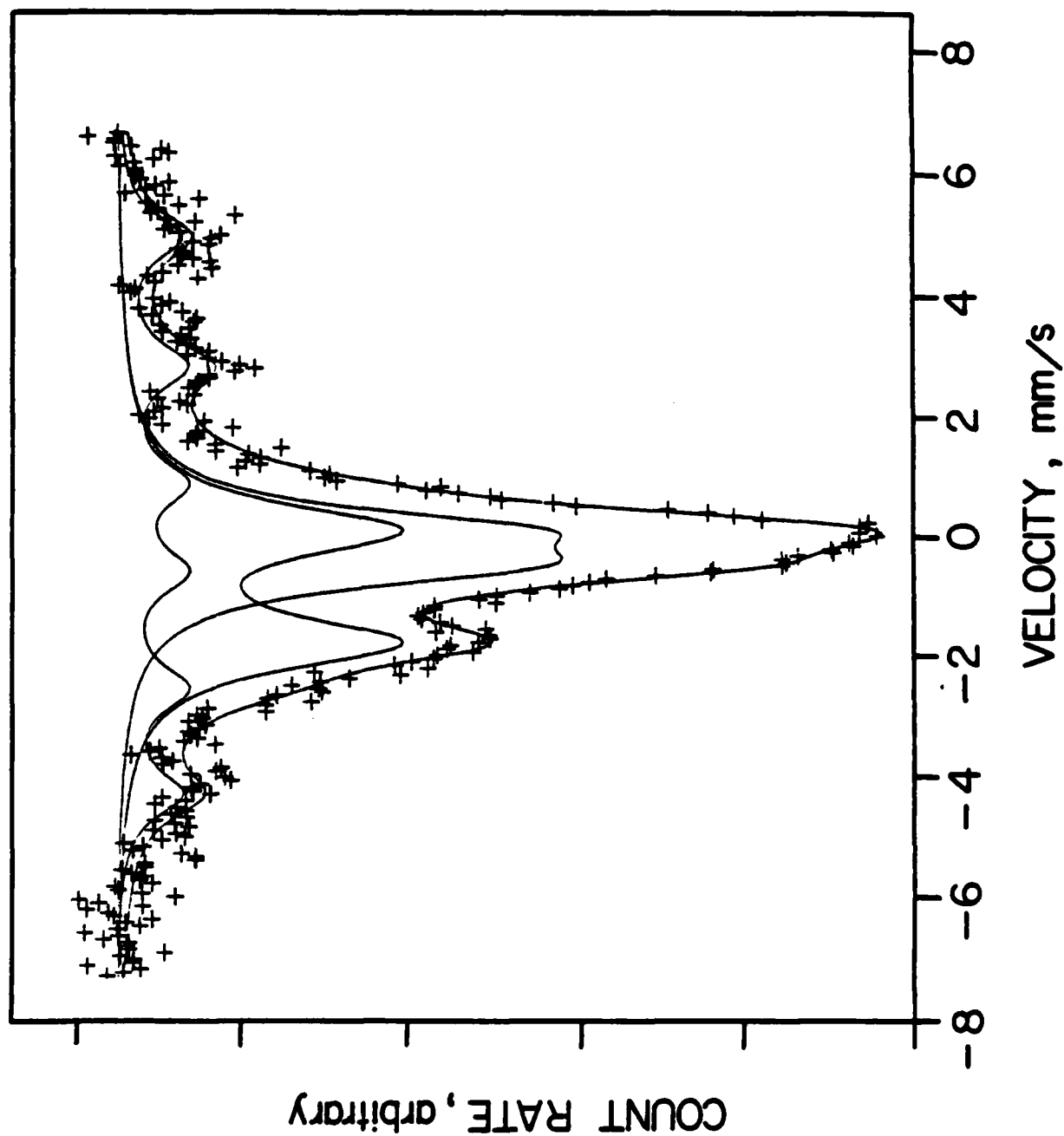


Figure 2. ^{57}Co Mössbauer emission spectrum of sample after coating with polybutadiene and baking at 200°C for 30 min. Compare spectrum with that in Figure 1.

Table I

Sample	Component	δ (mm/s)	Δ (mm/s)	$H_{5/2}$ (kOe)	Γ (mm/s)	Area of Component (mm/s)	A (%)
Spectrum of electrodeposit before applying the polybutadiene coating (Figure 1)	Fe ³⁺	-0.093	0.808		0.996	0.284	71
	Fe ²⁺	-0.952	2.248		0.540	0.016	4
	Fe ⁰	0.398	0.124	338	0.885	0.097	24
after applying polybutadiene coating but before baking	Fe ³⁺	-0.149	0.792		1.026	0.277	67
	Fe ²⁺	-0.925	2.096		0.786	0.020	5
	Fe ⁰	0.532	0.168	336	1.241	0.114	28
after baking the polybutadiene coating for 30 minutes at 200°C (Figure 2)	Fe ³⁺	-0.127	0.701		1.032	0.155	38
	Fe ²⁺	-0.883	2.214		1.216	0.153	38
	Fe ⁰	0.380	0.220	337	1.088	0.096	24

Chemical shift (δ) is given with reference to an enriched $K_4Fe(CN)_6$ absorber.

Δ = quadrupole splitting value

$H_{5/2}$ = hyperfine magnetic splitting

Γ = line width

A = relative amount of component

by the radiolysis of water molecules by the Auger electron ionization [6-8]. The reduction of the surface oxide is supported by the tentative conclusion of Castle and Watts [5] that the oxide on iron is partially reduced during the baking of polybutadiene coating on steel. The latter conclusion was tentative since it was based on X-ray photoelectron sputtering studies of stripped oxides and it is well known that the sputtering process may lead to changes in valence states of the cations in oxides [14].

The experiments described in Table 1 were repeated several times with similar results showing that the Mössbauer technique is sensitive at the level required to give information about the chemical nature of the organic coating-metal interface. The following conclusions can be drawn: (1) The contact between the cobalt metal and the polybutadiene is through an oxide or hydrous oxide at the interface. (2) No major changes at the cobalt interface occurred after application of the coating and before thermal treatment. (3) The oxide on cobalt does not thicken during the baking process. (4) Thermal treatment at 200°C causes a significant amount of conversion of Fe^{3+} to Fe^{2+} at the oxide-coating interface. (5) The reduction process cannot be a consequence of the reaction, $2\text{Co}^{3+} + \text{Co} = 3\text{Co}^{2+}$, during baking of the coating because the relative amount of unoxidized metal remains approximately constant before and after baking. (6) The conversion of Fe^{3+} to Fe^{2+} may be attributed to either a reduction of Co^{3+} to Co^{2+} or to the destabilization of Fe^{3+} by the dehydration of Co^{2+} oxide.

Small changes in the chemical shift and in the quadrupole splitting values before and after baking the polybutadiene may be significant, but we prefer to wait for further experiments with other metal-polymer coating systems before drawing further conclusions.

REFERENCES

- [1] W. Funke, Corrosion Control by Coatings (ed. H. Leidheiser, Jr.) 35-45, Science Press, Princeton, NJ, (1979).
- [2] H. Leidheiser, Jr., G. W. Simmons and E. Kellerman, J. Electrochem. Soc. 120, 1516-1518 (1973).
- [3] H. Leidheiser, Jr. and W. Wang, J. Coatings Technol. 53, No. 672, 77-84 (1981).
- [4] R. A. Dickie, J. S. Hammond and J. W. Holubka, Ind. Eng. Chem. Prod. Res. Dev. 20, 339-343 (1981).

- [5] J. E. Castle and J. F. Watts, Corrosion Control by Organic Coatings (ed. H. Leidheiser, Jr.) 78-86, National Association Corrosion Engineers, Houston (1981).
- [6] G. K. Wertheim, Accts Chem. Res. 4, 373-379 (1971).
- [7] N. N. Greenwood and T. C. Gibb, Mössbauer Spectroscopy, 373-379, Chapman and Hall, London (1971).
- [8] J. M. Freidt and J. Danon, J. Radiochim Acta 17, 173-190 (1972).
- [9] G. W. Simmons, E. Kellerman and H. Leidheiser, Jr., J. Electrochem. Soc. 123, 1276-1284 (1976).
- [10] G. W. Simmons and H. Leidheiser, Jr., Applications of Mössbauer Spectroscopy Vol. I (ed. R. L. Cohen) 85-125, Academic, New York (1976).
- [11] G. W. Simmons, Proc. 4th Int. Symp. on Passivity, 898-917, The Electrochemical Society, Princeton (1978).
- [12] T. L. Barr, J. Phys. Chem 82, 1801-1810 (1978).
- [13] D. W. Rice, P. B. P. Phipps and R. Temoureux, J. Electrochem. Soc. 126, 1459-1466 (1979).
- [14] R. Kelly, Surface Sci. 100, 85-107 (1980).

Part B. The Metal/Metal Coating Interface as
Exemplified by a Coating of Flame
Sprayed Aluminum on Cobalt

Henry Leidheiser recently served on a National Academy of Sciences Committee to review the application of flame-sprayed aluminum to corrosion protection of components of naval vessels. As a result of the discussions of the committee it became apparent that the type of bonding between a steel substrate and the aluminum was not known although the low bonding strength, typically 2,000-4,000 lbs/in², and the necessity to have the proper degree of roughness of the substrate, suggested that the adherence was primarily mechanical in nature. The following model experiments were carried out in order to explore this point.

The technique selected-emission Mössbauer spectroscopy has been used previously in studies of the interfacial region between a cobalt substrate and a polybutadiene coating [1]. The method requires the use of cobalt because Co-57 is the precursor for the excited state of Fe-57 which actually emits the gamma ray that is detected by the Doppler effect conventionally utilized to obtain a Mössbauer spectrum. The method is very simple in concept. Metallic cobalt is electrocoated with a very thin deposit of cobalt containing Co-57. A reference Mössbauer spectrum is obtained. The cobalt is spray coated with aluminum and another spectrum is obtained. Differences in the spectrum before and after spray coating with aluminum are indicative of chemical changes at the interface. A description of the experimental details will now be given.

The cobalt sheet in the form of a square, approximately 2 cm on a side, was sandblasted, scrubbed gently with a nylon brush under running distilled water, and immediately immersed in a plating bath containing $\text{CoSO}_4 \cdot 7\text{H}_2\text{O}$ doped with Co-57, 0.31 g/L; $\text{MgSO}_4 \cdot 7\text{H}_2\text{O}$ 100 g/L; H_3BO_3 30 g/L; pH = 4.0. A current density of 0.01 A/cm² was used. Two samples were prepared. One deposit was estimated to be approximately 5 nm in thickness and the other was estimated to be approximately 10 nm in thickness. The resulting cobalt electrodeposit consisted of an ionic component (presumably the surface oxide) and a ferromagnetic metallic component (the unoxidized metal). A computer evaluation of the spectrum of the thicker deposit is given in Table I in which it will be noted that the metallic component composed 56% and the ionic component composed 44% under the assumption that the recoil fraction was the same for all components.

After the original spectra had been obtained, the samples were maintained in a desiccator for approximately two weeks before being transported to Stony Brook for the flame spraying process. Both samples retained their clean appearance between the time of preparation and flame spraying. The samples were maintained in a vertical position through use of a magnetic holder and were flame sprayed in two passes with the gun pointing in a direction normal to the specimen surface. The resulting coating was approximately 0.01 cm thick. Adherence of the coating was poor at the edges but the coating on the major fraction of the surface exhibited satisfactory adherence. The adherence was not measured quantitatively because of the difficulty in working with a radioactive sample.

The spectra for the thicker electrodeposit are given in Figure 1 for the cobalt surface immediately after preparation and in Figure 2 for the sample after the application of the aluminum. Superposition of the two spectra indicated that they were identical in all respects. The following conclusions can be drawn:

Table I

Mössbauer Parameters of Thin Electrodeposit after
Exposure to the Atmosphere

<u>Component</u>	<u>Chemical Shift*</u> (mm/sec)	<u>Quadrupole Splitting</u> (mm/sec)	<u>Magnetic Hyperfine Splitting</u> (kOe)	<u>Half Width at Half Max.</u> (mm/sec)	<u>Area Fraction</u>
Metallic	+0.394	0.00	337	1.03	56%
Divalent Species**	-0.658	2.80		1.13	7%
Trivalent Species**	+0.009	0.754		0.94	37%

* - with respect to potassium ferrocyanide

** - Gamma ray emission is from Fe-57 species. There is not necessarily a 1:1 relationship between the originating Co-57 species and the Fe-57 atom that emits the gamma ray.

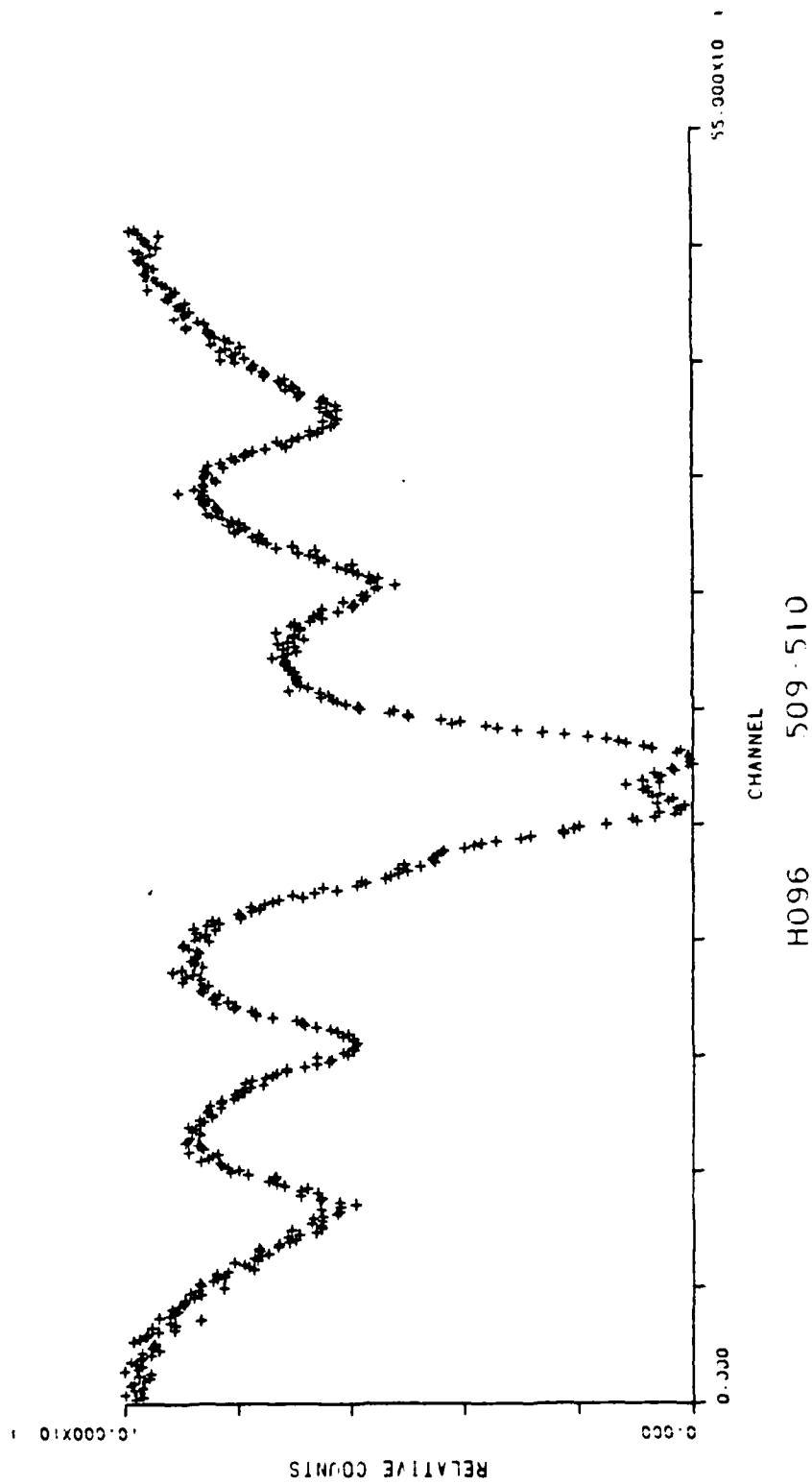


Figure 1. Mössbauer emission spectrum of a cobalt electrodeposit doped with Co-57.

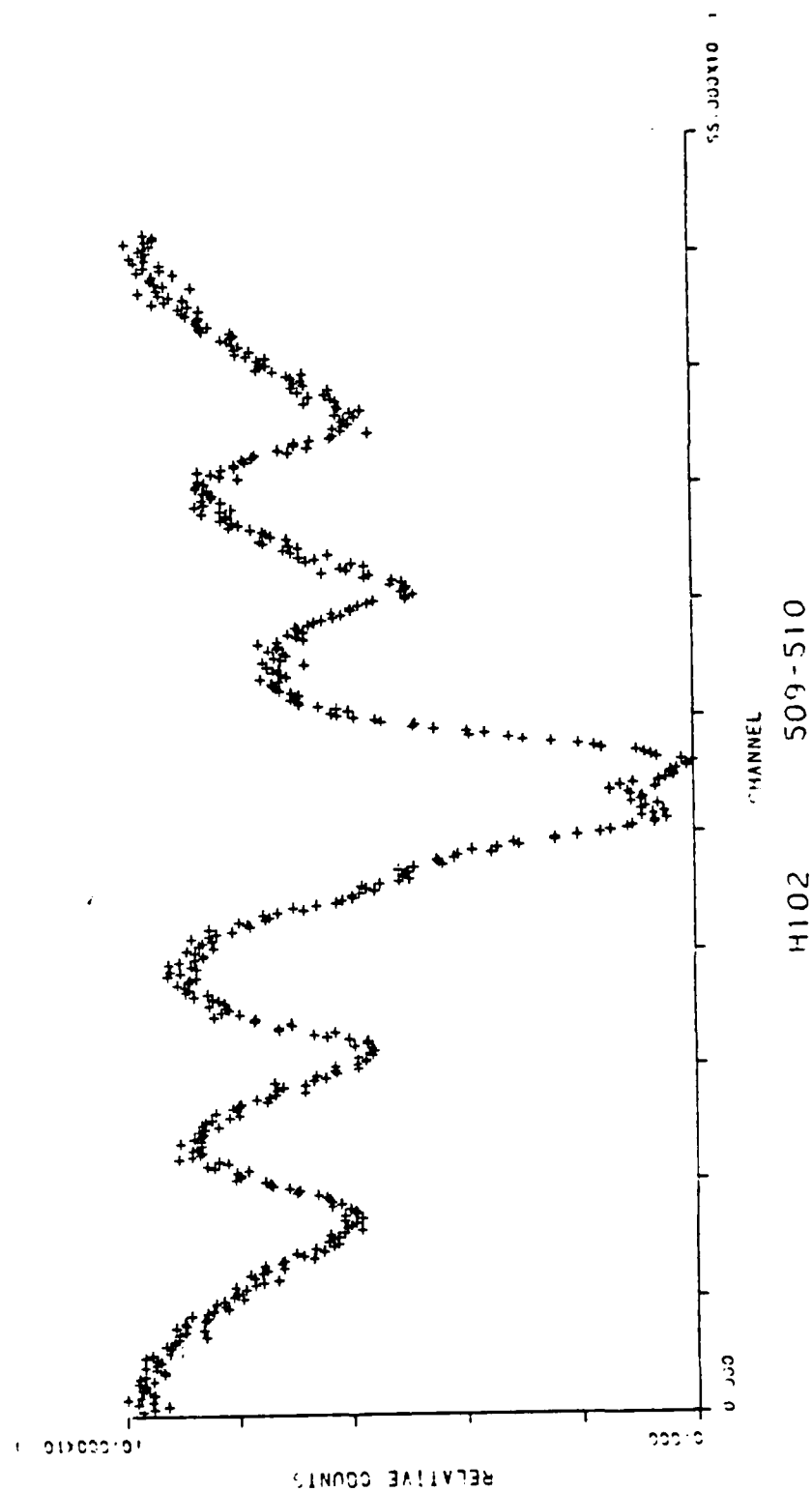


Figure 2. Mössbauer emission spectrum of the same cobalt sample used in Figure 1 after coating with flame-sprayed aluminum.

(1) The oxide film on cobalt remained constant in amount before and after flame spraying. Thus, aluminum did not reduce the oxide film and the oxide film did not thicken.

(2) There was no evidence of a change in the chemical nature of the oxide film on cobalt. The 37/7 ratio of the trivalent/divalent species was the same before and after flame spraying.

In summary, it can be concluded that a flame-sprayed aluminum coating has no significant effect on the chemical nature of a cobalt surface such as normally exists during exposure to air at room temperature. The bonding between cobalt and flame sprayed aluminum does not involve a chemical reaction and is largely, or perhaps exclusively, mechanical in nature. It appears reasonable that this conclusion in the case of cobalt can be extended to steel because there are many similarities in the chemical behaviors of the surface oxides on cobalt and iron.

REFERENCE

- [1] H. Leidheiser, Jr., S. Musić and G. W. Simmons, *Nature* 297, No. 5868, 667 (1982).

Program #4. Determination of the Acidity of Iron Oxide Surfaces

INTRODUCTION

The adhesion of organic polymers to inorganic oxides, such as those on steel surfaces and iron oxide pigments, has been shown to result entirely from acid/base interactions between the polymer and the oxide. Hydrogen bonds have been shown to be a subject of acid/base interactions and dipole/dipole interactions have been shown to be so negligibly small that no experimental evidence for them has yet been found. It is therefore important to find a method of measuring and predicting acid/base interactions in the bonding of organic polymers to metal oxide surfaces, especially the oxide layers of steel.

RESULTS AND DISCUSSION

A major improvement in the accuracy and reliability of adsorption data obtained using the Microscal flow microcalorimeter has been achieved by the addition of an in-line Perkin Elmer LC-75 variable wavelength UV flow detector to monitor the concentration of the probe molecule in the effluent stream. Thus, the adsorption enthalpy is directly determined using the flow microcalorimeter while the number of moles adsorbed under the trial conditions can be determined by the difference between a calibration curve and the actual effluent concentration as a function of time. Previous analysis of the enthalpy data required the use of a site area per molecule which was determined from static (equilibrium) adsorption isotherms after equilibration times of up to three days. The flow microcalorimeter, on the other hand, actually yields kinetic adsorption data since the enthalpy output is observed as a function of time after the replacement of a pure carrier solvent stream percolating through the powder adsorbent bed by a dilute solution (1 to 50 millimolar concentration) of the probe molecule in the same carrier solvent. Thus, the strong acid-base interaction of pyridine adsorption onto iron oxide from cyclohexane results in a substantial enthalpy while the very weak base benzene in cyclohexane shows no observed enthalpy despite the evidence from the UV detector that the benzene is being adsorbed by the iron oxide surface. In this second case, the adsorption

enthalpy of benzene is almost precisely balanced by the desorption enthalpy of the displaced cyclohexane molecules.

The following technique has been employed to select an appropriate concentration range for analysis of a UV absorbing probe molecule in a UV transparent carrier solvent:

1. The UV absorbance of the probe is determined as a function of concentration and wavelength in the Hitachi 200 spectrophotometer using a 1 cm pathlength quartz cell.

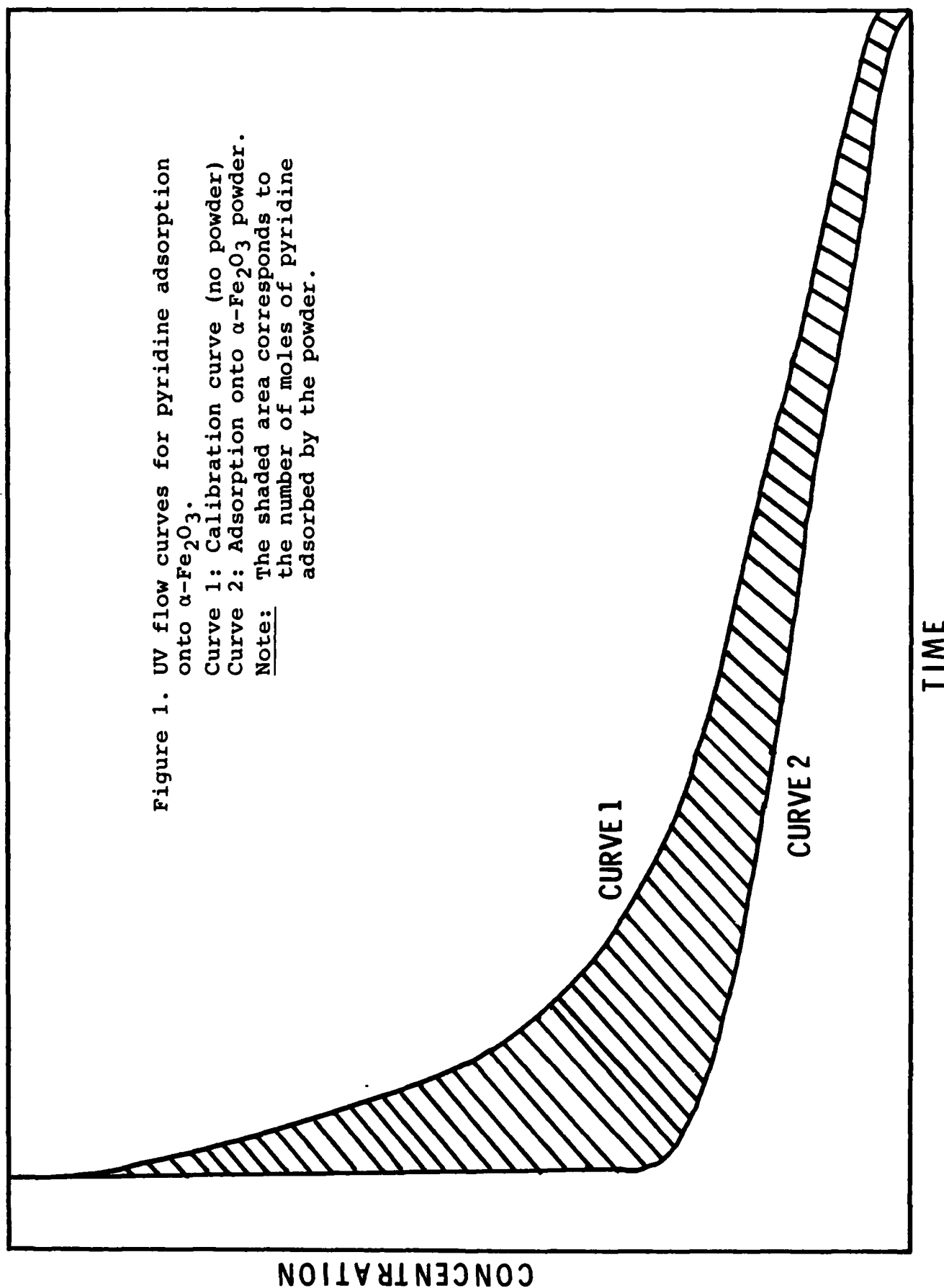
2. A wavelength is then selected where Beer's law is satisfied, i.e., absorbance is proportional to concentration over the desired concentration range of interest. It is essential that the response be linear since the difference in absorbance between the calibration curve and the trial run at any given time indicates the number of moles removed from that particular volume element of solution due to adsorption onto the powder bed.

3. The S-shaped curve produced by replacing the flow of pure carrier solvent through the cell by the selected probe concentration is then determined, yielding a concentration profile versus time.

A significant degree of broadening was observed in the response curve (pyridine concentration as a function of time) compared to the ideal sharp boundary for plug flow conditions (Figure 1). Broadening associated with internal mixing in the UV cell is reported by Perkin Elmer to be approximately 150 microliters. The broadening due to the UV cell plus the diameter reduction connection between the microcalorimeter and the detector was determined to be approximately 200 microliters while the total broadening obtained for the system was 450 microliters. The remaining source for internal mixing appears to be the .0625 I.D. outlet from the microcalorimeter since replacement of the inlet, bed and outlet portions of the microcalorimeter by .0625 I.D. stainless steel tubing results in the identical curve shape. The total broadening in the flow system corresponds to four min of flow time under the current operating conditions (6.6 ml/hr).

The number of moles of pyridine adsorbed can be determined from the area difference between the calibration curve and the trial curve produced when the pyridine solution is passed through the haematite bed (note the shaded area in Fig. 1). With rapid adsorption onto the powder, a delay time is observed which represents "complete" removal of the pyridine from the solution (to the limits of detection) as it passes through the powder bed. In this instance, the calibration curve must be offset from the trial curve by an appropriate time interval corresponding to this sorption period. This interval is determined by measuring the time from the first detected adsorption or desorption heat recorded by the microcalorimeter to the first recorded response

Figure 1. UV flow curves for pyridine adsorption onto $\alpha\text{-Fe}_2\text{O}_3$.
Curve 1: Calibration curve (no powder)
Curve 2: Adsorption onto $\alpha\text{-Fe}_2\text{O}_3$ powder.
Note: The shaded area corresponds to the number of moles of pyridine adsorbed by the powder.



by the UV detector. The difference in these flow times is used to calculate the appropriate offset of the calibration curve. This time interval corresponds to the flow volume from the top of the sample bed to the UV detector cell and thus is constant for a given trial, although it may change slightly from one trial to another due to differences in sample volume or bed packing. A ten sec error in determining the offset time would result in a 10% error in the calculated number of moles adsorbed. The sensitivity of the instrument can be calculated using the following formula for mixed flow:

$$C = C_0 [1 - \exp(-t/t_r)] \quad (1)$$

where,

C = observed concentration

C_0 = initial concentration

t = time

t_r = residence time of the system calculated from the area difference between the calibration curve and plug flow and corresponding to 136 microliters

The initial inlet concentration is $2.8 \times 10^{-2}M$ pyridine due to broadening in the flow system (compared to the overall concentration of the pyridine solution of $5 \times 10^{-2}M$). After 5 sec flow into the UV cell, the calculated concentration of pyridine is $1 \times 10^{-3}M$ due to mixing in the cell. After 10 sec, the concentration is $2 \times 10^{-3}M$. Thus, a detectable quantity of pyridine is present within the time interval required for accurately determining the offset time.

The fundamental importance of controlling water in the organic liquid and on the surface of the oxide has been emphasized in our previous report. We have chosen an *in situ* evacuation technique under mild conditions (10 min at 1 torr), followed by wetting of the iron oxide powder with cyclohexane of a fairly low controlled water content (10 to 20 ppm). A one hr equilibration time at the current operating temperature of 40°C appears to be sufficient since no changes in the number of moles adsorbed or the enthalpy of adsorption occur for increased times unless the cyclohexane has an unacceptably high water content (35 ppm or more). In that case, the pyridine adsorption peak is attenuated by the desorption enthalpy of water displaced from the iron oxide surface. We currently have no analytical technique capable of quantifying the amount of water displaced from the iron oxide surface as a function of time although the possible application of a flow infrared cell is being considered.

We have obtained good reproducibility in the enthalpy per mole of pyridine adsorbed for concentrations in the plateau region of the Langmuir adsorption isotherm (Table I). As previously demonstrated, the enthalpy per weight charged is a

Table I

<u>Pyridine Surface Density</u> ($\times 10^{10}$ moles/cm ²)	<u>Adsorption Enthalpy</u> (kcal/mole)
6.6	3.07
7.2	3.16
5.45	3.38
6.3	3.05
5.55	2.82
5.3	3.08
5.1	3.13
5.55	3.06

95% confidence limit: $3.09 \pm .13$

strong function of the sample weight due to the location of the two thermistors in the design of the Microscal flow microcalorimeter. All data presented were obtained for a sample charge corresponding to the maximum in the plot of enthalpy per weight charged vs. sample weight, i.e., a 150 mg sample of Pfizer $\alpha\text{Fe}_2\text{O}_3$ R-2199 (Lot E9036) with a BET surface area of 10 m²/gm. Figure 2 is a plot of the area response on the flow microcalorimeter vs. the electrical heat input through a wire coil placed in the sample bed. The calibration constant determined from the slope of this graph is 3.27×10^{-6} kcal/cm² for a recorder attenuation of 2000 μ volts full-scale deflection.

We have not as yet obtained reproducible pyridine adsorption data at equilibrium concentrations lower than the plateau region of the Langmuir adsorption isotherm. We believe that this difficulty is due to slight variations in the water content from run to run. A Karl Fischer automatic titrimeter has been ordered to enable routine analysis of water in both the inlet and exit streams to determine better the active role of water in this system. Some general trends observed as the equilibrium pyridine concentration is decreased are: The number of moles adsorbed is decreased, the enthalpy per mole adsorbed is increased, and the adsorption kinetics are slower. For example, there is essentially no change in the total enthalpy observed by decreasing the equilibrium pyridine concentration from 40 to 10 millimolar while the number of moles adsorbed is reduced by 66%. Below 10 millimolar pyridine in cyclohexane, both the enthalpy and number of moles adsorbed are decreased. These figures are based upon the number of moles

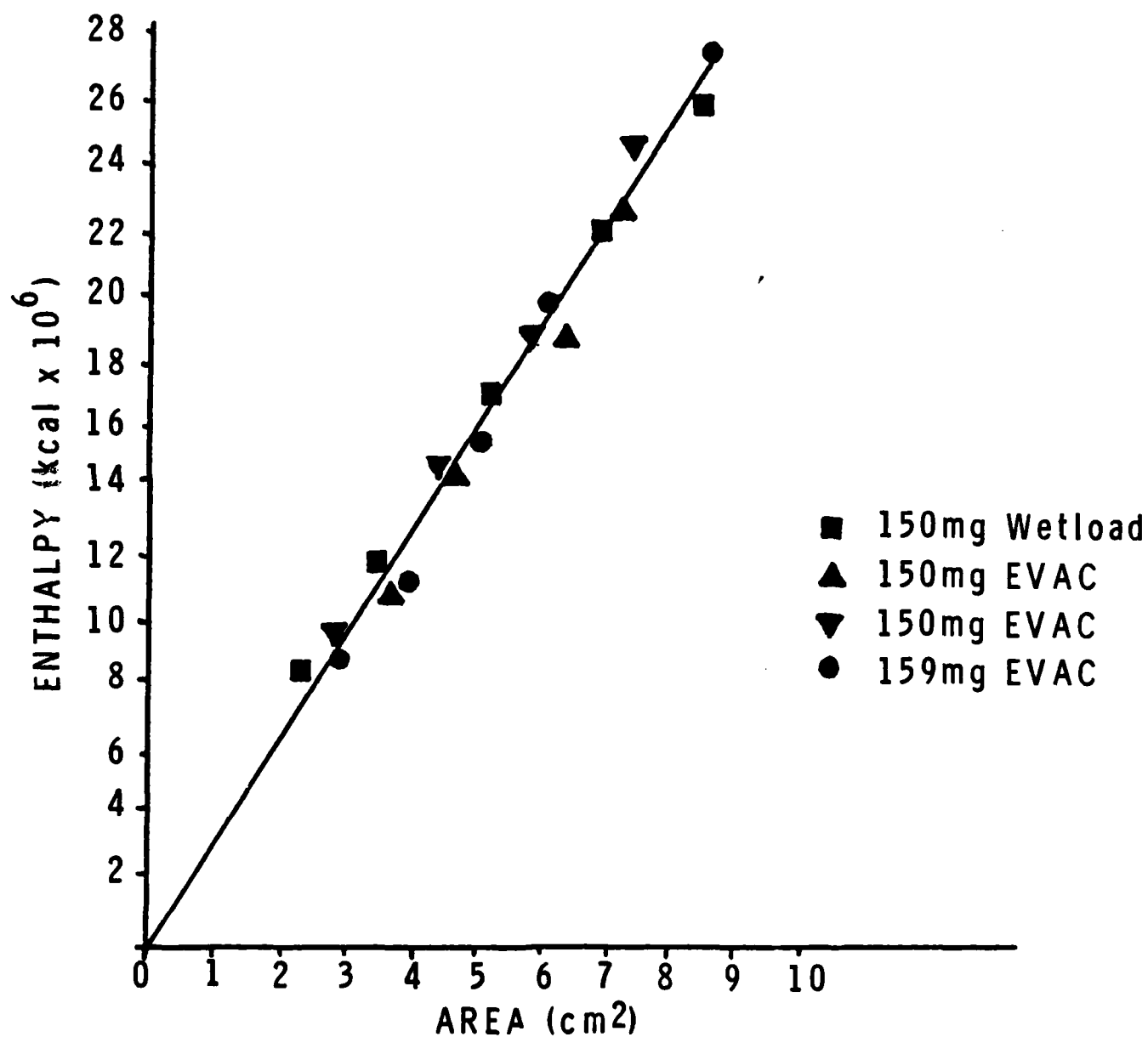


Figure 2. Microscal flow microcalorimeter calibration data. Recorder attenuation: FSD = 2000 μ volts.

adsorbed during the total time duration of the enthalpy peak. In all cases, the pyridine surface density continues to increase after no further enthalpy is observed.

Figure 3 presents "slice" data taken from different trial runs at various pyridine equilibrium concentrations to demonstrate the decrease in adsorption enthalpy with increasing surface coverage. Most of the data for the lower surface density values had to be obtained for low equilibrium concentrations since a minimum slice width of five min was required for accuracy in this "cut and weigh" technique. (We are currently investigating computerization of our equipment which would make time slice data readily accessible at much smaller time widths.) This graph illustrates that there is scatter in the data gathered to date even for subsequent trials on a fresh bed which used the same pyridine solutions. The data obtained for the water contaminated systems are consistent with the view that the water is blocking the more active sites for pyridine adsorption since these data are generally lower in enthalpy at the corresponding site density than samples given a standard evacuation.

Preliminary survey work continued this year to screen additional acids and bases (i.e., 4-picoline, triethyl amine, iodine, phenol) in our modified flow system to ensure adequate detection capabilities for both the enthalpy and UV concentration sensitivity. It is believed that once the variability in the water content can be pinned down and remedied, these systems can be promptly evaluated. We have also done some cursory polymer adsorption work utilizing the microcalorimeter alone. These results using poly(2-vinyl pyridine) were very promising since a substantial adsorption peak was produced which returned to the baseline in a reasonable time interval. A comparison between adsorption of the polymer and its low molecular weight analog is presented in Figure 4. Polymer adsorption work is expected to receive increased attention in the next year.

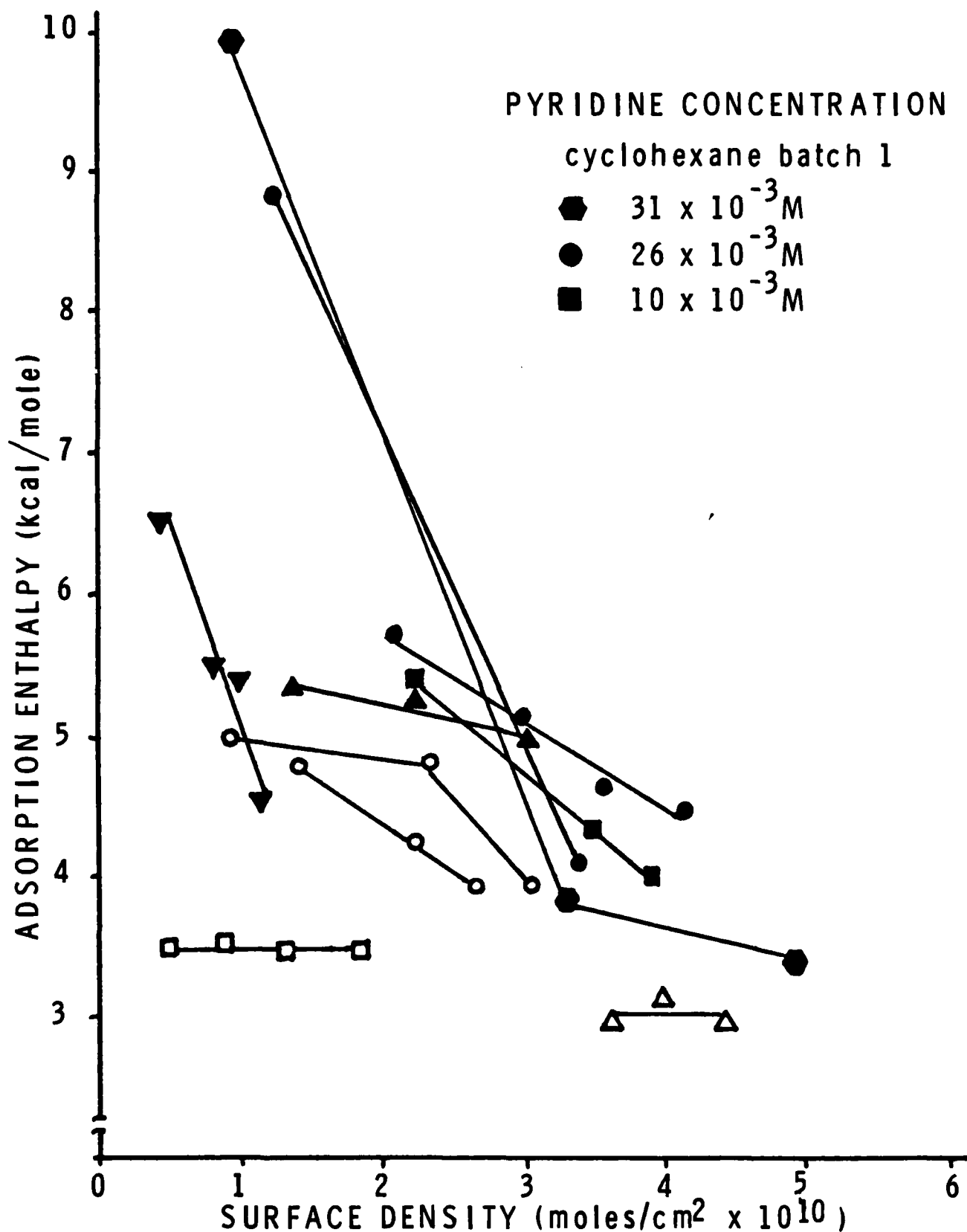


Figure 3. Enthalpy of pyridine adsorption from cyclohexane onto iron oxide powder. The closed symbols represent data for a normal 10-minute evacuation procedure. The open symbols represent data with a deliberate excess of surface water as a result of decreased evacuation time.

FSD = 2000 μ V
FLOW RATE = 6.6 ml/hr
CONCENTRATION = 4×10^{-2} EQ/LITER
PYRIDINE IN CYCLOHEXANE
— PYRIDINE
--- POLY (2-VINYL PYRIDINE)

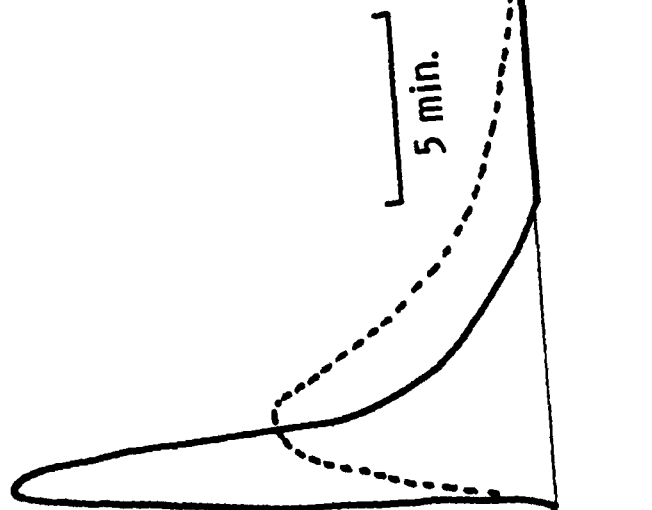


Figure 4. Flow microcalorimeter recorder traces for the comparative adsorption and desorption peaks obtained for pyridine and poly(2-vinyl pyridine) on α -Fe₂O₃.

Program #5. Ion Exchange Properties of Iron Surfaces

INTRODUCTION

The loss of coating adhesion on metal objects due to cathodic corrosion delamination is a commonly observed problem [1,2]. Studies past and present have attempted to halt this process by compositional changes in the coating, or surface pretreatment (i.e., conversion coatings) of the metal. Such alterations may halt cathodic attack in the surface layers of either the coating or the substrate, but the interfacial bond may continue to fail. It is therefore of great importance to attain the strongest possible interaction between a coating-substrate system in order to resist the attack of the cathodic corrosion reaction.

This study focuses on the surface chemistry of planar metal oxides to understand more fully and to promote their strong chemical interaction with polymer coatings. The analysis employs AES (Auger Electron Spectroscopy) and XPS (X-ray Photoelectron Spectroscopy) along with classical surface chemistry methods.

Background

Metals exposed to atmospheric gases readily form an "equilibrium" surface oxide layer. These oxides then interact with moisture in the air (or from solution treatments) to form a surface hydroxyl layer [3-5]. It is with such a layer that a coating interacts. The possible modes of interaction include dispersion forces, dipole interactions, and acid-base (hydrogen bonding) reactions. Mechanical coupling of coating and substrate has also recently been shown as an important consideration for adhesion; however, strict dependence upon such a mode of attachment yields little resistance to chemical attack [6]. The most energetically stable interaction is via acid-base (H-bonding) interaction. Fowkes [7,8] has shown the strength of adhesive bonds between a polymer and a filler (an oxide such as silica) can be correlated with the relative acidic or basic strength of the polymer, filler, and solvent.

Planar, low-surface area materials will be used in this study. Efforts to characterize oxide surfaces have been reported for high surface area materials [9]. The results of these studies do not represent a precise determination of the acid-base nature of the surface hydroxyl because the techniques used cause a shift in the surface reaction equilibria. It is our goal to characterize the surface hydroxyls on low surface area specimens by determining

both the number and acid-base strength.

Before the investigation of the surface OH could be accomplished, methods had to be developed to prepare specimens with the minimum amount of competing contamination. Significant progress has been made in our preparation procedure as evidenced by comparison of the spectrum shown in Figure 1 of an earlier specimen with the spectrum shown in Figure 2 for a specimen prepared by current procedures.

The improvements in specimen cleanliness can be attributed to two major changes in procedure. The first was the construction of a quartz tube furnace with a gas manifold (zero grade gases were used) to prepare the substrate (Fig. 3). In this apparatus the specimen substrate (Fe 99.9+%) was hydrogen annealed under high temperature and then directly oxidized and hydrated, with minimal exposure to the atmosphere.

The solutions with which the specimens are treated to characterize the surface hydroxyls had been suspected as a source of contaminants. By the use of ultrapure chemicals (KOH ultrapure, from Alpha, < 30 ppm Na, < 0.3 ppm Ca), the presence of some unwanted ions has been eliminated. Much of the carbonaceous contamination has been eliminated by distilling water in a quartz glass still under N₂ and then running the water through a Barnstead "Organic Pure" unit.

Method

Once confidence had been established in the specimen preparation technique, characterization experiments were continued. The method used for characterizing the acid strength of the surface hydroxyl is ion exchange as a function of pH.

Surface ion exchange of hydroxyls as a function of pH has been well documented [10-15]. Use of such a technique allows for the generation of a point-by-point "titration" curve of the surface hydroxyls. Specimens exposed to cations (or anions) at various pH's demonstrate changing cation (or anion) surface concentration.

The exchange of an ion such as K⁺ depends only on the developed surface charge, due to surface hydroxyl deprotonation. The heat of interaction for such ions under these conditions has been determined to be nearly zero [11]. Multiple charged ions, however, display a thermodynamic favorability for the surface hydroxyls and are referred to as specifically adsorbed ions. Such behavior interferes with the simple cation exchange desired by allowing for adsorption in the absence of surface ionization.

The extent of ion exchange at the surface is followed by AES and XPS. The coverage of the surface depends upon the K_a of the surface hydroxyl, the exchange constant K_f, and possible hydration of the cation in solution. In this investigation, K_f is assumed to represent 100% exchange, because of the overwhelming cation

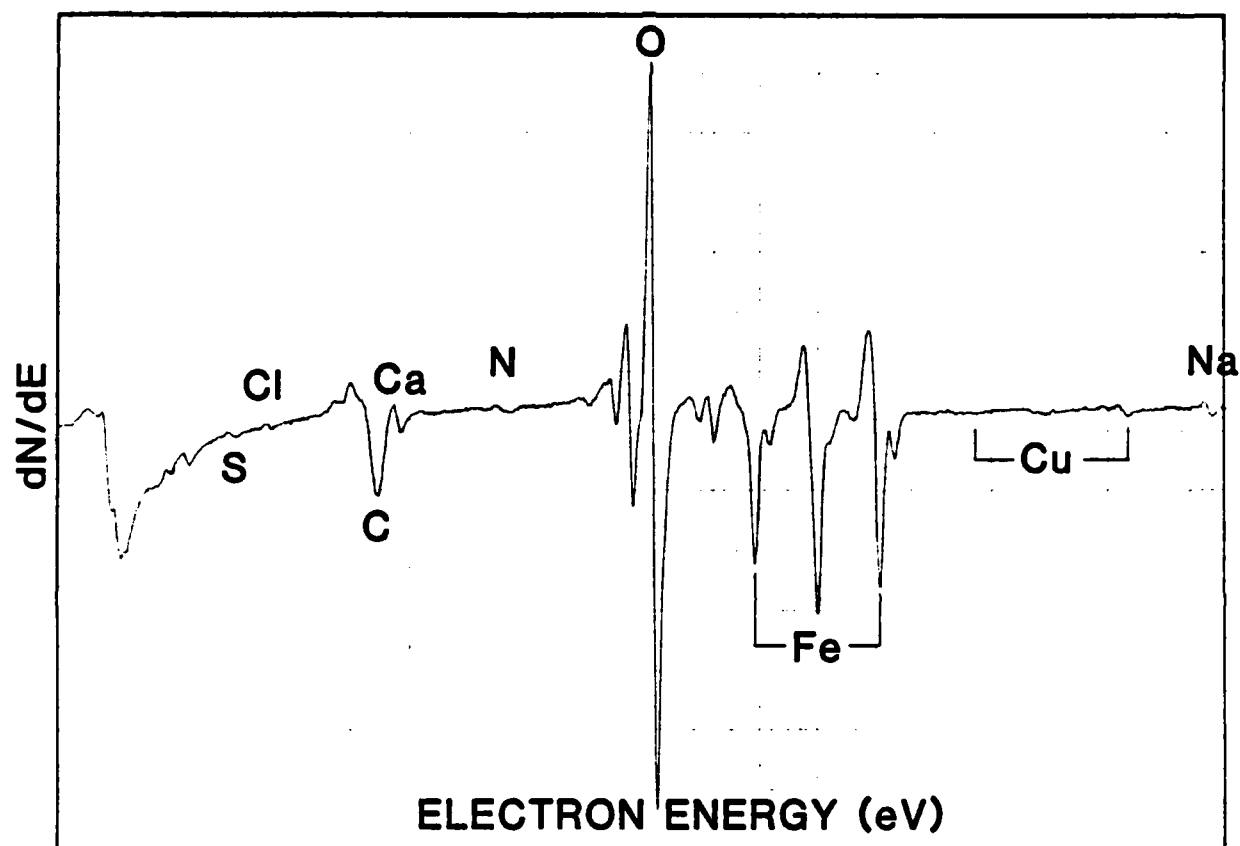


Figure 1. Auger electron spectrum of a specimen before procedural improvements.

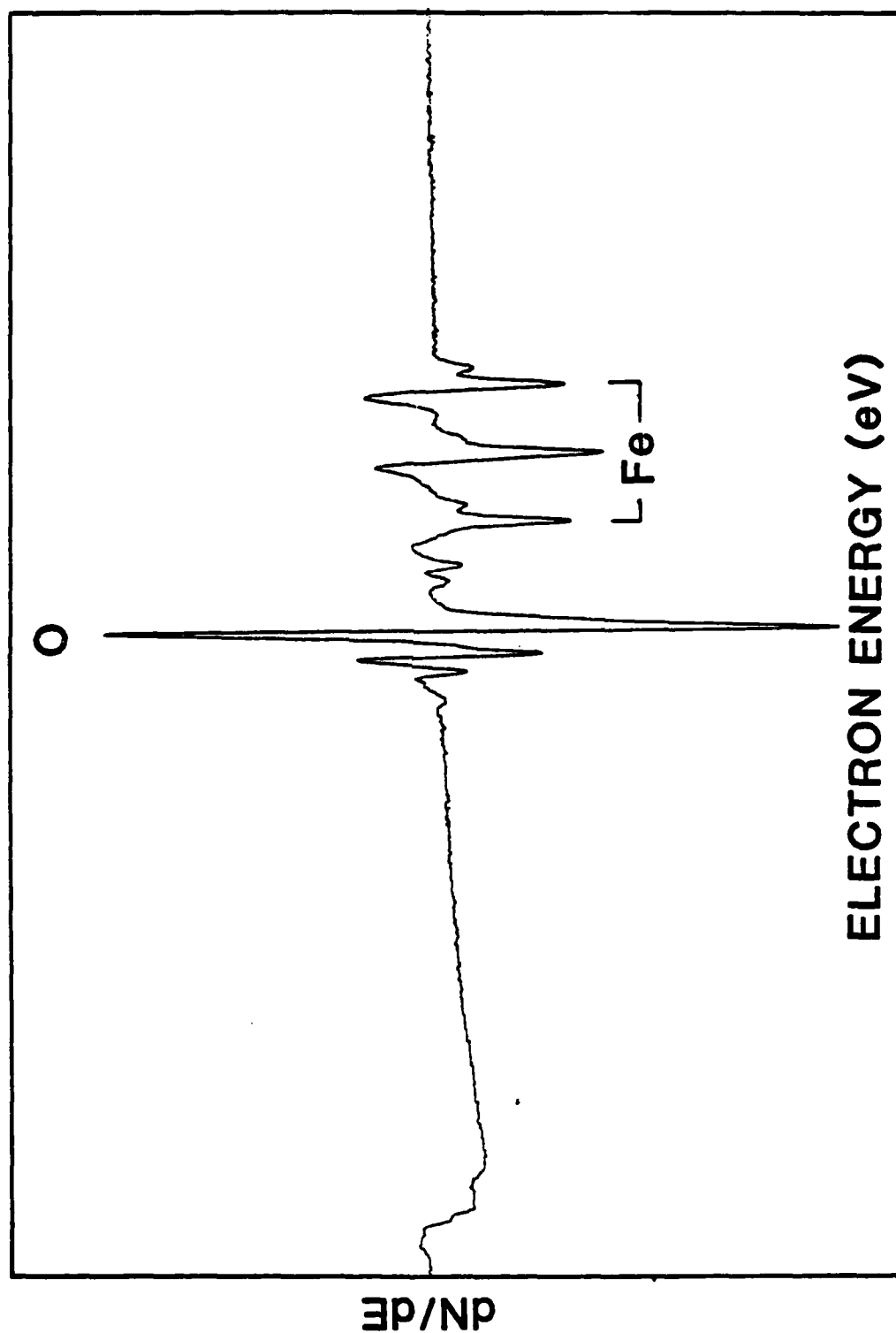


Figure 2. Auger electron spectrum of "clean" control sample.

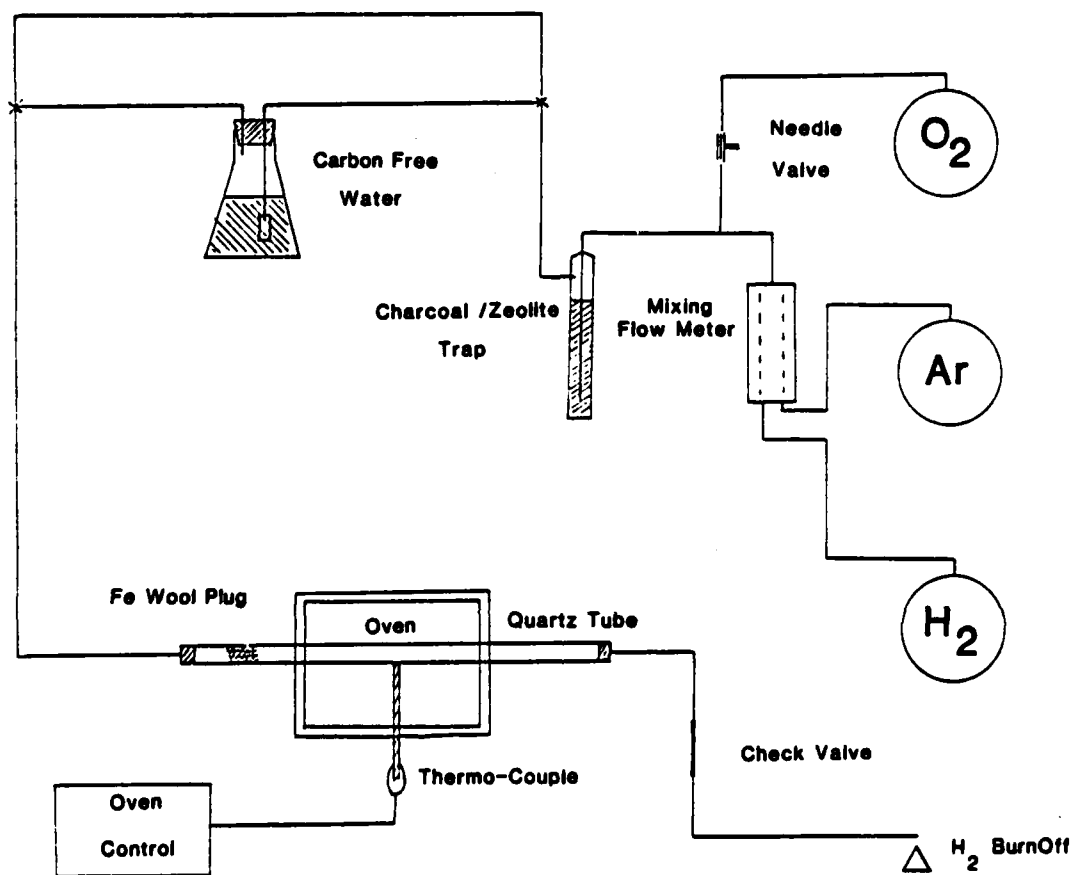


Figure 3. Quartz tube furnace with a high purity gas manifold.

concentrations present in solution compared to the numbers of surface hydroxyls. The use of a singly ionized cation, K^+ , removes any consideration of hydration or specific adsorption. These factors can be incorporated into an expression which should model the surface-solution equilibria. These surface equilibria, written for a cation M^+ , are given below.



The sum of the surface hydroxyls, ionized hydroxyls and exchanged hydroxyls is a constant representative of the total number of exchangeable hydroxyls, N_o (units of sites/ m^2).

$$[\equiv \text{FeOH}] + [\equiv \text{FeO}^-] + [\equiv \text{FeO}^-\text{M}^+] = N_o \quad (\text{sites}/\text{M}^2) \quad (3)$$

It is assumed that equilibrium is reached during the 300 sec immersion period. It is further assumed that all ionized sites at a given pH are exchanged since the solution concentration of cations is in large excess of the total number of exchangeable hydroxyls.

$$N_o = [\equiv \text{FeOH}] + [\equiv \text{FeO}^-\text{M}^+] \quad (4)$$

$$K_a = \frac{[\equiv \text{FeO}^-][\text{H}^+]}{[\equiv \text{FeOH}]} = \frac{[\equiv \text{FeO}^-\text{M}^+][\text{H}^+]}{[\equiv \text{FeOH}]} \quad (5)$$

For convenience, the fraction, θ , of the total available hydroxyls which have undergone exchange, i.e., coverage, is defined by the

following ratio, $\theta = \frac{[\equiv \text{FeO}^-\text{M}^+]}{N_o}$. Using this definition of the

fraction of exchange, θ , in Equation (4) and substituting the result into Equation (5), gives the following results.

$$\frac{[\equiv \text{FeO}^-\text{M}^+]}{N_o} + \frac{[\equiv \text{FeO}^-\text{H}]}{N_o} = 1 \quad (6)$$

$$\frac{[\equiv \text{FeOH}]}{N_o} = 1 - \frac{[\equiv \text{FeO}^-\text{M}^+]}{N_o} = 1 - \theta \quad (7)$$

$$K_a = \frac{\theta}{1-\theta} [\text{H}^+] \quad (8)$$

From Equation (8), two useful final equations can be obtained as follows:

$$\log \frac{\theta}{1-\theta} = \text{pH} + \log K_a \quad (9)$$

$$\theta = \frac{1}{(H^+/K_a) + 1} \quad (10)$$

For Equations (9) and (10), θ is measured as cation coverage at any pH_i relative to the saturation coverage at pH_s .

$$\theta = \frac{M^+(\text{pH}_i)}{M_{\text{max}}^+(\text{pH}_s)} \quad (11)$$

Cation coverage is calculated by normalizing the potassium Auger peak height with the Fe (635 eV) peak height.

There are two unknowns in Equations (9) and (10): the hydroxyl dissociation constant K_a and the saturation coverage value, M_{max}^+ . Once the saturation coverage value has been attained experimentally, K_a can readily be obtained (Eqn. (9)).

The results obtained after implementation of the new specimen procedures are shown in Figure 4. The solid line shown in Figure 4 is based on Equation (10) and is included for comparison with the data. There is a large amount of scatter in the data, but some groups of points do show the expected trends.

Our experimental techniques are being evaluated to account for the scatter in the data. One concern is the electron beam induced desorption and mobility of potassium ions during the Auger analysis. Scanning beams have been used in order to "average" over a large sampling area. Despite this, the beam may cause significant desorption and/or ion mobility. It is proposed that XPS be used to determine the relative changes in potassium ion coverage. X-Radiation is expected to perturb the surface to a lesser degree than with electron beams. Another concern is in the method used to remove the solution from the surface without affecting the exchanged ion concentration. Any form of aqueous rinsing would upset the pH equilibrium established on the surface. The procedure which has been used is to rinse the specimen with ethanol directly after removal from the K^+ -containing solution. The ethanol removes the water, dissolves any KOH and hopefully leaves the surface unperturbed. Presently a forced stream of ethanol is being used which may affect the exchanged surface layer. Simple immersion in ethanol will be tried as an alternative method of removing the solution.

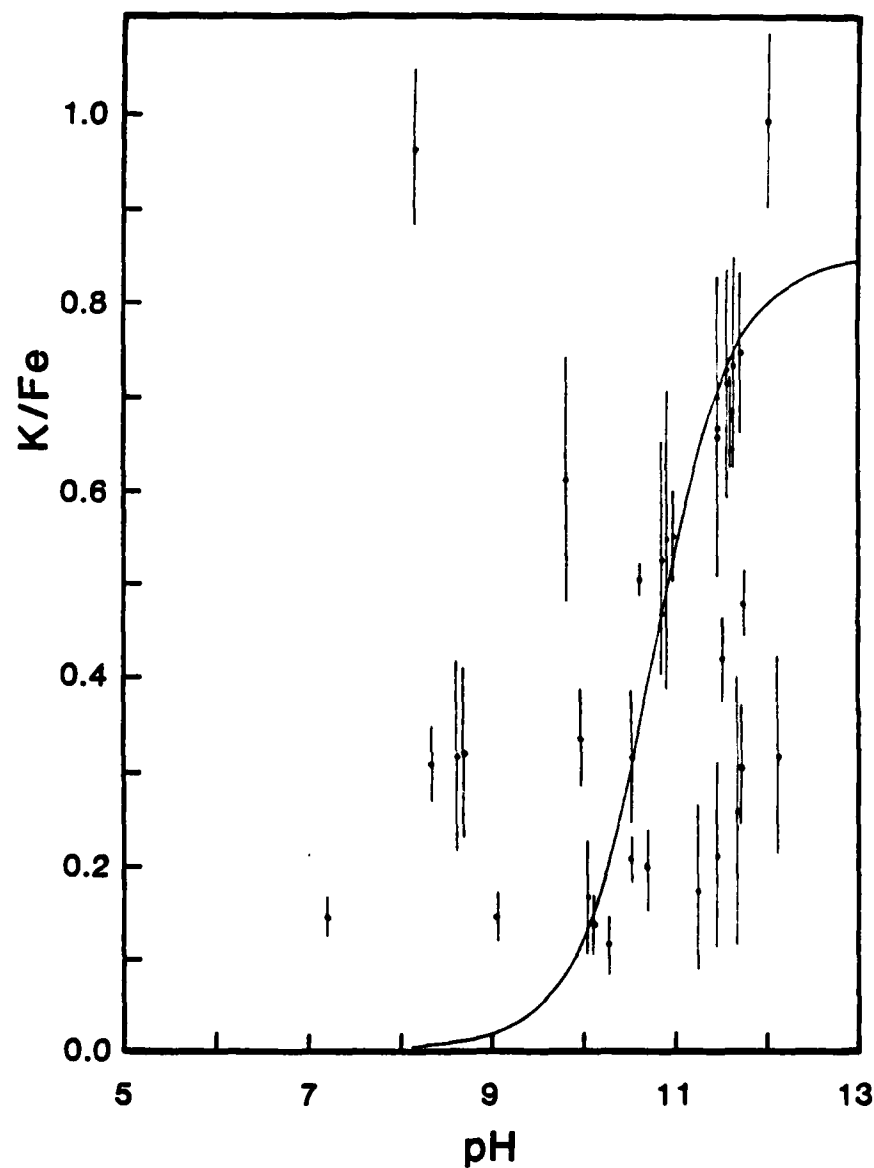


Figure 4. Plot of K/Fe Auger peak intensity ratios. Each point is the mean of several trials on different areas of one specimen. The error bars represent one standard deviation about the mean. The solid curve is a plot of Eqn. (10).

Proposed Further Work

Despite the difficulties encountered thus far, it is felt the goal of this work is worth further effort. If the changes in experimental procedures proposed above prove unsuccessful, the use of potassium will be reappraised. Larger group IA ions or other non-specifically absorbed ions may be more effective in determining the acid-base properties of surface hydroxyls on low surface area specimens.

REFERENCES

- [1] H. Leidheiser, Jr., W. Wang, J. Coatings Tech. 53, 77-84 (1981).
- [2] H. Leidheiser, Jr., Croatica Chemica Acta 53 (2), 197-209 (1980).
- [3] M. W. Roberts, P. R. Wood, J. Elect. Spect. and Rel. Phen. 11, 431 (1977).
- [4] J. Kruger, H. T. Yolken, Corrosion 20, 29 (1964).
- [5] "Thermodynamics of Wetting of Solids," W. H. Wade, N. Hackerman, Adv. Chem. Ser. #43, c. 1964, p. 222.
- [6] J. S. Ahearn, T. S. Sun, C. Froede, J. D. Venables, SAMPE Quarterly, Oct. 1980, p.39.
- [7] "Donor-Acceptor Interactions at Interfaces," F. M. Fowkes, Ed. Leing Huang Lee, Adhesion and Adsorption of Polymers, Part A. Plenum c. 1980, p. 43.
- [8] "Pigment-Matrix Interactions," F. M. Fowkes, Proceedings of Corrosion Control by Coatings Conference, Lehigh University, Nov. 13-15, 1978.
- [9] A. Breeuwsma, J. Lyklema, Fara. Diss. Chem. Soc. 52, p.324.
- [10] C. P. Huang, W. Stumm, J. Coll. Int. Sci. 43 (2), 409 (1973).
- [11] D. L. Dugger, J. H. Stanton, B. N. Irby, B. L. McConnell, W. W. Cummings, R. W. Maatman, J. Phys. Chem. 68 (4), 757 (1964).
- [12] P. W. Schindler, B. Furst, R. Deck, P. U. Wolf, J. Coll. Int. Sci. 55 (2), 469 (1976).
- [13] H. Hohl, W. Stumm, Ibid., p.281.

- [14] M. M. Benjamin, J. O. Leckie, *Ibid.* 79 (1), 209 (1981).
- [15] "Molecular Structure and Electrostatic Interactions at Polymer-Solid Interfaces," J. C. Bolger, A. S. Michaels in Interface Conversion, Eds. P. Weiss, D. Cheever, Elsevier Pub. Co., c. 1969.

Program #6. Investigation of Phosphated Steel Surfaces
by Laser Raman Spectroscopy

INTRODUCTION

Phosphate conversion coatings have two advantages for the modification of steel. They convert the steel surface to a more stable, corrosion-resistant material and provide a good base for the application of organic coatings. The phosphate coating is deposited as a consequence of the high pH generated at the cathodic areas during superficial corrosion of the metal substrate. Three major phosphating systems in use today are based on iron phosphate, zinc phosphate and manganese phosphate.

The chemical nature of the phosphate and its interaction with the substrate and organic coating are important in understanding better the protective properties of the phosphate. A further interest is the interaction of the system (phosphate, substrate, organic coating) as a whole in the presence of aggressive environments. A technique which may lend insight to this problem and permits the non-destructive examination of the phosphate beneath the organic coating is Laser Raman Spectroscopy.

OBJECTIVES

To address the phosphate investigation, four goals were outlined as follows:

- (1) To record the Raman spectra of phosphated steels using zinc, iron and manganese phosphates and to compare the spectra with their mineralogical counterparts.
- (2) To find a suitable organic coating which would permit the examination of the phosphate beneath the coating.
- (3) To identify some corrosion products of steel and build up a reference library of their spectra.
- (4) To expose the organically-coated phosphate samples to aggressive environments and identify the corrosion products which may have formed.

EXPERIMENTAL

Spectra were recorded using an Instruments S.A. Molecular Optics Laser Examiner (MOLE), Raman Microprobe. A Spectra Physics Model 164 Argon ion laser served as the source for which the 514.5 nm excitation line was used. Scattered radiation was collected at 180° to the incident light using a 100X NPL (0.90 NA) metallurgical objective from Leitz. Detection was accomplished with a Model 126 wide range photometer from Pacific Precision Instruments and a RCA 31043 photomultiplier tube cooled to -30°C with a Products for Research thermoelectric housing (Model TE-104RF).

Cold rolled steel samples cut to a size of 2 cm x 6 cm were abraded with 320 grit metallographic paper and cleansed with ALCONOX followed by rinsing with distilled water. The samples were phosphated by immersion for 10 min. in AMCHEM Granodine 46S, a zinc-based phosphating agent of AMCHEM Co. or Thermoil Granodine 112, a manganese-based phosphating agent, rinsed with distilled water and allowed to dry in a desiccator.

The organic coating, a polyester-melamine (XA-633 #2 and Cymel 300), was applied to samples with a #20 wire-wound bar and cured in an oven for 30 min at 150°C.

Reference mineral samples were obtained from Wards Scientific Establishment. These samples were mounted in epoxy and polished to yield a flat surface.

The different iron oxides and oxyhydroxides were prepared by Sveto Musić.

Spectra presented are the result of co-adding four separate spectra taken at different locations on the sample. This improved the signal-to-noise ratio by a factor of two.

RESULTS AND DISCUSSION

Zinc-Based Phosphate System

When phosphating steel with a zinc based phosphating agent three different crystalline structures are known to form on the surface [1]. The three constituents are phosphophyllite $\text{Zn}_2\text{Fe}(\text{PO}_4)_2 \cdot \text{H}_2\text{O}$, hopeite $\text{Zn}_3(\text{PO}_4)_2 \cdot 4\text{H}_2\text{O}$, and iron hureaulite $\text{Fe}_5\text{H}_2(\text{PO}_4)_4 \cdot 4\text{H}_2\text{O}$, the quantity of each being dependent on bath conditions. The spectrum in Figure 1a is that of steel phosphated with a zinc-based phosphating agent. Figure 1b presents the spectrum of hopeite, a tertiary zinc phosphate crystallizing in the ortho-rhombic system, with four waters of hydration. Comparison of the two spectra (Fig. 1a and 1b) indicates that the major constituent formed is hopeite.

Manganese-Based Phosphate System

Manganese based phosphating of steel produces a surface structure known as hureaulite $(\text{Mn}, \text{Fe})_5\text{H}_2(\text{PO}_4)_4 \cdot 4\text{H}_2\text{O}$. [2]. Hureaulite is an acid phosphate of manganese crystallizing in the monoclinic form. The spectrum of manganese phosphated steel is shown in Figure 2a; this spectrum correlates very well with that of the spectrum of hureaulite shown in Figure 2b.

Polymer-Coated Systems

It is desirable to examine the phosphate beneath an organic coating in order to simulate real systems.

Figure 3a illustrates the Raman Spectrum of a polyester-melamine coated on steel. This system was selected over the commonly used polybutadiene system due to its low background signal, transparency, and most of all its lack of fluorescence. Polybutadiene and a number of other organic coatings fluoresce, which radiation competes with the Raman signal.

Manganese phosphated steel with a topcoat of polyester melamine produced the Raman spectrum presented in Figure 3b. This spectrum exhibits all signals due to the phosphate underlayer and polymer top layer.

Corrosion Products

The Raman spectra of four pure corrosion products of steel occurring at ambient conditions are presented in Figures 4a, 4b, 5a and 5b. They are $\alpha\text{-FeOOH}$, $\gamma\text{-FeOOH}$, $\alpha\text{-Fe}_2\text{O}_3$ and $\gamma\text{-Fe}_2\text{O}_3$,

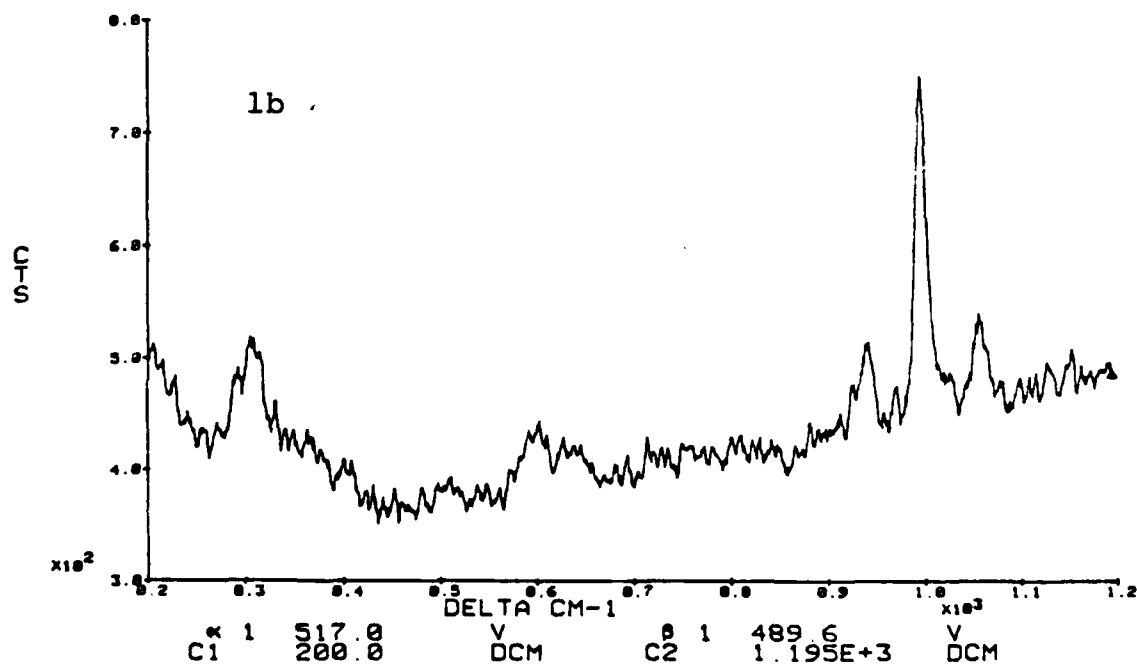
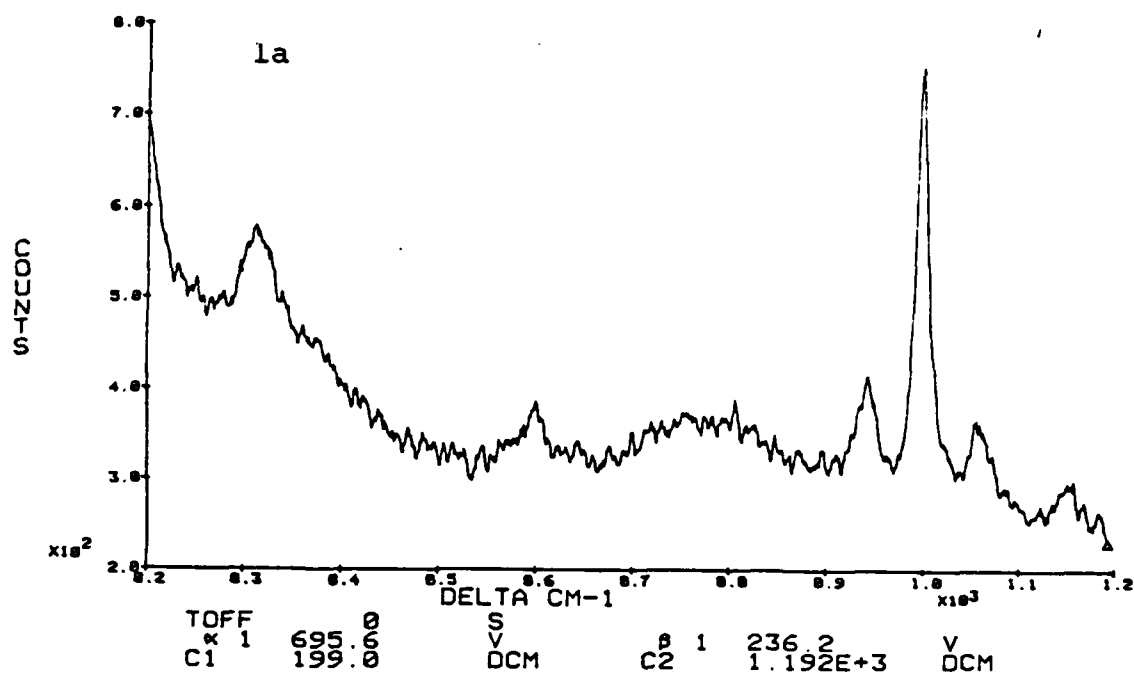


Figure 1a. Zn based phosphate coating on steel.

Figure 1b. Hopeite

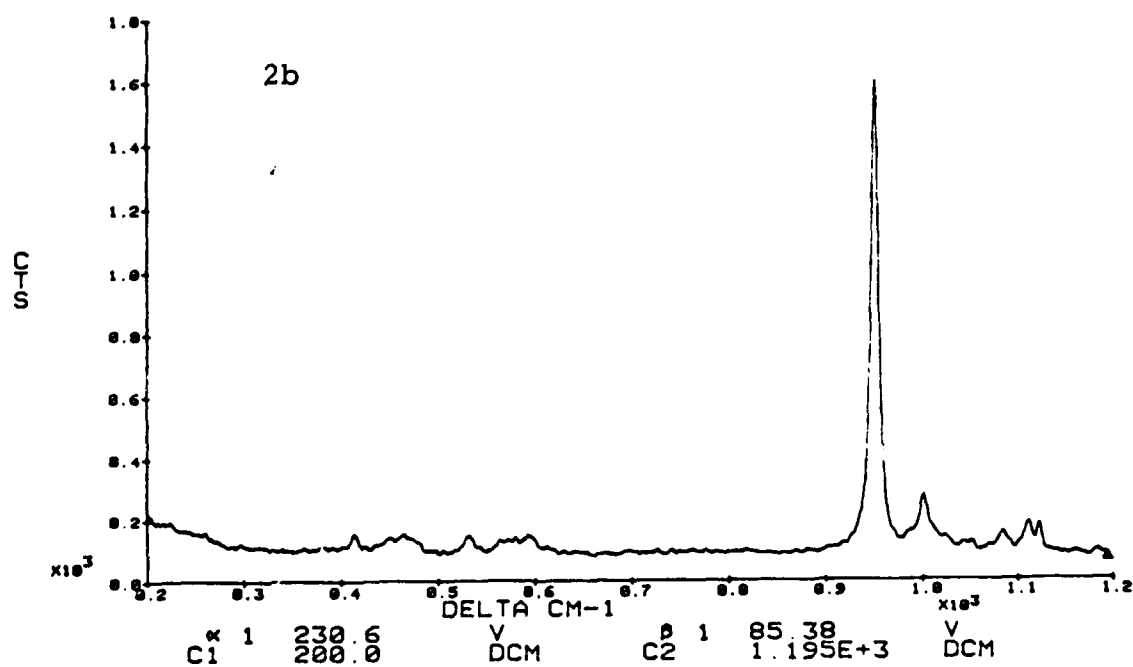
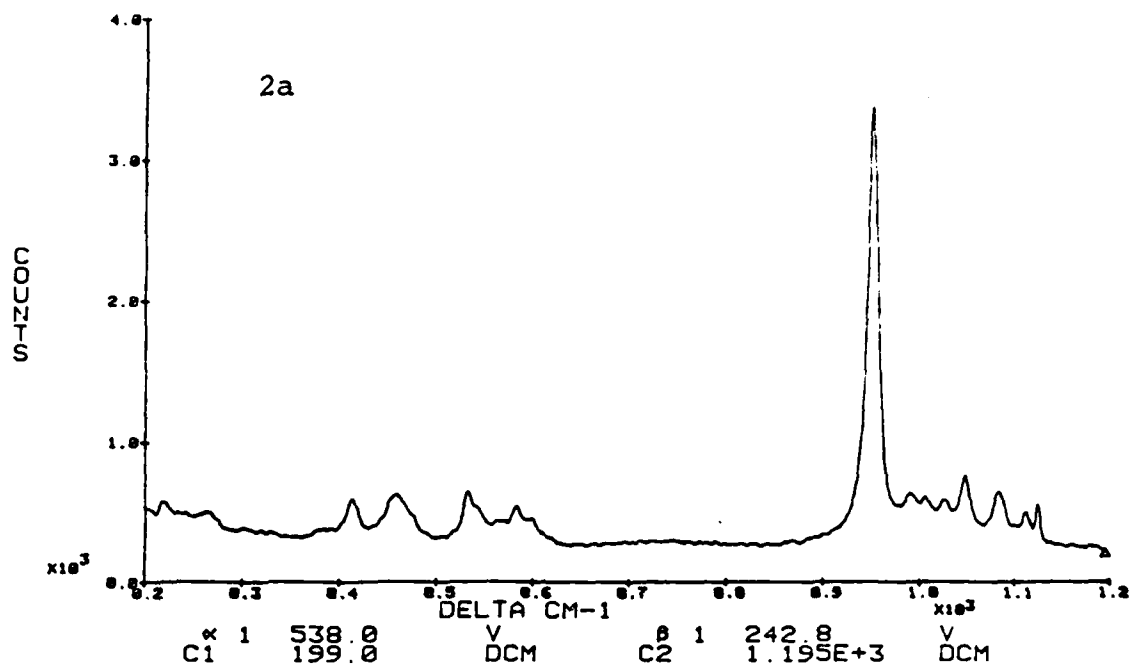


Figure 2a. Mn based phosphate coating on steel.

Figure 2b. Hureaulite

AD-A124 044

CORROSION CONTROL THROUGH A BETTER UNDERSTANDING OF THE
METALLIC SUBSTRAT. (U) LEHIGH UNIV BETHLEHEM PA CENTER
FOR SURFACE AND COATINGS RESE. H LEIDHEISER ET AL.

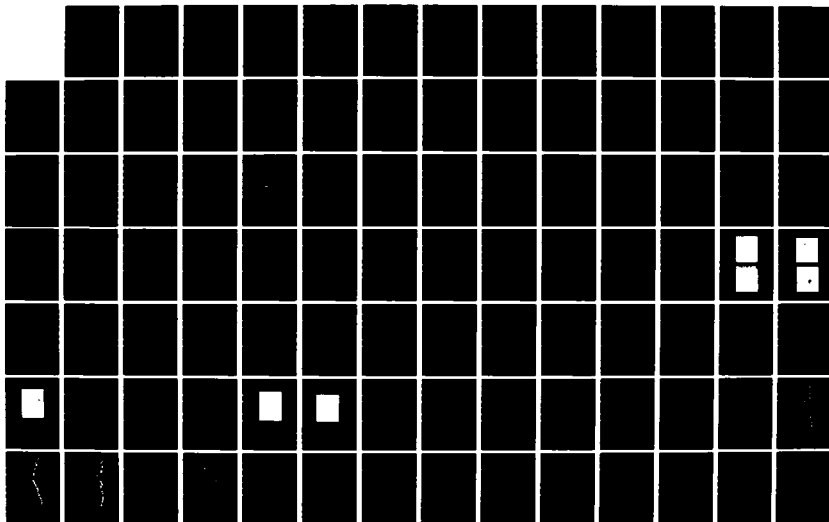
2/3

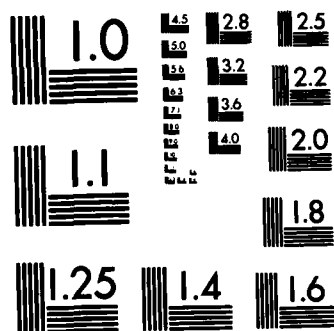
UNCLASSIFIED

01 DEC 82 N00014-79-C-0731

F/G 11/6

NL





MICROCOPY RESOLUTION TEST CHART
NATIONAL BUREAU OF STANDARDS-1963-A

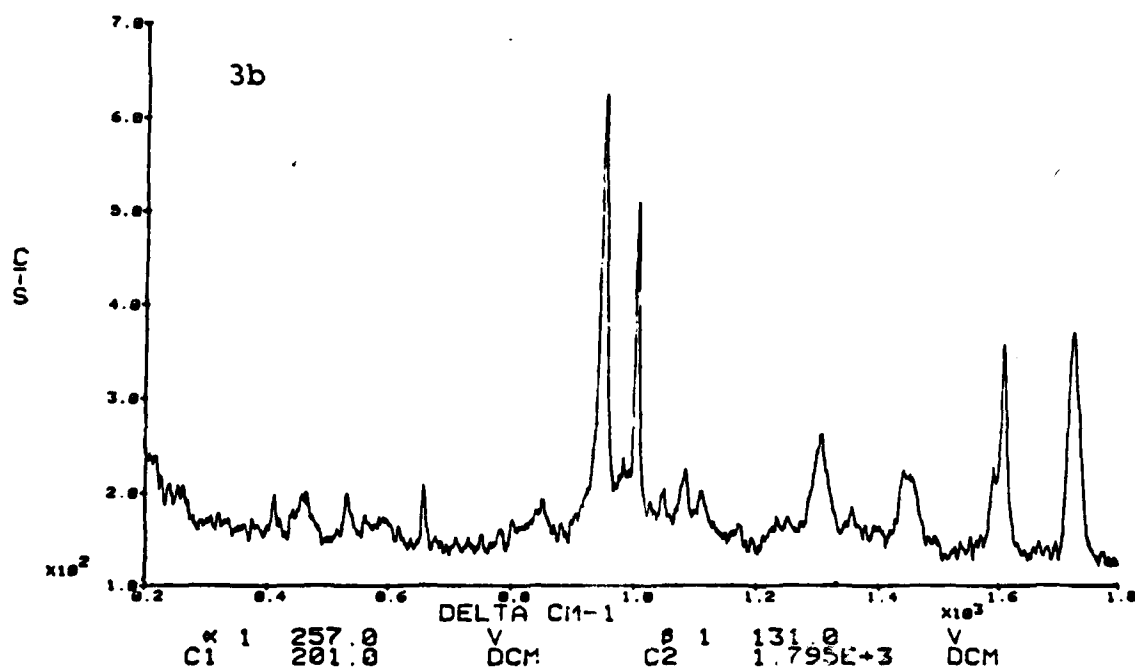
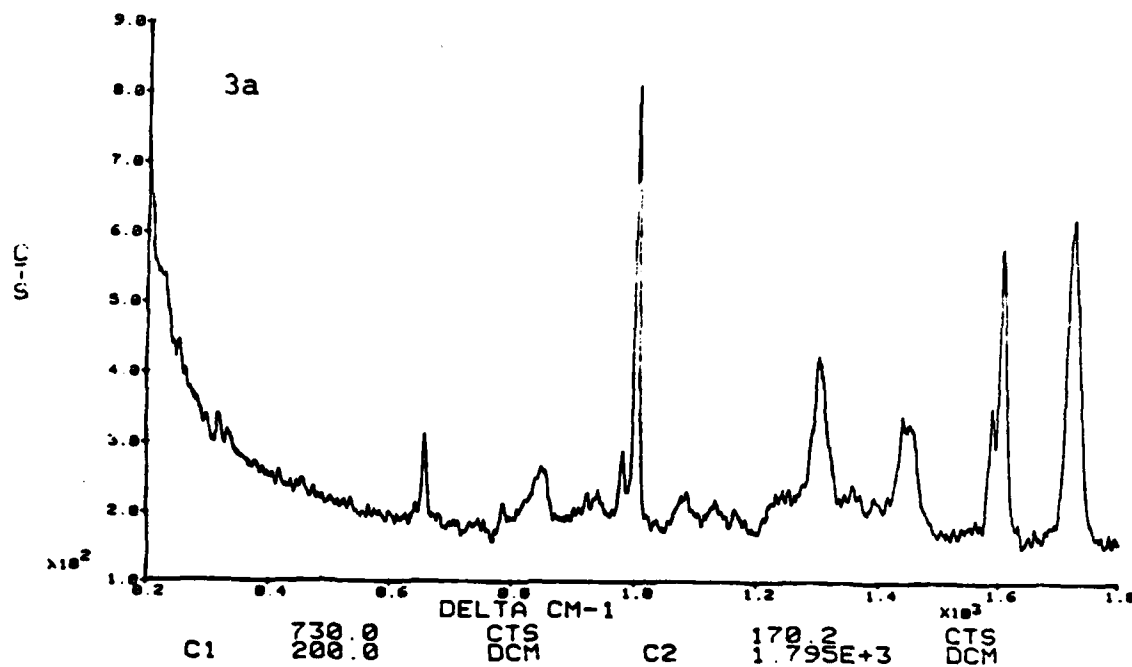


Figure 3a. Polyester-melamine organic coating.

Figure 3b. Polyester-melamine overcoat on Mn based phosphate coated steel.

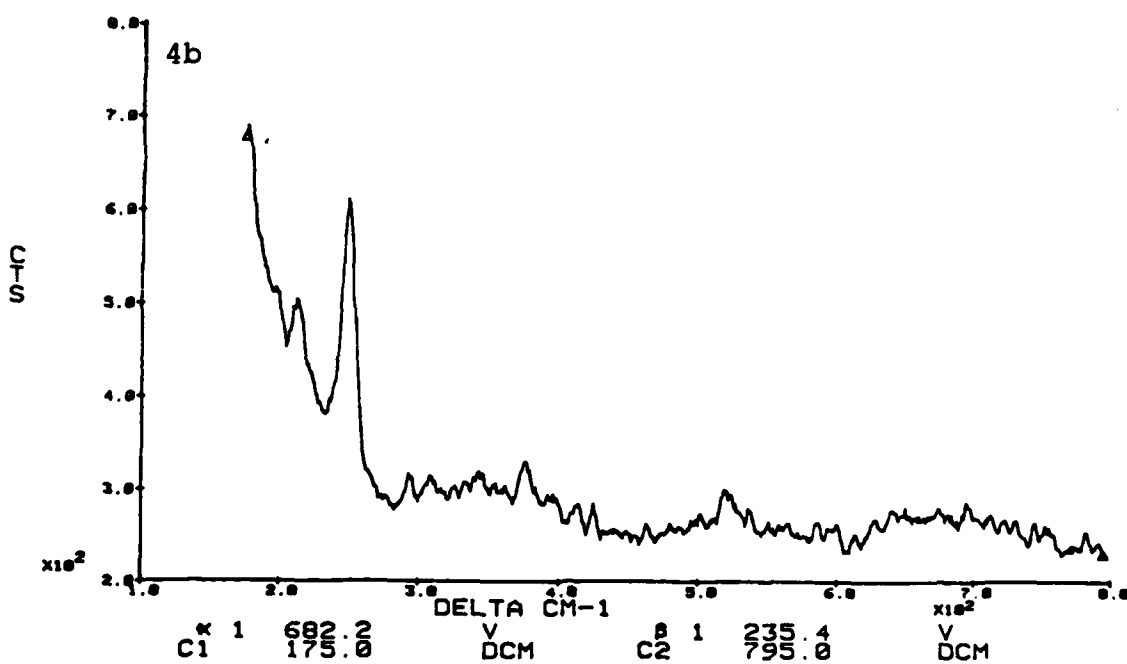
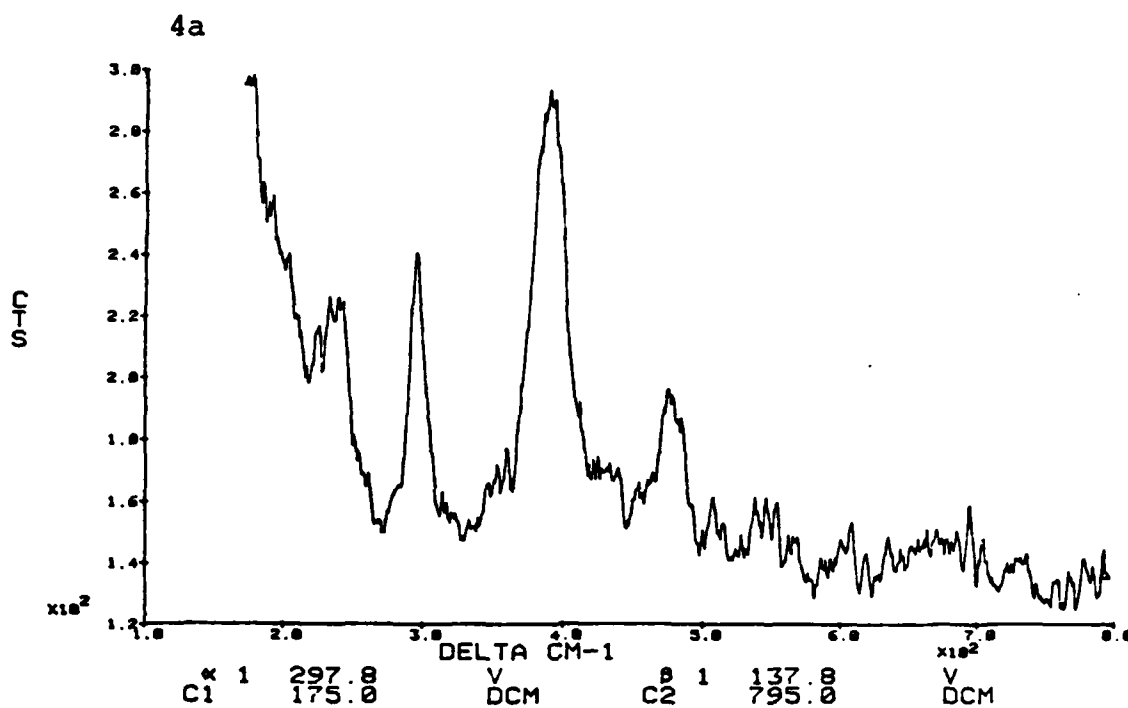


Figure 4a. Alpha FeOOH

Figure 4b. Gamma FeOOH

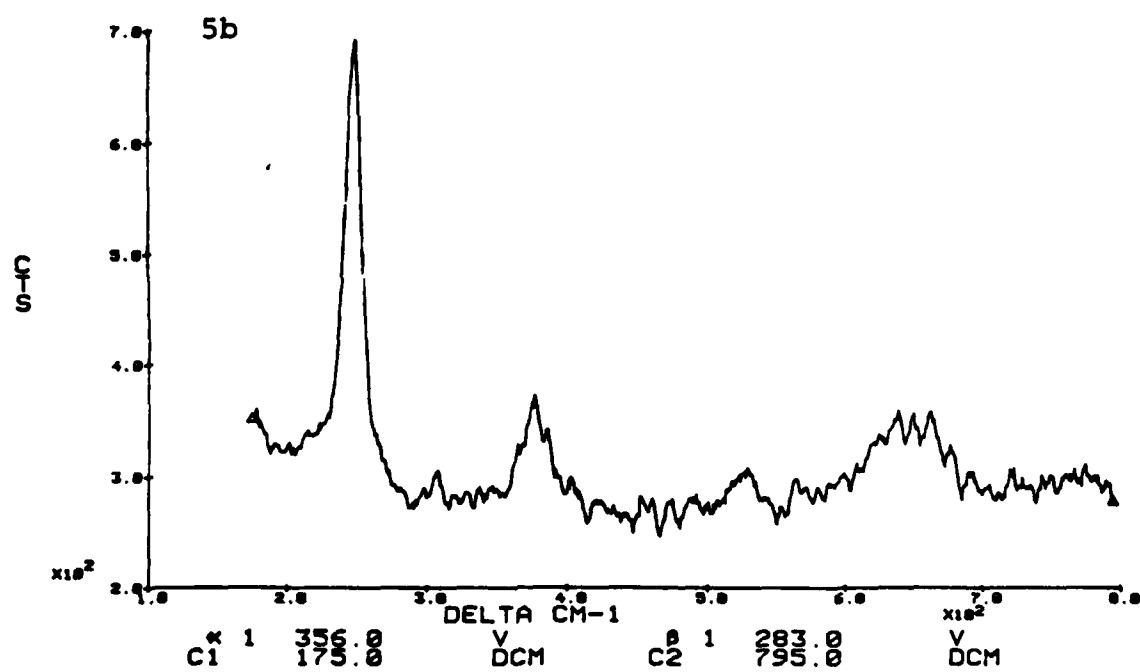
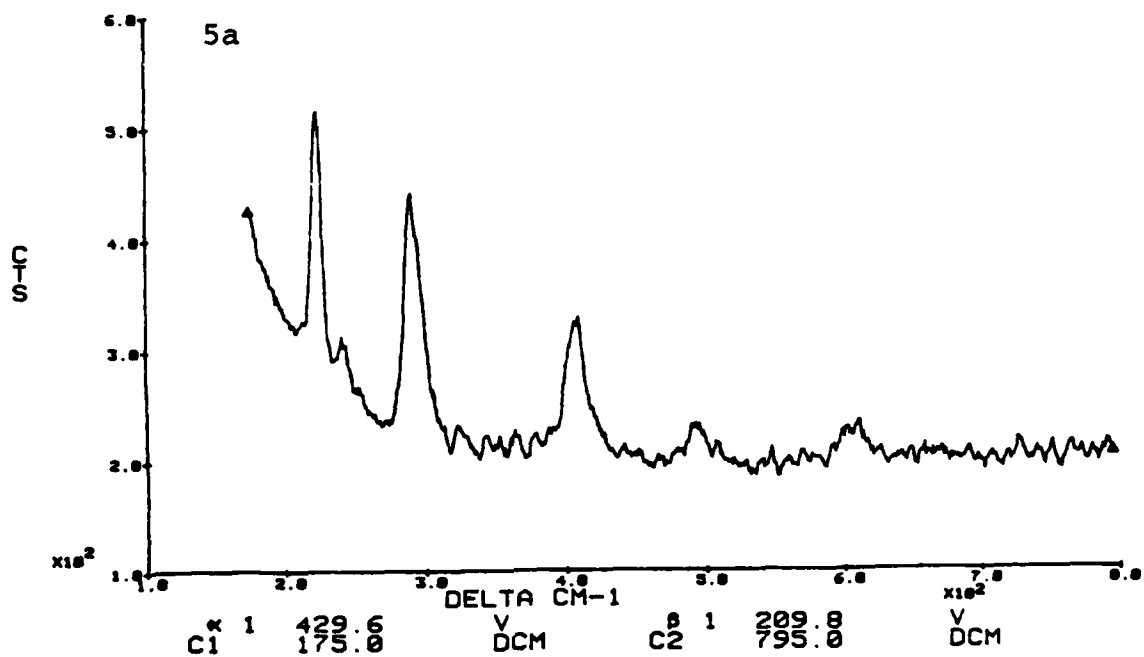


Figure 5a. Alpha Fe_2O_3

Figure 5a. Gamma Fe_2O_3

respectively. These samples when first examined underwent thermal degradation detected by visual inspection and spectra that were nonreproducible. To alleviate this problem, the samples were evaporated from a water suspension onto a microscope slide. This technique improved the thermal conduction between the glass slide and the sample allowing reproducible spectra to be obtained with no loss of sample integrity.

CONCLUSIONS

In conclusion the results presented show that Laser Raman Spectroscopy is a viable technique for the investigation of phosphate coatings on steel and more importantly that examination of the phosphate is possible under a polymer topcoat. Future study will include the examination of the iron-based phosphate system and the changes which occur when the phosphate, substrate and organic coating as a whole are subjected to aggressive environments.

REFERENCES

- [1] "Phosphating of Metals", G. Loria, Finishing Publications Ltd. Chapter 4 (C) (1974).
- [2] Ibid

Program #7. Detection of Aggregated Water in Polymer Coatings

INTRODUCTION

In the previous report the technique of time domain spectroscopy was introduced as a method for detecting aggregated water in polymer coatings. The technique which allows one to obtain dielectric information at high frequencies is reviewed in the literature by van Germert [1]. Progress in obtaining dielectric information on polymer coatings has resulted in the testing of several liquids and polymer systems. Initial measurements indicate that water within a polymer coating does affect the high frequency dielectric spectrum. Further investigation is continuing in order to determine how different types of water, mobile, aggregated or interfacial, affect the dielectric response of a coating.

TECHNIQUES STUDIED

The experimental system as outlined in the previous report has been completed. The arrangement of the sample cell dictates the limitations of a particular technique and requires specific data analysis techniques. Thus for each type of cell a separate computer program had to be written in order to obtain the dielectric response. Two sample cell arrangements have been tested using the time domain "spectrometer". The first sample cell was chosen for its simplicity, thus allowing a "debugging" of the spectrometer system. The second sample cell was chosen because it could be adapted to measure polymer coatings.

The first sample cell employed a single response technique whereby only the first reflection from a dielectric sample is considered. While this cell could only be used for liquids, it did serve to get reference spectra which could then be compared with that found in the literature. Figure 1a shows the sample cell configuration. The cell is essentially a slightly modified 30 cm coaxial air line held vertically. Sample liquid is allowed to percolate up into the line thus forming an interface for reflection. Details of the technique are given by Tuxworth [2]. One of the liquids tested was 1-propanol. The dielectric spectrum

SINGLE REFLECTION CELL

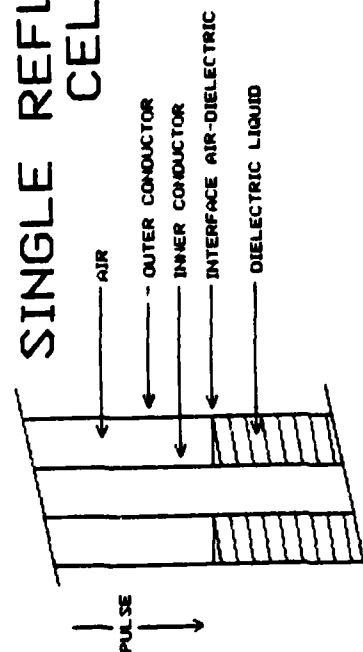


FIGURE 1a
Single Reflection Cell

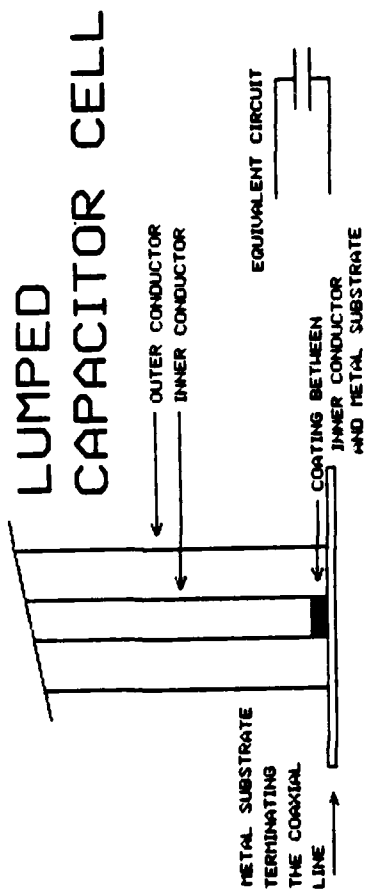


FIGURE 1b
Lumped Capacitor Cell

is shown in Figure 2. It can be seen that overall agreement with literature values is good. The bumps at the high frequencies are attributed to spurious reflections within the coaxial lines which in future work should be eliminated.

Once the initial liquid measurements proved successful, a cell was designed that could provide a single reflection from a polymer coating. Due to the fact that a coating is by nature thin, a different sample arrangement is dictated. Shown in Figure 1b is a cell which allows polymer coatings on metal substrates to be measured. This cell design is a variation of a technique developed by Iskander [3]. The cell requires a small amount of sample and, in effect, treats the sample dielectric as a small shunt capacitor terminating a coaxial line. Initial measurements were carried out on liquids and results were compared to values found in the literature. Figure 3 shows the dielectric spectrum for 1-octanol. The spectrum is qualitatively in good comparison with the literature when the sources of error are considered. Specific errors occur when measuring liquids because of uncertain knowledge of sample thickness and configuration. Again the bumps at high frequencies and the slight rise in the ϵ' value are attributed to the unwanted reflections within the coaxial lines.

DATA ON POLYMER SYSTEMS

The data obtained on liquids with the new cell design proved to be valid enough to allow preliminary measurements on some polymer systems. Solid polymer systems have the advantage over liquids in that the shape and thus sample thickness are well defined. Slight errors will occur due to air gaps between the sample and coaxial line interface. These errors will result in a small deviation of the ϵ' and ϵ'' values and are not very troublesome.

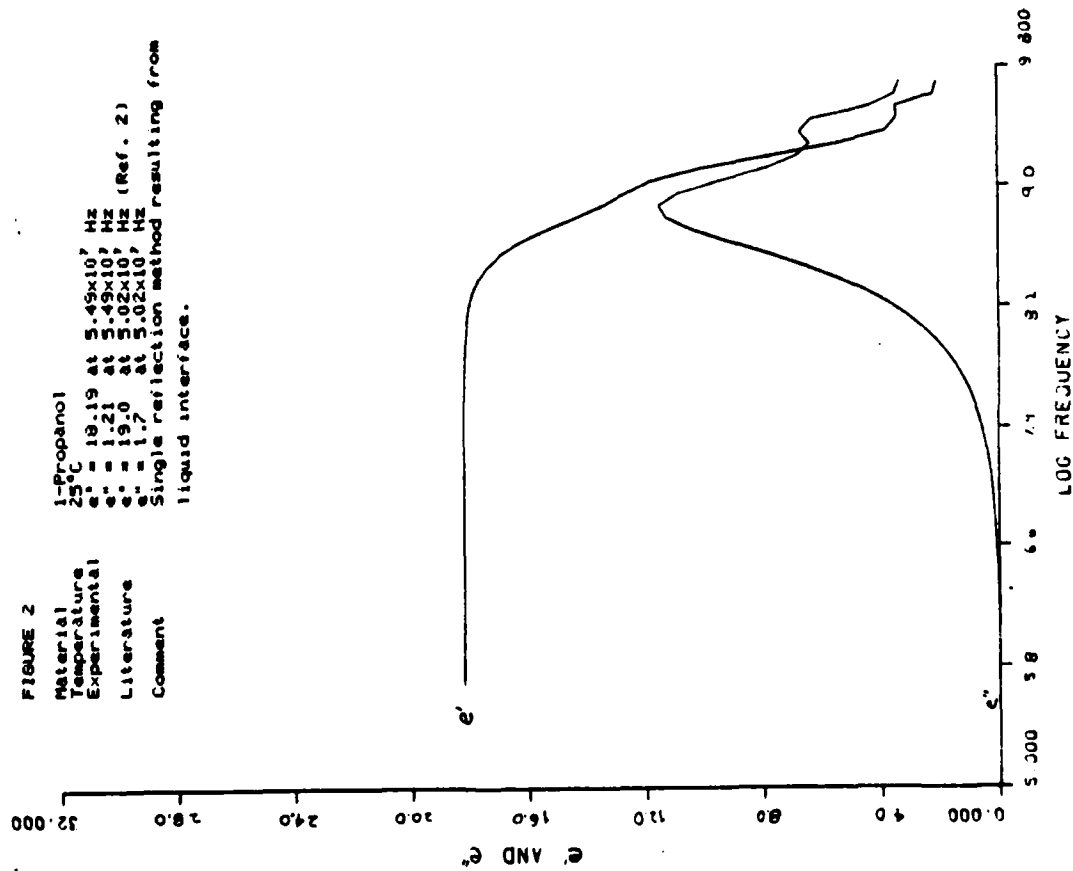
A good standard for high frequency dielectric work is Teflon. Figure 4 gives the results for a sample of Teflon taken from a sheet roughly 0.24 mm thick. The low frequency ϵ' value is in very good agreement with the literature value. Of particular interest is what looks like a dielectric loss at about 8.8 on the log frequency scale. This loss is not expected for Teflon and ideally should not occur. At this time no reason can be given for the loss and an investigation into its origin is continuing. Some possible reasons may include instrumental artifacts arising again from unwanted reflections.

Initial studies of polymer coatings were carried out using polyvinyl acetate (PVAc). This polymer system was chosen because data exist on the states of water as a function of percent uptake. It has been reported by Johnson [4] that when water is present in

FIGURE 2

Material
Temperature
Experimental
Literature
Comment

1-Propanol
25°C
 $\epsilon' = 19.19$ at 5.45×10^7 Hz
 $\epsilon' = 1.21$ at 5.45×10^7 Hz
 $\epsilon' = 19.0$ at 5.02×10^7 Hz (Ref. 2)
 $\epsilon' = 1.7$ at 5.02×10^7 Hz
Single reflection method resulting from
liquid interface.

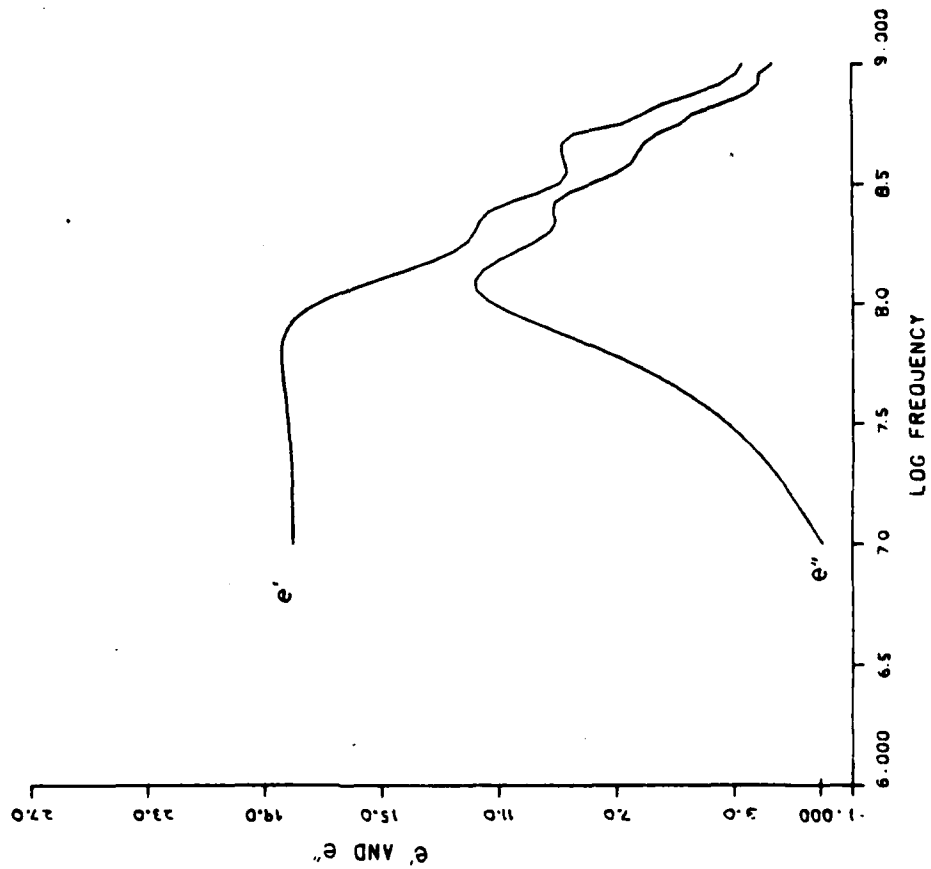


1-PROPANOL DIELECTRIC

FIGURE 3

Material
Thickness
Temperature
Experimental
Literature
Comment

Octanol
0.305 mm
25°C
 $\epsilon' = 19.11$ at 1.93×10^7 Hz
 $\epsilon' = 1.57$ at 1.93×10^7 Hz
 $\epsilon' = 9.5$ at 2.00×10^7 Hz (Ref. 3)
 $\epsilon' = 1.4$ at 2.00×10^7 Hz
Liquid sample is in the lumped capacitor cell, there is
uncertainty in the thickness and shape of the sample.



DIELECTRIC RESPONSE

PVAc above five percent by weight, a separate phase will exist in the form of clusters. This separate phase will be similar to aqueous phase water as opposed to polymer associated water present when the water content is below five percent. Polymer coatings were prepared by dissolving PVAc beads in toluene and applying the mixture to a steel substrate. The samples were baked to remove the solvent and then cooled and stored in a desiccator. Water was placed in the samples by subjecting them to steam until the polymer appeared a milky white (evidence of clustered water).

A free film of PVAc was also prepared in a similar manner. Figure 5 gives the results for a 0.59 mm film of PVAc. The low frequency ϵ' value is again in good agreement with the literature value. As with Teflon there seems to be a dielectric loss at about 8.8 log frequency. This loss is rather high if it is due to the polymer. One would expect, as with Teflon, that there would be no loss mechanism in this region. The reason for this loss is still not known. It is, however, repeatable in all measurements.

A coating of PVAc on steel yielded the spectrum in Figure 6. The coating was .65 mm thick and the ϵ' value was again in good agreement. One thing to notice is the presence of the unexplained loss mechanism as with the free film. Water was added to this sample and the dielectric spectrum was recorded. Figure 7 gives the resultant spectrum. Two things are immediately apparent: the increase in ϵ' at lower frequencies and the evidence of another loss mechanism (the second rise in ϵ''). The increase in ϵ' can be directly attributed to the presence of water in the coating. Evidence suggests that this may be due solely to aqueous phase water and not polymer associated water. The evidence comes from the fact that no change in ϵ' was observed for a free film of PVAc that was immersed in water but not steamed. No milky white color resulted but the polymer was noticeably softened indicating that there was some uptake of associated water but no clustering. A second difference is the second rise in ϵ'' . This effect is tentatively attributed to interfacial water of some kind.

The previous procedure was repeated for another coating in which the cell was cooled to 5°C. A foam cooler with ice was used for cooling the cell. Cooling a sample causes the relaxation and hence the dielectric loss to shift to a lower frequency. Figure 8 shows the dielectric response of a cooled sample, 0.59 mm thick. The value of ϵ' is in agreement as expected; however, along with the usual loss peak there is a second loss peak as seen in the steamed samples. Although not conclusive, this loss may be attributed to interfacial water, meaning water between the polymer and metal interface. Interfacial water is presumed present because of condensation on the metal surfaces of the cell, particularly the tip of the inner conductor. Also noticed is the shift of the unexplained loss to lower frequency. Steaming the sample and then taking the dielectric spectrum at low temperature resulted in Figure 9. The spectrum exhibits the expected rise in ϵ' but also shows a marked rise in ϵ'' which had not occurred before in

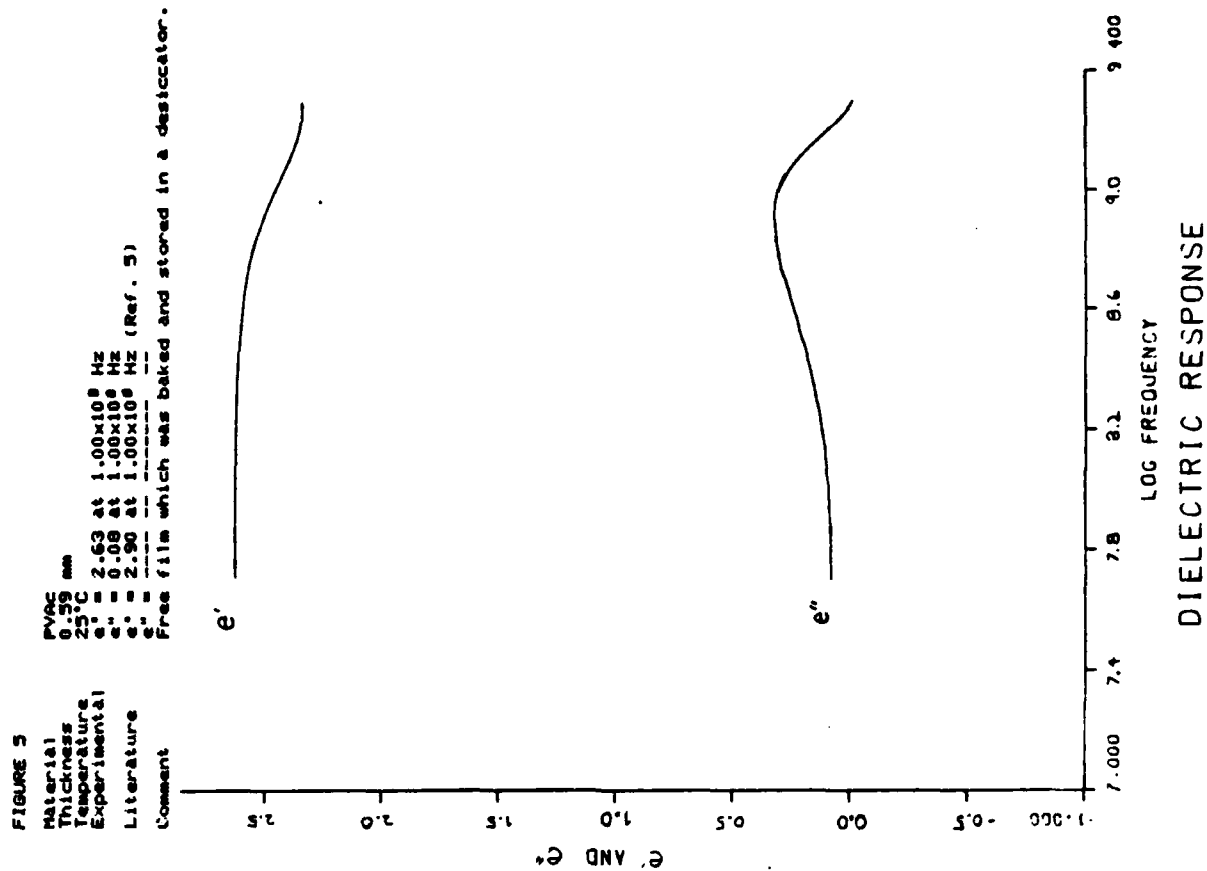
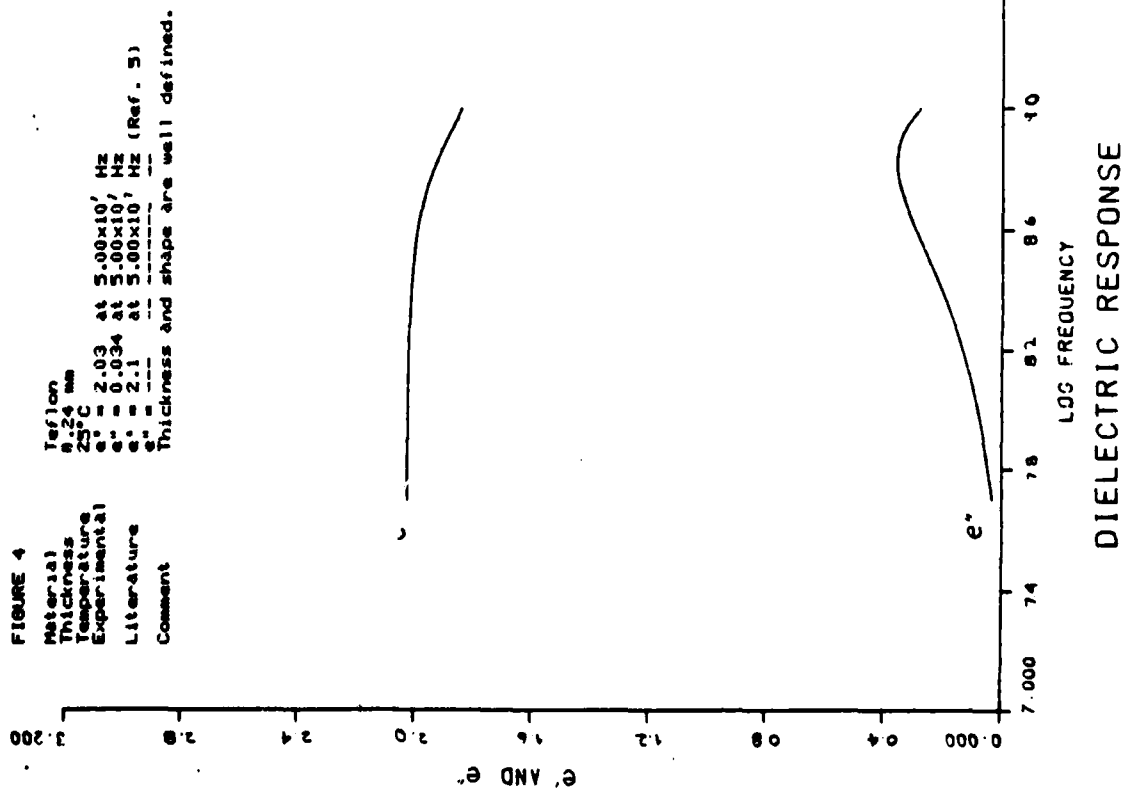


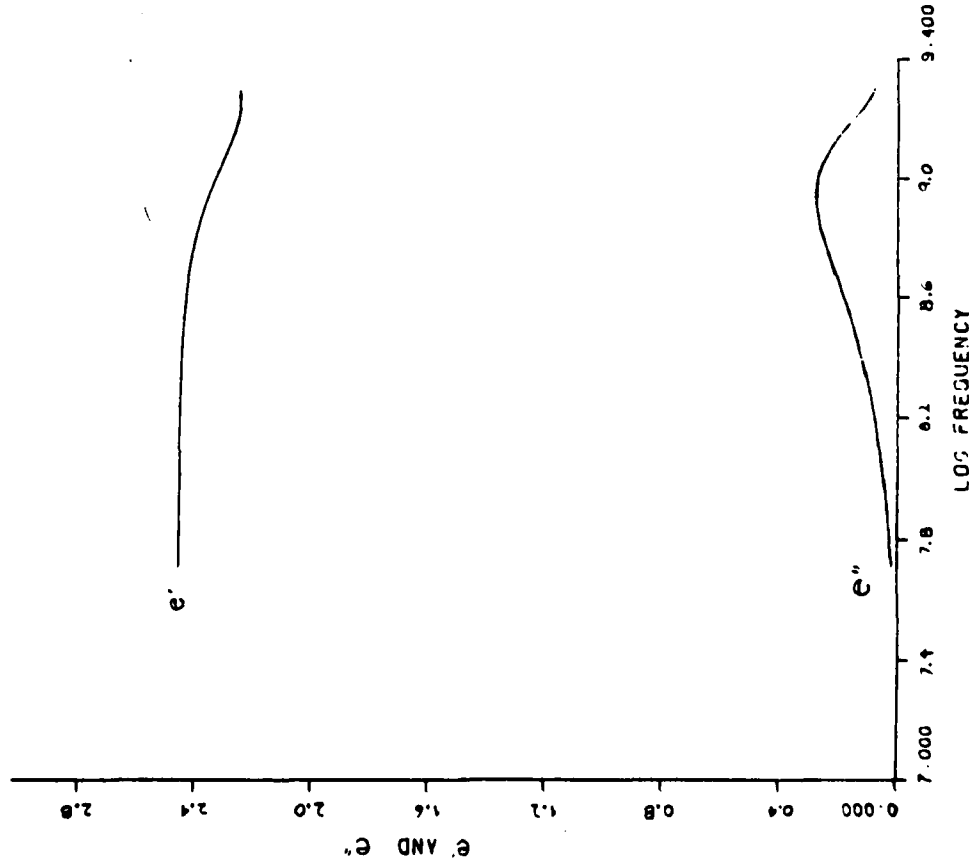
FIGURE 6

Material
Thickness
Experimental
Literature
Comment

PVAC
0.65 mm

25°C
 ϵ' = 2.45 at 1.00×10^8 Hz
 ϵ'' = 0.45 at 1.00×10^8 Hz
 ϵ' = 2.90 at 1.00×10^8 Hz (Ref. 5)
 ϵ'' = -----

Film was cast on steel substrate baked and stored in a desiccator.



DIELECTRIC RESPONSE

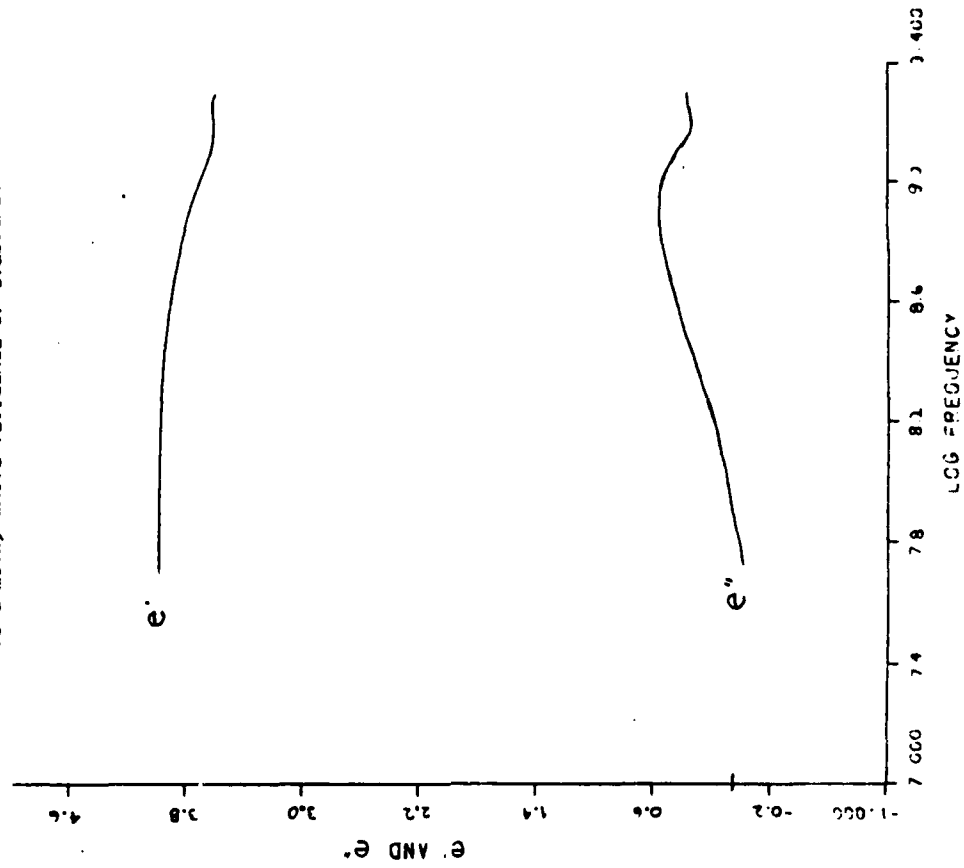
FIGURE 7

Material
Thickness
Experimental
Temperature
Comment

PVAC
0.97 mm

25°C
 ϵ' = 3.98 at 1.00×10^8 Hz
 ϵ'' = 0.86 at 1.00×10^8 Hz

The sample is the same one as figure 6, but was steamed to a milky white (evidence of clusters)



DIELECTRIC RESPONSE

FIGURE 8

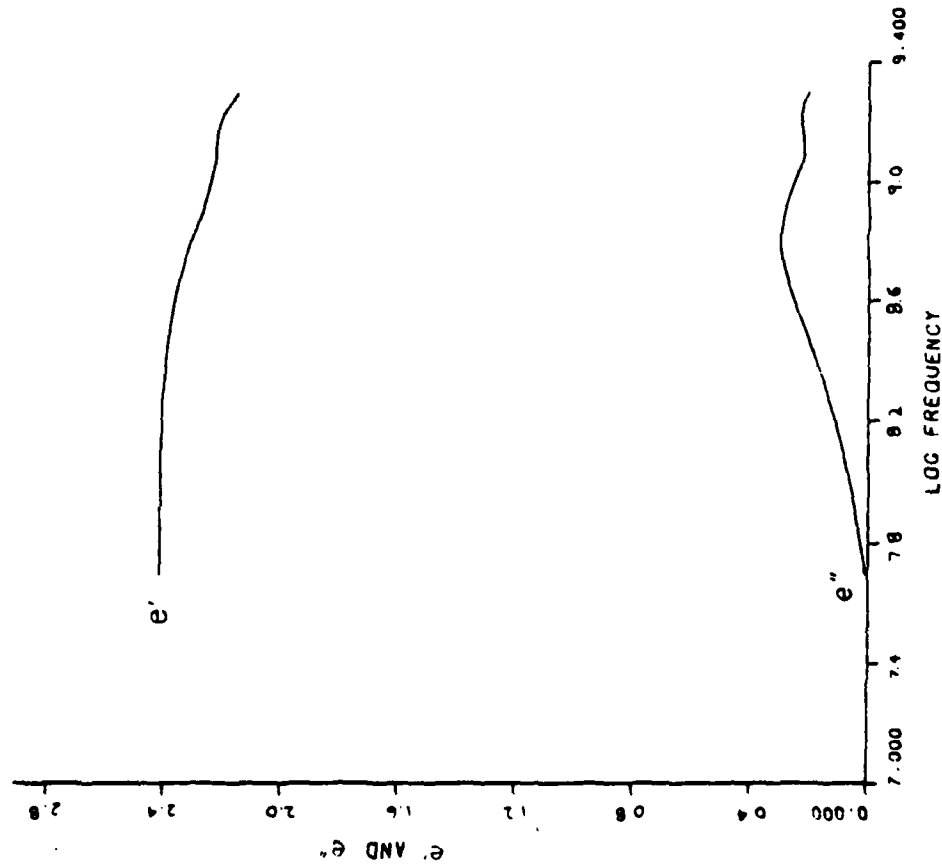
Material
Thickness
Experimental
Literature
Comment

PVAC
0.53 mm
5°C

$\epsilon' = 2.41$ at 1.00×10^8 Hz
 $\epsilon'' = 0.06$ at 1.00×10^8 Hz

$\epsilon' = 2.50$ at 1.00×10^8 Hz (Ref. 5)

A film cast on steel was cooled in cooler with ice,
condensation was on all metal parts.



DIELECTRIC RESPONSE

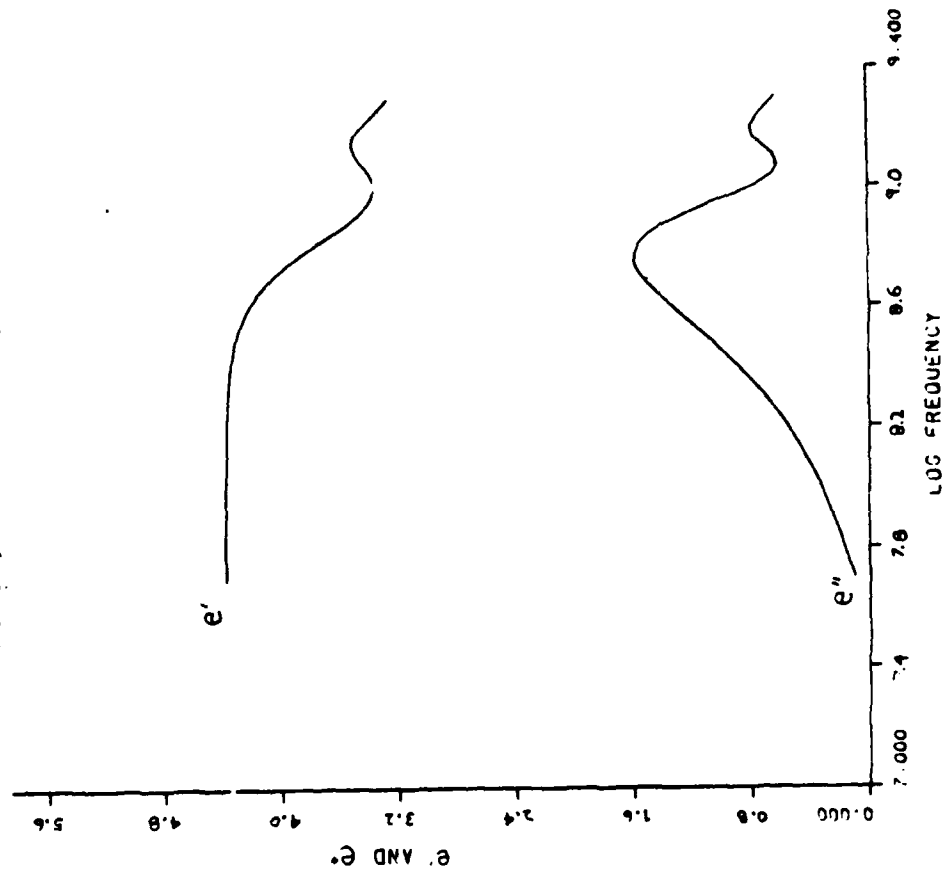
FIGURE 9

Material
Thickness
Experimental
Temperature
Comment

PVAC
0.50 mm
5°C

$\epsilon' = 4.38$ at 1.00×10^8 Hz
 $\epsilon'' = 0.31$ at 1.00×10^8 Hz

The sample was the same one as figure 8, but was steamed
to a milky white then cooled to 5°C.



DIELECTRIC RESPONSE

steamed samples. No interpretation is offered at this time pending further work.

CONCLUSIONS AND FUTURE PLANS

At this time any conclusions are premature. Several statements, however, can be made about the results thus far. First, the low frequency ϵ' values for Teflon and PVAc correspond quite well with the literature values indicating that the system is functioning properly at these frequencies. Second, there is a definite increase in ϵ' when a sample is steamed and no increase when small amounts of water are present. There is speculation as to detection of interfacial water. Preliminary results show effects due to water and merit further investigation.

The biggest experimental problem is the presence of unwanted reflections. Steps have been taken to remove many of these from the system and should result in less noise (bumps) at the higher frequencies. Also a new cell is being designed which should give better data at high frequencies.

Once the system has been upgraded, measurements of percent water and change in ϵ' and ϵ'' will be taken in order to find a relationship between the two. This type of relationship has already been found for water in PVAc at low temperatures and low frequencies [4]. It is hoped that a thorough understanding of a model system such as PVAc will enable conclusions to be drawn on the states of water in other coating systems.

One goal of the investigation is the creation of "state maps" for different coating systems. A state map is a three-dimensional plot consisting of the type of scans pictured here, dielectric loss vs. frequency, with an added third dimension which could be either temperature or time (a time axis would allow one to observe the states of water as a function of diffusion through the coating towards the interface). Because dielectric measurements are a translational spectroscopy, water found in different states, mobile, aggregated, interfacial, will have different types of relaxations. Thus, by compiling parameters in three dimensions, different states may be easily characterized.

REFERENCES

- [1] M. J. C. van Germert, Philips Res. Repts. 28, 530, 1973.
- [2] R. W. Tuxworth, PhD Thesis, University of Wales, 1975.
- [3] M. F. Iskander and S. S. Stuchly, IEEE Trans. Instrum. Meas. IM-21, 425, 1972.
- [4] G. E. Johnson, H. E. Bair, S. Matsuoka, E. W. Anderson, and J. E. Scott, "Water in Polymers," ACS Symposium Series 127, American Chemical Society, Washington, D.C., 1980.
- [5] Arthur R. Von Hippel, Editor, "Dielectric Materials and Applications," The M.I.T. Press, 1954.

Program #8. Radiochemical and Electrochemical Measurements of Diffusion in Organic Coatings

INTRODUCTION

The protective properties of an organic coating applied to a metal substrate are governed, in part, by the adhesion of the coating to the substrate and by the permeability of the coating to environmental elements (water, oxygen, and ions) [1,2]. The permeability of a coating can be determined using several techniques. The most common of these involves the use of a free film as a barrier between an electrolyte solution and distilled water [3-12]. The rate of diffusion of ions through the film may be determined using electrical resistance techniques [3], by using ion-selective electrodes [4,5], or radiotracer counting [6-12] to monitor specific ion concentration in the distilled water cell. For mounted films, desorption techniques [5], surface counting [13], and autoradiographs [14] are common tools. In addition, water uptake can be monitored by measuring the capacitance of the coated system as a function of exposure time, and comparing the dielectric response for the system to that for water [15].

We recently reported on an AC impedance technique for monitoring the breakdown of organic coatings on steel [1]. In the present study, this technique will be used in conjunction with an ion permeability study using radiotracer techniques.

BACKGROUND AND EXPERIMENTAL

Radiotracer methods are based on the principle that isotopes of an element display similar chemical properties while exhibiting distinct nuclear properties. Thus by doping a solution of species M with a trace amount of radioactive *M (known activity), the reactions of M can be monitored by following *M . The use of trace concentrations of *M minimizes mass-transport effects.

In this study we are looking at four types of nuclear processes: beta (β^-), gamma (γ), positron (β^+) and electron capture (ϵ). These are reviewed below.

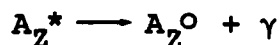
1. Beta processes

(a) β^- -emission: $A_Z \longrightarrow A_{(Z+1)^+} + \beta^- + \text{Energy}$

(b) β^+ -emission: $A_Z \longrightarrow A_{(Z-1)} + e^- + \beta^+ + \text{Energy}$

(c) electron capture: $A_Z \longrightarrow A_{(Z-1)} + \text{Energy}$

2. Gamma processes: Energy released during electron relaxation



Both β^+ and electron capture processes are accompanied by emission. In these schemes, A designates the nuclear mass, Z the number of electrons.

The half-life of a species is a measure of its decay rate, specifically the time required for one-half the initial concentration to decay. That is, for $N = 1/2 N_0$,

$$N = N_0 \exp(-t/\tau)$$

$$\ln 2 = t_{1/2}/\tau$$

$$t_{1/2} = .693 \tau$$

where τ is the mean lifetime of the radioactive species. For ion uptake experiments, an experimental time frame during which at least 95 percent of the initial isotope concentration is retained would be optimal. From the above, the time frame t would be

$$t \leq .074 t_{1/2}$$

$$\text{for } N \geq 0.95 N_0$$

Times greater than t require corrections for isotope loss due to decay.

In this study, .5M NaCl was doped with ^{22}Na , ^{36}Cl or an equal amount of both isotopes. ^{22}Na emits two gamma rays (.511 and 1.28 MeV) as a result of positron emission and electron capture. It has a mean half-life of 2.63 years. ^{36}Cl is a beta-emitter (.711 MeV), with a half-life of 3.1×10^5 years. Over a period of 100 days, 93 percent of the sodium-22 and 99.9 percent of the chlorine-36 remain active. For most experiments reported on here, the time

frame t is less than 100 days.

The concentration of the ions which penetrate an organic coating can be determined by monitoring the activity of the radio-tracer. A G-M radiation counter (Nuclear Chicago Model 151) was used to detect all beta decays. The count rate was recorded as time (seconds) per 1000 (detected) events relative to a background scan. These data were subsequently converted to counts per minute (cpm). The ^{22}Na gammas were monitored using a Nuclear Chicago Model 132-A gamma counter with a NaI crystal detector, calibrated using a ^{137}Cs standard. The instrument was set in the baseline mode to allow the detection of most gamma producing events. Events were recorded over a five-min period, and the average counts per min relative to background were determined. The results obtained by these procedures have a "standard statistical error" of about 3% for 1000 counts due to the random nature of the decay process.

Radiotracer Calibration Procedure

A calibration procedure involving the use of both the γ and β^- counters was developed to allow the simultaneous determination of the diffusion rates for Na^+ and Cl^- into a coating. A $1\text{ }\mu\text{Ci/ml}$ -.5M NaCl base solution was prepared for each isotope from stock .1mCi solutions in a two-step dilution procedure. This solution was then used to prepare 10ml of a $.1\text{ }\mu\text{Ci/ml}$.05M NaCl solution (B) which, in turn, was diluted to make 10 ml of $.01\text{ }\mu\text{Ci/ml}$.005M NaCl (soln. A). Test plates were prepared by placing drops of the test solution on a lightly polished piece of cold rolled steel (approximately 4 cm^2) and evaporating off the water. Disposable pasture pipets were used for this procedure. The average drop volume was determined to be $2.50 \times 10^{-2}\text{ ml}$, making the average NaCl concentration per drop 1.25×10^{-7} and $1.25 \times 10^{-6}\text{ mol/drop}$ for solutions A and B, respectively. For the ^{22}Na samples, 1,2,3,4,6 and 8 drops of each solution were placed on the test plates. The same procedure was followed for the ^{36}Cl specimens, but only solution A was used. The plates with the residual radioactive salts were coated with Rust-O-Leum #7791 (white satin) Paint and allowed to dry for at least 24 hr.

Beta-counts were taken for each of the 18 samples, and a log-log plot of the concentration (in moles) vs. average counts per min was constructed for each isotope (Fig. 1). Gamma counts for the samples were also taken. As expected, the ^{36}Cl samples showed no gamma activity at the energy selected. The ^{22}Na gamma activity was plotted against the corresponding beta counts (Fig. 2), giving a direct correlation between the two processes and allowing the ^{22}Na beta activity to be distinguished from the total. These three curves provide the means for obtaining direct concentration readings from radiotracer counts.

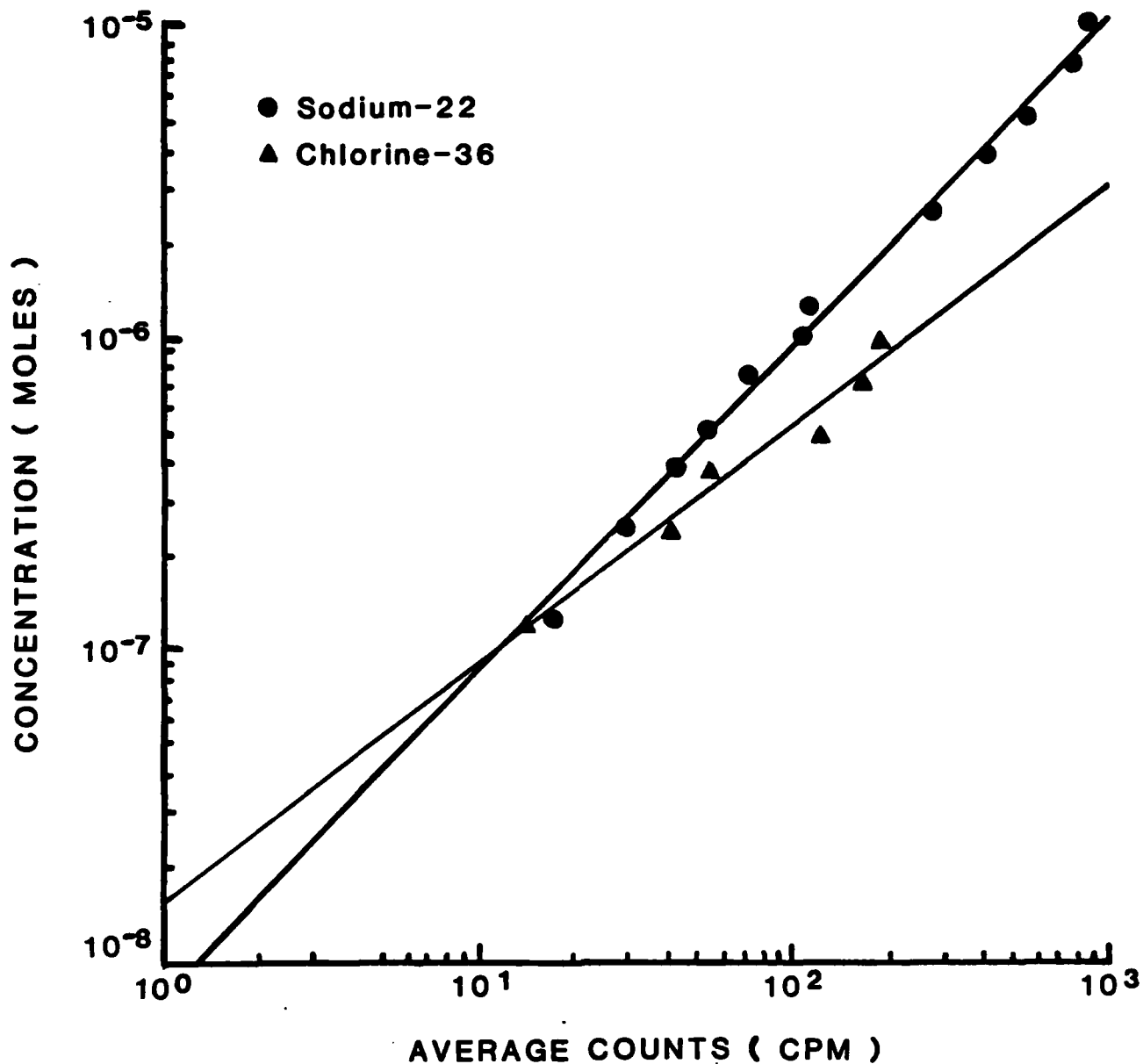
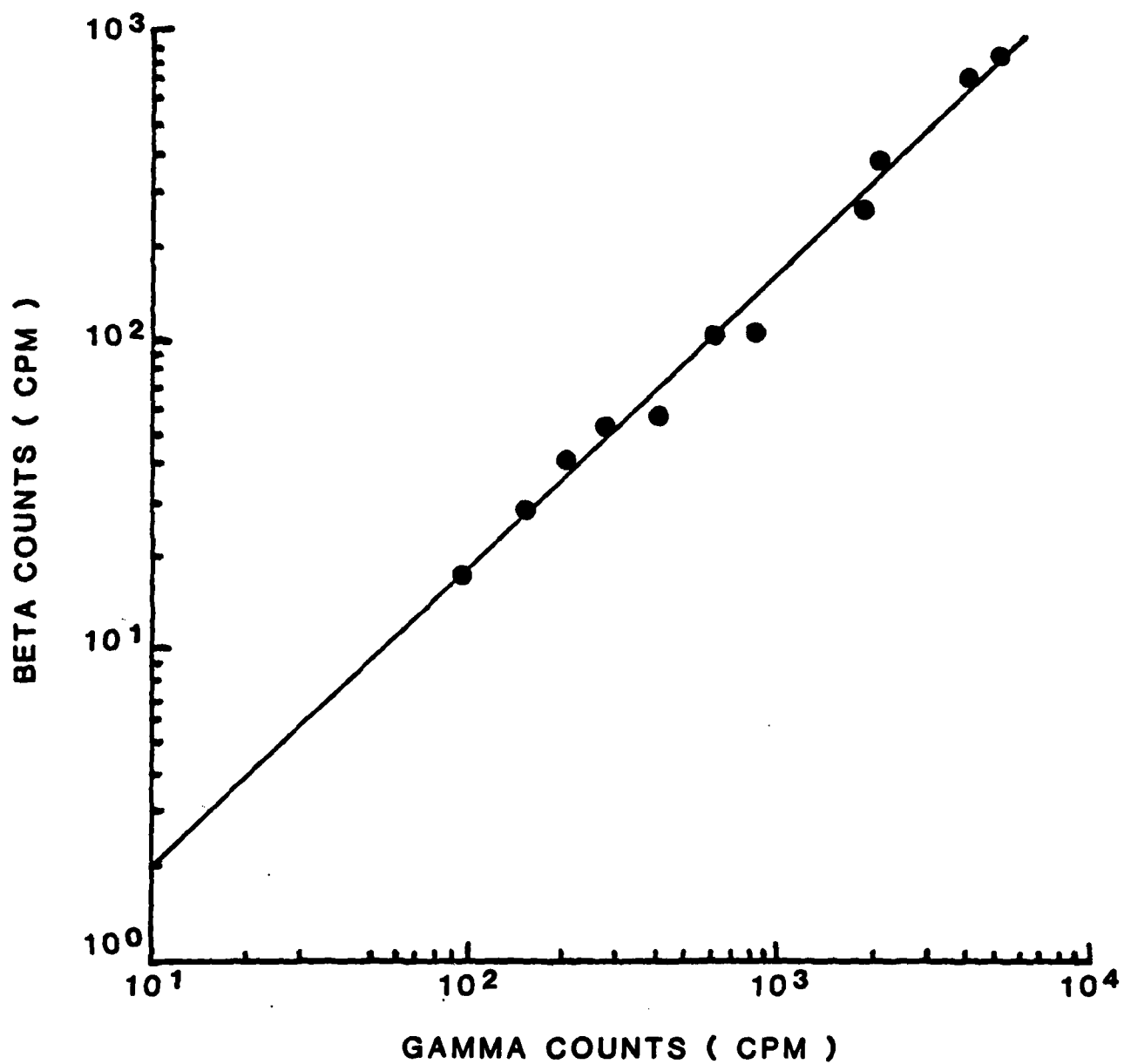


Figure 1. Calibration curves for ^{22}Na and ^{36}Cl beta counts. Chlorine: Slope - .7558; Intercept - 1.615×10^{-8} moles. Sodium: Slope - 1.045; Intercept - 7.552×10^{-9} moles.



Radiotracer Measurements

The radioisotopic study of the sodium chloride permeability of various organic coatings on cold rolled steel was carried out in two phases. The first phase consisted of survey runs with coating integrity and thickness as parameters. The second phase involved the determination of ion concentration within the coatings as a function of exposure time. From these measurements diffusion coefficients for each ion were determined.

The survey study of ion uptake by protective organic coatings was conducted in two parts. For these initial studies, the isotope concentrations were estimated at $0.7 \mu\text{Ci/ml}$. The first segment consisted of monitoring the uptake of ^{22}Na by polybutadiene ($60 \mu\text{m}$) on cold-rolled steel for different coating conditions. Cells consisting of one-inch diameter cylinders cemented to the coated plates with silicone were set up for three systems: intact coating (no imposed defects), a single point defect, and a single point defect under -1.5 V (vs Au) applied potential. Three ml of doped sodium chloride solution were added to each cell. After an initial exposure period, the cells were emptied, rinsed thoroughly with distilled water, and the ^{22}Na uptake was determined by monitoring the $.511 \text{ MeV}$ gamma using the gamma counter. All measurements were taken over a 5 min period relative to a background γ -count. After counting, the solution was replaced in the cells and the procedure repeated at various exposure times until visible signs of corrosion were observed.

The second series of samples consisted of epoxies and polybutadiene of various thicknesses on cold-rolled steel exposed to ^{22}Na and ^{36}Cl doped NaCl. The epoxies chosen were Epon 1001-F/Emerez 1511 deposited from a .30 xylene/.60 butylcellusolve solution and a commercially available 2-component green epoxy. The coating thicknesses were 70, 59, 46 and $20 \mu\text{m}$ for the Epon system, 46 and $48 \mu\text{m}$ for the green epoxy. Polybutadiene samples of 10, 13 and $17 \mu\text{m}$ were used for ^{22}Na uptake studies only. For this series, 1.1 cm diameter cells filled with .7ml doped solution were used. Counts of the rinsed cells were obtained using the radiation counter.

For the second phase, cold-rolled steel plates, polished with 600 grit paper, then rinsed with distilled water and methanol, were coated with Rust-O-Leum #7791 alkyd paint, polybutadiene, and epoxy. A series of alkyd samples was also prepared with a primer coat (Rust-O-Leum #7773). The study of the alkyd topcoat will be focused on here.

The alkyd coated plates were air cured for a period of approximately 3 weeks. A series of 3 cm^2 samples were cut from these plates, and the coating thicknesses determined with a magnetic gauge. Twenty-four samples (coating thickness: $28 - 50 \mu\text{m}$) were chosen for exposure to the radiotracer solution, with duplicate samples saved for impedance measurements. Capped vials were cut and mounted to make cells approximately 1.4 cm in diameter and 1.5 cm deep.

The isotope solution was prepared by diluting a solution containing 5 ml each of $1\mu\text{Ci/ml}$ ^{22}Na and ^{36}Cl in $.5\text{M NaCl}$ to $.25\text{M}$, giving an isotope:ion ratio half that used for calibration. This concentration was confirmed in a survey run for samples exposed to this solution. The ion uptake determined using the calibration curve is half the actual value. Equal volumes of isotope solution were added to each cell and the cells capped.

The counting procedure is identical to that described for calibration. Prior to counting, the cells were emptied and residual solution removed with a pipet. This step was followed by a ten-fold distilled water rinse and drying with a Kimwipe. After all beta and gamma counting was complete, the solutions were returned to the cells and the caps replaced. Tracer counts were taken after 1, 12 and 24 hr exposure and continued on a daily basis. Exposure was terminated when a sample showed a surface defect, rusting or severe blistering. The poor wet adhesion of the coating occasionally resulted in blistering at short exposure times. Blistered samples were included in the summary of results.

Impedance Measurements

The AC impedance of the 24 duplicate samples was measured at 1000 Hz using the method previously described. The cells were the same dimensions as those used for the tracer study to minimize differences between sample sets. Sixteen readings were taken during the first 24 hr exposure to $.5\text{M NaCl}$. Additional readings were taken daily until coating failure was observed. Failure was defined as the time at which either corrosion product was visually observed or the impedance measurements showed a pseudoinductive response (a negative quadrature value). In addition, the cell potential, relative to the internal Ag/AgCl reference electrode, was recorded prior to taking the impedance readings.

RESULTS AND DISCUSSION

Figures 3-5 show the results of the two-part survey of ion uptake as a function of coating integrity and thickness. The effect of coating integrity on the uptake of sodium by polybutadiene can readily be seen in Figure 3. An increase in the rate of sodium diffusion is observed as the coating integrity decreases. This observation can be explained by examining the changes which occur at the coating-metal interface. For an intact coating, there is a random distribution of cathodic and anodic sites across the surface and the only path for an ion to take is through the coating. When a defect is imposed, a cathodic region forms about the

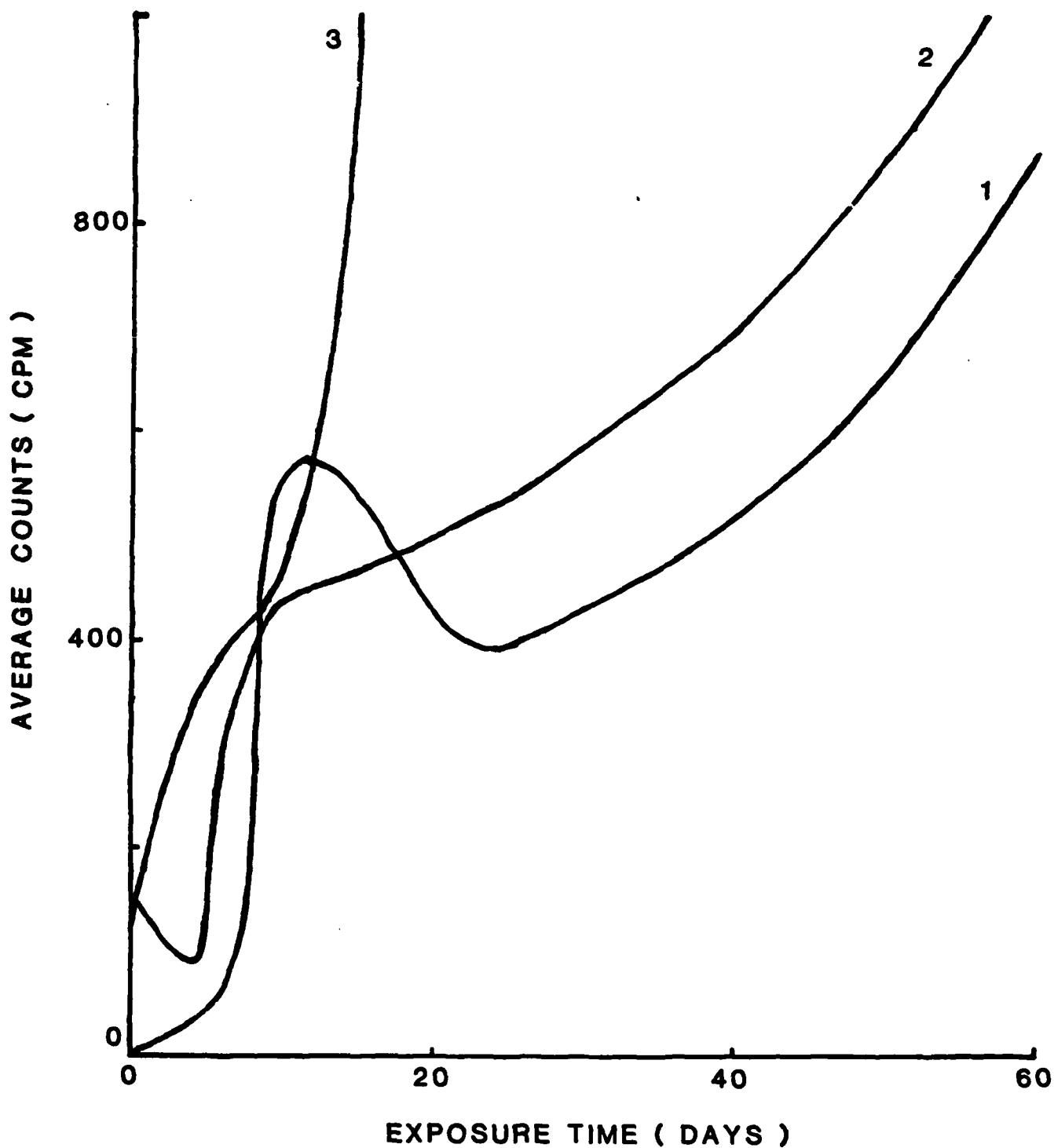


Figure 3. Gamma counts for polybutadiene exposed to $^{22}\text{NaCl}$:
1. Intact coating; 2. Pint defect, no applied potential; 3. Point defect, -1.5 v vs. Au wire.

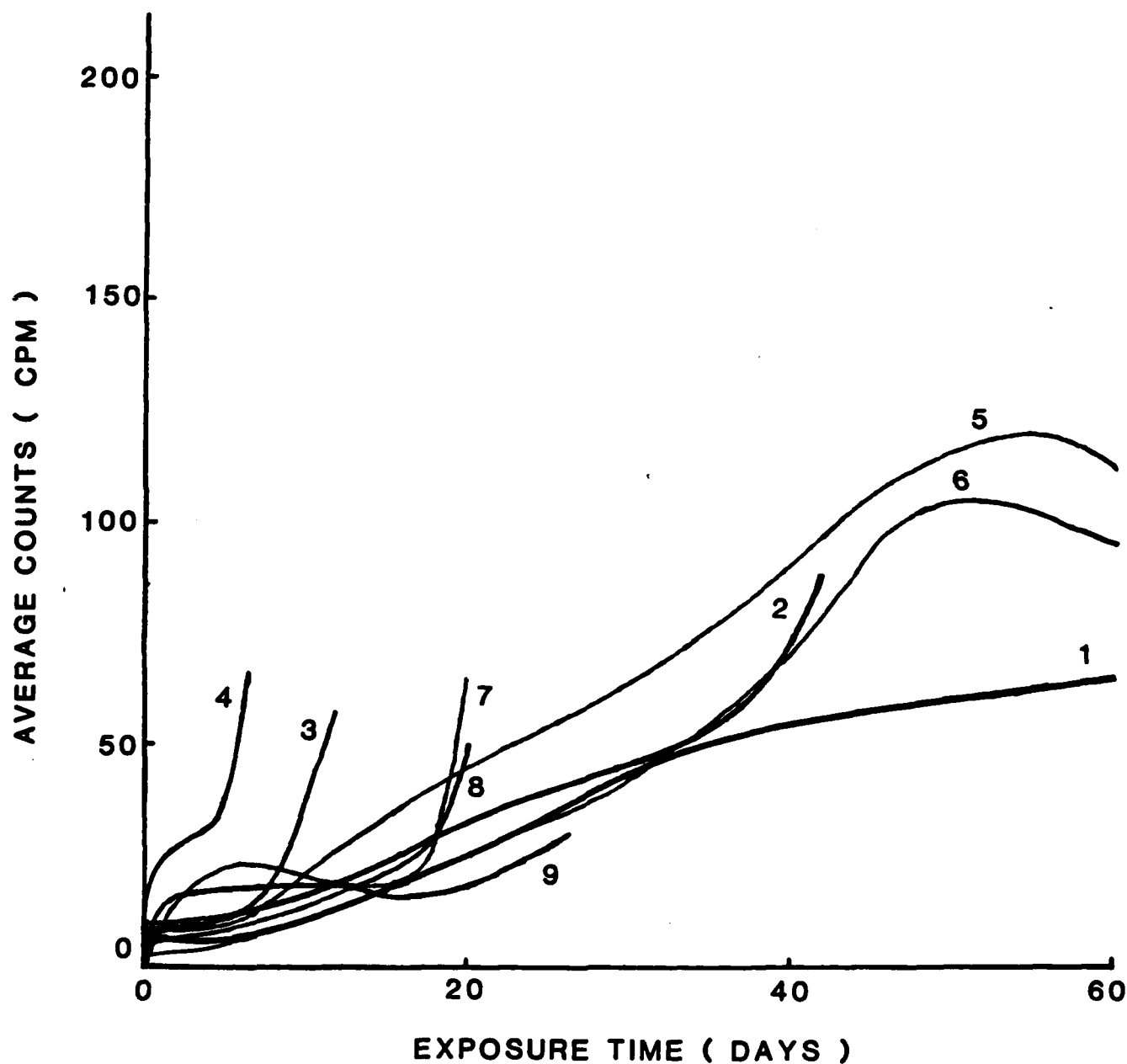


Figure 4. Total tracer counts for coatings exposed to $^{22}\text{NaCl}$.
 Curves 1-4: Epon 1001-F/Emerez 1511, 70, 59, 46 and 20 μm , respectively; 5 and 6: 2-component (green) epoxy, 46 and 48 μm , respectively; 7-9: polybutadiene, 10, 13 and 17 μm , respectively.

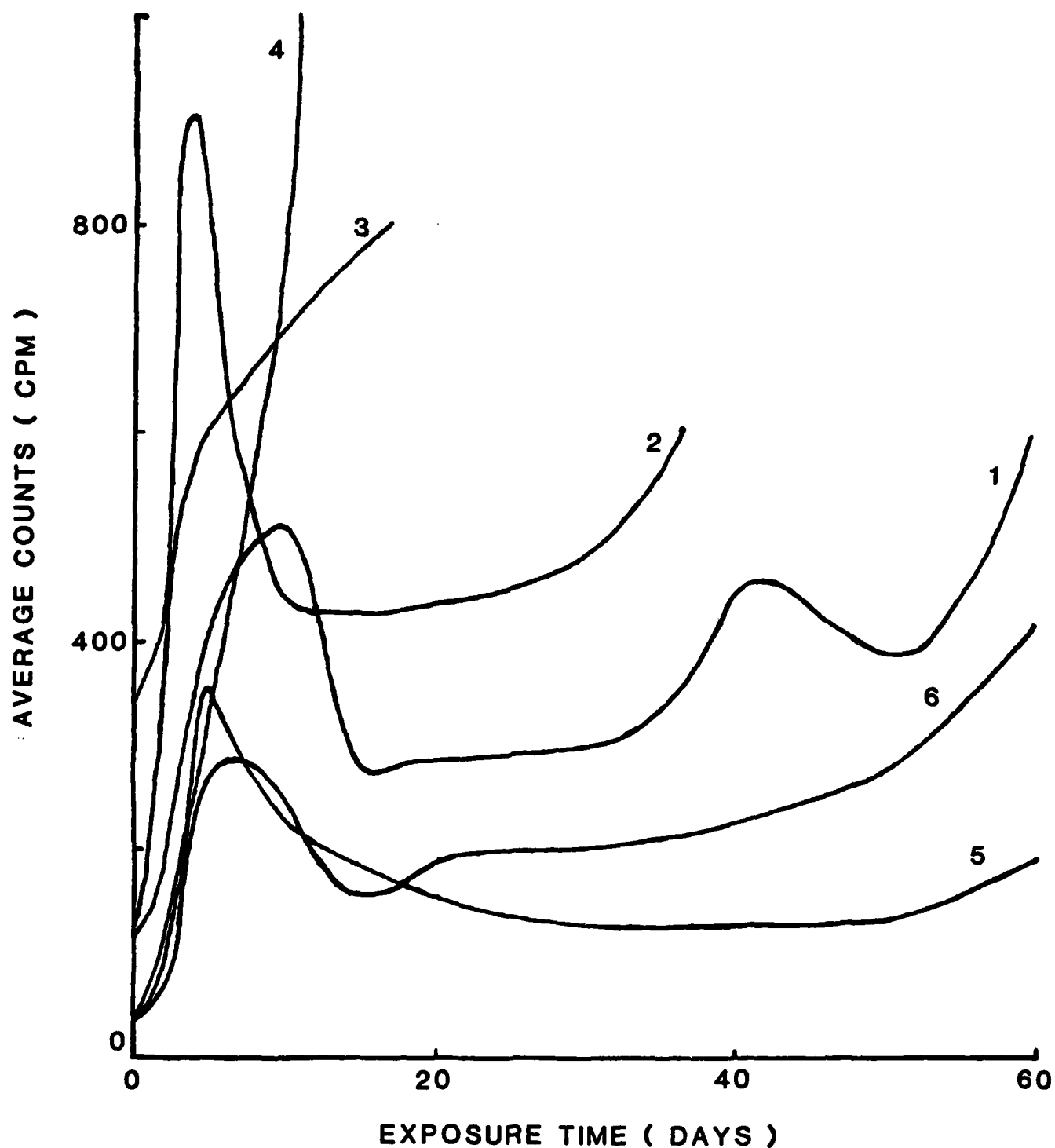


Figure 5. Beta counts for epoxies exposed to Na^{36}Cl . Curves 1-4: Epon 1001-F/Emerez 1511, 70, 59, 49 and 20 μm , respectively; 5 and 6: 2-component (green) epoxy, 46 and 48 μm , respectively.

defect (an anode). A lateral diffusion pathway is thus introduced giving two pathways to the (condensed) cathodic region. By applying a cathodic potential to the system, a potential gradient is set up which attracts sodium ions to the surface. In addition, cathodic disbonding increases the amount of solution under the coating and, in turn, the rate of lateral diffusion. Therefore, one would expect to find an increased rate of sodium uptake with the increase in the cathodic area beneath the coating.

A similar relation is observed for the second series of samples. The beta counts for Na^{36}Cl exposed samples, Figure 5, show an increase in the rate of ion uptake with decreasing coating thickness. The thickness difference between the green epoxy samples is within measurement error, which accounts for the similar response for both. The effect of the inhibitors in the green epoxy can be seen by the shift to longer exposure times relative to Epon sample #3. The total counts (beta plus gamma) for the $^{22}\text{NaCl}$ samples (Fig. 4) follow the same ordering as the ^{36}Cl samples. The relative uptake of sodium and chlorine should not be compared since the absolute concentrations of the isotopes were unknown.

The concentration of sodium and chloride ions retained by the alkyd coating as a function of exposure time can be seen in Figures 6a-d. The chloride plots appear linear from the initial exposure time. However, a large scatter in the data at short exposure times makes it difficult to determine an exact slope in several cases. This scatter suggests that initially chloride ions are preferentially adsorbed on the coating surface, and the amount retained after rinsing is random.

The sodium plots show a marked curvature at short exposure times. In general, there is much less scatter in the sodium data, suggesting the ions are retained within the coating. Alkyd paints are known cation exchangers, which may account for part of this retention [17]. Further studies must be made to determine what effect the exchange has on the sodium uptake measurements. The linear portion of the curves is nearly parallel to the chloride plots and will be used to estimate the diffusion coefficient for sodium through alkyd paint on cold-rolled steel.

The results of the impedance measurements on duplicate samples are given in Figures 7-9. Recently we reported [1] that $\tan \theta$, the ratio of the imaginary (Z'') to real (Z') component of the impedance, is a convenient means of monitoring coating breakdown. As the time of exposure to an electrolyte approaches the lifetime of the coating, conductivity of the coating increases and the current rises. This behavior results in a drop in $\tan \theta$ with exposure time. Failure was defined as that time when $\tan \theta$ crossed zero.

One disadvantage to using $\tan \theta$ is that it involves two changing parameters. A single parameter function we call Delta (Δ) will be introduced here [16]. Delta is defined as the ratio of Z'' at

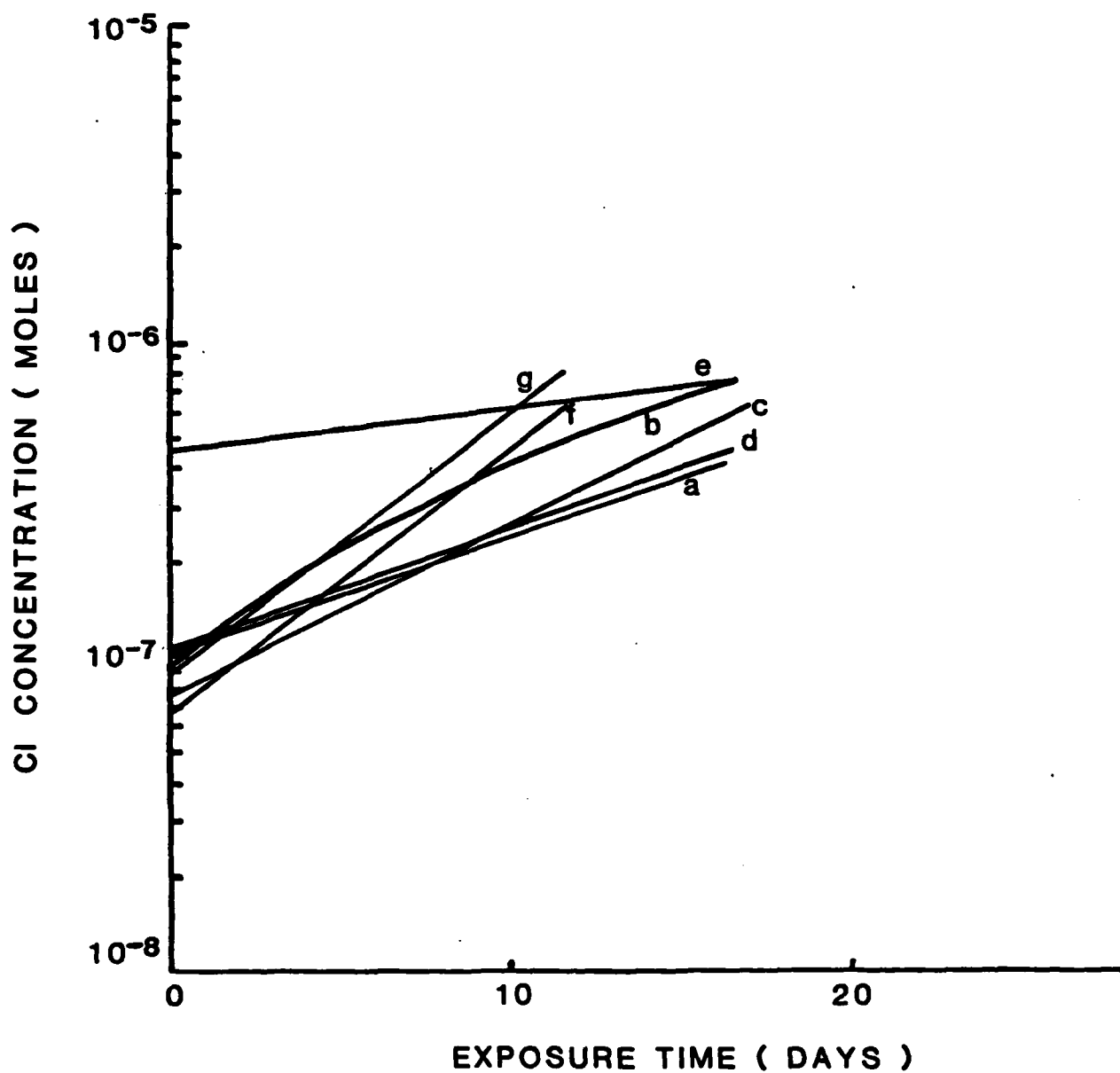


Figure 6a. Chloride uptake by alkyd paint as a function of exposure time. See Table II for key to plate series.

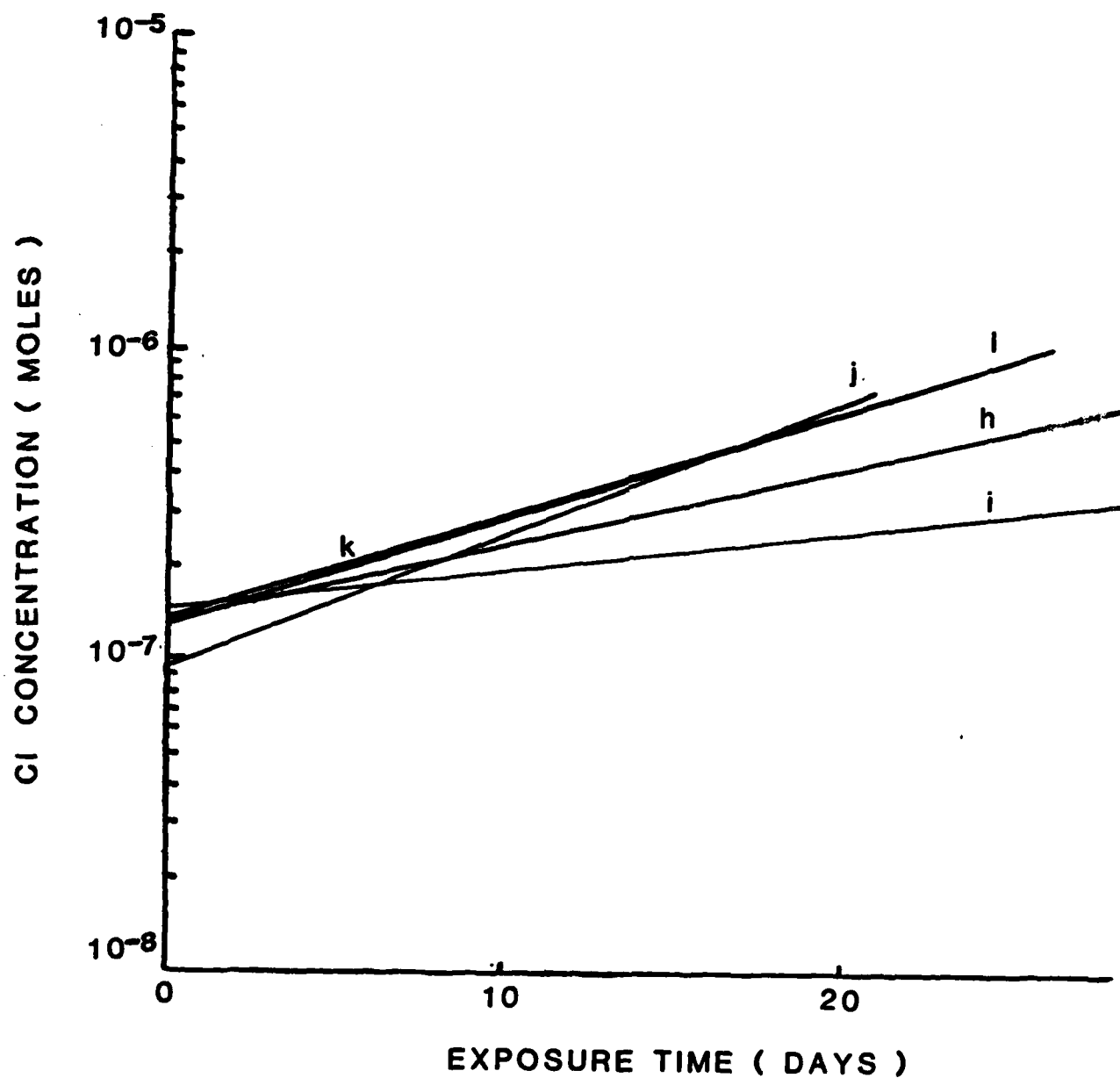


Figure 6b. Chloride uptake by alkyd paint as a function of exposure time. See Table II for key to plate series.

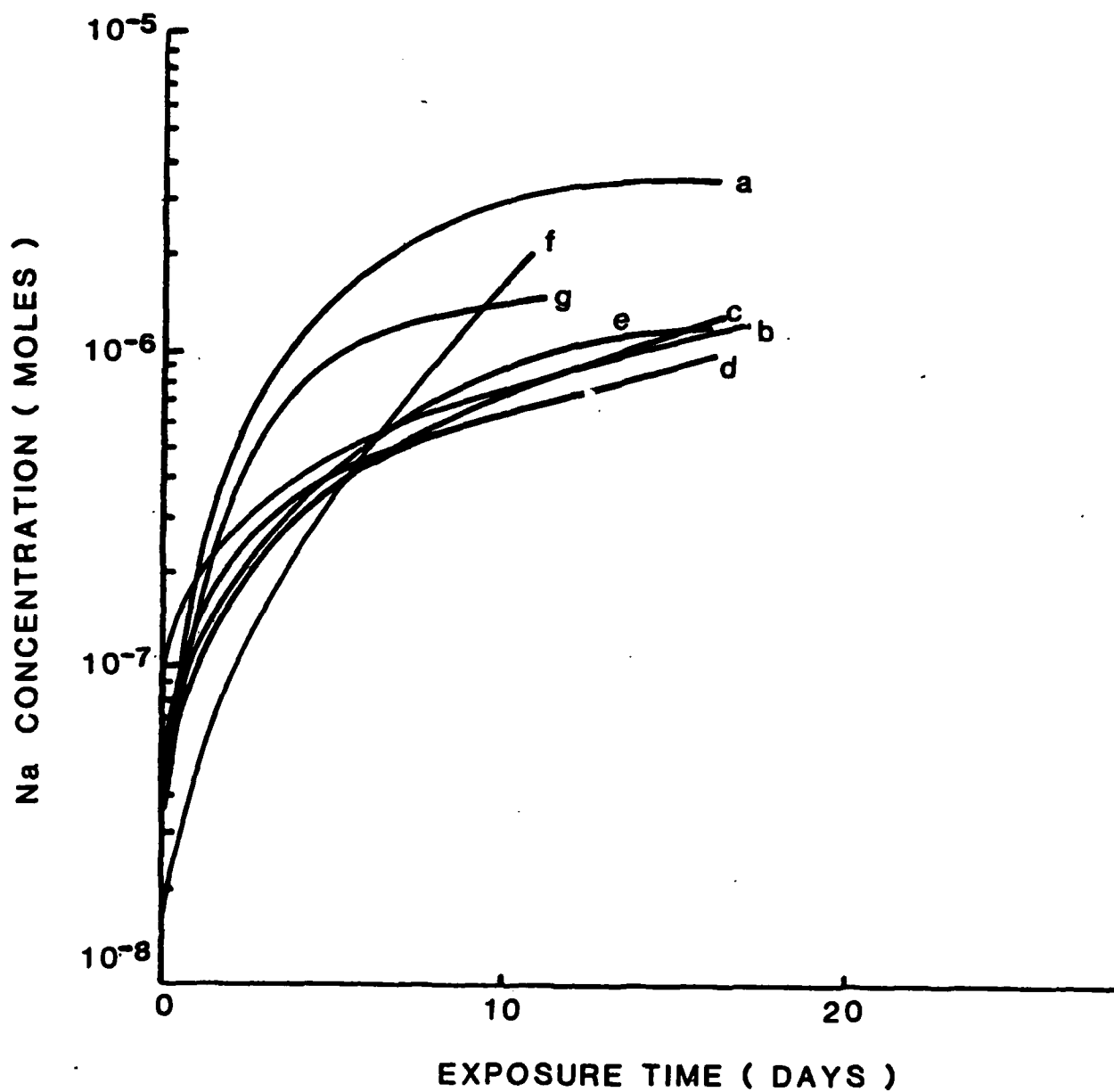


Figure 6c. Sodium uptake by alkyd paint as a function of exposure time. See Table II for key to plate series.

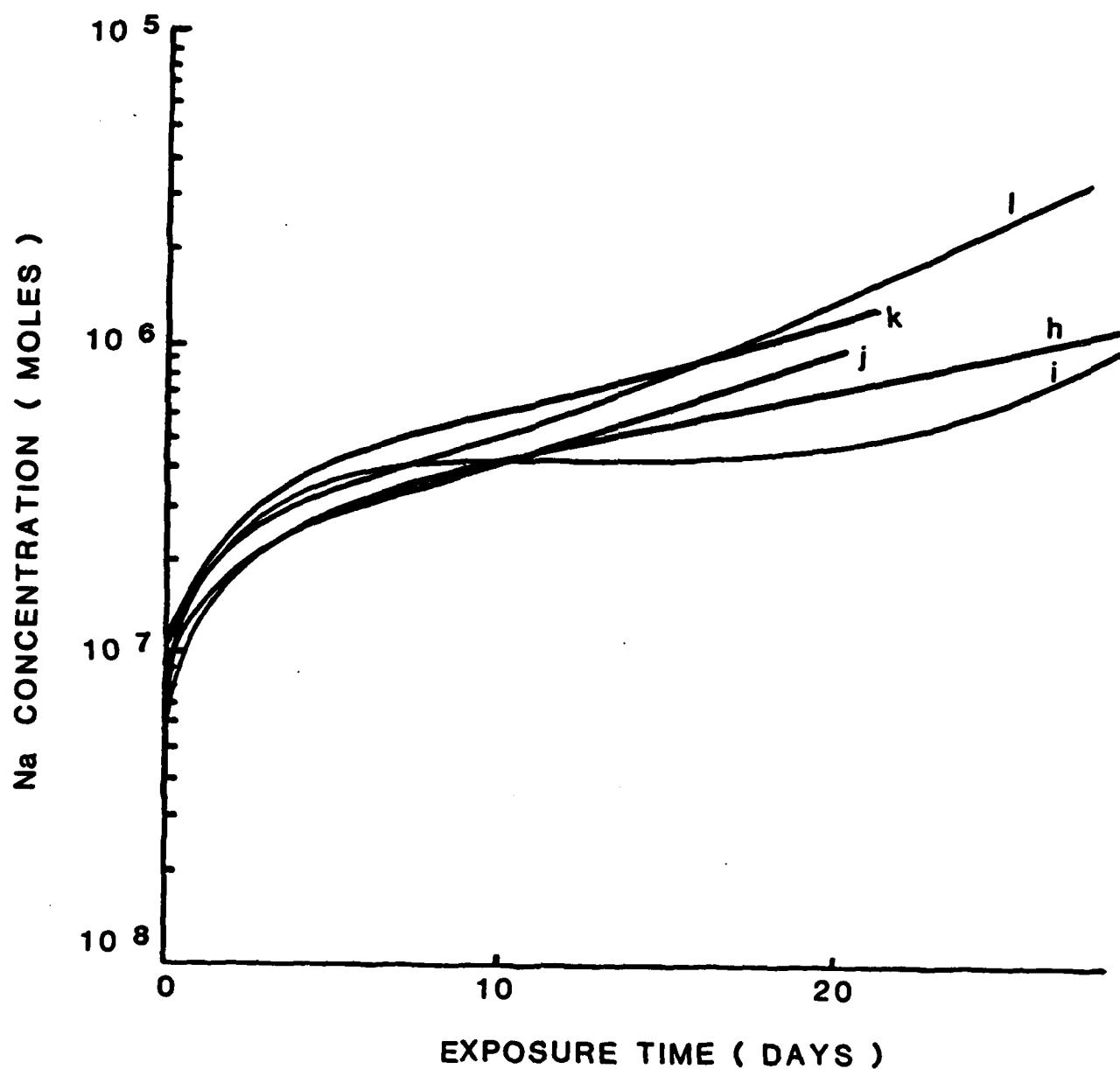


Figure 6d. Sodium uptake by alkyd paint as a function of exposure time. See Table II for key to plate series.

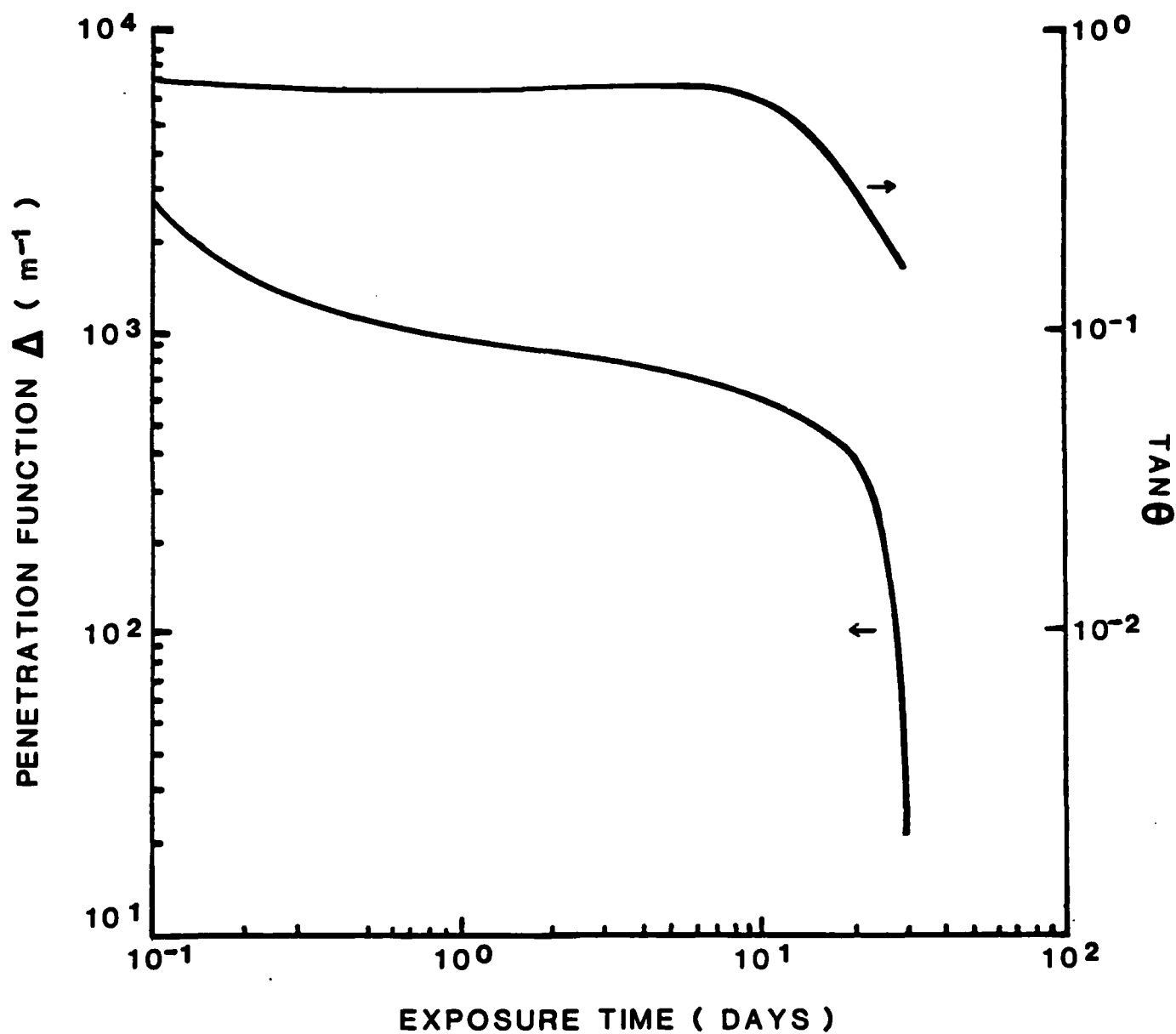


Figure 7. $Tan \theta$ and penetration function Δ as a function of exposure time for plate series 1.10 (28 μm).

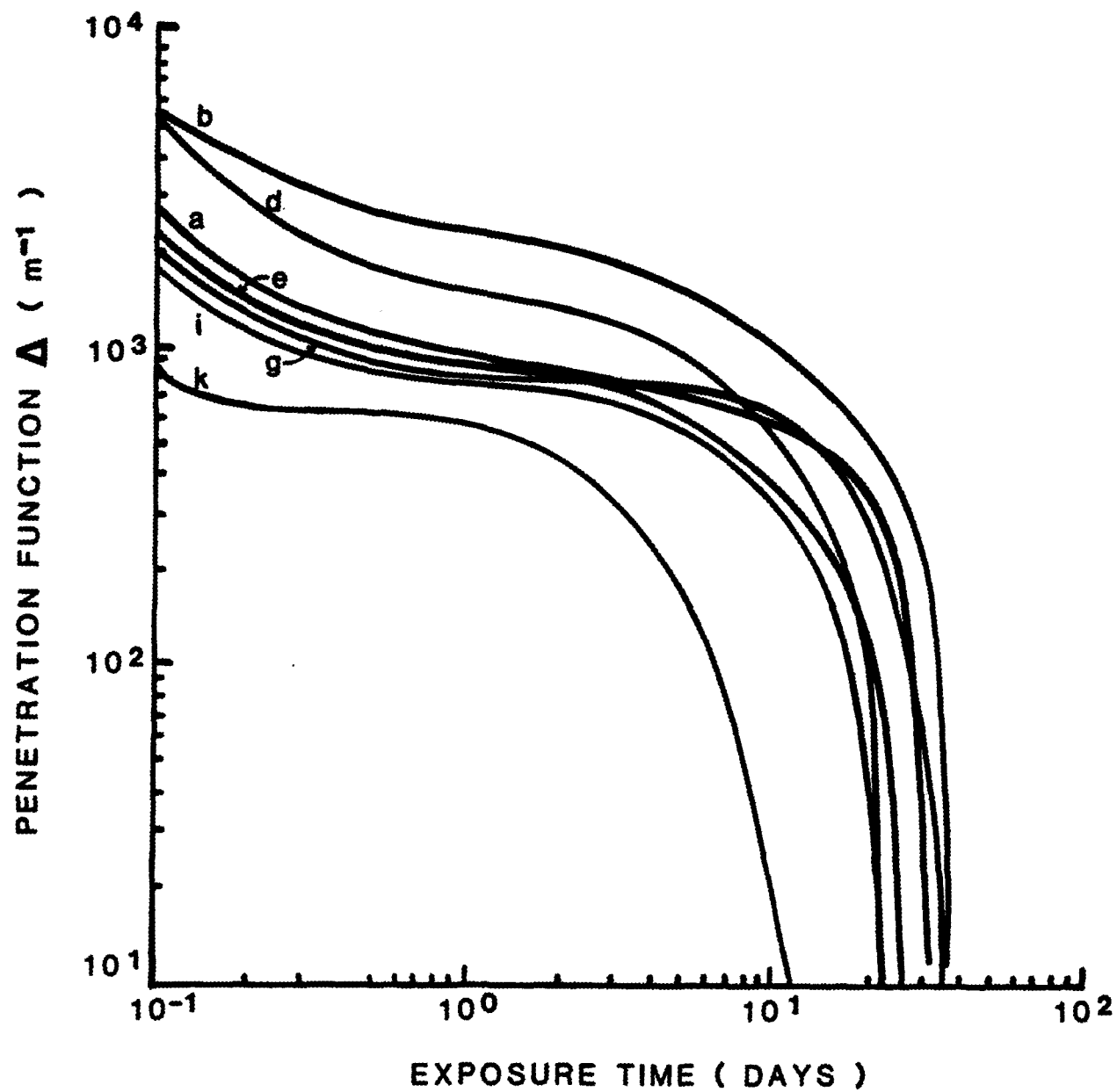


Figure 8. Penetration function Δ vs. exposure time for several alkyd series. See Table II for key to plate series.

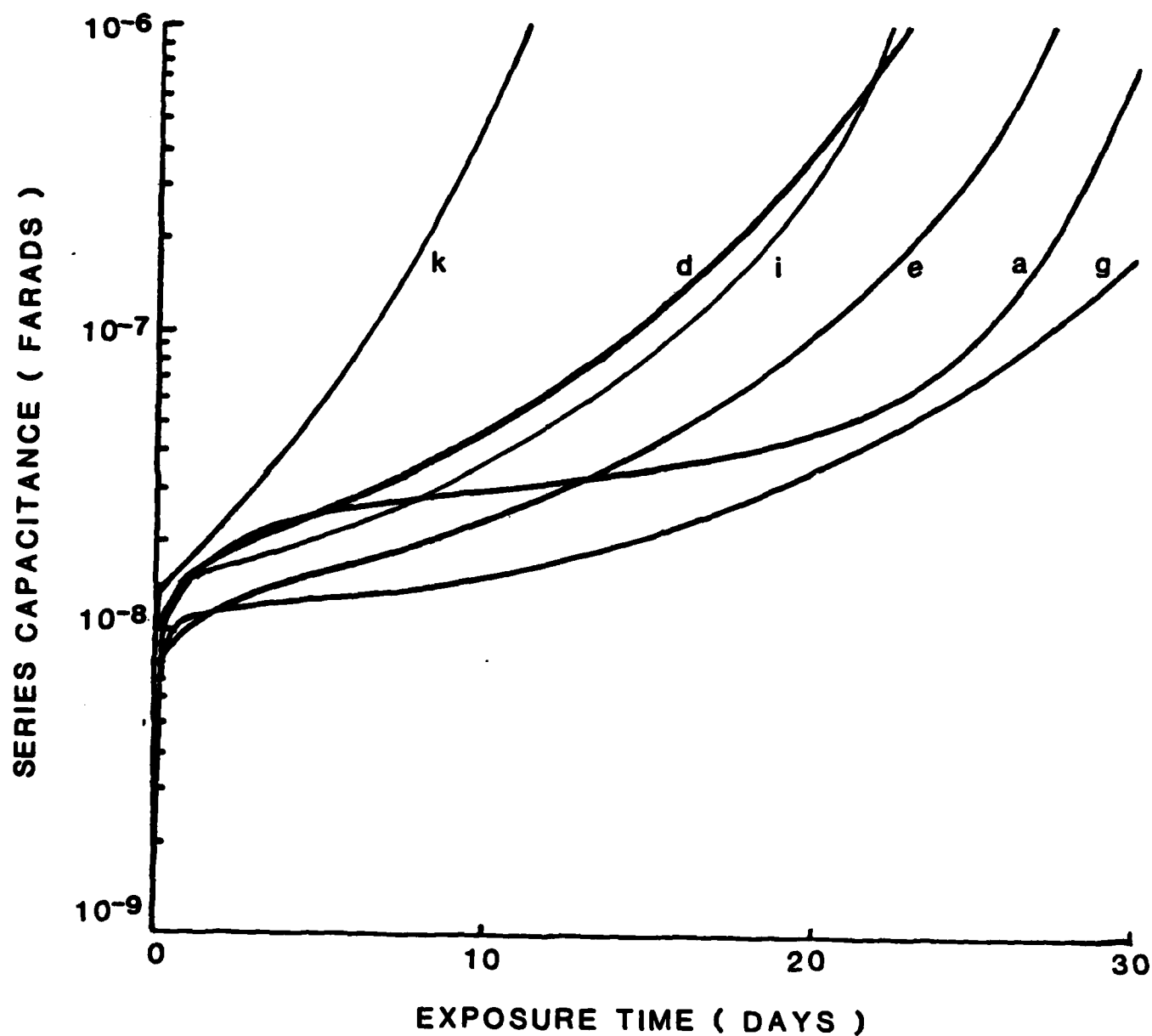


Figure 9. Series capacitance as a function of exposure time for alkyd paint on cold-rolled steel. See Table II for key to plate series.

time t to that when $t=0$, normalized to the coating thickness. This approach is equivalent to looking at the ratio of the dielectric constants. Figure 7 compares this "Penetration Function" with $\tan \theta$ for a single plate series. The sharper failure point shown by the Penetration Function makes it more suitable for this study. Figure 8 gives Delta as a function of time for several plate series.

Since Delta is proportional to the ratio of dielectric constants, or more directly the series capacitance (assuming the simplest model for the coating system), it would be to our advantage to look at this function as well. Figure 9 shows the change in capacitance with exposure time for those series given in Figure 8. The plateau regions of these curves are indicative of an equilibrium point in water uptake and an overall change in the rate of water uptake. A calculation of the amount of water within and under the coating was made using Eqn. (1).

$$\chi_{H_2O} = \log[(C_t - C_1)/C_0] / \log 80 \quad (1)$$

where,

C_0 = coating capacitance at the time of immersion

C_t = capacitance at exposure time t

C_1 = value of the capacitance when the plateau region is extrapolated back to $t = 0$

80 = dielectric constant of water

χ_{H_2O} = volume fraction of water

Figure 10 shows the volume of water within the coating as a function of exposure time for several series.

To determine the diffusion coefficient for water, we apply Fick's Law of diffusion. The flux across a surface of area A is given by

$$J = \frac{1}{A} \frac{dQ}{dt} = -D \frac{dc}{dx} \quad (2)$$

or

$$J = \frac{1}{A} \frac{CdV}{dt} = C \cdot \frac{1}{A} \cdot (A \cdot l) \frac{dx}{dt} = C \cdot l \frac{dx}{dt} \quad (3)$$

Assuming a constant volume equal to that of the coating, the slopes of the curves in Figure 10 can be used to calculate the diffusion coefficient D_{H_2O} :

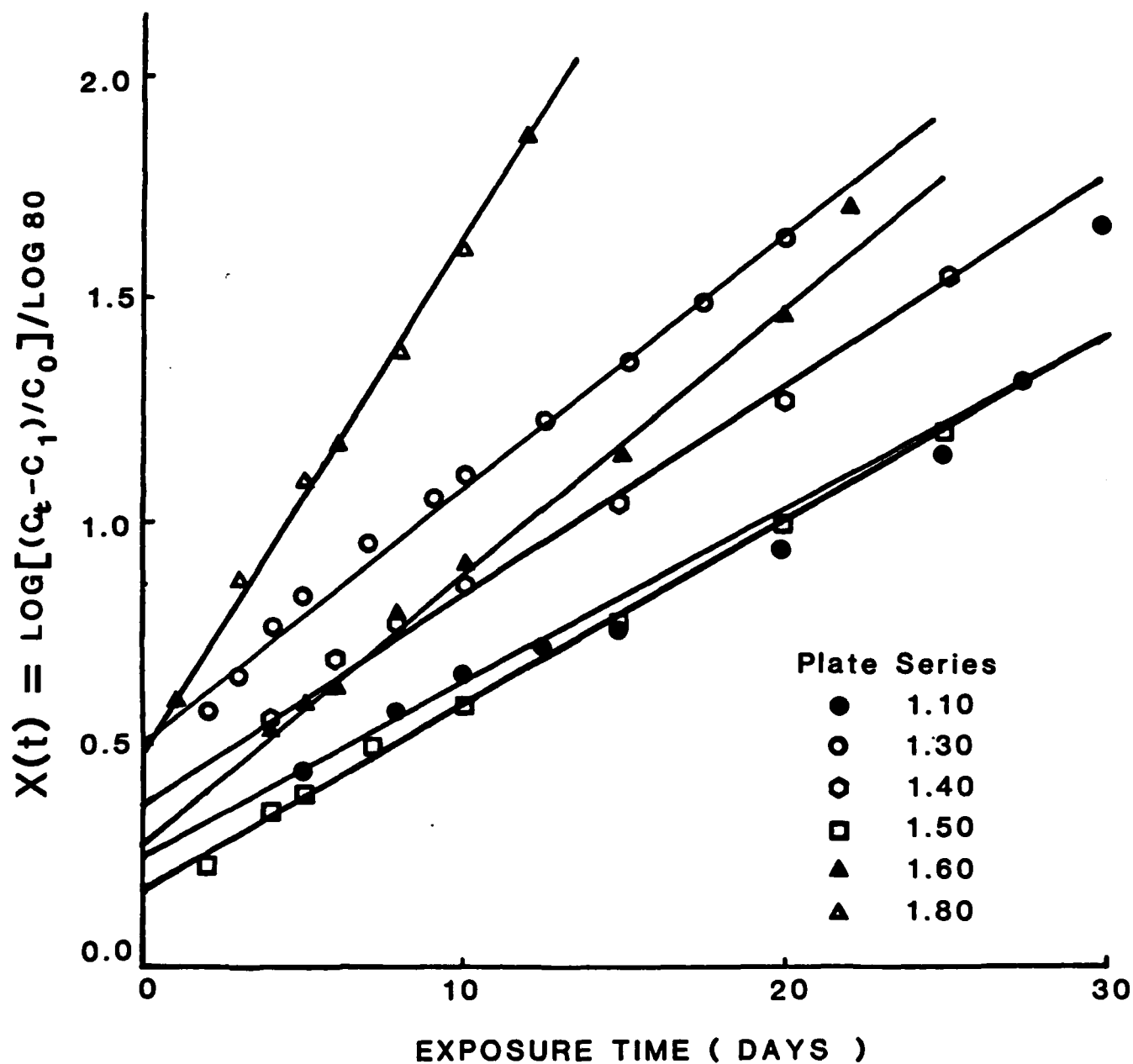


Figure 10. Relative volume fraction of water in alkyd paint $[X(t)]$ as a function of exposure time.

$$|D_{H_2O}| = C \cdot \ell \cdot \frac{dX_{H_2O}}{dt} \cdot \frac{d\ell}{dC} \approx \ell^2 \cdot \frac{dX_{H_2O}}{dt} \quad (4)$$

where ℓ is the coating thickness. The diffusion coefficients for water calculated for these series are listed in Tables I and II.

As stated earlier, the plateau region marks a change in diffusion rate of water into the coating. The diffusion coefficient of water at three hr exposure was calculated using Eqn. (1), and making the assumption that in this region C_1 and C_0 are equivalent. The results (Table I) show a marked difference in the diffusion coefficient, confirming a changing diffusion rate with exposure time.

The correlation between ion and water uptake, as the capacitance, is represented by plate series 1.30 in Figure 11. Initially water uptake dominates as depicted by the large values for the slopes. These data support the results found in Table I. The change of slope corresponds to the increase in ion transport with exposure time. The linearity of the latter segments of the curves suggests that the rate of ion diffusion is highly dependent on the rate of water diffusion. In addition, the curves for sodium and chloride are nearly parallel, again suggesting similar diffusion rates.

As stated earlier, sodium and chloride ion diffusion coefficients were calculated from the slopes of the linear portion of the curves in Figures 6a-d. The ion flux is defined by

$$J = \frac{1}{A} \cdot \frac{d(\# \text{ moles ions})}{dt} = \frac{1}{A} \cdot (\text{slope}) \quad (5)$$

The diffusion coefficient becomes

$$|D| = \frac{2}{A} \cdot (\text{slope}) \cdot \frac{\ell}{C} \quad (6)$$

where C is the ion concentration in the bulk solution (2.5×10^{-4} moles cm^{-3}), and the factor 2 corrects for the isotope:ion ratio. The results of these calculations are given in Table II. The mean diffusion coefficient for sodium is within a standard deviation of the mean value of that for chloride. These values are of the same magnitude as those for sodium and chloride through free films.

The ion diffusion coefficients are also of the same magnitude as the long-term diffusion coefficient for water. This result implies that the ions are being carried with the water as it diffuses through the coating. The data also lend credence to the theory that ionic diffusion through the coating is by means of aqueous pathways in the coating.

Table I

D_{H_2O} for First 3 Hours Exposure
(D in cm^2/hr)

<u>Plate Series</u>	<u>D_{H_2O}</u>
1.10	1.67×10^{-6}
1.30	2.72×10^{-6}
1.40	2.60×10^{-6}
1.50	3.10×10^{-6}
1.60	3.29×10^{-6}
1.80	5.41×10^{-6}
<hr/> \bar{X}	<hr/> 3.13×10^{-6}
$\sigma (N-1)$	1.25×10^{-6}

Table II
Average Diffusion Coefficients for Water, Na⁺, Cl⁻
for Alkyd Paint on Cold Rolled Steel
D in cm²/hr

Curve	Plate Series	Thickness	No. Samples (a)	D _{Na⁺}	D _{Cl⁻}	D _{H₂O}
a	1.10	28 μm	2	1.43 × 10 ⁻⁷	1.09 × 10 ⁻⁸	1.26 × 10 ⁻⁸
b	1.15	29	2	4.02 × 10 ⁻⁸	2.47 × 10 ⁻⁸	--
c	1.25	32	2	5.21 × 10 ⁻⁸	2.24 × 10 ⁻⁸	--
d	1.30	33	2	3.56 × 10 ⁻⁸	1.45 × 10 ⁻⁸	2.59 × 10 ⁻⁸
e	1.40	36	1	5.78 × 10 ⁻⁸	1.26 × 10 ⁻⁸	2.49 × 10 ⁻⁸
f	1.45	37	2	1.52 × 10 ⁻⁷	3.58 × 10 ⁻⁸	--
g	1.50	38	1	1.08 × 10 ⁻⁷	4.89 × 10 ⁻⁸	2.49 × 10 ⁻⁸
h	1.58	40	2	2.94 × 10 ⁻⁸	1.54 × 10 ⁻⁸	--
i	1.60	41	2	1.94 × 10 ⁻⁸	5.83 × 10 ⁻⁹	4.18 × 10 ⁻⁸
j	1.78	45	2	4.05 × 10 ⁻⁸	2.76 × 10 ⁻⁸	--
k	1.80	46	2	5.10 × 10 ⁻⁸	2.53 × 10 ⁻⁸	9.97 × 10 ⁻⁸
l	2.00	51	4	1.15 × 10 ⁻⁷	3.43 × 10 ⁻⁸	--
Average	\bar{X}	39	(24)	7.03 × 10 ⁻⁸	2.32 × 10 ⁻⁸	3.83 × 10 ⁻⁸
St. Dev.	σ(N-1)	7.8		4.62 × 10 ⁻⁸	1.23 × 10 ⁻⁸	3.15 × 10 ⁻⁸

(a) Number in impedance or radiotracer series.

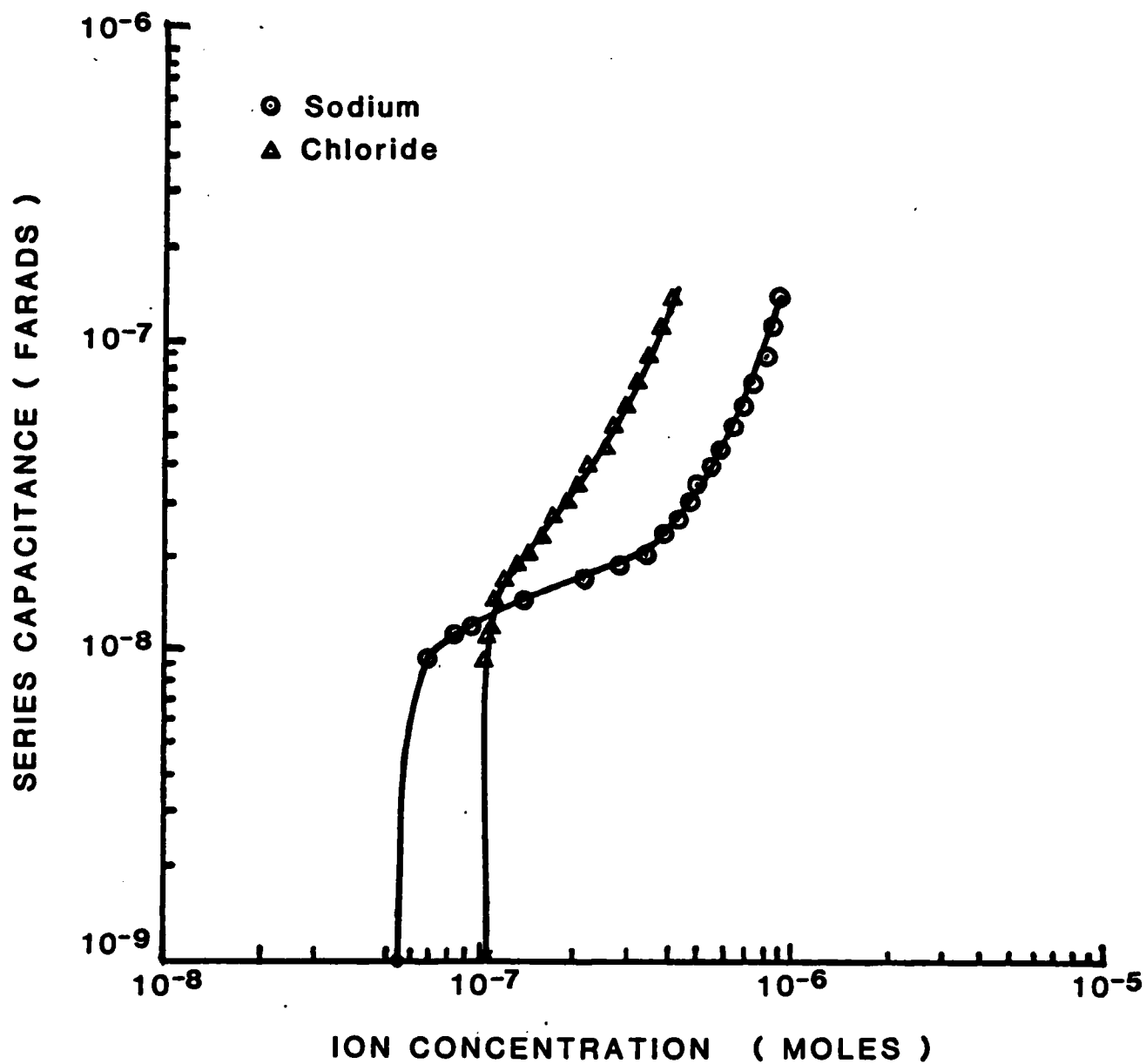


Figure 11. Series capacitance vs. ion concentration for plate series 1.30.

CONCLUSIONS

It has been shown that radiotracers can be used to monitor quantitatively the uptake of ions by a coating. When combined with capacitance data obtained using impedance techniques, diffusion coefficients for water and the ions can be obtained. For the alkyd system, two diffusion coefficients were observed for water: one extremely rapid at the initial period of exposure, a second after diffusion reached an equilibrium rate. During this equilibrium stage the coating swells and ions are transported through the coating with the water, probably through pores. Diffusion coefficients obtained by these methods are of the same magnitude as those found for free films, adding validity to these results.

REFERENCES

- [1] J. M. Parks, M. C. Hughes and H. Leidheiser, Jr., Paper presented at Electrochem. Soc. Meeting, Denver, Colo, October 15, 1981.
- [2] M. C. Hughes and J. M. Parks, "Corrosion Control by Organic Coatings," H. Leidheiser, Jr., Editor, Natl. Assoc. Corrosion Engrs., Houston, Texas, p.45 (1981).
- [3] G. W. Rothwell, J. Oil Colour Chem. Assoc. 52, 219 (1969).
- [4] J. D. Murray, J. Oil Colour Chem. Assoc. 56, 210 (1973).
- [5] J. D. Murray, J. Oil Colour Chem. Assoc. 56, 507 (1973).
- [6] A. L. Glass and J. Smith, J. Paint Technol. 38(495), 203 (1966).
- [7] A. L. Glass and J. Smith, J. Paint Technol. 39(511), 490 (1967).
- [8] A. L. Glass and J. Smith, Isotop. Radiat. Technol. 8(1), 60 (1970).
- [9] T. Sabu, I. S. Mishra, S.P.S. Khalsa and S. K. Das, Technology (Sindri) 8(2), 171 (1971).
- [10] M. Svoboda, D. Kuchynka and B. Knappek, Forbe und Lack 77(1), 11 (1971).

- [11] T. Sabu, S. K. Das and K. C. Bonevji, Paint India (Bombay) 31(10),3 (1981).
- [12] V. G. Amesikov, T. V. Krivova, G. M. Rankin and I. F. Yazikov, Russ. J. Phys. Chem. 55(8), 1159 (1981).
- [13] A. Fialkiewicz and M. Szanderowski, J. Oil Colour Chem. Assoc. 57, 259 (1974).
- [14] D. A. Bayliss and H. Broy, Mater. Perform. 20(11), 29 (1981).
- [15] R. E. Touhsaent and H. Leidheiser, Jr., Corrosion 28(12), 435 (1972).
- [16] H. Ponte and E. Braches, Adhesion (11), 321 (1979).
- [17] U. Ulvarsson, M. L. Khuller and E. Wählin, J. Oil Colour Chem. Assoc. 50, 254 (1967).

Program #9. Drying and Curing of Epoxy Films

ABSTRACT

Once a coating formulation is selected, drying conditions, such as temperature, air velocity and relative humidity become the most important parameters in determining the final properties of the dried coating films. Drying curves were obtained for four different aqueous-based epoxy systems and one organic solvent-based epoxy system in a homemade wind tunnel under various drying conditions of relative humidity 10-52%, air velocity 0-76 cm/sec and temperature 77-104°F. The drying curves of the aqueous based latex system, and to a lesser extent the aqueous solubilized formulations, showed that the initial low and constant flux rate is followed by a sudden increase in flux which may or may not drop down again at the advanced stages of drying. This phenomenon was taken as an indication of "skin" formation at the surface of the coating film. This phenomenon did not exist in drying of films cast from organic solvents. These results together with a chemical engineering analysis of the drying curves were reported in an M.S. thesis by B. I. Aremu, Lehigh University, 1981.

Recently, drying curves for the same five epoxy systems were generated under milder drying conditions. Increasing the relative humidity, at constant temperature and air velocity, resulted in increasing the time at which the upswing in the flux curves takes place during the advanced stages in drying. The morphological studies on the dried films using scanning electron microscopy have been initiated. Films dried under drastic drying conditions showed rough surfaces and cracks. Mild drying conditions yielded smoother films and a lesser number of cracks. Tests on the corrosion protection performance of films dried on steel substrates under various drying conditions are in progress.

INTRODUCTION

It is generally agreed that corrosion protection by organic coatings is controlled by adhesion, oxygen, ion, and water permeability properties of the coating film. All of these coatings properties are controlled by the organic coating formulation. However, once these coating formulations are selected, the drying conditions become the most important parameters in determining the properties of the coating film.

Air drying is the most widely used method in removing solvent from coatings films. Temperature, relative humidity and air flow velocity are the drying parameters studied in this connection. Usually, drying rate curves for a given coating formulation, i.e., flux of solvents vs. drying time, are generated as a function of the above drying parameters. These drying rate curves are valuable: (i) in predicting drying patterns especially under intense drying environments; (ii) in providing information about the mechanism of film formation and its consolidation, (iii) in reflecting the formation of certain types of defects during the drying step such as skin formation, blisters, and cracks.

Recognizing the important role played by the rates of drying of organic coatings in corrosion protection, it was decided to conduct a systematic study on drying of five different systems of epoxy resin-curing agent mixtures: (i) solvent based Epon 1001 and Emerez 1511; (ii) aqueous-based latex of Epon 1001 and Emerez 1511 [Lehigh Formula]; (iii) modified aqueous-based latex of Epon 1001 and Emerez 1511 [Lehigh Formula]; (iv) modified Epi-Rez 510 liquid epoxy resin and Epi-Cure W-50-8535 [Celanese formulation]; and (v) modified Epi-Rez 510 liquid epoxy resin and Epi-Cure WC-60-8537 [Celanese formulation].

OVERALL OBJECTIVES

1. To generate drying curves for the above five systems of epoxy-curing agent (unpigmented and pigmented) under different drying parameters (temperature, relative humidity and air flow velocity).
2. To study the morphology of the above dried epoxy films.
3. To study the corrosion protection performance of the above dried epoxy films.
4. To correlate the effect of drying conditions on the morphology and corrosion protection performance of epoxy coatings.

SUMMARY OF PROGRESS TO DATE

During the first two years on this program, drying curves were generated for thin films cast on glass substrates from all the above five epoxy systems. The drying curves were generated gravimetrically in a homemade wind tunnel under low to medium drying conditions of relative humidity 10-52%; air velocity 0-76 cm/sec; and temperature 25-40°C.

Distinct differences in the drying behaviors were observed for the various epoxy systems. The drying curves of the aqueous-based latex system, and to a lesser extent the aqueous solubilized celanese formulations, showed that the initial low and constant flux rate is followed by a sudden increase in flux which may or may not drop down again at the advanced stages of drying. This phenomenon was taken as an indication of "skin" formation at the surface of the coating film. The point in time at which this phenomenon takes place was found to depend on the drying conditions and the coating formulation. This phenomenon did not exist in drying of films cast from organic solvents. The results were reported in an M.S. thesis [B. I. Aremu, Lehigh University, 1981].

During the past year drying curves of the above epoxy systems were generated, in a modified wind tunnel, under milder drying conditions. Morphological studies of the dried films has been initiated using scanning electron microscopy. Also, work on the effect of drying conditions of the epoxy systems on the corrosion protection performance has been initiated, using the cathodic delamination technique developed by Dr. Leidheiser's group.

EXPERIMENTAL RESULTS

Our efforts during the past year were directed towards (i) extending the drying curves of the five epoxy systems to higher percent humidity range (>50%), thereby subjecting the film to relatively milder drying conditions; (ii) characterization of the morphology and corrosion protection performance of epoxy films dried under different conditions.

Drying Curves. In preparation for this phase of the work, the wind tunnel previously used was modified to improve the drying conditions and to increase the sensitivity of measurements of temperature, air velocity and relative humidity in the test chamber. Experiments were carried out to repeat some of the trials performed earlier at a temperature of 86°F, relative humidity of 30%, and an air velocity of 76.2 cm/sec, using the modified wind tunnel to evaluate the effect of equipment modifications on the drying rates of epoxy resin-curing agent systems. The results, shown in Figure 1, indicated similar trends in drying behavior of the five

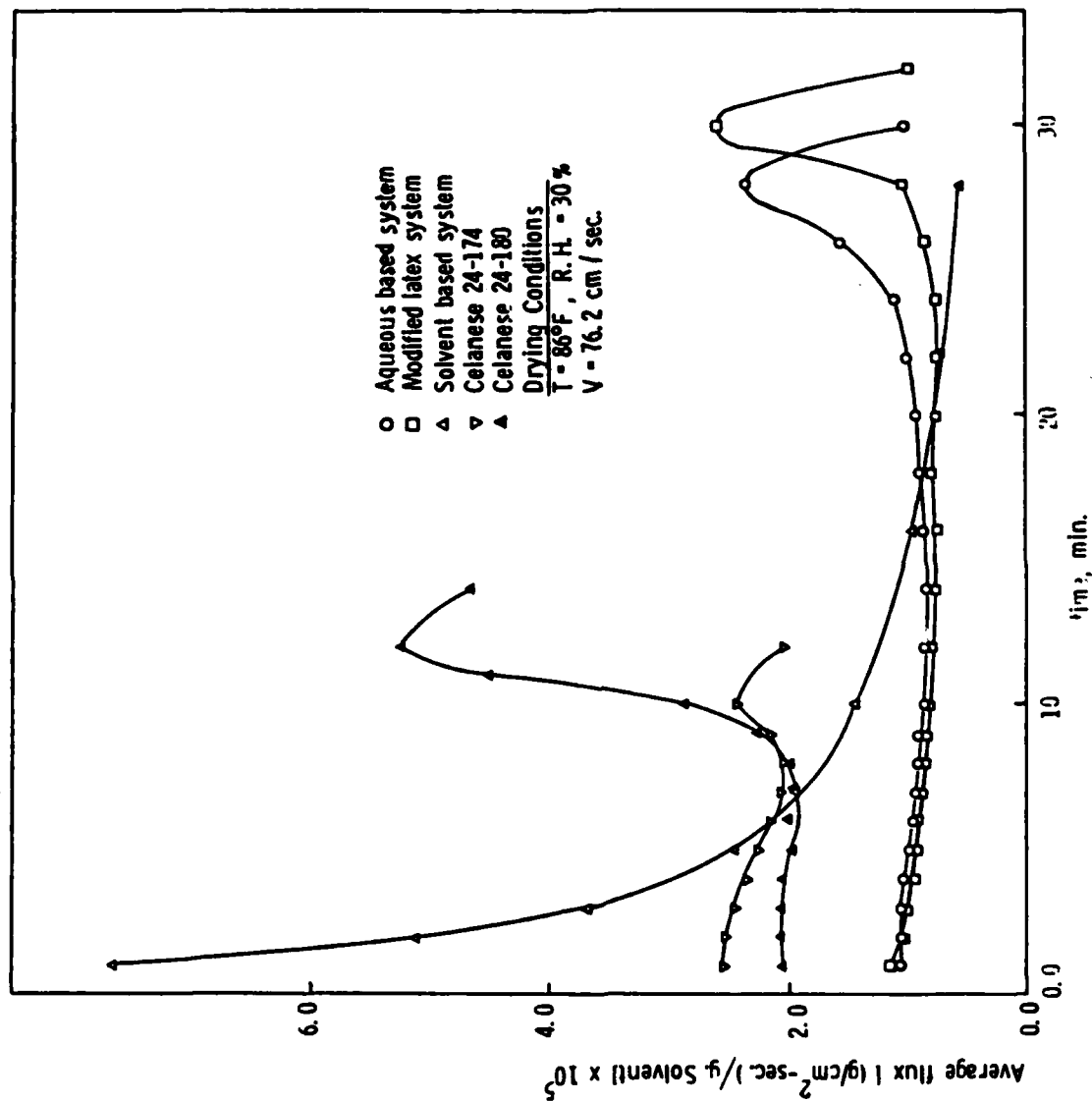


Figure 1. Experimental drying rate (flux) vs. drying time for various epoxy-curing agent systems, at temperature $T = 86^{\circ}\text{F}$, relative humidity $\text{R.H.} = 30\%$ and air velocity $V = 76.2 \text{ cm/sec}$.

epoxy systems as compared to the data obtained earlier by Aremu. The solvent-based solution and aqueous-based latex exhibit highest and lowest values of flux, respectively. The modified latex and aqueous-based modified Celanese formulations were found to have values intermediate between the solvent-based solution and aqueous-based latex. The drying rates of the aqueous-based latex, the modified latex, and the Celanese formulations, were found to decrease with drying time till most of the water in the film was removed, then it finally increased towards the end of the drying operation. The solvent-based system exhibited the highest drying rates at the beginning of the drying operation and its approach to constant drying rate was the fastest. The values of drying rates determined with the modified wind tunnel, were higher in the case of the solvent-based system and slightly lower for the modified and aqueous-based latexes as compared with the previous results of Aremu. The drying rate values for the modified Celanese formulations were in the same range.

Further trials were conducted by increasing the relative humidity to 50% and 59%, keeping the temperature and air velocity constant. Figure 2 shows the average flux versus time curves at a temperature of 86°F, relative humidity of 50%, and air velocity of 76.2 cm/sec. The drying rates of the aqueous-based latex, the modified latexes and the aqueous-based modified Celanese formulations, were reduced significantly, compared to the drying at 30% relative humidity. However, the drying rate of the solvent-based system remained almost unaffected. The drop in the flux at the end of the drying operation in the case of the aqueous-based latex and the modified latex systems was not observed at the 50% relative humidity. The relative humidity of the drying air was further increased to 59%, keeping the air velocity at 76.2 cm/sec and temperature at 86°F. Figure 3 shows the average flux versus drying time curves for the different systems under study. A similar trend in the drying behavior was observed in all five systems, as was obtained earlier at lower humidities with the exception of the lack of drop in average flux at the end of the drying operation. There was no change in the drying behavior of the solvent-based system. As expected, lower values of flux were obtained for all the systems at 59% relative humidity as compared to 30% and 50% relative humidities, with the exception of the solvent-based system, where the values remained almost constant. This observation of the sudden increase in the flux during the advanced stages of drying of water-born coating systems has been attributed, qualitatively, to evaporation from ruptured skin at the surface of the drying coating film [1,2]. It is proposed that the surface skin is formed during the early stages of film drying followed by rupture or "popping" in the later stages of drying due to entrapped air bubbles or insufficient dissipation of internal stress within the drying film. The current drying experiments of Figures 1-3 give other evidence for this phenomenon. Assuming that the point at which the average flux starts to increase is taken as an indication of initiation of "rupture" or "popping of the surface skin,

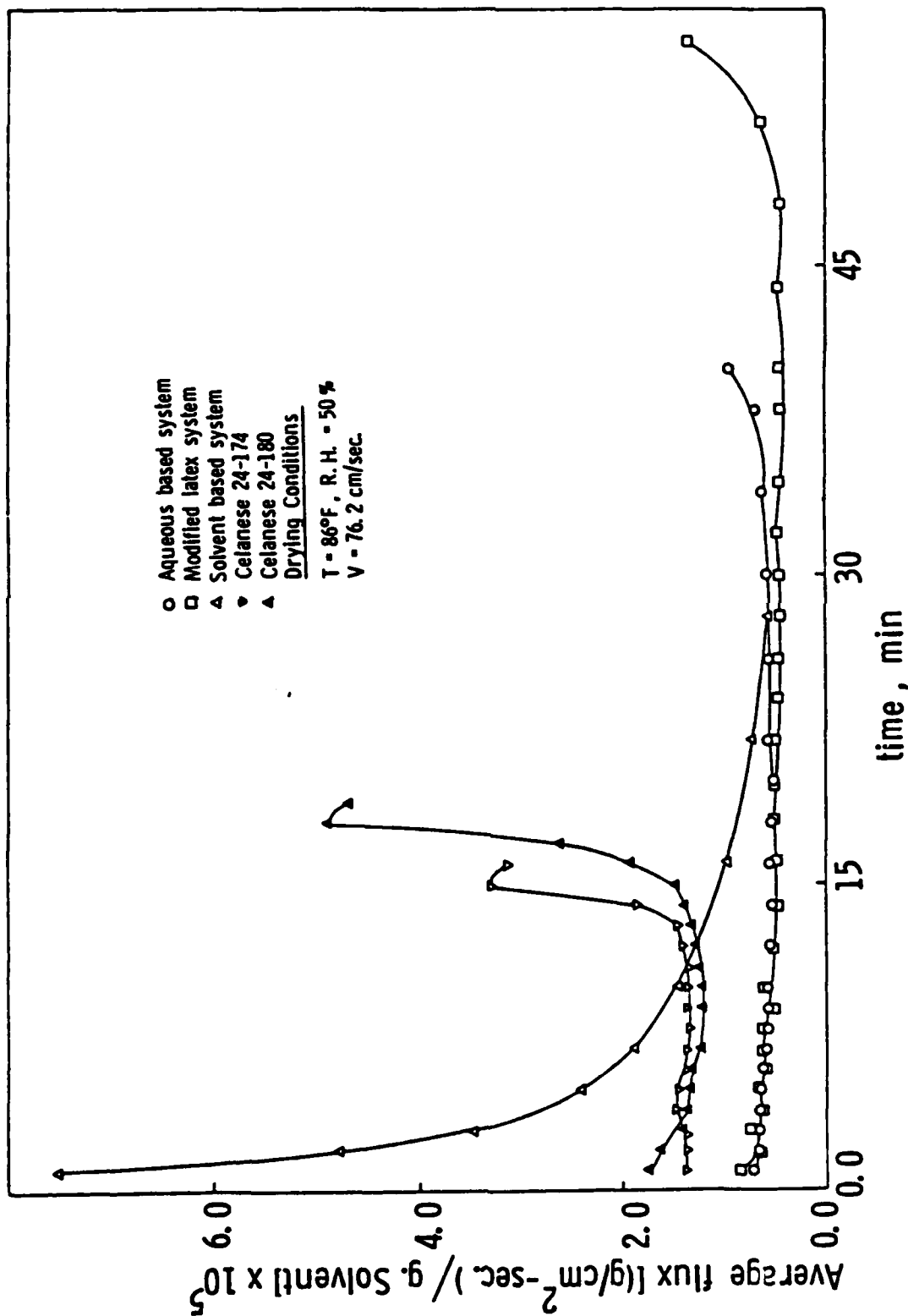


Figure 2. Experimental drying rate (flux vs. drying time for various epoxy-curing agent systems, at temperature $T = 86^\circ\text{F}$, relative humidity R.H. = 50% and air velocity = 76.2 cm/sec.

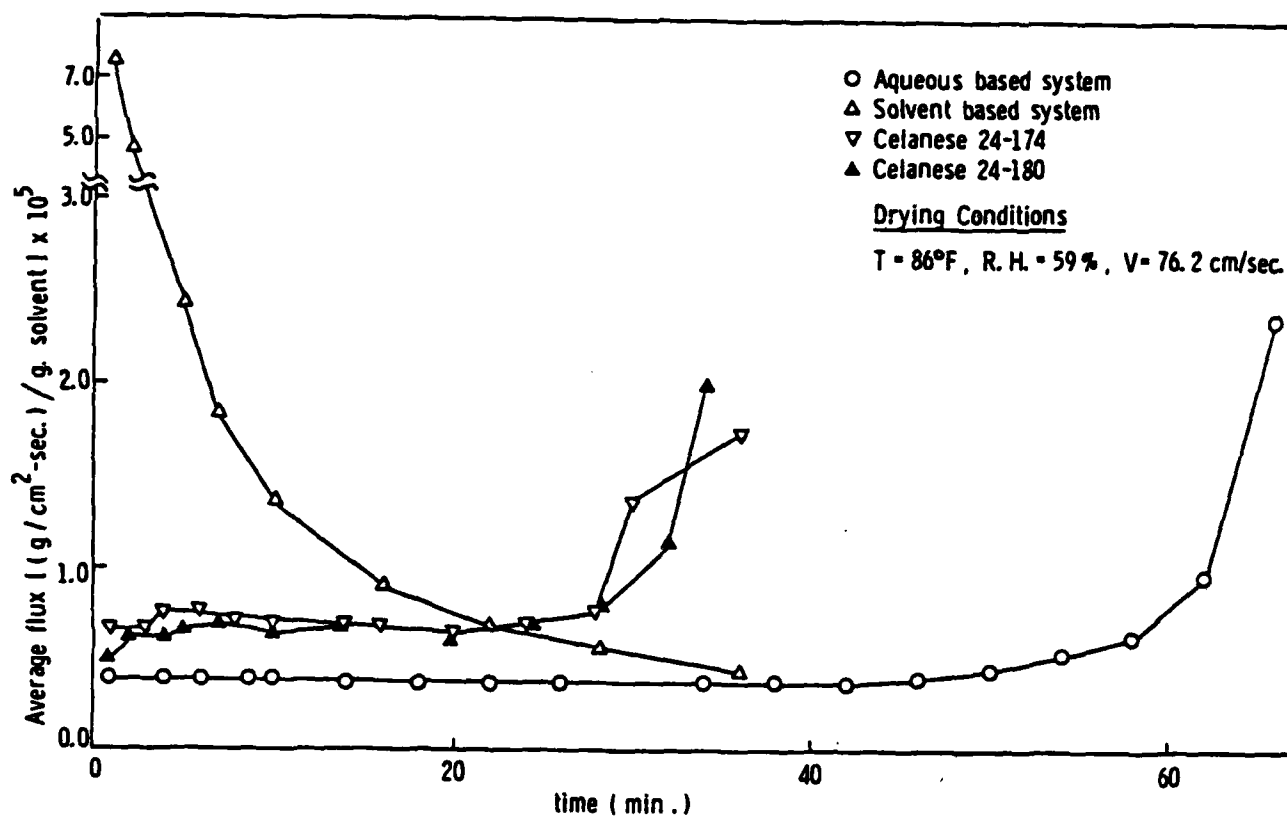


Figure 3. Experimental drying rate (flux) vs. drying time for various epoxy-curing agent systems at temperature T = 86°F, relative humidity R.H. = 59%, air velocity = 76.2 cm/sec.

it is clear from Figures 1-3 that the time required to reach this rupture point increases with increasing relative humidity. Table I summarizes these observations in drying of the four aqueous epoxy systems at three different relative humidities. The increase in relative humidity, at a constant drying temperature (86°F) and air velocity (76.2 cm/sec), results in a decrease in the flux during the initial stage of drying and an increase in the time at which the flux starts to increase in the advanced stages of drying. The magnitude of this effect depends on the epoxy formula used. The time to inflection in the drying curve was always the shortest for Celanese formula 24-174, and the longest for the modified latex system, with the other two formulations in between. This relative behavior is perhaps related to the differences in rate of curing and the way in which stress is built-up in the drying film in the different epoxy formulations. The ruptures in the film surface have been detected by scanning electron microscopy as discussed later.

Instantaneous flux versus drying time curves at 59% relative humidity are shown in Figure 4. The instantaneous flux in case of the Celanese formulations decreased with drying time. However, at the rupture of popping point in the film, the instantaneous flux increased slightly, but remained less than the initial instantaneous flux. On the other hand, the instantaneous flux for the aqueous-based latex system remained almost constant for a long period of time and then increased to a value higher than the initial instantaneous flux, followed by a decrease. These drying results for the latex system while confirming the results of Aremu, however, remain unexplained. The instantaneous flux of the solvent-based system is the highest initially but drops rapidly.

An attempt was made to bring the initial solid contents of the aqueous-based latex and Celanese formulations to the same level and to compare their drying behavior under identical drying conditions. This experiment was infeasible because it was difficult to increase the solids content of the Emerez 1511 emulsion beyond 20% and in case of the Celanese formulations, it was not possible to make a continuous film below 30% solids. Hence the drying fluxes of the Celanese formulations could not be compared with those of aqueous-based latex at the same initial solids. However, drying experiments were carried out on Celanese formulations 24-174 and 24-180, by varying their initial level of solid contents. Figure 5 shows the instantaneous flux of drying Celanese formulation 24-174 and 24-180 at different levels of solid contents under the same drying conditions. It is evident that a higher initial solid content leads to higher drying rates, particularly in the initial stages of drying operation. Another interesting observation was a slight increase followed by a decrease in flux at the end of the drying process, the effect being more pronounced for systems with the lower initial solids. Figure 6 shows the drying rates of Celanese formulations 24-174 and 24-180, with approximately the same initial solids content. Both systems exhibited similar trends in their drying behavior and the values of drying rates were very close. From these results it can be concluded that the initial level of solids does influence the drying characteristics of the coating system.

TABLE I

Effect of Relative Humidity on Initial Flux
and Time to Inflection in Drying Curves of
Aqueous-Born Epoxy Films at T = 86°F and V = 76.2 cm/sec

Epoxy Formula	Percent Relative Humidity	Initial Flux $\left(\frac{\text{g/cm}^2\text{-sec}}{\text{g solvent}}\right) \times 10^5$	Time to inflection (min)
Celanese 24-174	30	2.55	8
	50	1.39	13
	59	0.67	27
Celanese 24-180	30	2.09	9
	50	1.73	15
	59	0.63	27
Aqueous- based Latex	30	1.08	23
	50	0.71	40
	59	0.39	58
Modified Latex	30	1.15	28
	50	0.82	50
	59	-	-

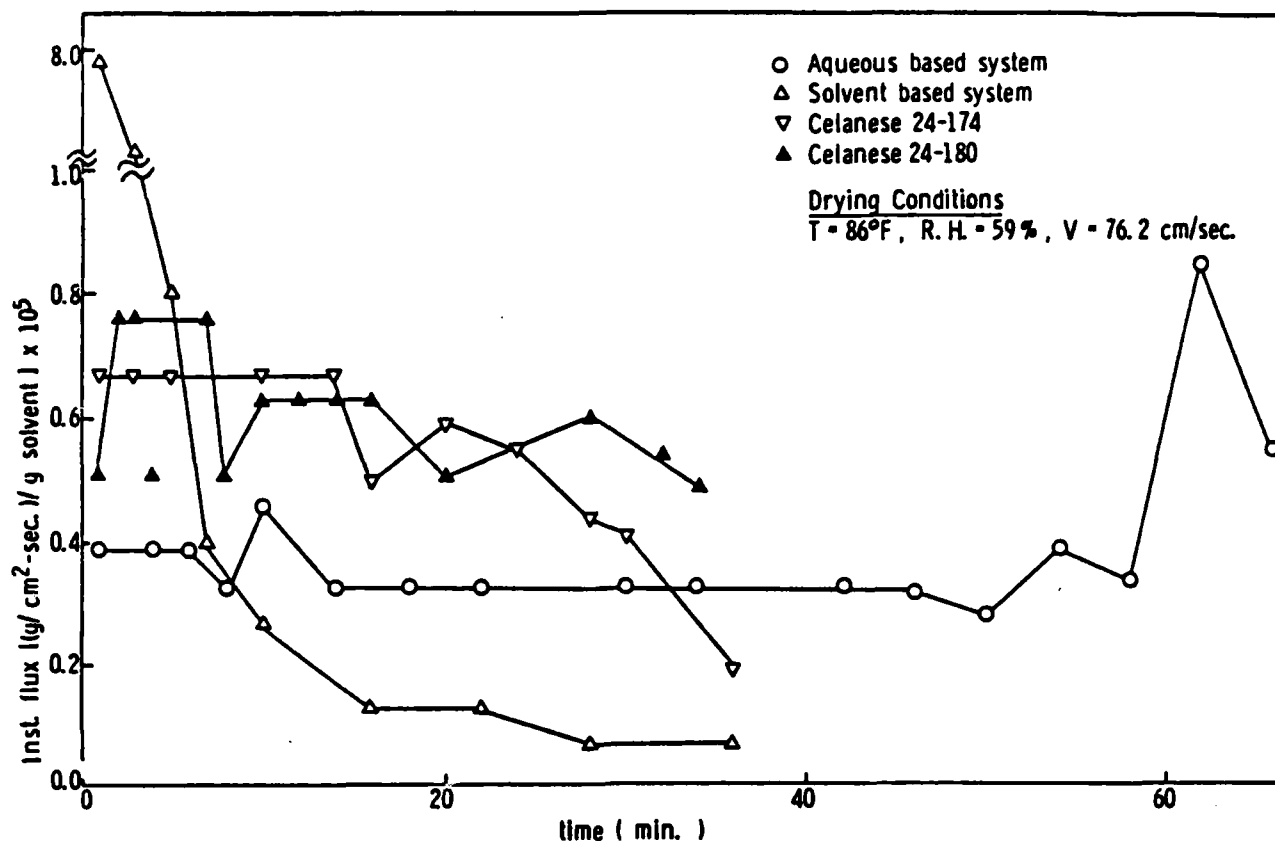


Figure 4. Instantaneous drying rate vs. drying time for various epoxy-curing agent systems at temperature of $T = 86^{\circ}\text{F}$, relative humidity $\text{R.H.} = 59\%$ and air velocity = 76.2 cm/sec .

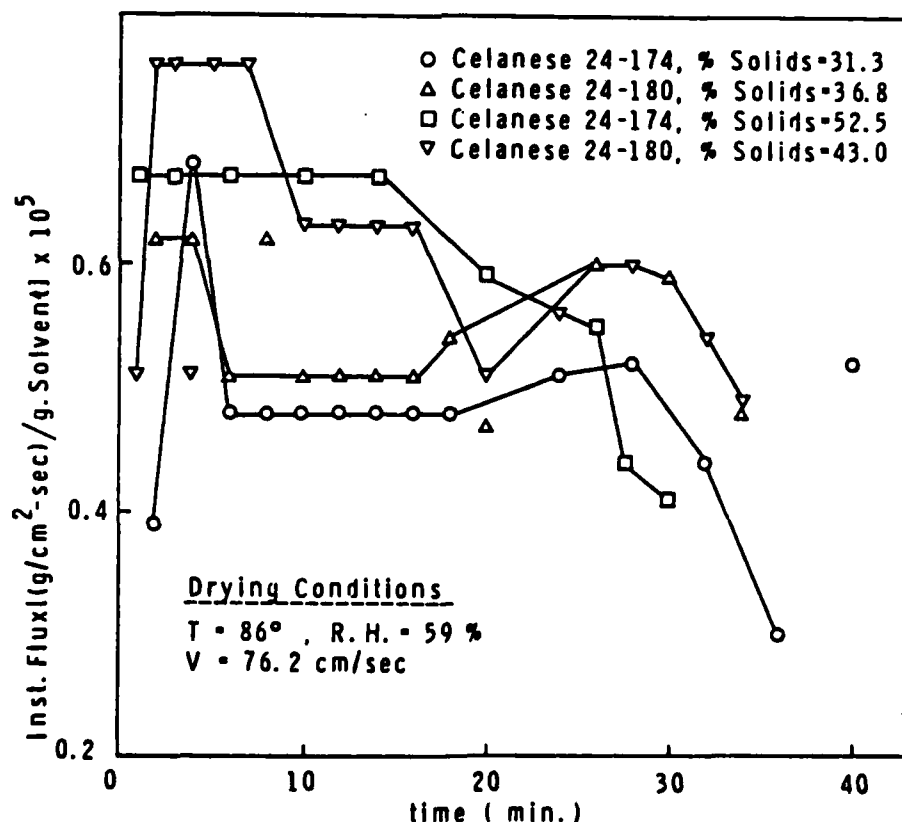


Figure 5. The effect of initial percent solids on the instantaneous drying rate vs. time for two commercial epoxy-curing agent aqueous-based systems at temperature $T = 86^{\circ}\text{F}$, relative humidity $\text{R.H.} = 59\%$ and air velocity 76.2 cm/sec .

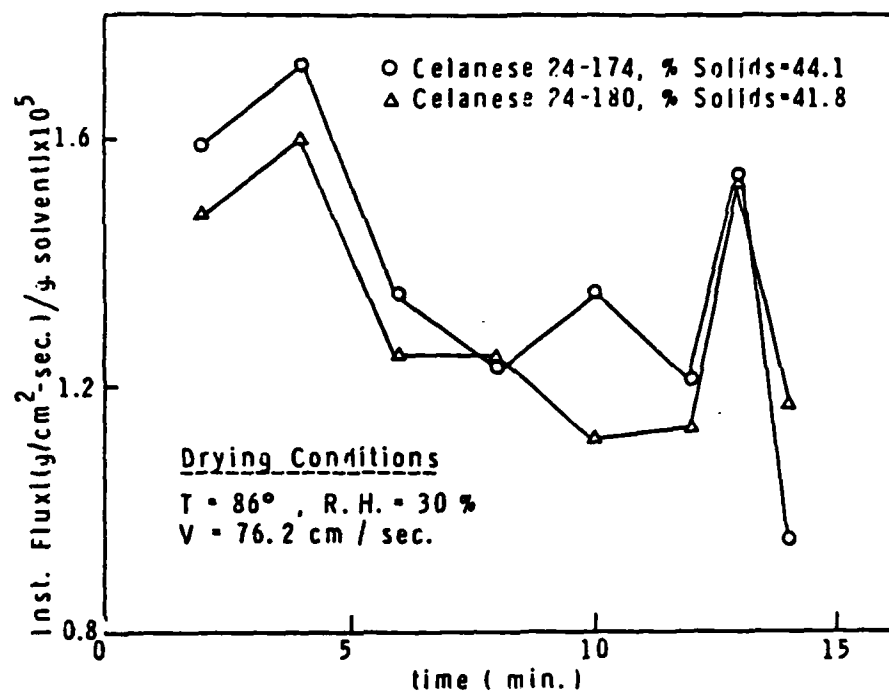


Figure 6. Drying curves for the two commercial epoxy-curing agent systems at roughly equal initial percent solids.

Morphological Studies. The surface morphology of all the five epoxy systems, dried at a temperature of 86°F, air velocity 76.2 cm/sec and relative humidity 59%, was studied using the scanning electron microscope. The film specimen to be observed was cut with a blade, peeled off the glass plate, attached to the metallic stub and coated with gold/palladium before examination under the microscope. The solvent-based films were transparent, strong, and had the strongest adhesion to the glass substrate, whereas the films from aqueous-based latexes were milky, brittle, and had a comparatively lower adhesion to the substrate. Films from the Celanese formulations 24-174 and 24-180 had fairly good adhesion to the glass substrate and were more transparent compared to the aqueous-based latexes. All the films showed some degree of sensitivity to the high temperature encountered during the microscopic examination, particularly at higher magnifications. Films from the solvent-based and Celanese formulations exhibited higher resistance to the electron beam damage as compared to the aqueous-based latex films.

The surface morphology of films cast from the aqueous-based latex, and the solvent-based systems and Celanese formulations 24-174 and 24-180 at the far end of the drying plate, are shown in Figures 7, 8, 9 and 10, respectively.

Differences were observed in the surface morphology of the films formed from various epoxy resin-curing agent systems. Micrographs of the films made from aqueous-based latexes and aqueous-based modified Celanese formulations showed cracks and a rough surface. The surface of the film from Celanese formula 24-180 is smoother and had a fewer number of cracks as compared to Celanese formula 24-174. However, the films from the solvent-based system showed very little or no cracking and were comparatively smoother.

Little variation existed in the surface smoothness and cracking tendency of the same film as a function of the distance from the leading edge. Almost all the water-based systems, i.e., aqueous-based latexes and aqueous-based modified Celanese formulations exhibited rougher surfaces and a greater number of cracks in the film close to the leading edge. This effect was not observed in the films made from solvent-based solutions where the film at the leading edge and far end of the drying plate were similar in appearance. Films at the leading edge are subjected to more drastic drying and, therefore, lose water earlier than the film at the far end which dries at the end of the drying operation. It appears that mild drying conditions yield better film formation in terms of better smoothness and lesser number of cracks for aqueous-based latexes and aqueous-based modified Celanese formulations. The morphological studies will be continued to gain more quantitative correlations between the drying conditions and film appearance and defects.

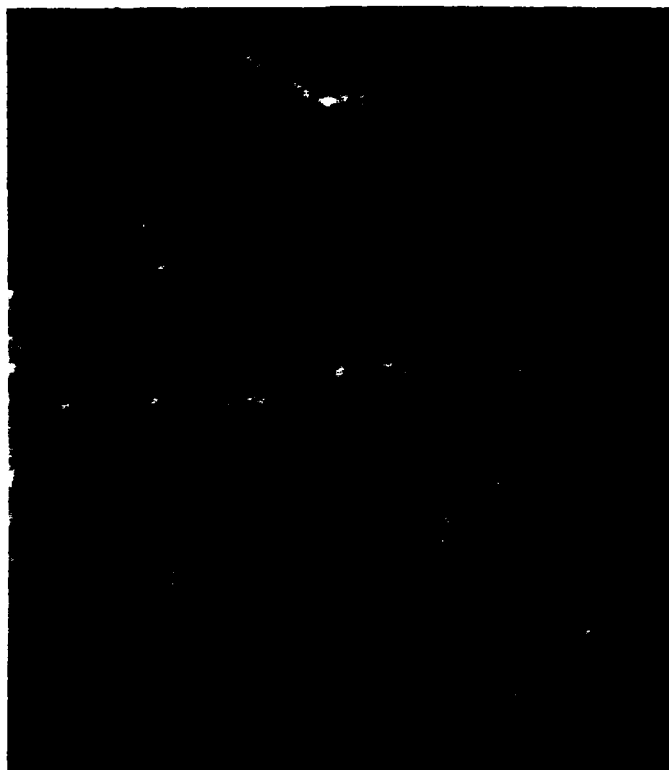


Figure 7: Surface morphology of aqueous based latex system at the far end of drying plate



Figure 8: Surface morphology of solvent based system at the far end of drying plate.



Figure 9: Surface morphology of Celanese Formula
24-174 at the far end of the drying plate.



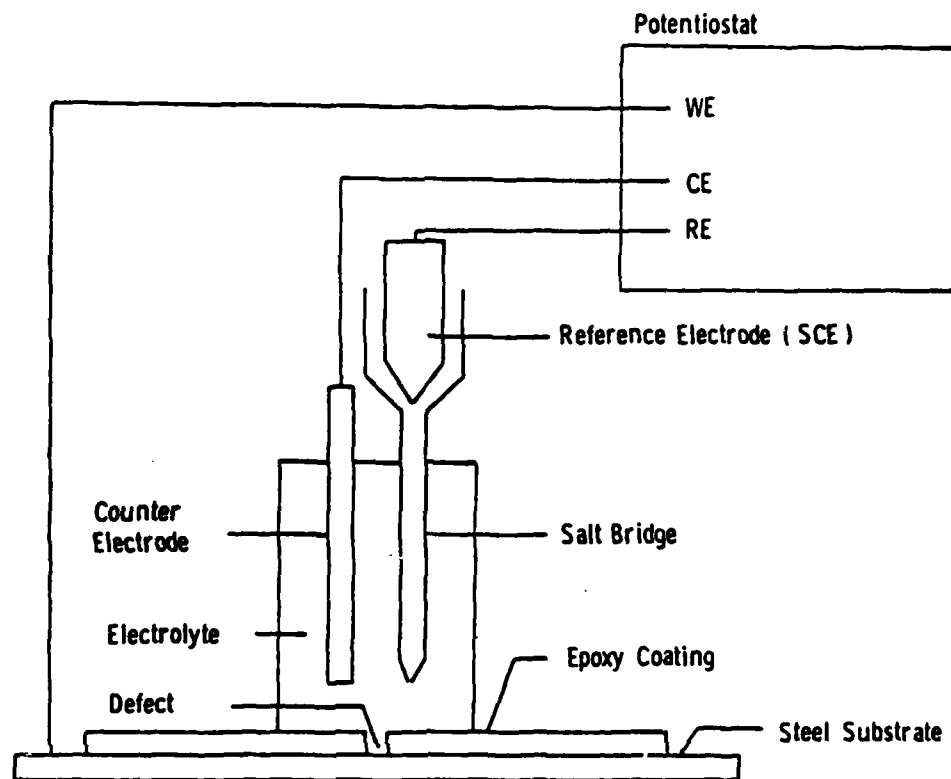
Figure 10: Surface morphology of Celanese Formula
24-180 at the far end of the drying plate.

Corrosion Protection Performance. The second phase of this study has been initiated during this period to evaluate the corrosion protection performance of different epoxy resin-curing agent systems and to correlate the morphology and corrosion resistance of these systems as a function of their drying behavior and curing time. To expedite this phase, films were dried on steel panels, 6 inches long, 4 inches wide and 0.02 inches thick supplied by the Q-Panel Company, Ohio. The panels selected for this study are of the type QD with smooth finish. The sample preparation involved degreasing the panels with trichloroethane followed by grinding with a 600 grit silicone carbide grinding paper and finally washing with distilled deionized water and methanol.

Films from different epoxy systems were cast on steel panels using a 10 mil gap draw-down applicator. These films were dried under known conditions of temperature, relative humidity and air velocity, in the drying tunnel. The cathodic delamination technique [3] was used to evaluate the corrosion protection performance of these systems. The test is based on the principle that a coating delaminates in the vicinity of a coating defect when the metallic substrate is made a cathode while immersed in an electrolyte. Just before the test is initiated, the coating is damaged by pressing a pointed instrument into its surface. The exposed substrate was approximately 0.003 inch² in area.

The experimental arrangement is shown schematically in Figure 11. The cathode potential was sensed relative to a saturated calomel electrode (SCE). All measurements were made in 0.5 M NaCl. The potential of the cathode was held constant at -1.5 during the experiment by means of a potentiostat, monitored continuously with a voltmeter. After a number of trials, the duration of the delamination experiment was selected to be eight hr. The delaminated area was determined after the completion of the experiment by pressing a piece of adhesive tape against the surface and measuring the area that was removed.

Films from the solvent-based system and Celanese formulations 24-174 and 24-180 were dried at a temperature of 86°F, relative humidity 59% and air velocity 76.2 cm/sec. Due to the difference in the level of solid contents of different systems, films of different thicknesses were obtained. Film thickness from solvent-based system, and Celanese formulations 24-174 were in the range of 1.9-2.1 mil, and the film thickness for Celanese formulations 24-180 was in the range of 0.9-1.1 mil. It was found that films from the Celanese formula 24-174 were most resistant to cathodic delamination while films from the solvent-based system were least resistant and Celanese Formula 24-180 was intermediate between the two. If the film surface at the defect was pulled immediately after the delamination experiment, a greater area of film was delaminated than could be seen visually by change in color of the delaminated film. It was, therefore, decided to determine the delaminated area one day after the delamination experiment. It was also observed that some delamination of the film occurred around the defect when it was immersed in the electrolyte for



Schematic diagram of experimental arrangement.

Figure 11. A schematic diagram of the experimental arrangement used in the Cathodic Delamination Technique for testing corrosion protection performance.

eight hr in the absence of an applied cathodic potential except for Celanese formulation 24-174. However, no delamination of film took place when the film was pulled with an adhesive tape in case of samples that were not exposed to the electrolyte or cathodic potential.

FUTURE WORK

1. To compare the corrosion protection performance of different epoxy films at the same film thickness.
2. To study the morphology and resistance to cathodic delamination as a function of curing time and drying characteristics of epoxy films.
3. To initiate work on the pigmented-epoxy systems: drying curves, morphological studies and corrosion protection performance.
4. To initiate work on polyurethane coatings - drying curves, morphological studies and corrosion protection performance.

REFERENCES

- [1] T. Tmai and K. Tsubowchi, J. Coatings Technol 52, No. 666, (1980).
- [2] B. Aremu, M. S. Thesis, Lehigh University (1981).
- [3] H. Leidheiser, Jr. and W. Wang, J. Coatings Technol. 53, No. 672, 77-84 (1981).

Program #10. Cathodic Electrodeposition
of Polymer Latexes

ABSTRACT

Cathodic electrodeposition is an electrochemical process employed in applying protective coatings on metal substrate, with the advantage of obtaining very uniform film thickness even on recessed areas, as well as superior inherent qualities in corrosion protection. Cathodic electrodeposition from latex-based coating systems offers the added advantages over the solubilized polymer-based systems, of less electrical energy requirements and producing coatings films with much less water sensitivity. This program deals with the deposition behavior of cathodic electrodeposition from latex-based coatings.

The kinetics of film growth were studied during the cathodic electrodeposition process of single-component Epon 1001 latex and a mixture of two-component Epon 1001-amine curing agent latex system. The current-time curves generated at constant applied voltage were analyzed to calculate the mass of deposited film vs. time relationship and the coulombic efficiency of deposition from these latex systems was found to be high, 60-98 mg/coulomb; 3-8 times higher than the reported coulombic efficiency of polymer solubilized systems. A linear relationship was established between the mass of deposited film and deposition time, indicating that the presence of the film does not affect continued film growth. A mechanism was proposed for the cathodic electrodeposition of latex particles, which involved nonionic accumulation of the particles at the cathode followed by coalescence of the particles under the effect of the electrical pressure.

A polyurethane-modified acrylic graft copolymer cationic latex system was prepared by a three-step-process involving solution polymerization, emulsification and emulsion polymerization. Studies on the cathodic electrodeposition behavior of this latex have been initiated. The kinetics of the electrodeposited film growth at constant applied voltage were determined.

Current-time curves at constant applied voltages have been generated over a range of voltages 50-225 v, and the coulombic efficiency for deposition has been calculated. Much better coating films were produced with this polyurethane latex system compared to the epoxy latex. The well-behaved polyurethane latex system lends itself to a more quantitative analysis of important electrodeposition process parameters such as, percent solids in the bath, surface charge density of the particles, pH and agitation.

INTRODUCTION

Cathodic electrodeposition is an electrochemical process employed in applying protective coatings on metal substrates. The cationic coatings material migrates under the influence of an external electric field and deposits on the cathode, which is the metal object to be coated. Owing to the superior inherent qualities in corrosion protection of the cathodically deposited coatings over those deposited anodically, cathodic electrodeposition has recently assumed major commercial significance in the industrial and automotive areas. Most of the fundamental studies of electrodeposition were carried out on solubilized polymer resin systems electrodeposited cathodically or anodically. In contrast, information on the kinetics of cathodic electrodeposition of polymer latexes is practically nonexistent. Wessling et al. [1] have reported on the cathodic electrodeposition of quaternary ammonium ions stabilized latexes. However, the kinetics aspect of the process was not dealt with.

Electrodeposition of latex-based coatings has the advantage of less electrical energy consumption requirement by one order of magnitude compared to the polymer solubilized-based coatings. Also, one has the advantage of being able to use polymer latexes with much higher molecular weight, and much fewer functional groups, than in the case of solubilized polymer-based coatings, thus producing coatings films with much less water sensitivity.

Overall Objectives

1. To determine the kinetics of film growth during the cathodic electrodeposition process of aqueous latex systems as corrosion resistant coatings.
2. To study the mechanism of film formation from latex systems during the cathodic electrodeposition process.

3. To study the morphology and corrosion protection performance of cathodically electrodeposited coating films.

Summary of Progress to Date

During the first two years on this program, studies were conducted on the kinetics of film growth during the cathodic electrodeposition process of a single-component Epon 1001 latex, as well as of a mixture of two-component epoxy-amine curing agent latex system. The cationic latex systems were prepared by direct emulsification using mixed emulsifier systems. The electrodeposition experiments were conducted under constant applied voltage using a cold-rolled steel plate as the cathode and two carbon rods as anodes. The current-time curves were recorded and the weights of film deposited during a given time were determined gravimetrically. The data were analyzed to generate mass-time relationships and the coulombic efficiency of deposition. The effects of applied voltage in the range of 80-280 v, temperature rise in the film, and agitation on the electrodeposition process were studied.

The coulombic efficiency from the two different latex systems were in the range of 60-98 mg/coulomb, which is 3-8 times higher than the reported coulombic efficiency of polymer solubilized systems. The mass of the deposited film increased linearly with time, with two different deposition rates; an initial high deposition rate followed by a much lower deposition rate. The increase in the applied voltage increased the rate of deposition in the initial step and had no effect on the second step. The second slow rate deposition step is due to the consolidation of the deposited film. The linear relationship between the mass of deposited film and time is taken as an indication that the presence of the film does not affect continued film growth. Consequently, a mechanism was proposed for the cathodic electrodeposition of latex particles which involves the accumulation of particles at the cathode and initiation of coalescence between the particles under the effect of the electrical pressure. This proposed mechanism is in contrast to the ionic mechanism, which is proposed to explain the deposition from solubilized polymers. In this mechanism, neutralization of the cationic functional groups on the polymer backbone takes place by reaction with the anionic hydroxyl ions generated at the cathode followed by flocculation of the coatings material on the cathode. These are basic differences because the mechanism determines the different process parameters which must be controlled. For example, the particle concentration and electrophoretic mobility should have a strong influence on the electrodeposition based on the accumulation mechanism, but will have no effect on electrodeposition based on the flocculation mechanism.

The electrodeposition of the two-component epoxy-curing agent latex system was found to be complicated by the concurrent occurrence of heteroflocculation between the particles of the two

components and a crosslinking chemical reaction at the particle's interface. The occurrence of these two phenomena made it difficult to carry out a detailed quantitative description of the electrodeposition process. Consequently a decision was made to develop a single-component polyurethane latex system for cathodic electrodeposition.

A polyurethane-modified acrylic graft copolymer cationic latex system was prepared by a three-step process involving solution polymerization, emulsification and emulsion polymerization. Studies of the cathodic electrodeposition of the above latex have been initiated during this period. The kinetics of the electrodeposited film growth at constant applied voltage have been studied.

Progress

Our efforts during the past year were directed toward the following:

1. Completing the interpretation of the kinetic data of film growth from cathodically electrodeposited epoxy-curing agent latex mixture.
2. Preparation and characterization of a cationic latex system from polyurethane-modified acrylic graft copolymer.
3. Studies of the cathodic electrodeposition process from the cationic polyurethane latex system.

Cathodic Electrodeposition of Epoxy-Curing Agent Latex System

A Master's Report entitled "Kinetics and Mechanism of Cathodic Electrodeposition of Epoxy Latexes" was completed by Arif Humayun in January 1982 and accepted by the Department of Chemical Engineering. The report's abstract is summarized as follows:

Most of the fundamental studies of electrodeposition have been carried out with polymer resins that are solubilized with acids or bases, rather than with discrete particles such as latexes. Solubilized polymer resins, when electrodeposited, coalesce easily to form a coherent film which is resistant to the passage of electricity. In contrast, the process of film formation by electrodeposition from a dispersion is more complex, and may be the result of an entirely different mechanism. While the mechanism of film growth from solubilized systems electrodeposited anodically has been fairly well studied, information on the kinetics

of cathodic electrodeposition of polymer latexes is practically nonexistent.

In the present studies, the kinetics and mechanism of film growth during the cathodic electrodeposition process at constant voltage of an epoxy latex were investigated. Experimental data showed that film growth at the beginning was fast and strongly dependent upon the applied voltage. The film was conducting at this stage. A more gradual growth rate followed at longer deposition times, a fact suggestive of consolidation and compaction of the deposited film. During the second stage of film growth, the rate of growth was independent of the applied voltage and the film became more insulating. The current density field strength relationship was non-ohmic in nature. The film mass (or thickness) increased linearly with deposition times for both stages. A qualitative explanation of the experimental observations in terms of a "concentration-accumulation" mechanism was attempted.

Investigation of the kinetics of film growth from epoxy resin-curing agent latex mixtures was also carried out. In contrast to the epoxy latex system, the film mass for the two-component system was directly proportional to the deposition time. However, the overall behavior of the two-component system was not as straightforward as the single component system. The kinetics of deposition could perhaps be complicated by the concurrent heterogeneous flocculation of the mixed latex particles and the chemical reaction of the epoxide and amide groups.

An attempt was made to explain the mechanism of film formation from this system also by the "concentration-accumulation" mechanism. This mechanism involves the formation of a fixed layer of coalesced polymer particles next to the cathode, and a fluid layer of uncoalesced particles which could be re-dispersed. The initiation of coalescence between the particles in the fixed layer is the result of the "electrical pressure" associated with the fluid layer. Weights of the film deposited at the cathode were found to decrease to a limiting value when the films were left in the bath with the current turned off (following deposition). Redispersion of the particles from the fluid layer back into the deposition bath was indicated. A mass balance of emulsifier concentration in the coating bath before and after deposition also supported the above mechanism.

Preliminary studies on the morphology of the deposited films indicated that temperature buildup within the film during deposition affects the coalescence of the polymer particles.

Preparation and Characterization of Cationic Polyurethane Latex

The latex system currently under investigation is a polyurethane-modified acrylic graft copolymer. A sample recipe used for the preparation of this latex is shown in Table I. The preparation of this latex involves a three-step process, comprised of a solution polymerization step, an emulsification step, and subsequent emulsion polymerization [2]. In the first stage, a solution of isophorone diisocyanate (3-isocyanatomethyl-3,5,5-trimethyl cyclohexyl isocyanate, Veba Chemie, AG), 2-hydroxy propyl methacrylate (2-HPMA), butyl acrylate, and isobutyl methacrylate is prepared. Isophorone diisocyanate has two differently combined isocyanate groups, with the aliphatic isocyanate group about ten times as reactive as the cycloaliphatic one. Consequently, one of the isocyanate groups may be specifically reacted with the active

Table I

Polyurethane-Modified Acrylic Latex Recipe

<u>Component</u>	<u>Moles</u>	<u>Unit Wt. %</u>
2-Hydroxy Propyl Methacrylate	1	4.0
Isophorone Diisocyanate	3	17.5
Polyol PCP-0200	2	27.8
Butanol	1	2.1
Butyl Acrylate	4.6	15.4
Isobutyl Methacrylate	8.4	31.2
Acrylic Acid	1.1	<u>2.0</u>
		100.0

Distilled Deionized H₂O - 400 gm.

Hexadecyl Trimethyl Ammonium Bromide (3% based on monomer) - 3 gm

Hexadecane (4% based on monomer) - 4 gm.

hydroxyl of the 2-HPMA while leaving the second isocyanate available for further reaction. The reaction is accomplished by adding dibutyl tin dilaurate, a low-temperature catalyst, to the solution and agitating at 60°C for 1/2 hr. The system is inhibited with phenothiazine to prevent bulk free radical polymerizations of the vinyl groups at this stage. Following the reaction of a portion of the isophorone diisocyanate with the 2-HPMA, a caprolactone diol (Polyol PCP-0200, Union Carbide) is added to the solution and reacted with the isophorone diisocyanate for 1 hr at 80°C. This solution then consists of urethane prepolymer with a calculated MW of ≈ 2000 terminated at one end with a reactive vinyl group, dissolved in a monomer solution of butyl acrylate and isobutyl methacrylate. The solution is then cooled, and 2% hexadecane (based on total monomer) is added.

The second stage of the synthesis route involves emulsification of the above monomer solution by essentially the same technique used in the formulation of the Epon 1001 emulsions [3] and consists of preparation of a crude emulsion, followed by sonification and homogenization to yield a stable emulsion.

The final preparation stage consists of free radical emulsion polymerization of the resulting emulsion. The emulsion is added with agitation to a solution of initiator and surfactant at 60°C over a period of four hr. In this synthesis route, a water soluble azo-type free-radical initiator, V-50 (2-2'-azobis (2-amidino-propane) HCl, Crescent Chemical Co.) is used, which imparts a positive (bound) charge to the latex particles. Following addition of the monomer solution, the reaction is continued at 60°C for another 12 hr, resulting in essentially complete conversion. Finally, the latex is vacuum stripped to remove any residual monomer, and the solids adjusted to the desired level.

Several variations on this process have been examined, including elimination of the pre-emulsification step and addition of the initiator solution to the monomer emulsion. However, large amounts of coagulum were obtained upon polymerization with the above modifications. Consequently the original process outlined earlier appears to be the most effective in producing stable polyurethane latex. An additional variation was attempted by substitution of an oil-soluble initiator (lauroyl peroxide) for the azo-type. In this method, the initiator is dissolved in the prepolymer solution prior to emulsification, and initiation takes place in the monomer emulsion droplets as the temperature is raised to the polymerization temperature of 60°C. This method of initiation is advantageous in that it does not affect the charge of the particles, thus simplifying the characterization of the surface charge density and the specific area of surfactant molecules adsorbed on the latex particles.

Along with the variation in the polymerization process, the composition of the acrylic (main) polymer chain has been varied, while holding the ratio of acrylic to polyurethane graft constant at 1:1 (W/W). The original formulations of the polyurethane-modified acrylic polymer latex yielded glassy, brittle films which

did not adhere well to the carbon steel substrate. Two percent acrylic acid (based on monomer) was added to the formulation, and the adhesion was found to improve significantly. It has been reported that the glass transition temperature (T_g) of a polymer greatly affects its electrodeposition performance, and that for optimal performance the polymer should be marginally film-forming at deposition temperature [4]. The ratio of butyl acrylate to isobutyl methacrylate BA/IBMA was varied; and good films (flexible, not tacky, not glassy) were obtained by drying at room temperature with a weight ratio of 27:63 BA/IBMA (the remaining 10% of the acrylic chain consisting of acrylic acid and 2-HPMA).

Complete characterization of the polyurethane-modified acrylic latex is essential to the understanding of the electrodeposition behavior of this system. As a first step in this characterization, the average particle size and size distribution of the polyurethane latex was determined using cold-stage transmission electron microscopy. Since the acrylic portion of the polymer is transparent to the electron beam, staining with phosphotungstic acid was necessary prior to examination of the latex particles. As can be seen in Fig.1, the latex has a relatively broad particle size distribution, with a number average particle diameter, D_n , of 63 nm, and a polydispersity index (D_w/D_n) of 1.49.

Differential scanning calorimetry (DSC) was used to determine the glass transition temperature (T_g) of an air-dried sample of the polyurethane latex. The sample was scanned twice from 200°K to 400°K, at heating rates of 20°C/min and 10°C/min. Essentially identical profiles were obtained for the two runs. A broad T_g was observed, spanning from 250°K (-23°C) to 305°K (32°C). This broadened T_g could indicate that some phase separation is occurring in the polymer system; however, more work will be required in this area to determine the cause conclusively.

An attempt was made to determine the specific area of adsorption for the HDTMAB-surfactant molecules on polyurethane-modified acrylic polymer latex particles. This calculation is made by determining the surfactant concentration in the latex serum, and then applying a mass balance on the total surfactant. The serum replacement technique was used for this analysis. This technique involves separation of the latex serum by pumping water through a latex sample confined in a cell with a Nuclepore filter, and measuring the concentration of surfactant in the effluent stream [5]. Problems have been encountered with the soft latex particles blocking the Nuclepore filter (forming, essentially, a "filter cake" of coagulated polymer); however, it is expected that inverting the cell and lowering the latex solids will help prevent this difficulty.

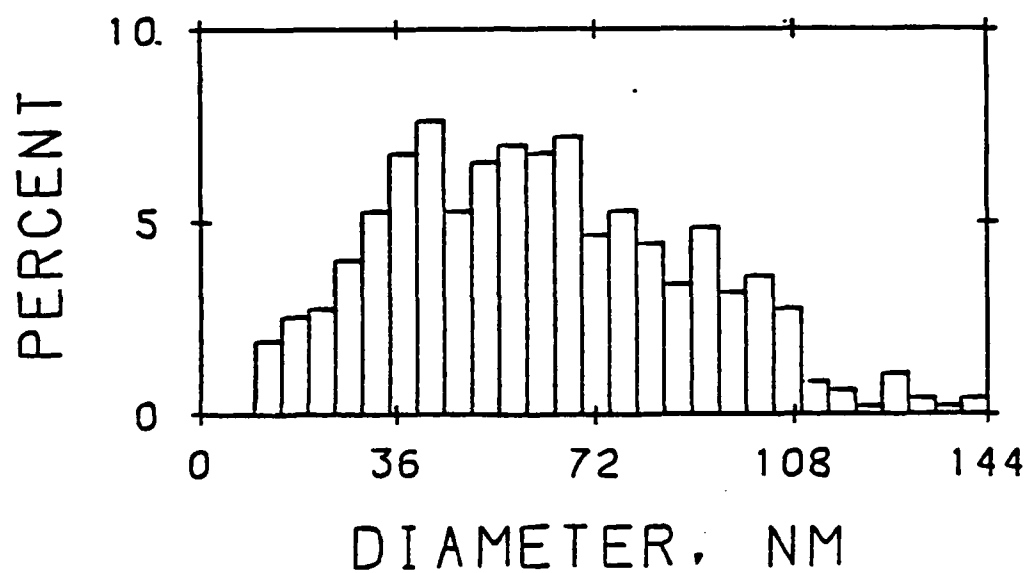


Figure 1. Histogram of polyurethane-modified acrylic latex particle size distribution.

Cathodic Electrodeposition of Cationic Polyurethane Acrylic Latex

During this report period studies of the electrodeposition behavior of the single-component polyurethane acrylic latex have been initiated. Cold-rolled steel sample plates were coated with the latex at applied constant voltages ranging from 50 to 250 v. and for periods of 2 sec to approximately 30 sec (to current cutoff). The latex solids content in the deposition bath was constant at 10%, and a fresh latex sample was used for each deposition. Following each electrodeposition experiment, the coated sample was dip-rinsed with deionized water and dried at room temperature under vacuum to constant weight. Coating thicknesses were measured with a micrometer and averaged over the coated area.

The current-time behavior of the polyurethane latex deposited until current cutoff at various applied voltages may be seen in Figure 2. The shapes of the current-time curves depend strongly on the deposition voltage. At low voltage the film remained conducting for a longer time, as is evident from Figure 2a; the current was relatively constant at 0.18 A for a period of 8 sec, after which it slowly decreased to a constant value of 10 mA. As the applied voltage was increased, the maximum current increased and the current cutoff took place at a progressively shorter time indicating that the formation of an insulating film was more rapid (Fig. 2:a-g). The current-time curve for the highest applied voltage tested (225 v, Fig. 2, curve g) shows a smooth, rapid current cutoff, thus no film rupture occurred. For this series of applied voltages, the optimum (in terms of rapid current cutoff, high coulombic efficiency, and good film quality) was 225 v. By merely raising the applied voltage, a uniform coating with fully coalesced particles and smooth surface is obtained as shown in the scanning electron micrograph in Figure 3.

The film weight deposited as a function of applied voltage was also examined for this series of coated samples. As can be seen in Table II, raising the voltage from 50 v to 225 v caused the film thickness to decrease uniformly from 16.7 mil to 11.1 mil, while the time to current cutoff decreased from 30 sec to 8 sec. These data appear to conflict with those reported earlier for the Epon 1001 single-component latex system [6]; however, deposition was ended prior to current cutoff in these earlier tests and, therefore, the reported film thickness reflects the different rate of growth at different voltages, not the ultimate film thickness. As observed with the polyurethane system under examination, at higher voltages the film becomes insulating much more rapidly than at the lower voltages, and the ultimate film buildup was consequently reduced. The residual amperage (the small current remaining after "cutoff") increased very slightly with increasing applied voltage, varying from 10 mA at 50 v to 20 mA at 225 v. This slight increase can be explained by realizing that in all cases the film did become insulating and a higher applied voltage would naturally result in a higher residual current.

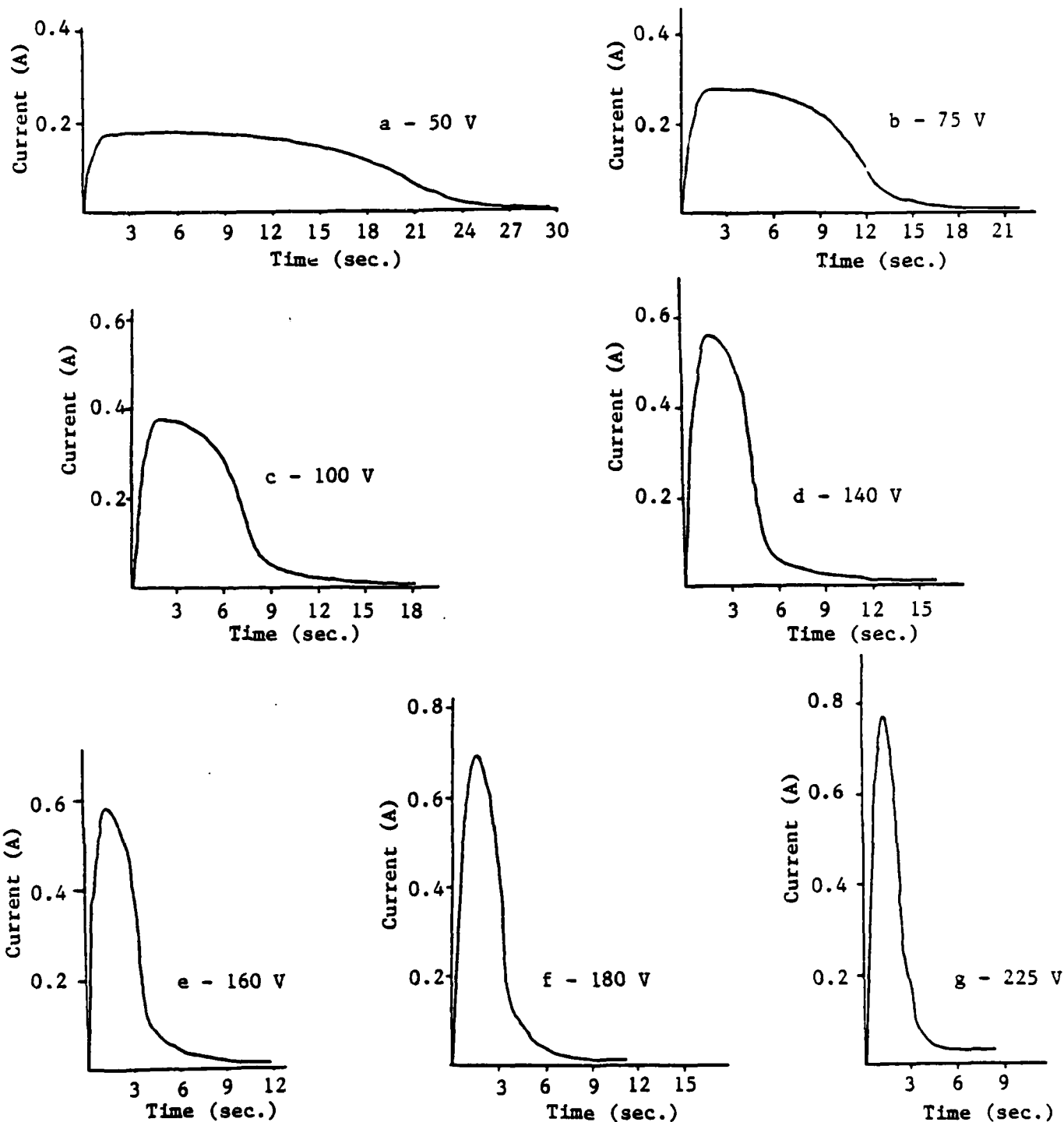


Figure 2. Current-time curves for cationic polyurethane latex deposited at constant initial bath solids of 10% and constant applied voltage of: (a) 50 v; (b) 75 v; (c) 100 v; (d) 140 v; (e) 160 v; (f) 180 v; and (g) 225 v.

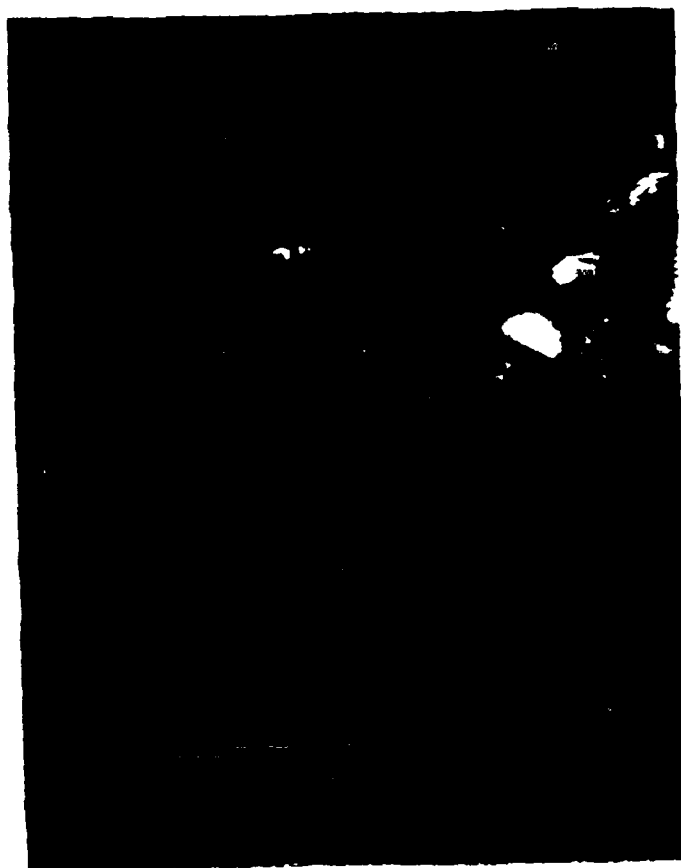


Figure 3. Scanning electron micrograph of polyurethane acrylic latex deposited at 200 v. Magnification = 2000 X.

Table II

Mass of Film Deposited and Film Thickness as a Function
of Deposition Voltage for Polyurethane Acrylic Latex.
Deposition Continued to Current Cutoff

<u>Applied Voltage, v</u>	<u>Time to Current Cutoff, s</u>	<u>Thickness, mil</u>	<u>Film Mass, mg/cm²</u>
50	30	16.6	19.1
75	21	15.6	18.4
100	19	15.7	18.5
120	17	14.6	18.0
140	16	12.6	16.0
160	15	12.1	15.2
180	12	11.2	14.2
200	10	11.1	13.7
225	8	11.1	13.4

A series of depositions was performed at 200 v starting with 10% solids in the bath, reusing the same latex bath without readjustment of the solids in order to observe the effect of multiple deposition on the electrodeposition behavior. The current-time curves for these multiple depositions are shown in Figure 4. The maximum current and the time to current cutoff both are seen to increase with increasing number of depositions from the same bath. In addition, the residual amperage increased from 20 mA in the 1st deposition, to 80 mA in the 7th deposition. Film rupture also begins to occur by the 4th deposition, as indicated by the second peak in the current-time curve, after the initial current cutoff (curves c & d, Fig. 4). This rupture of the film is a result of the increased gassing that occurs with multiple depositions from the same bath; the effect of gassing on the film morphology can be clearly seen in Figures 5 and 6. As deposition takes place, the emulsifier molecules associated with the depositing latex particles desorb and are redispersed, thus increasing the concentration of the emulsifier in the bath. The film rupture, increased gassing, and current-time behavior of the multiple depositions occur due to the higher bath conductivity associated with the redistribution of the emulsifier molecules during deposition and subsequent increased emulsifier concentration in the bath.

The coulombic efficiency, defined as the mass of polymer deposited per coulomb of charge passed, was calculated for the deposition of the polyurethane acrylic latex under various deposition conditions. As shown in Table III, the coulombic efficiency increased slightly as the applied voltage was increased from 50 to 200 v. This increase in coulombic efficiency may be a result of the more rapid current cutoff that is observed at higher voltages. The film is deposited and becomes insulating before the conductivity of the bath is raised significantly by the desorption of emulsifier from the deposited particles. The coulombic efficiency was also calculated for the series of depositions made from the same bath at 200 v and given in Table IV. From Table IV it is apparent that the increasing bath emulsifier concentration associated with multiple depositions causes a significant decrease in the coulombic efficiency; by the 7th deposition from the same latex sample, the coulombic efficiency has dropped 28% below the initial value.

For comparison the coulombic efficiency was also determined for a commercial cathodic electrodeposition coating system (PPG Cationic Electrodeposition Primer). The commercial system gave a much lower maximum current and more rapid current cutoff than the polyurethane latex (Fig. 7), resulting in a much thinner deposited film (0.25 mil). The coulombic efficiency of electrodeposition for the commercial coating ($E_{app} = 150$ v), was only 30 mg/coul, compared to 75 mg/coul for the experimental latex system.

The kinetics of electrodeposition for the polyurethane modified acrylic latex were determined by measuring the mass of polymer deposited as a function of time at constant applied voltage. The initial kinetic data are shown in Figure 8 for electrodeposition at 150 v. As was found for the single-component Epon 1001 latex, an induction period is observed prior to which no deposition takes

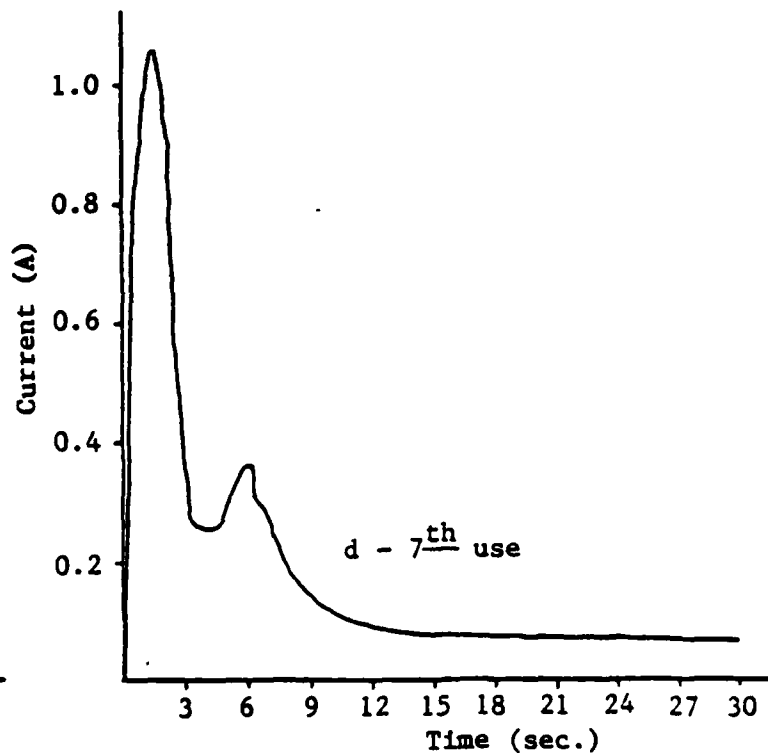
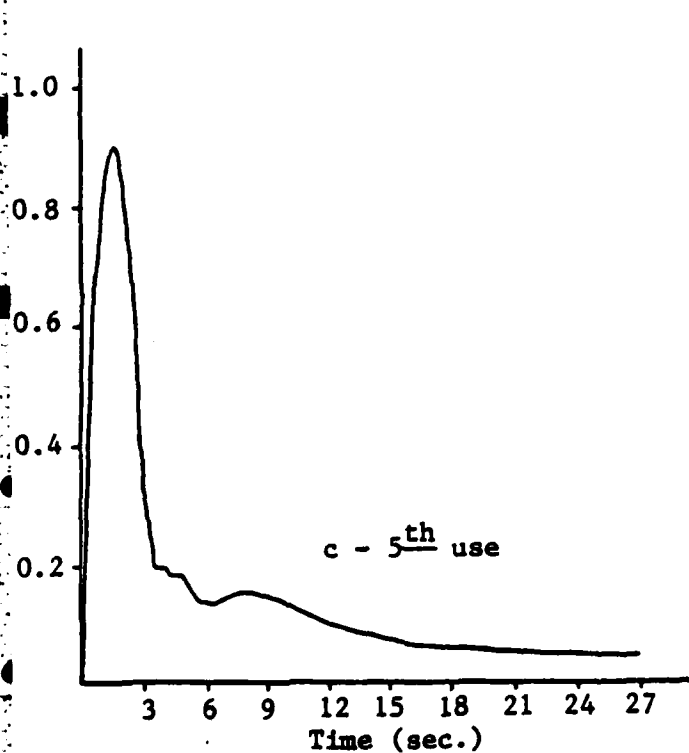
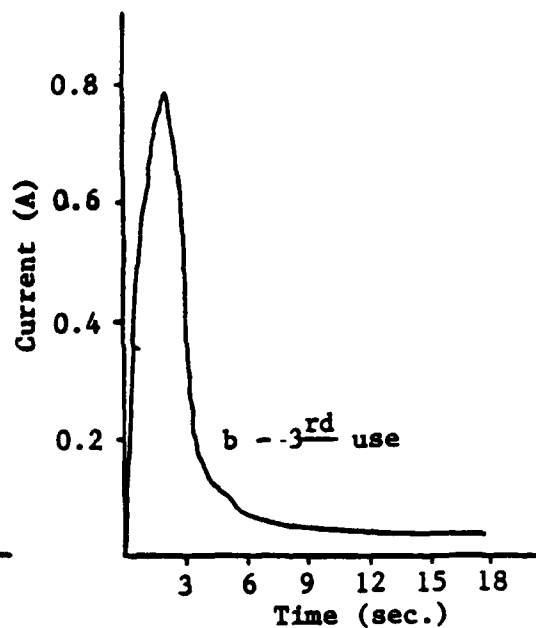
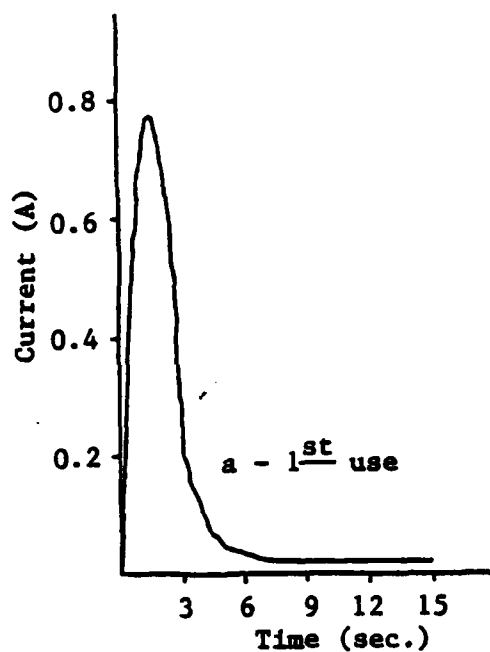


Figure 4. The effect of multiple deposition from the same bath on the current-time curve. Starting bath solids = 10%; deposition voltage constant at 200 v: (a) 1st deposition; (b) 3rd deposition; (c) 5th deposition; (d) 7th deposition.



Figure 5. Scanning electron micrograph of polyurethane-modified acrylic latex deposited at 200 v. Film thickness = 13 mil. Fourth use of same bath. Magnification = 200 X.



Figure 6. Scanning electron micrograph of polyurethane-modified acrylic latex deposited at 75 V. Film thickness = 16 mil. Magnification = 100 X.

Table III

Coulombic Efficiency as a Function of Applied Voltage for
the Electrodeposition of Polyurethane Acrylic Latex

<u>Applied Voltage</u>	<u>Coulombic Efficiency</u>
50 v	64. mg/coul
100 v	76. mg/coul
140 v	78. mg/coul
180 v	80. mg/coul
200 v	83 mg/coul

Table IV

Coulombic Efficiency as a Function of Number of Depositions
from the Same Sample of Latex. Polyurethane Acrylic
Latex Deposited at 200 v

<u>Number of Depositions</u>	<u>Coulombic Efficiency</u>
1	83. mg/coul
2	80. mg/coul
3	79. mg/coul
4	73. mg/coul
5	67. mg/coul
6	65. mg/coul
7	60. mg/coul

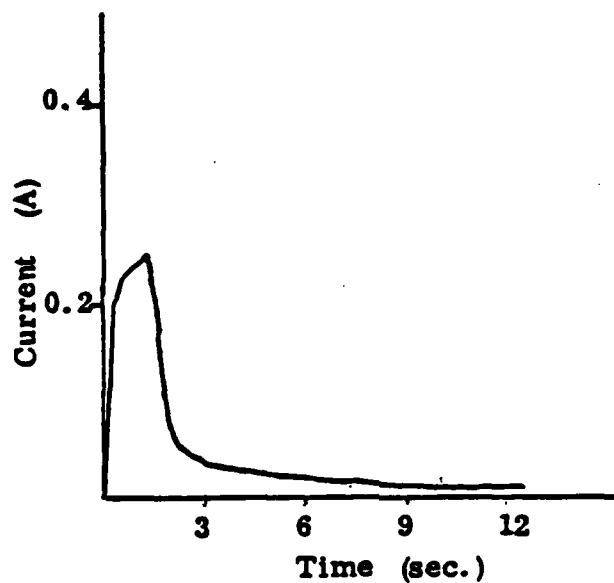


Figure 7. Current-time curve for a commercial PPG cationic electrodeposition primer. Both solids = 10%, and applied voltage = 150 v.

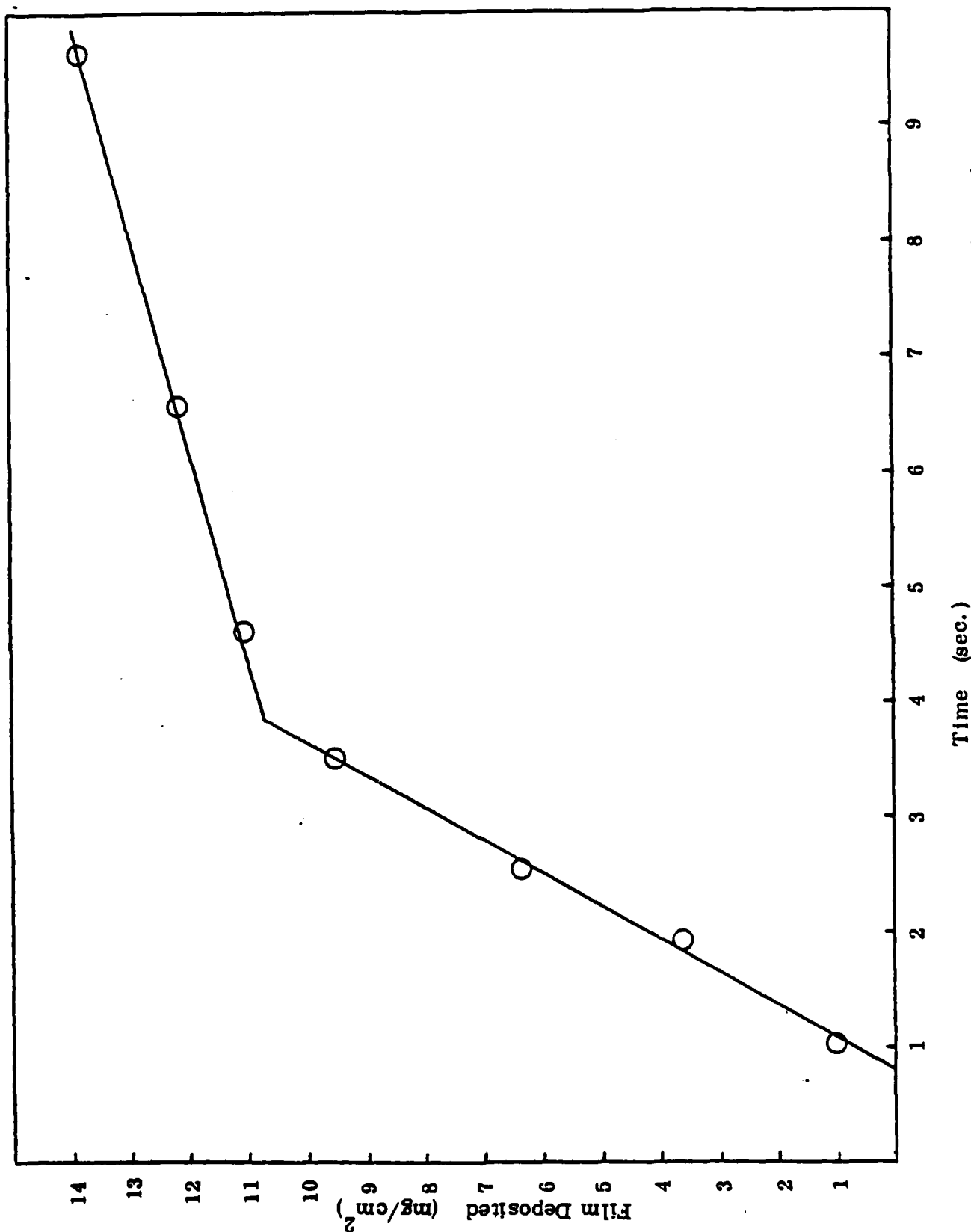


Figure 8. Mass of film deposited as a function of deposition time for cationic polyurethane modified acrylic latex. Deposition voltage = 150 v.

place. Since the emulsifier for the two systems is the same (hexadecyl trimethyl ammonium bromide), and this quaternary ammonium surfactant is known to retain its charge over a broad pH range, it is believed that this induction period is the time required to establish a sufficient accumulation of latex at the cathode to induce coagulation via a nonionic concentration coagulation mechanism.

The kinetic data show that the film grows linearly with time, at two distinct rates. This linear dependence of the mass deposited on the deposition time indicates that the growth of the film at the cathode is unimpeded as deposition continues, up to the end of the first linear growth period. The onset of the second growth rate corresponds well with the current cutoff observed on the current-time curves; thus during the second growth stage the film resistance increased and reduced the rate of further film growth. This reduction is clearly seen upon calculating the numerical values of the growth rate. For electrodeposition of the polyurethane latex at 150 v, the growth rates were calculated from the slope of the film mass deposited versus time plot (Fig. 8). During the initial, unimpeded growth stage the rate of deposition was $3.6 \text{ mg/cm}^2\text{-sec}$, while during the second period the rate dropped to $0.6 \text{ mg/cm}^2\text{-sec}$.

Future Work

Future work with the cationic polyurethane-modified acrylic latex system includes:

1. Extension of the film growth kinetic study to various applied voltages, and comparison of the results obtained with those for the Epon 1001 latex.
2. Further characterization of this latex, with the serum replacement technique, to accurately determine the specific area of the adsorbed emulsifier molecules.
3. Determination of the effect of the following parameters on the cathodic electrodeposition process:
 - particle size distribution
 - pH stability of the latex
 - rate of agitation of the E.D. bath
 - type of emulsifier used to stabilize the latex
 - varying the latex particle surface charge density at constant particle concentration in deposition bath
 - varying latex particle concentration in deposition bath at constant surface charge density

4. Investigate the corrosion protection performance and film morphology of the polyurethane-modified acrylic latex electrodeposited films.

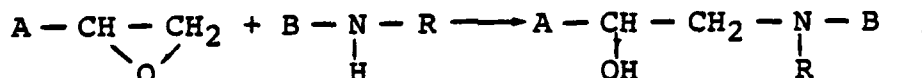
REFERENCES

- [1] R. A. Wessling, D. S. Gibbs, W. J. Settinegri and E. H. Wagner, "Electrodeposition of Coatings," G.E.F. Beaver, Editor, American Chemical Society, 1973, p.110.
- [2] J. W. Vanderhoff, M. S. El-Aasser, and J. P. Hoffman, U.S. Patent 4,070,323 (1978).
- [3] J. W. Vanderhoff, M. S. El-Aasser, and J. Ugelstad, U.S. Patent 4,177,177, Dec. 4, 1979.
- [4] R. A. Wessling, Proc. 6th Intern. Conf. on Org. Coating Sci. Technol., pp.650-710 (1980).
- [5] M. S. Ahmed, M.S. Thesis, Lehigh University, 1981.
- [6] First Annual ONR Report, p.107 (1980).

Program #11. Application of Laser Raman Spectroscopy
to the Analysis of Electrodeposited Epoxy Resin

INTRODUCTION

In the preparation of epoxy films on steel, aqueous emulsions of Epon 1001 (diglycidyl ether of bisphenol A) and Emerez 1511 (a polyamide prepared from dimer acids and a diamine) are mixed and cathodically electrodeposited on the steel. The Emerez 1511 serves as the curing agent for the Epon 1001, presumably by reaction of the residual free amine groups of the Emerez with the epoxy groups of the Epon:



where A represents the residue attached to the epoxy group in Epon 1001, and B represents the residue attached to the amine group in Emerez 1511. The symbol R stands for either H, if the reactive amine is primary, or an organic moiety, if it is secondary.

The intent is to electrodeposit the Epon and Emerez in stoichiometric ratio, but this is very hard to achieve. The amount deposited depends strongly on the diffusion characteristics of the two reactants. One is likely to get layering and uneven film formation. We therefore wished to have a method of spot checking the deposited film, to determine whether the film is homogeneous, or, if not, the degree of variation from spot to spot. Chemical analytical methods are not applicable because such methods are destructive, and too large a sample is required to furnish the required point-to-point information.

We wished to investigate the applicability of the laser Raman microprobe to this problem, since this instrument is capable of examining areas as small as $1 \mu\text{m}^2$. In order for such examination to be effective, spectra must be obtained which are capable of indicating quantitatively the ratio of Epon to Emerez deposited. We also felt that in order to understand better the Raman spectra it is important to have as a reference some chemical information about the films examined.

In this progress report we describe studies of films cast from solvent rather than electrodeposited, since only in this way can the ratio of the reactants be controlled easily.

Raman Spectra

Films were cast by mixing solutions of Epon 1001 and Emerez 1511 in 1:1 methyl isobutyl ketone/toluene solvent. The mixtures were placed in aluminum evaporating dishes, and the solvent was allowed to evaporate at room temperature for several days [1].

Raman spectra were obtained with a "Molecular Optics Laser Examiner" (MOLE), which is the trade name for the Raman microprobe manufactured by Instruments S.A., Inc. The excitation source was the 5145 Å line emitted by a Spectra Physics Model 164 Argon ion laser. The laser beam was focused down to an area of the order of magnitude of $1 \mu\text{m}^2$ by means of a 100X NPL Leitz objective, and the scattered light was collected over a large angle by means of the same objective. The scattered light was detected by an RCA 31034 photomultiplier tube cooled to -30°C by means of a thermoelectric housing made by Products for Research (Model TE-104 RF).

Figures 1, 2 and 3 show, respectively, Raman spectra of Epon 1001, Emerez 1511, and a solvent cast film obtained by mixing stoichiometric amounts of the two reactants. (The stoichiometry was based on reacting one gram-equivalent of epoxy from Epon 1001 with one gram-equivalent of amine from Emerez 1511.) Each spectrum, of course, represents only a few μm^2 at most of the surface of each sample, but repeat spectra on different areas showed no significant differences. The strong 1124 cm^{-1} line in the spectrum of the stoichiometric mixture is an artifact caused by a fluorescent lamp and is to be disregarded.

A strong peak at 1609 cm^{-1} exists for Epon which is absent in the Emerez spectrum. The strongest peak in the Emerez spectrum occurs at 1442 cm^{-1} ; this peak is not apparent in the Epon spectrum, although there is a minor peak close by at 1460 cm^{-1} . The 1:1 stoichiometric mixture displays the 1609 cm^{-1} Epon peak, and also a composite peak at $1448\text{--}1461 \text{ cm}^{-1}$ that coincides roughly with both the Emerez 1442 cm^{-1} peak and the Epon 1460 cm^{-1} peak. It is interesting, however, that the ratio of the height of the 1461 cm^{-1} peak to the height of the 1609 cm^{-1} peak is much greater for the stoichiometric mixture than for the Epon 1001 alone. Accordingly, we thought that this peak ratio might serve as an indication of the relative amounts of Epon and Emerez present, since the presence of Emerez serves to intensify the 1461 cm^{-1} peak. The significance of this peak will be discussed in a subsequent section.

Trial of Peak Ratio Method

We used a base line calculation method. With the sample in place and all machine parameters adjusted so as to give maximum peak definition, we read the spectrum at five frequencies: 1400 , 1450 , 1500 , 1610 and 1630 cm^{-1} . For each frequency we allowed the pen to record for one min, and then passed to the next frequency. We took the highest and the lowest readings for the one min period

EPON 1001

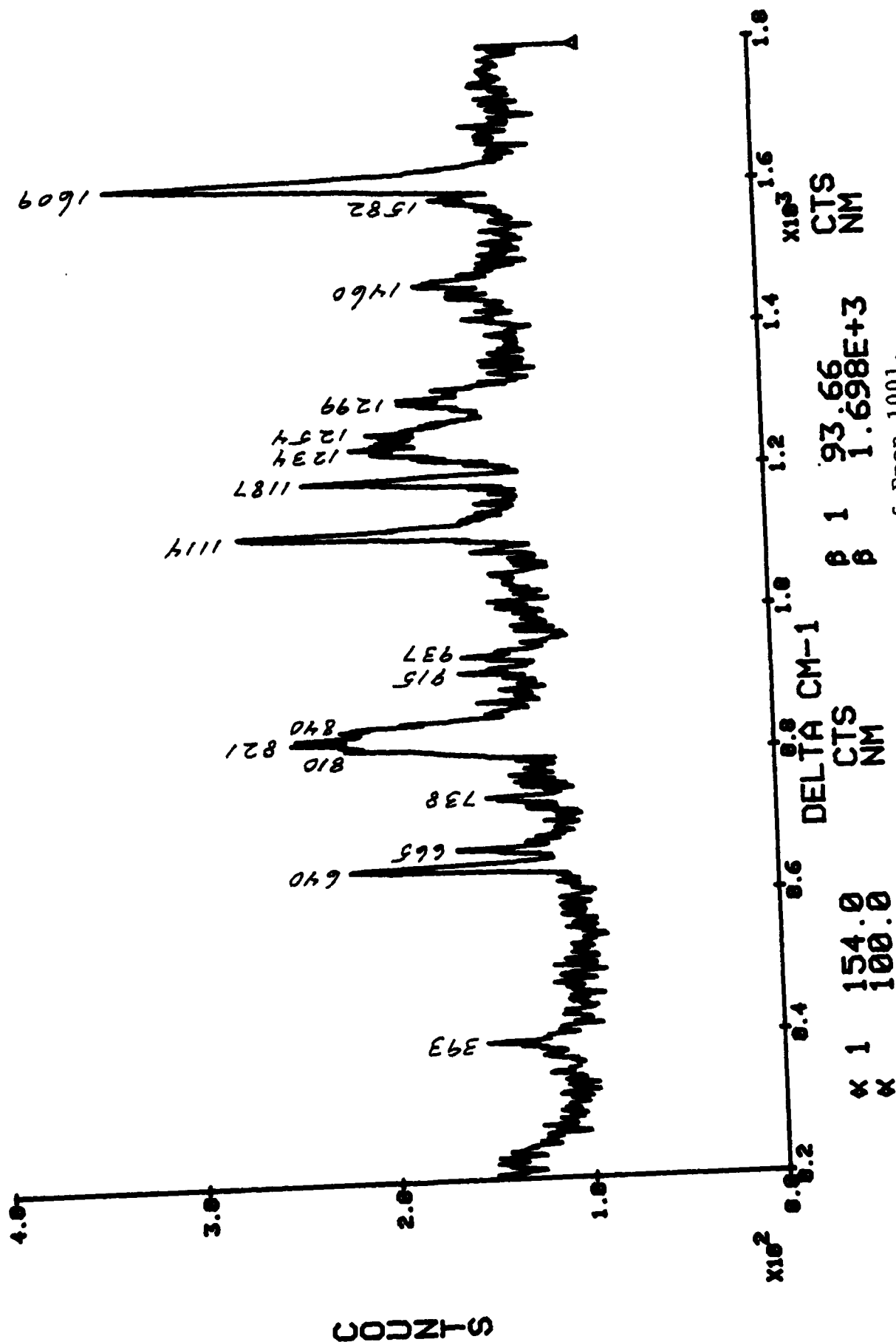


Figure 1. Raman spectrum of Epon 1001.

EMEREZ 1511

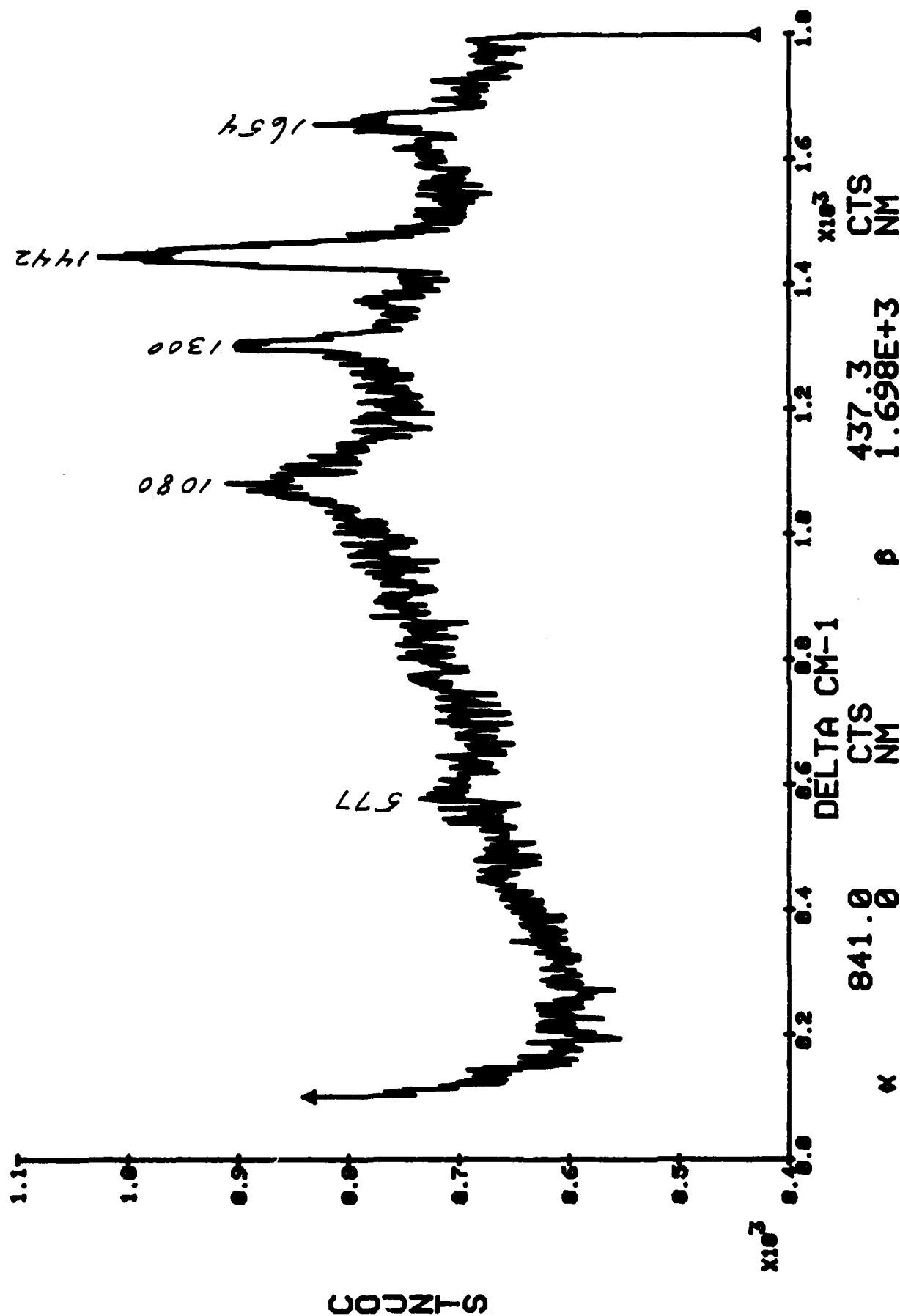
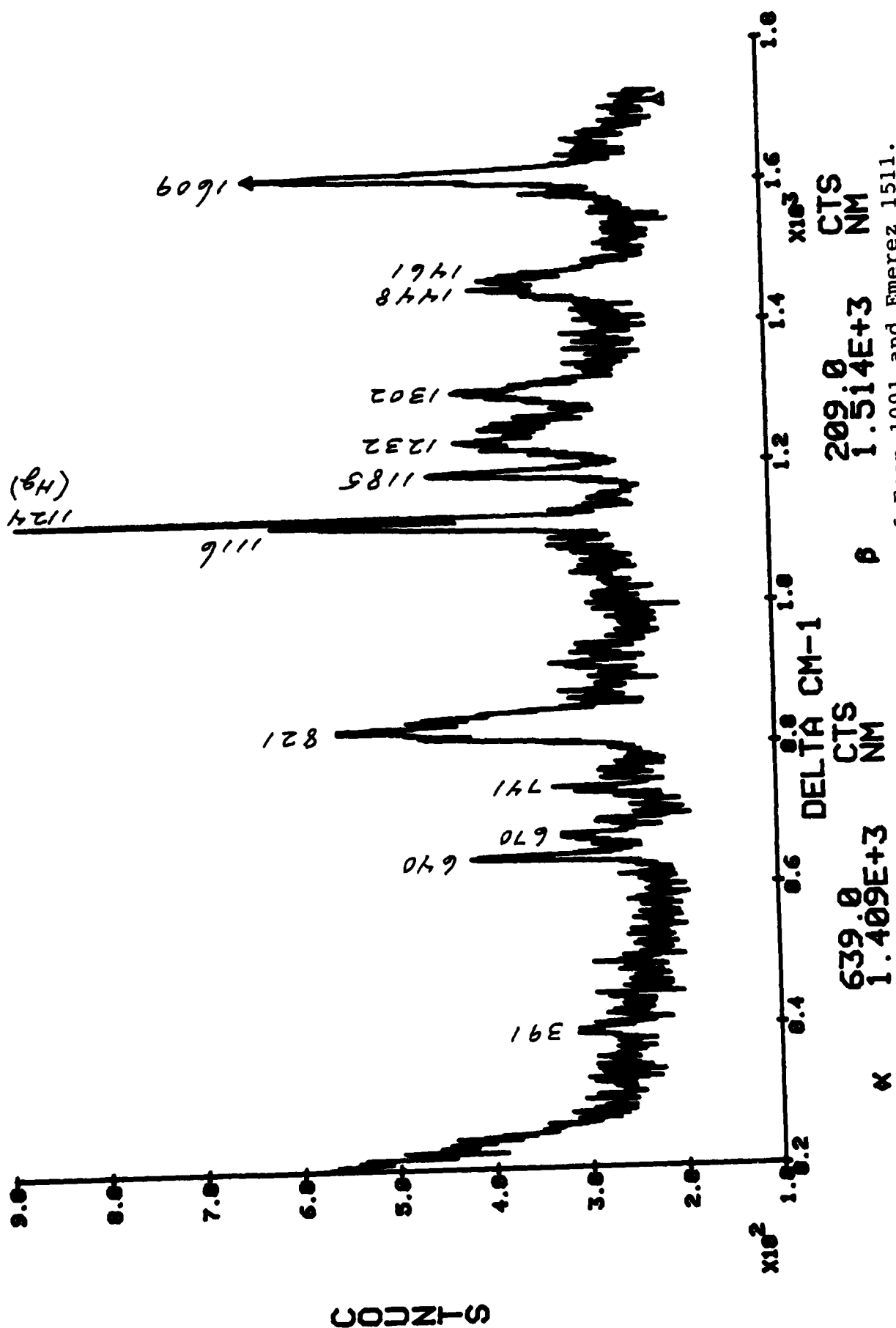


Figure 2. Raman spectrum of Emerez 1511.

STOICH MIXTURE



and accepted the average of the two as being the value for that frequency. The peak ratio was calculated as follows:

$$\text{Peak ratio, \%} = \frac{V_{1450}}{V_{1610}} \times \frac{\frac{50 V_{1400} + 50 V_{1500}}{100}}{\frac{20 V_{1500} + 110 V_{1630}}{130}} \times 100 ,$$

where V_{1400} represents the value at 1400 cm^{-1} , etc.

Figure 4 shows a typical recording for a sample. The initial decay of the pen position was caused by fluorescence of the sample, which gradually diminishes as the sample is irradiated with the laser beam. No reading was taken until the pen position was reasonably constant, at which time the first one min period began.

Table I shows the samples prepared and the peak ratios obtained for them. Three values of peak ratio were obtained for each sample at different positions on the surface. It is clear that the average peak ratio value correlates with the Emerex 1511 content. The difference in means between Column 1 and Column 2 is significant at the 99% confidence level; that between Columns 2 and 3 to the 90% confidence level (by Student's t test).

Table I
Peak Ratio Values for Different Ratios
Of Emerex 1511 to Epon 1001

Stoichiometric Ratio Emerex 1511/Epon 1001	0.75	1.00	1.25
Sample No.	22	1	9
Peak ratio, %	37.1	41.5	47.5
	29.5	50.0	45.9
	32.6	34.4	35.4
Sample No.	23	2	10
Peak ratio, %	28.8	40.2	45.4
	40.3	38.5	48.7
	37.4	47.7	52.4
Sample No.	24	3	11
Peak ratio, %	31.0	39.9	50.6
	32.0	38.5	42.2
	28.9	41.0	42.6
Average peak ratio	33.07	41.30	45.63
Pooled std. dev., all values =	4.72%		

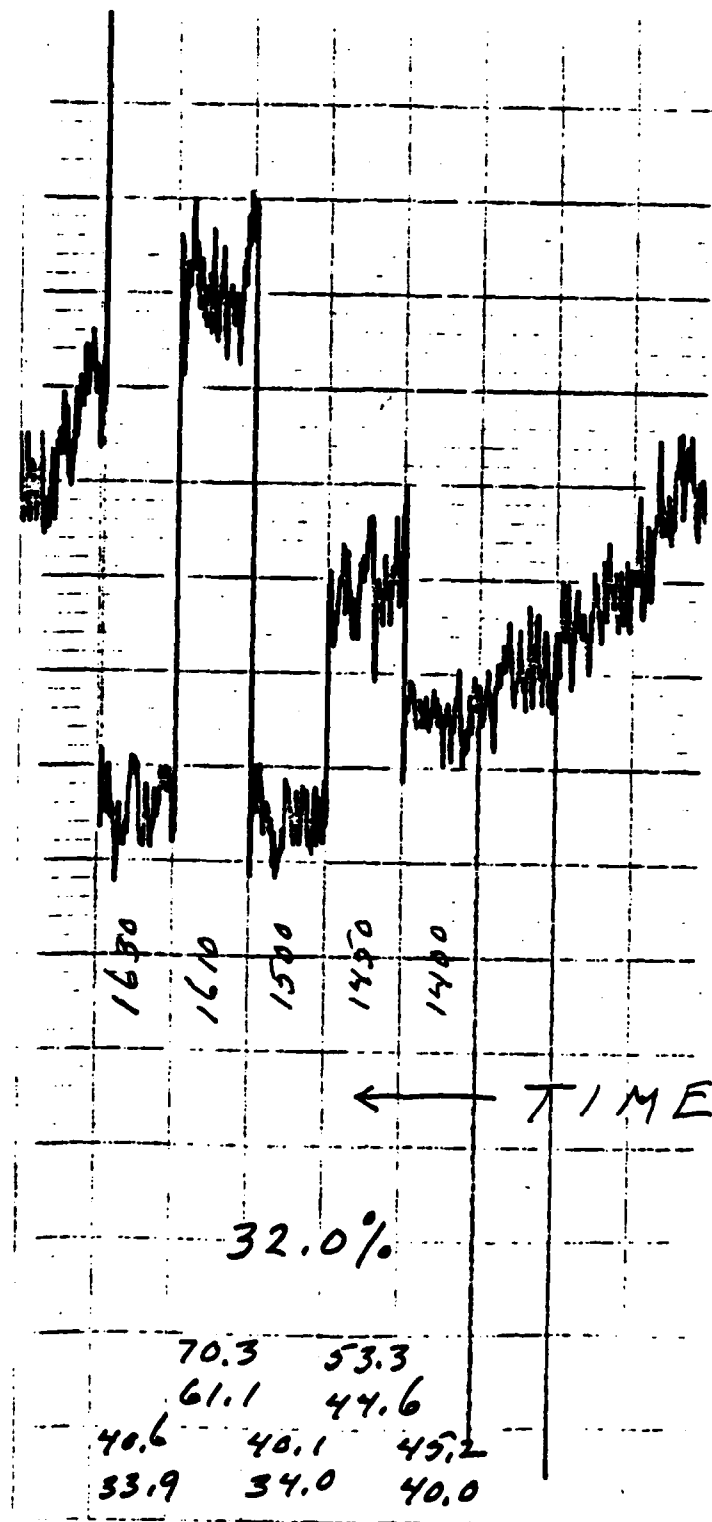
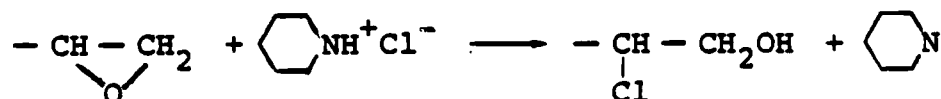


Figure 4. Specimen tracing for peak ratio method.

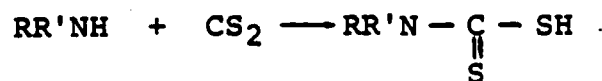
Chemical Investigation

The nature of the two peaks which are being used for the peak ratio method deserves further study. The 1609 cm^{-1} peak appears to be unaffected by the addition of Emerez, whereas the peak at $1448\text{--}1461\text{ cm}^{-1}$ increases in magnitude as Emerez is added. Two possible explanations are (a) that the latter peak represents Emerez 1511 itself, and (b) that it rather represents degree of cure, since undoubtedly considerable cure occurs even at room temperature. Three facts support hypothesis (b): (1) Even though there is a peak in the spectrum of the stoichiometric mixture at 1448 cm^{-1} that is very close to the Emerez 1442 cm^{-1} peak, none of the other Emerez peaks appears in the mixture spectrum. (2) Emerez does not have the 1461 cm^{-1} peak, which instead characterizes Epon 1001 and can well represent a feature that is strengthened by cure. (3) A literature reference states that the 1608 cm^{-1} peak of an epoxy resin is independent of the state of cure, whereas the 1460 cm^{-1} line increases in intensity with state of cure [2].

In order to obtain further insight into the chemical nature of the resin and the specific changes that correlate with the peak ratio, we performed a series of chemical analyses by the method of Bell [3]. The method is to react the epoxy groups with excess pyridinium chloride, which loses HCl to the epoxy group, and then back-titrate the residual HCl potentiometrically with standard NaOH:



Then CS_2 is added to convert primary and secondary amines to dithionic acids, which are then titrated potentiometrically with NaOH:



A series of tests with Epon 1001 alone and Emerez 1511 alone showed that the method gave excellent results for the epoxy groups in Epon 1001 but very poor results for the amine groups in Emerez 1511. The CS_2 part of the method was therefore abandoned.

A new series of samples was prepared, as shown in Table II. To make sure that complete cure was effected, these samples (unlike those which are the subject of Table I) were heated at 150°C for one hour. The results of epoxy determinations are shown in Table II. The calculated percentage of the original epoxy that

Table II
Epoxy Content Remaining after Cure

<u>Sample No.</u>	<u>Stoichiometric Ratio, Emerez 1511/Epon 1001</u>	<u>% Epoxy Found</u>	<u>Calculated % of Original Epoxy Remaining</u>
Epon 1001	0	8.46	100.0
Epon 1001	0	8.41	100.0
1	0.25	2.98	39.4
2	0.25	3.19	42.3
3	0.50	0.74	10.8
4	0.50	0.77	11.2
5	0.75	0.29	4.6
6	0.75	0.25	4.0
7	1.00	0.34	5.9
8	1.00	0.39	6.8
9	1.50	0.81	16.3
10	1.50	0.81	16.3
11	2.00	1.16	26.6

remains after cure is plotted as a function of stoichiometric ratio in Figure 5. The dashed line represents what we would expect on the basis of complete stoichiometric reaction, and the solid line represents what was actually found. It is obvious that fairly good reproducibility was obtained on duplicate samples, but it is not clear if we are indeed measuring epoxy groups on the cured samples or if interference exists. Additional chemical work will be needed to resolve this problem.

We were unable to obtain Raman spectra on any of the samples of Table II (except, of course, the Epon 1001 itself) because a large amount of fluorescence completely swamped the Raman lines. Since the samples of Table I gave usable spectra, we conclude that the fluorescence resulted from the treatment at 150°C. Fortunately, our purposes do not require running the spectra after the heat treatment, since we wish to measure homogeneity of the film immediately after electrodeposition. Nevertheless, we are investigating possible methods of reducing interference from fluorescence in Raman spectroscopy.

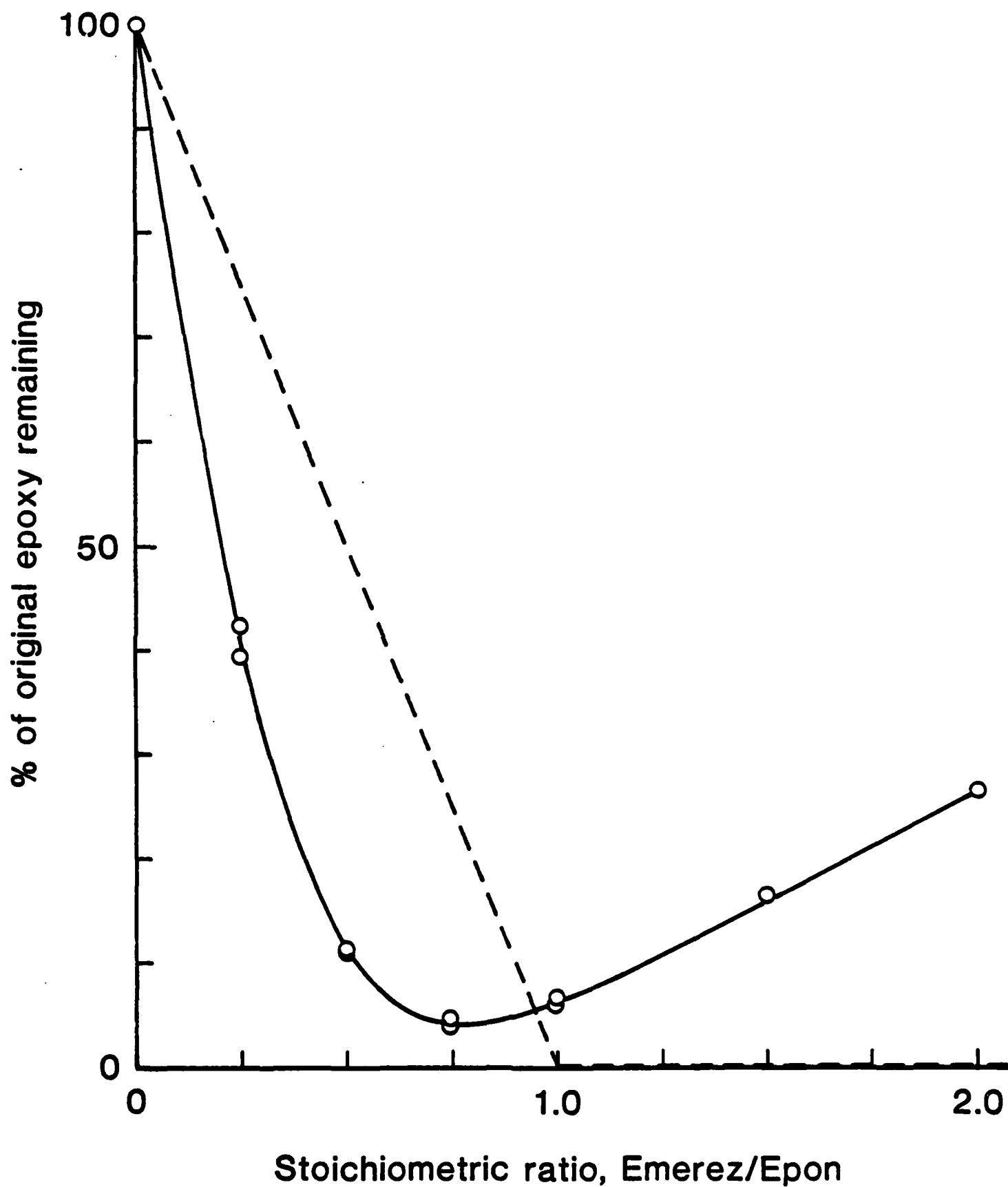


Figure 5. Percentage of original epoxy that remains after cure as a function of stoichiometric ratio.

Future Work

Although the peak ratio method shows promise, we are not sure of the significance of the peaks, nor are we able to obtain a direct correlation between the peak ratio and some other directly measurable quantity. To this end, we will continue analytical work on solvent-cast samples of known initial composition, and will correlate the results obtained with Raman measurements on the same samples. Simultaneously, we will continue our efforts to get meaningful Raman results on cured samples despite the presence of fluorescence. After we are in a position to understand the Raman results, we will begin to apply the method to electrodeposited samples.

REFERENCES

- [1] All samples were prepared by Ata-Ur Rahman, graduate student on the ONR project.
- [2] C. S. Lu and J. L. Koenig, Papers Presented at 163rd Meeting of the American Chemical Society, Division of Organic Coatings and Plastics Chemistry 32, No. 1, 112-116 (1972).
- [3] J. P. Bell, J. Polym. Sci. A-2, 8, 417-436 (1970).

Program #12. Pigment/Binder Interactions
and Corrosion Protection

ABSTRACT

The permeabilities of zinc and glass-bead-filled epoxy films to water vapor are sensitive to the interfacial adhesion and hence to the extent of acid-base interaction. The tighter the interface, the lower the permeability. As predicted by theory, the permeability of the composite may exceed that of the matrix alone if the filler and matrix are not well-bonded. With zinc-filled films, poor initial interfacial adhesion permits the generation of corrosion products that quickly fill up the pores and reduce the permeability to that of a well-bonded composite. The permeability is also lower, the more rigorous the curing condition.

INTRODUCTION

During the past year, research has been continued on the role of pigment-binder interaction in protective coatings. In the last report it was shown that the degree of filler-matrix interaction in corrosion-resisting zinc-epoxy systems can be controlled by varying the electron-donating ability of the binder. Confirming recent ideas about the importance of acid-base or hydrogen-bonding interactions [1] to interfacial adhesion, maximum and minimum adhesion to the acidic (electron-accepting) zinc surface was found for basic and acidic polymers, respectively. Thus the superior performance of matrixes that did not wet the zinc well [2] could be explained in fundamental terms; the weaker the acid-base interaction, the greater the ability of the zinc to form inhibitive and pore-sealing compounds in the presence of water.

The question of the effect of interfacial adhesion on permeation to oxygen and water is also of interest. Accordingly, this report describes progress with an examination of permeability to water vapor in typical zinc-epoxy systems and also in model glass-bead-filled polymeric matrixes. Again, emphasis is being given to the role of interfacial adhesion; a study of the effects on oxygen permeability is also planned.

Permeability in Pigment-Binder Systems

The transport of a permeant through a composite material complex; the presence of an impermeable second phase reduces the effective area and increases the path length (tortuosity) in proportion to the volume of the second phase [3-5]. In the limiting case of good adhesion, the permeability coefficient P is given by:

$$\frac{P_c}{P_p} = \frac{v_p}{1 + 1/2v_f} \quad (1)$$

where v is volume fraction of an isotropic inclusion and the subscripts c and f refer to the composite and polymer, respectively. If the adhesion is poor (as with incomplete wetting) or if the interface is hydrophilic, P_c may exceed the value predicted [3,6,7], while immobilization of matrix at the interface may decrease the value of P_c [1,8]. Thus permeability in such systems is very sensitive to the nature of the interfacial interactions.

Other effects may occur as well. These include variations in composition and pigment distribution across the film thickness [8], the geometry of the pigment [4], and variations in such properties as crosslink density and residual solvent.

An interesting example is the case of zinc-based epoxy coatings discussed above. Paradoxically, poor wetting appears to be desirable for two reasons: to develop conductive chains of zinc that offer short-term cathodic protection and to permit the formation of inhibitive zinc compounds that also seal the pores [2,9]. Our earlier research [10,11] confirmed a role of acid-base interaction in controlling the interfacial adhesion; we suggest that the formation of the zinc corrosion products yields a tight and relatively impenetrable interface.

EXPERIMENTAL

The Model System

Glass beads were selected for the model system because their surfaces can be readily modified to vary their electron donor/acceptor behavior, e.g., by treatment with an acid or with a coupling agent. The case of an epoxy (acidic polymer) can be modelled by use of a high-molecular-weight linear phenoxy resin, which is also used in commercial practice as a binder for zinc. Use of a phenoxy resin obviates the complications associated with cross-linked systems (though not the problem of residual solvent). Common basic polymers such as polystyrene and poly(methyl

methacrylate) can also be used. Thus a wide range of acid-base combinations can be obtained. It is hoped that inverse gas chromatography can be applied in order to determine directly the extent of acid-base interaction [12].

Materials

Epon 1001F (Shell) and Polyamide 1511 (Emerez) constituted the binder for the epoxy system, and zinc dust #22 (N.J. Zinc Co.; av diameter, 8 μ m) the pigment. Glass spheres, type 3000 (untreated) and type 3000-CP03 (treated with silane) with particle sizes of less than 45 μ m, were supplied by Potters Industries. The phenoxy resin used was supplied by the Union Carbide Corporation.

Film Preparation

The formulation of the 80% zinc/epoxy films and the film-casting procedure have been reported elsewhere [10]. The glass-bead-filled epoxy specimens and unfilled controls were cast in small aluminum pans and cured as described earlier [11]; film thicknesses ranged from 0.2 mm (for the 3000-CP03 bead system) to 0.1 mm (for the others).

Test Procedures

Moisture-vapor permeability was determined using a permeation cup method (ASTM D-1653) at room temperature; calcium chloride was used as desiccant. Values of P were calculated over a time range from t_{i-1} to t_i (sec) from the values of the weight loss of water ($G_{i-1}-G_i$) from the following [13]:

$$P = \frac{(G_i - G_{i-1})d}{A \cdot (t_i - t_{i-1})\Delta P} \quad (2)$$

where P = permeability coefficient ($\text{g}\cdot\text{cm}/\text{cm}^2\cdot\text{Pa}\cdot\text{sec}$), G = water loss (g), d = film thickness (cm), $\Delta P = (p_1 - p_2)$ [p_1 and p_2 being the partial pressures of water vapor on opposite sides of the film (P_a)], A = sample area (cm^2), and t = time of experiment (sec).

Fracture surfaces were coated with an Au/Pd layer and examined using an ETEC scanning electron microscope.

RESULTS AND DISCUSSION

Effect of Fillers on Permeability to Water Vapor

Figure 1 shows the water vapor permeability, expressed as milligrams of water vapor loss against $\sqrt{\text{time}}$, of several epoxy films with similar curing history. Using these data, the permeability coefficient, P , was calculated according to Equation (2). Corresponding values of P for pairs of points from Figure 1 are plotted in Figure 2.

It can be seen that all films undergo two distinct regions common in transport behavior: an initial dynamic period in which dramatic changes occur in P , followed by a static (equilibrium) stage reflected in a constant P . There is a general trend towards a decrease in water vapor transport with time. However, the zinc-filled epoxy is the least permeable of the group and appears to reach equilibrium at a faster rate, attaining a constant P between 50 to 80 hr. In contrast, the value of P for the other epoxy samples did not begin to level off until after 110 hr.

This behavior can be attributed to the reactive nature of the zinc particles with respect to water, which accelerates the production of zinc corrosion products. If a pore-blocking mechanism is assumed, the permeability of the initially porous coating should fall considerably after a short period of time. In effect, the volume fraction of the impermeable filler is increased. Direct evidence for the formation of corrosion products is given in Figure 3, which shows the fracture surfaces of the zinc-pigmented films before (Fig. 3a) and after (Fig. 3b) a 24 hr exposure to water vapor in the permeability cup. A closer look at Figure 3a reveals that some zinc corrosion products have formed on the zinc surface of these one-year-old films. Continuous contact with water vapor results in the deposition of more and more zinc compounds around the pigment particles, eventually completely filling the pore. These micrographs suggest that a dramatic decrease in permeability should be observed during the first 24 hr. Indeed, this is the case (see Fig. 2).

Electrochemical studies by Rajagopalan et al. [14] correlate quite well with our findings. Measurement of the galvanic current of 70-80% zinc-pigmented coatings shows a dramatic reduction in the current passing through the film during the first 70 to 90 hr. The link between this rapid drop in the current and the production of zinc compounds is quite clear. The deposition of corrosion products (which have been analyzed to be chlorides or carbonates [15]) on the zinc surface renders the film more resistant to electron transport because of the non-conductive nature of these zinc salts.

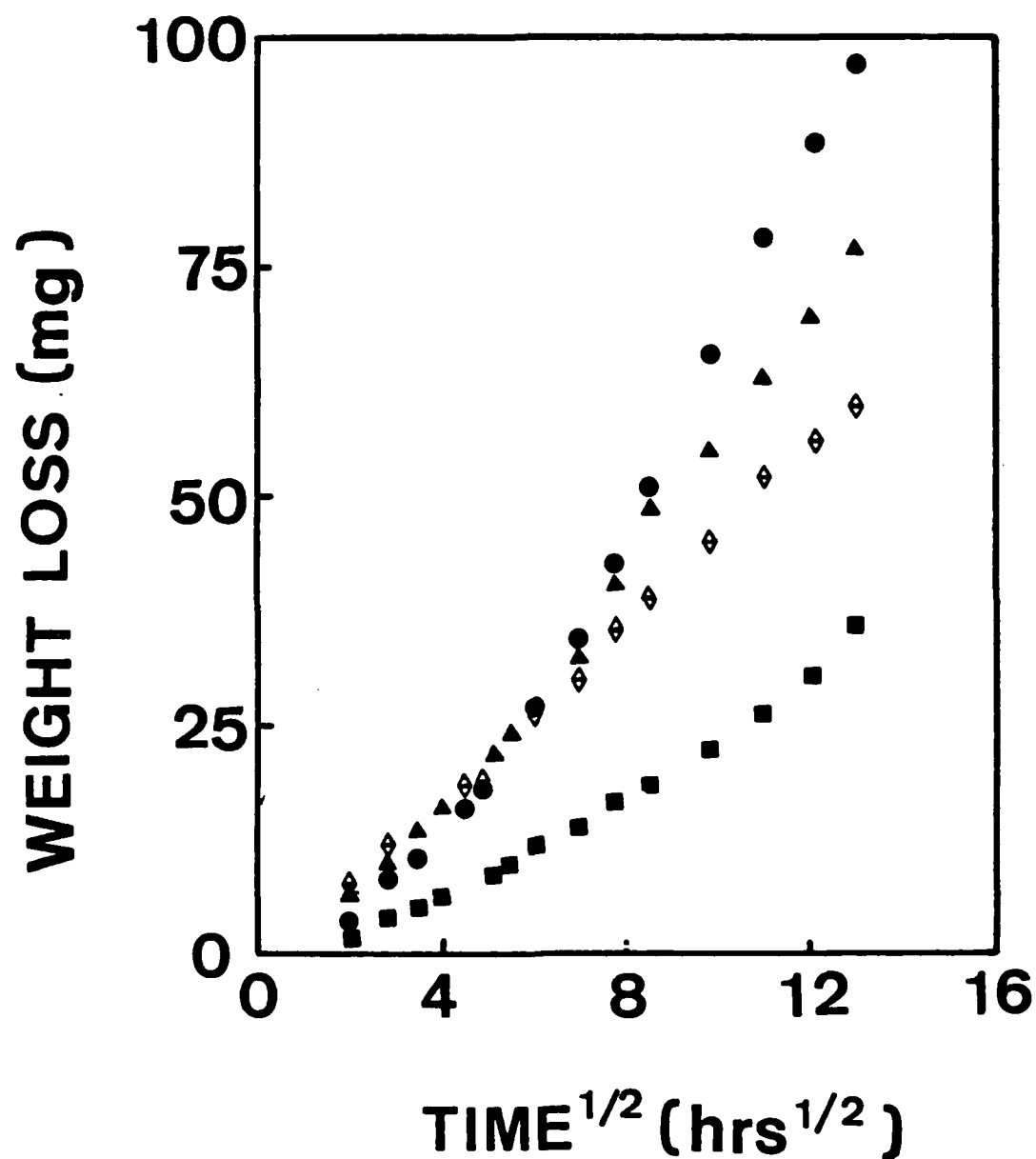


Figure 1. Weight Loss of Water Vapor for Filled Epoxy Films

- 61 Vol. % Glass (3000)
- ◊ 61 Vol. % Glass (3000-CP03)
- 36 Vol. % Zinc
- ▲ Unfilled Control

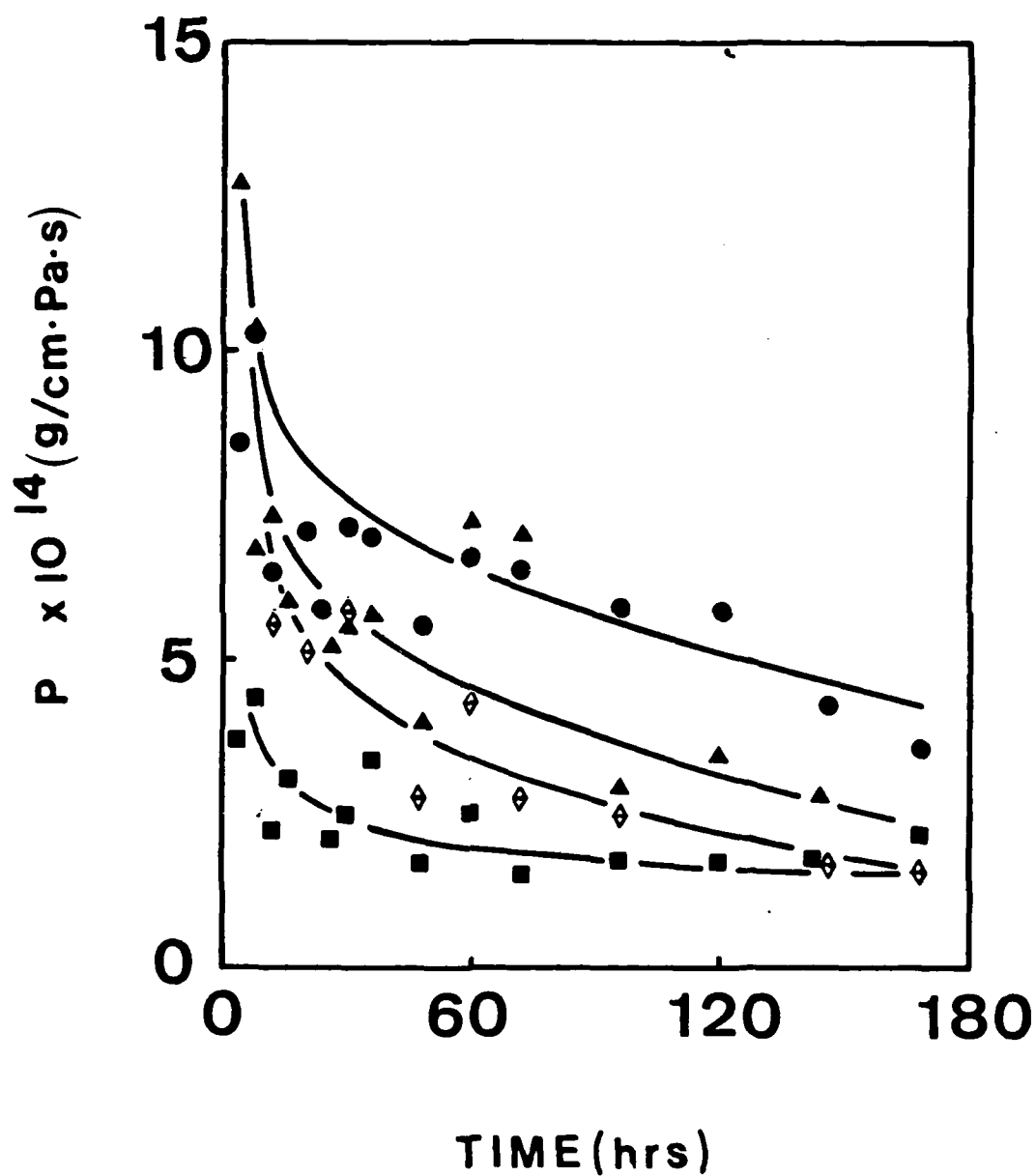


Figure 2. Permeability Coefficient for Filled Epoxy Systems

- 61 Vol. % Glass (3000)
- ◊ 61 Vol. % Glass (3000-CP03)
- 36 Vol. % Zinc
- ▲ Unfilled Control

AD-A124 044

CORROSION CONTROL THROUGH A BETTER UNDERSTANDING OF THE
METALLIC SUBSTRAT. (U) LEHIGH UNIV BETHLEHEM PA CENTER
FOR SURFACE AND COATINGS RESE. H LEIDHEISER ET AL

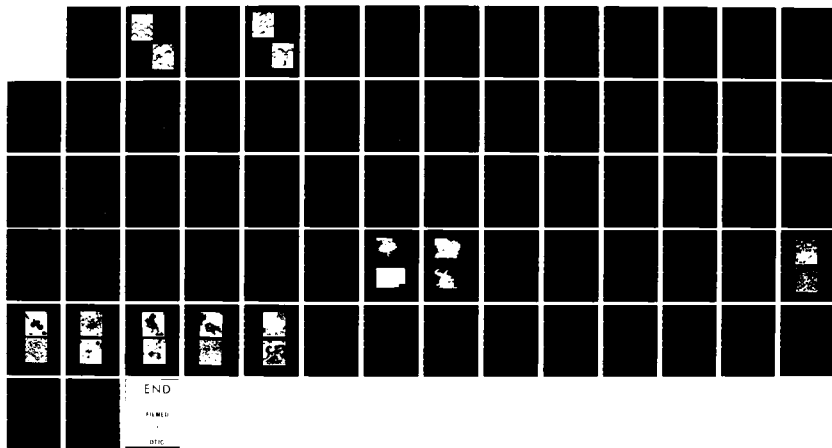
3/3

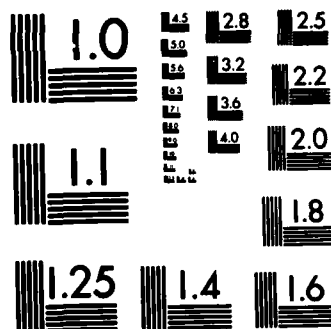
UNCLASSIFIED

01 DEC 82 N00014-79-C-0731

F/G 11/6

NL



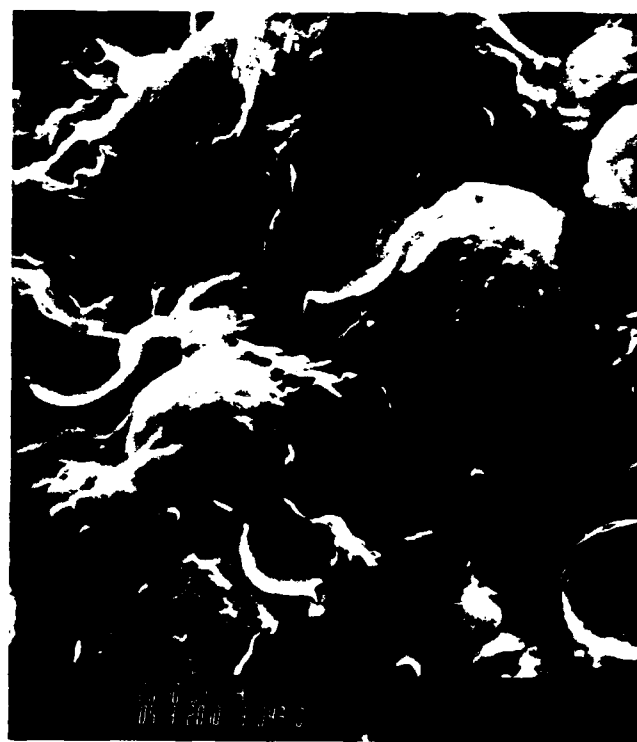


MICROCOPY RESOLUTION TEST CHART
NATIONAL BUREAU OF STANDARDS-1963-A



(a)

Figure 3. Scanning electron Micrographs of Fracture Surfaces of one-year-old zinc-pigmented epoxy films (80 wt. % zinc). (a) Before exposure to water vapor, (b) after a 24 hr exposure to water vapor.



(b)

The possible role of acid-base interaction in permeability can be ascertained by comparing the results of the glass-bead-filled epoxies (treated and untreated) and the unfilled epoxy. Figure 4 shows the fracture surfaces of the untreated (a) and treated (b) glass-bead-epoxy films. The epoxy binder adheres strongly onto the treated filler. Earlier studies have shown that this particular epoxy matrix behaves in an acidic manner [10, 11]. Recent work with polystyrene (basic) and phenoxy (acidic) films have demonstrated the basic nature of the treated glass beads. (Characterization by inverse gas chromatography should confirm these results.) Surprisingly, the untreated glass beads show no preference for either a basic or an acidic polymer.

In any case, the general lowering of P in the presence of glass spheres varies with the system. As shown in Table I, the zinc-filled film behaves essentially as predicted for a well-bonded, impermeable second phase.

Table I. Effect of Zinc and Glass Beads on Steady-State Permeability of Epoxy Films

<u>Material</u>	<u>$P \times 10^{14}$, gm-cm/cm², Pa · s</u>	
	<u>(experimental)</u>	<u>(predicted, eq. 1)</u>
Matrix	3.1	---
Zinc-filled	2.0	1.7
Glass-filled (3000)	3.9	0.9
Glass-filled (3000-CP03)	1.7	0.9

In contrast, the untreated glass beads, which do not interact strongly with the epoxy, increase the permeability of the matrix. As expected, the treated glass beads decrease the permeability, though not as much as expected. This latter effect may be due to a difference in crosslink density between the unfilled and filled matrix when cured at room temperature; greater decreases were observed in earlier studies with epoxies post-cured at 150°C [3, 9]. (See next section.)



(a)

Figure 4. Scanning Electron Micrographs of Fracture Surfaces of Glass-Bead-Filled Epoxy Films: (a) and (b), untreated and treated with coupling agent, respectively.



(b)

Effect of Curing Conditions

Figure 5 demonstrates the effect of curing condition on permeability. In general, the more rigorous the curing condition, the lower the permeability, and the higher the T_g , which increased from 47°C to 56°C as the curing temperature was increased. This observation is consistent with earlier findings on this project [11] and by others for a similar epoxy [16].

Effect of Cross-sectional Inhomogeneity

Figure 6 shows that permeability is lower when the side of the film that had been cast on the Teflon casting sheet faces away from the water in the permeation cell. (All permeability studies previously mentioned were run with a Teflon side down.) This suggests a barrier-related phenomenon, such as is encountered with laminates of different films [17,18]. Since the distribution of zinc particles was essentially uniform throughout, the effect must be generated by differences between the properties of the film layer and film/casting substrate interfaces. If the side exposed to air during the casting is less densely crosslinked during curing (and hence more permeable) than the side facing the Teflon, one might expect that the flux of water vapor would be higher when the more permeable side is presented to water vapor during the test [17]. However, this effect appears to be overcome by the more rapid development of zinc corrosion products in the originally more permeable layer.

FUTURE PLANS

The goals for the next year's studies are:

1. To complete studies of pigment/binder interaction in zinc/epoxy systems by tests of corrosion resistance of coated steel coupons, and of electrochemical response. Specimens studied will include examples of strong and weak interfacial adhesion. Thus the experiments will test the hypothesis that weak interfacial adhesion is desirable in this system.
2. To continue studies of model systems using glass beads as filler and various binders. Emphasis will be given to modification of the glass surface to obtain both electron-donating and electron-accepting character, and combinations with electron-donating and electron-accepting binders.

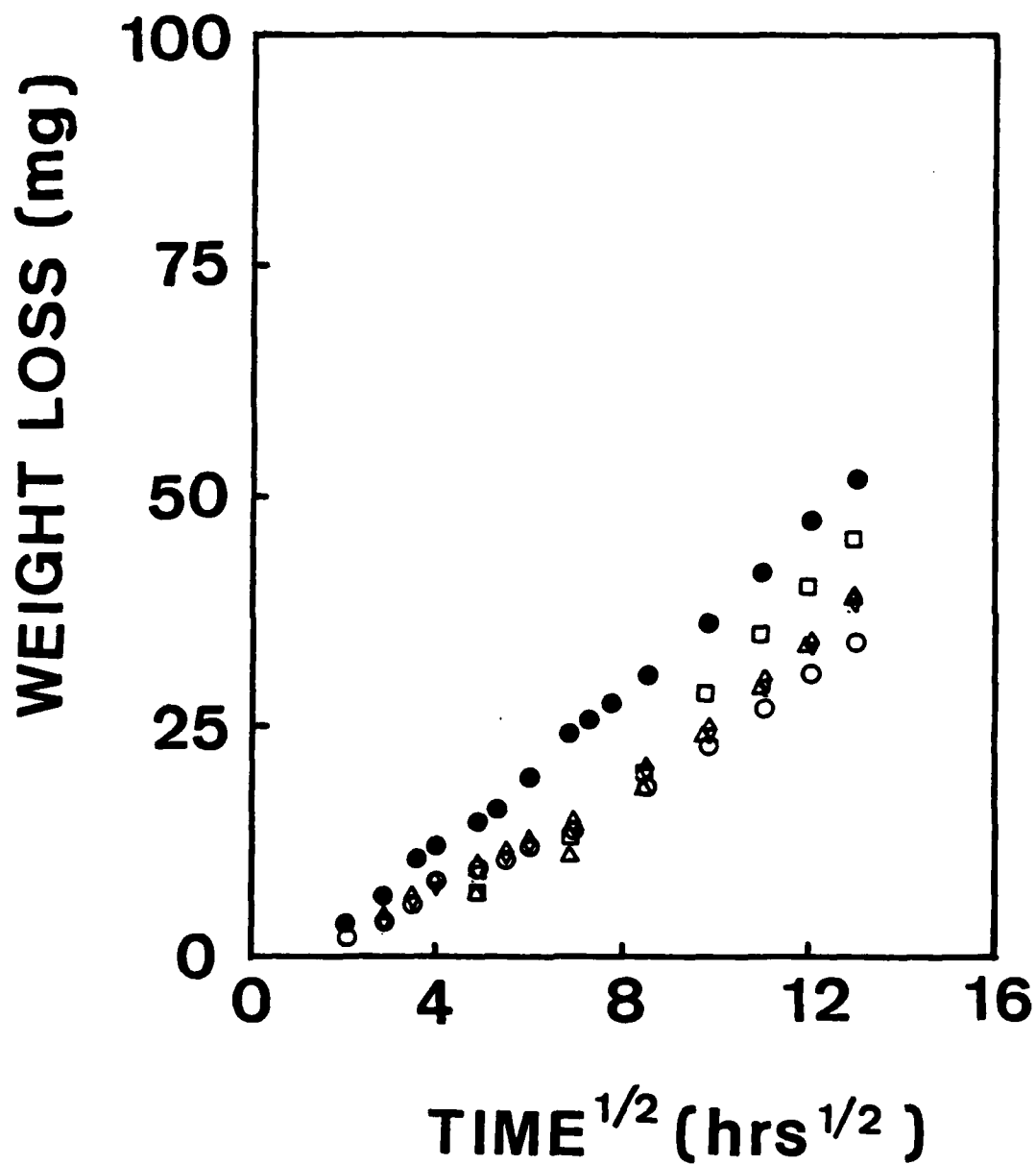


Figure 5. Effect of Curing Conditions on the Water Vapor Permeability of 80% - Zinc Filled Epoxy Films (0.1 mm Thick). Cured Vacuum: Δ, 28°C; □, 38°C; ○, 70°C; ◊, 90°C. Cured at 1 ATM Room Temperature, ●.

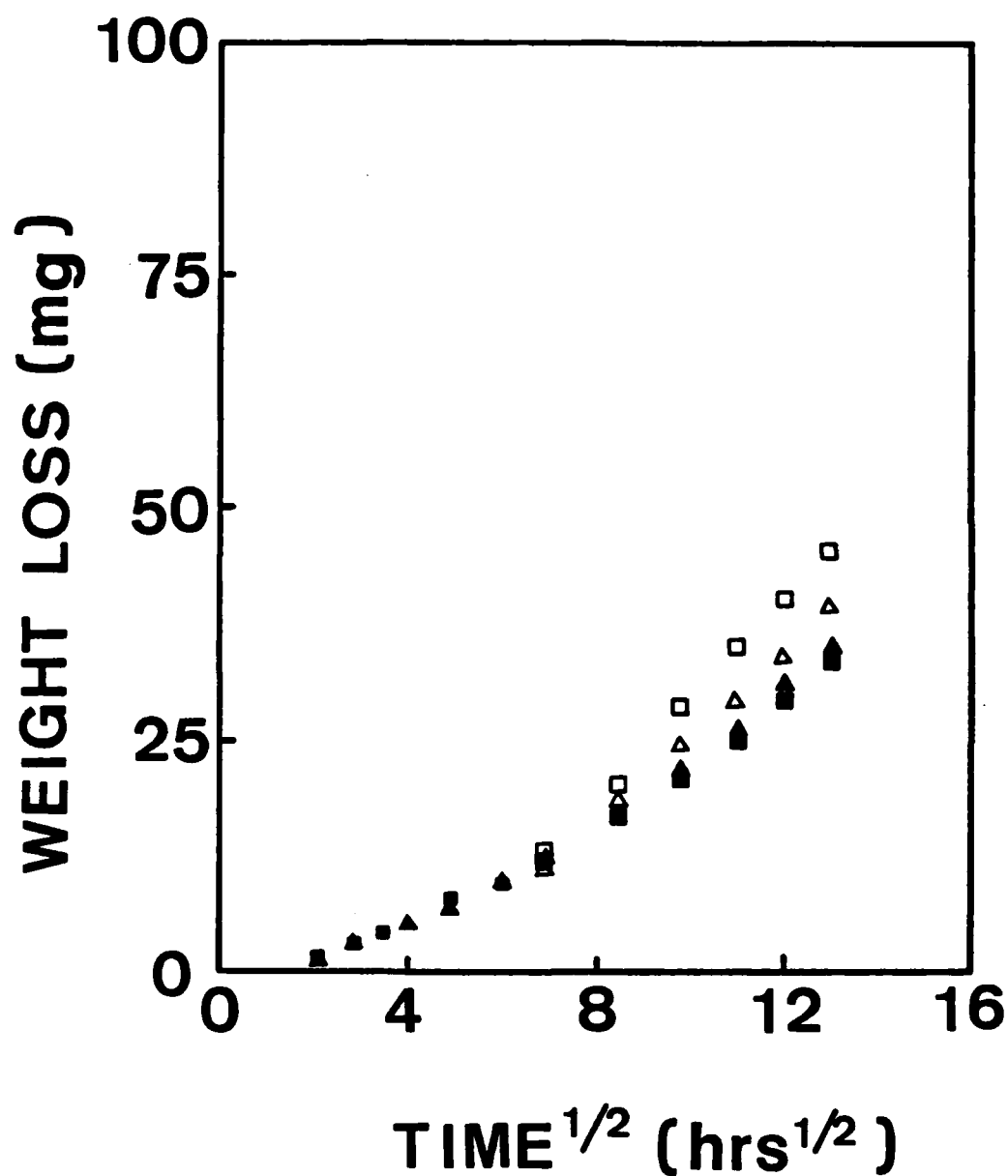


Figure 6. Effect of Film Placement (up or down) on water vapor permeability of 80%-zinc-filled epoxy films (0.1 mm thick). All samples cured under vacuum. Teflon side up: ▲ and ■, cured at 47 and 45°C, respectively. Teflon side down: △ and □, cured at 47 and 45°C, respectively.

Phenoxy resin will be of special interest as an electron-accepting binder because of its use as a binder for zinc in newer corrosion-resisting formulations; poly(methyl methacrylate) will serve as an electron-donating binder.

3. Specifically, to correlate the permeability (and mechanical behavior) of the coatings with the extent of interfacial adhesion, and with the acid-base character of the adhesion. Studies will be extended to include permeability to oxygen as well as water, and the use of inverse chromatography to characterize acid-base interactions will be explored.

REFERENCES

- [1] (a) F. M. Fowkes and M. Mostafa, I&EC Prod. Res. Dev. 17, 3 (1978).
(b) M. J. Marmo, et al., I&EC Prod. Res. Dev. 15, 206 (1976).
(c) J. Williams and J. A. Manson, Org. Coatings Plast. Chem. 42, 175 (1980).
- [2] F. Theiler, Corr. Sci. 14, 405 (1974).
- [3] J. A. Manson and L. H. Sperling, "Polymer Blends and Composites," Plenum Press, NY and London, Ch. 12 (1976).
- [4] L. E. Nielsen, J. Macromol. Sci. A1, 928 (1968).
- [5] G. S. Crank and W. R. Park, "Diffusion in Polymers," Academic Press, London (1969).
- [6] W. Funke, U. Zorll and B. G. K. Murphy, J. Paint Tech. 41(530), 210 (1969).
- [7] D. Y. Perera and P. M. Heertjes, J. Oil Col. Chem. Assoc. 54, 774 (1971).
- [8] (a) J. A. Manson and E. H. Chiu, J. Polym. Sci. Symp. 41, 95 (1973).
(b) J. A. Manson and E. H. Chiu, Polym. Preprints 14, 469 (1973).
(c) E. H. Chiu and J. A. Manson, Org. Coat. and Plast. Preprints, American Chemical Society 32, 162 (1972).
- [9] T. K. Ross and J. Wolstenholme, Corr. Sci. 17, 341 (1977).

- [10] J. A. Manson, J. -S. Lin and A. Tiburcio, Org. Coat. and Plast. Chem. 46, 121 (1982).
- [11] Annual Report, ONR Project "Corrosion Resisting Coatings," Lehigh University (1981).
- [12] H. P. Schreiber, M. R. Wertheimer and M. Lambla, J. Appl. Polym. Sci. 27, 2269 (1982).
- [13] E. Nilsson and C. M. Hansen, J. Coatings Tech. 53 (680), 61 (1981).
- [14] K. S. Rajagopalan, S. Guruviah and V. Chandrasekharan, Paintindia 25(7), 13 (1975).
- [15] D. S. Newton and B. M. Guest, J. Oil Col. Chem. Assoc. 48, 382 (1965).
- [16] J. D. Murray, J. Oil Col. Chem. Assoc. 56, 507 (1973).
- [17] C. E. Rogers, "Engineering Design for Plastics," ed. by E. Baer, Van Nostrand-Reinhold, New York, Ch. 9 (1964).
- [18] D. Y. Perera and D. V. Eynde 51(654), 74 (1979).

Program #13. Characterization of the Surface
Properties of Iron Oxides

INTRODUCTION

The development of protective coatings for corrosive materials requires a knowledge not only of the physical properties of the coating, but also the nature of the interaction of the coating with the substrate and the affinity of the metal oxide/coating interface for water. Water plays an essential role in the corrosion of iron [1]. The growth of rust layers on ferrous metals in the atmosphere where water vapor is present, or the retention of water by certain soils are additional examples. In addition, an understanding of the iron oxide-water system should provide insight into the broader problem involving adsorption of polar gas on an ionic solid. The experimental approaches used to study the surface properties of materials require high-surface-area, small-particle-size samples. Mössbauer spectroscopic and X-ray diffraction techniques have shown that α -Fe₂O₃, Fe₃O₄, γ -FeOOH, and β -FeOOH, among others, are present as corrosion products on iron exposed to the atmosphere [2].

Although a large body of literature exists in the area of gas adsorption on metal oxide surfaces, relatively little has been published for the adsorption of gases on iron oxides. Previous investigations in this laboratory by McCafferty and Zettlemoyer [3] studied the interaction of water vapor with α -Fe₂O₃ using heat of immersion [4], dielectric techniques [5,6], and adsorption thermodynamics. They concluded [7] that water vapor chemisorbs on bare α -Fe₂O₃ by a dissociative mechanism to form two hydroxyls per water molecule, the hydroxyl group adsorbing on a surface Fe³⁺ ion and the proton forming a second hydroxyl with an adjacent surface O²⁻ ion. The first layer of physically adsorbed water vapor on the hydroxylated substrate is localized by double hydrogen bonding of a single water molecule to adjacent hydroxyl groups, as was shown by energetic, thermodynamic, and dielectric arguments. The multilayer adsorption was proposed to develop in an ordered ice-like structure. Blyholder and Richardson [8] applied infrared spectroscopy to the investigation of the α -Fe₂O₃/water system. They concluded that physically adsorbed water was completely removed by prolonged outgassing at 25°C and that underlying surface hydroxyls were totally removed at 475°C. Jurinak [9] investigated the interaction of water with α -Fe₂O₃ at various activation temperatures. He showed that about 1/3 of the α -Fe₂O₃ surface is covered with chemisorbed or strongly

adsorbed water which, unless removed by high temperature activation, blocks water adsorption sites on the surface. Morimoto et al. [10] studied the amounts of chemisorbed and physisorbed water on α -Fe₂O₃. They took the hydroxyl groups remaining on the oxide surface into account and reported the ratio of the number of water molecules in the first physisorption layer to that of underlying hydroxyl groups to be about 1:2.

Modifications of surface properties by addition of surface active materials to the surface hydroxyls of silica is relatively common. Hexamethyldisilazane (HMDS) was chosen for this investigation because it reacts quantitatively with surface hydroxyls from the vapor phase even at room temperature. The interaction of HMDS was first reported by Stark et al. [11] and the reaction kinetics have been explored by Hertal and Hair [12,13]. Kiselev and his co-workers [14] examined the reaction of trimethylchlorosilane (TMCS) with silica, as did Hair and Hertal [15] for all the methyl chlorosilanes. Zettlemoyer and Hsing [16,17] first examined water interaction with silane-treated silica by a NIR technique. They explored the possibility of the NH₃ adsorption on HMDS-treated silica. Kiselev and co-workers [18] also investigated the interaction of water with TMCS-treated silicas.

The objectives of this study are concerned with the characterization of the intrinsic surface properties of corrosion products, and the extent and manner in which the surface properties can be changed by pretreatment conditions such as high temperature and chemisorption of surface active materials.

EXPERIMENTAL

The iron oxide samples used in this study were Fe₃O₄ and α -Fe₂O₃ obtained from Pfizer Inc., and α -FeOOH and β -FeOOH precipitated from solution according to experimental techniques described in another section of this report. The current research efforts are currently directed toward an investigation of the iron oxide samples prepared in this laboratory.

The argon gas adsorption isotherms for specific area determination were obtained at liquid nitrogen temperatures using a classical BET volumetric vacuum rig. The residual pressure of 10⁻⁶ Torr was monitored by an ion gauge. A capacitive electronic manometer equipped with a 1000 Torr differential pressure transducer (Datametrics, Inc.) was used to measure the argon gas pressure with a sensitivity of 10⁻³ Torr. Specific areas were calculated for argon molecular cross-section of 17 Å². The water adsorption isotherms were measured on a quartz spring (Worden Quartz Co.) balance with a sensitivity of 10 µg/g of sample. The

equilibrium water vapor pressure was measured with a 100 Torr capacitive differential manometer (Datametrics, Inc.).

The heats of immersion were measured in a thermistor type adiabatic calorimeter. The temperature changes in the calorimeter vessel were followed by measuring the change in resistance of the thermistor in a Wheatstone bridge and recording the off-balance of the bridge after amplification by a Hewlett-Packard DC Null Voltmeter 419A. The workable sensitivity was $1 \times 10^{-4}^{\circ}\text{C}$ with a background noise of $2 \times 10^{-4}^{\circ}\text{C}$ in water. The sources of error in this calorimeter, i.e., instrument sensitivity, reproducibility of heat of bulb breaking, and reproducibility of heat capacity determination led to a cumulative error of $+0.2\text{J}$ for each heat of immersion measurement.

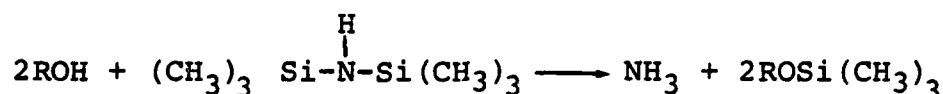
RESULTS AND DISCUSSION

Solid/Gas Interface

Water adsorption isotherm results had previously been reported on $\alpha\text{-Fe}_2\text{O}_3$ and Fe_3O_4 samples (Pfizer Inc.), and preliminary results on $\alpha\text{-Fe}_2\text{O}_3$ after treatment with hexamethyldisilazane, HMDS. This approach has been continued for HMDS-treated $\alpha\text{-Fe}_2\text{O}_3$ and Fe_3O_4 , and on $\alpha\text{-FeOOH}$ and $\beta\text{-FeOOH}$ which had been prepared in this laboratory. The experimental approach adopted here is designed to determine the degree of surface hydrophilicity of iron oxides as a function of activation temperature in the range of 25° to 400°C and after hydrophobing the surface with HMDS. The procedure measures the weight loss as a function of activation temperature, the water adsorption isotherms at 25°C after activation at the specified elevated temperature, and a second series of isotherms which follows the previous series after activation at 25°C . The intent is to compare the weight loss results to the amount of irreversibly adsorbed water after each isotherm, and also the decrease in monolayer capacity of the second isotherm activated at 25°C compared to the first isotherm which was activated at the elevated temperature. Since the intrinsic surface properties of the iron oxide samples are sought in this approach, the specific surface area, as determined from a BET analysis of argon adsorption isotherms at -195°C , was measured as a function of activation temperature.

One approach to hydrophobe iron oxide is by chemical treatment of the surface. Since surface hydroxyl groups on iron oxides are primarily responsible for the adsorption of water, the approach was to chemically treat these hydroxyls so as to render them hydrophobic. Silanes, in general, are known to react with the proton of hydroxyls whether they are part of the surface, or

of an organic or inorganic molecule. Hexamethyldisilazane, HMDS, was used to treat α -Fe₂O₃ and Fe₃O₄ according to the following reaction:



where R represents the iron oxide surfaces. HMDS adsorption isotherms were measured on α -Fe₂O₃ and Fe₃O₄ after activated at 100 and 400°C. Water adsorption isotherms were measured on these samples after the HMDS treatment and the results, with and without the HMDS treatment, are summarized in Tables I and II. Since it is assumed that the chemisorbed HMDS occurs according to the above chemical reaction, the amount of HMDS adsorbed is expressed in terms of trimethyl/silicon groups/100 Å². The irreversibly adsorbed HMDS, therefore, is expected to be due to chemisorbed trimethyl silicon. Although Zettlemoyer and Hsing [16] indicated the possibility of NH₃ adsorption, Blyholder and Richardson [8] showed that NH₃ upon chemisorption occupied the same surface site as H₂O which indicates that after HMDS reacts with surface hydroxyls, instead of being strongly adsorbed on surface hydroxyls, NH₃ stays on top of physisorbed water and does not contribute to the amount of irreversibly adsorbed HMDS.

The HMDS adsorption results for α -Fe₂O₃, Figure 1, show that the adsorption is more pronounced after 400°C activation. The amount of irreversibly adsorbed trimethyl/silicon was found to be 1.04 and 1.77 -Si(CH₃)₃ groups/100 Å² for the 100° and 400°C activated sample, respectively. The Fe₃O₄ results, on the contrary, show that HMDS adsorption is high for 100°C activation as indicated in Figure 2. The concentrations of irreversibly adsorbed trimethyl/silicon on Fe₃O₄ were 1.80 and 1.55 -Si(CH₃)₃ groups/100 Å² for 100° and 400° activation. It is interesting to note that the amount of chemisorbed trimethyl/silicon groups is proportional to surface hydroxyl concentration, the difference in monolayer values between first and second isotherm of untreated sample, and the ratio is 1/3 and 1/2 -Si(CH₃)₃/-OH for α -Fe₂O₃ and Fe₃O₄. The indication was that the surface hydroxyls were modified to -O-Si(CH₃)₃ on α -Fe₂O₃ and Fe₃O₄. If we assume one strongly adsorbed water molecule is adsorbed on two surface hydroxyls, it is reasonable to say that one -O-Si(CH₃)₃, with a cross sectional area of 40 Å² at most will be formed after removal of one strongly adsorbed water, which is the case for Fe₃O₄.

The first and second water adsorption isotherms for the HMDS-treated and untreated α -Fe₂O₃ activated at 100°C are presented in Figure 3. The monolayer results in Table I show that there is only a small decrease in water monolayer value after HMDS treatment. The monolayer values for the second isotherm shows a larger decrease, 0.87 molecules/100 Å². Another significant feature of the water adsorption results in the decrease in adsorbed water in

Table I

Gas Adsorption Results on α -Fe₂O₃ Treated with HMDS
after Temperature Activation

Activation Temp., °C	Treatment after Activation	Irreversibly Adsorbed		Irreversibly Adsorbed Water		W_{m1}^*		W_{m2}^{**}		$W_{m1}-W_{m2}$		W_m^{***}
		HMDS	$\text{Si}(\text{CH}_3)_3 / 100 \text{ \AA}^2$	100 \AA^2	molecules/	molecules/	molecules/	molecules/	molecules/	molecules/	molecules/	
					100 \AA^2	100 \AA^2	100 \AA^2	100 \AA^2	100 \AA^2	100 \AA^2	100 \AA^2	$\text{Si}(\text{CH}_3)_3 / 100 \text{ \AA}^2$
100	none	--		2.72		2.35	7.44	1.82	5.78	0.53	1.66	--
100	HMDS	1.04		0.64		2.22	7.04	1.55	4.91	0.67	2.13	1.04
400	none	--		6.26		2.16	8.80	1.52	6.20	0.64	2.60	--
400	HMDS	1.77		4.17		1.67	6.80	0.76	3.10	0.91	3.70	3.38

*First water adsorption isotherm monolayer at 25°C after indicated activation temperature and treatment.

**Second water adsorption isotherm monolayer at 25°C after activation at 25°C.

***HMDS adsorption isotherm monolayer at 25°C after indicated activation temperature.

Table II

Gas Adsorption Results on Fe_3O_4 Treated with HMDS
after High Temperature Activation

Activation Temp., °C	Treatment after Activation	Irreversibly Adsorbed HMDS $\text{Si}(\text{CH}_3)_3$ / 100 Å ²	Irreversibly Adsorbed Water molecules/ 100 Å ²	W_{m1}^*		W_{m2}^{**}		$W_{m1}-W_{m2}$		W_{m2}^{***}
				molecules/ mg/g	100 Å ²	molecules/ mg/g	100 Å ²	molecules/ mg/g	100 Å ²	$\text{Si}(\text{CH}_3)_3$ / 100 Å ²
100	none	--	2.24	2.15	9.41	1.77	7.77	0.37	1.64	--
100	HMDS	1.80	1.41	1.20	5.25	0.87	3.80	0.33	1.45	2.64
400	none	--	3.37	1.95	6.76	1.55	5.38	0.40	1.39	--
400	HMDS	1.55	2.47	1.31	4.55	0.85	2.95	0.46	1.60	1.89

*First water adsorption isotherm monolayer at 25°C after indicated activation temperature and treatment.

**Second water adsorption isotherm monolayer at 25°C after activation at 25°C.

***HMDS adsorption isotherm monolayer at 25°C after indicated activation temperature.

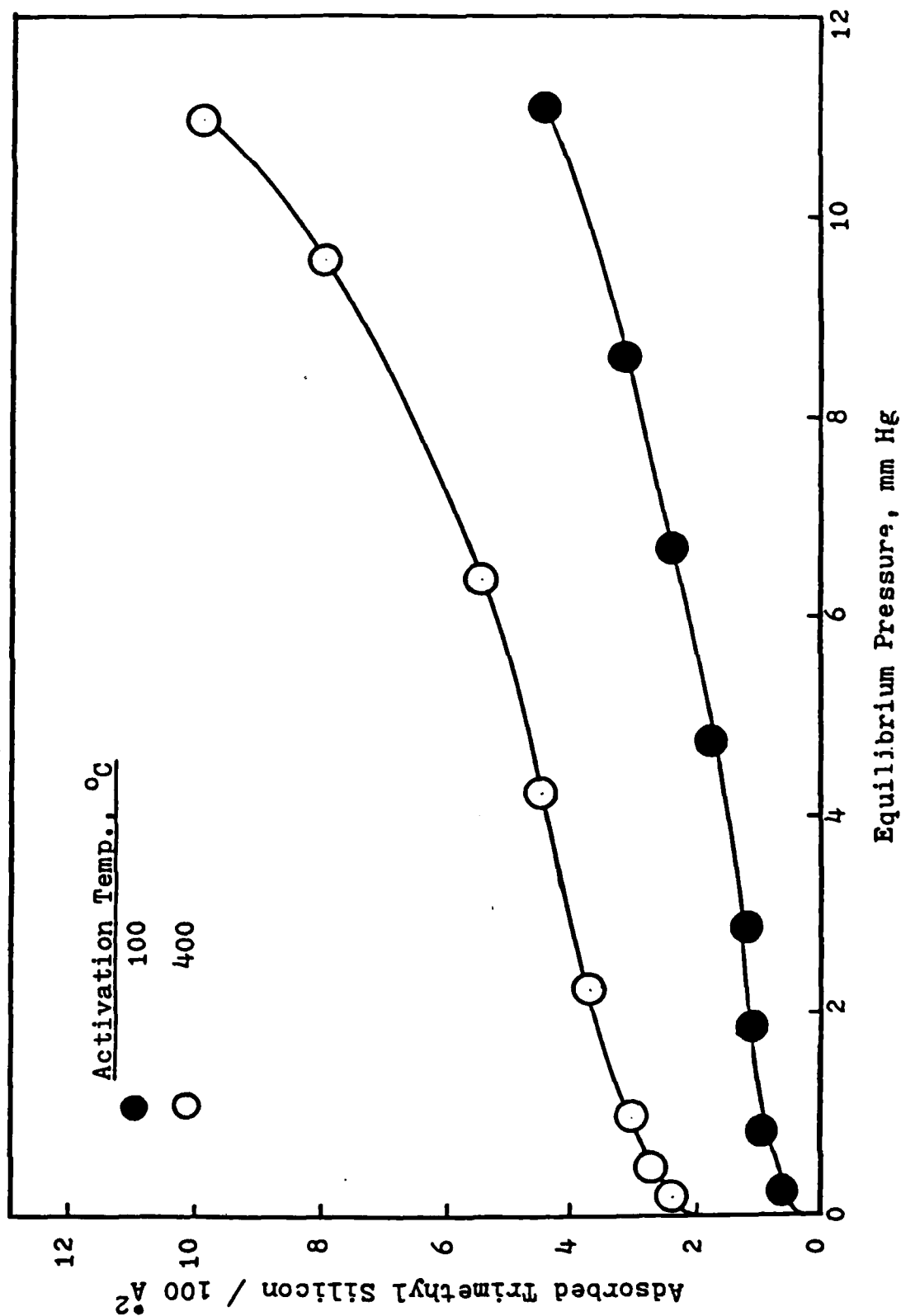


Figure 1. Adsorption isotherm of HMDS on $\alpha\text{-Fe}_2\text{O}_3$ after activation at 100 and 400°C.

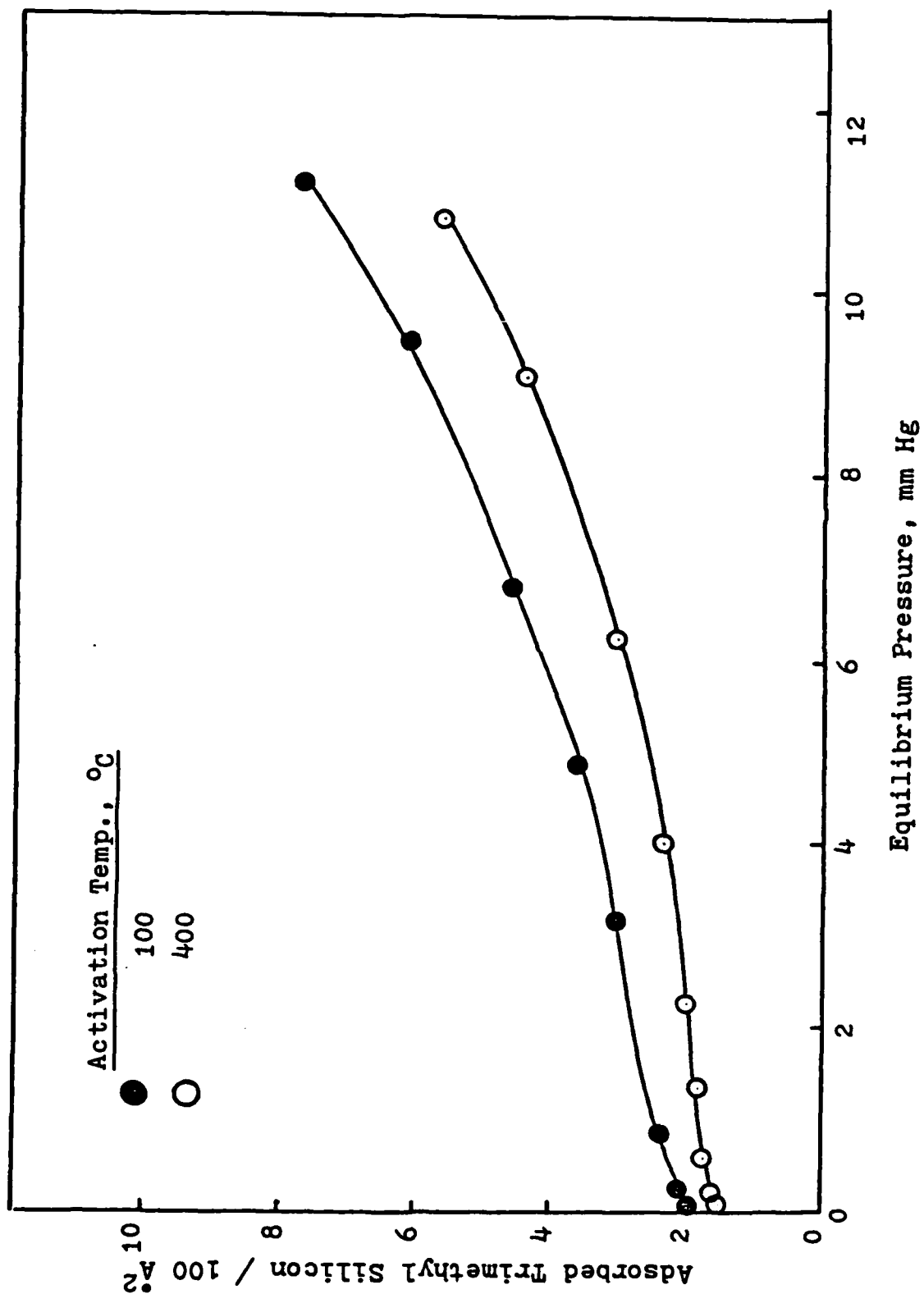


Figure 2. Adsorption isotherm of HMDS of Fe_3O_4 after activation at 100 and 400°C.

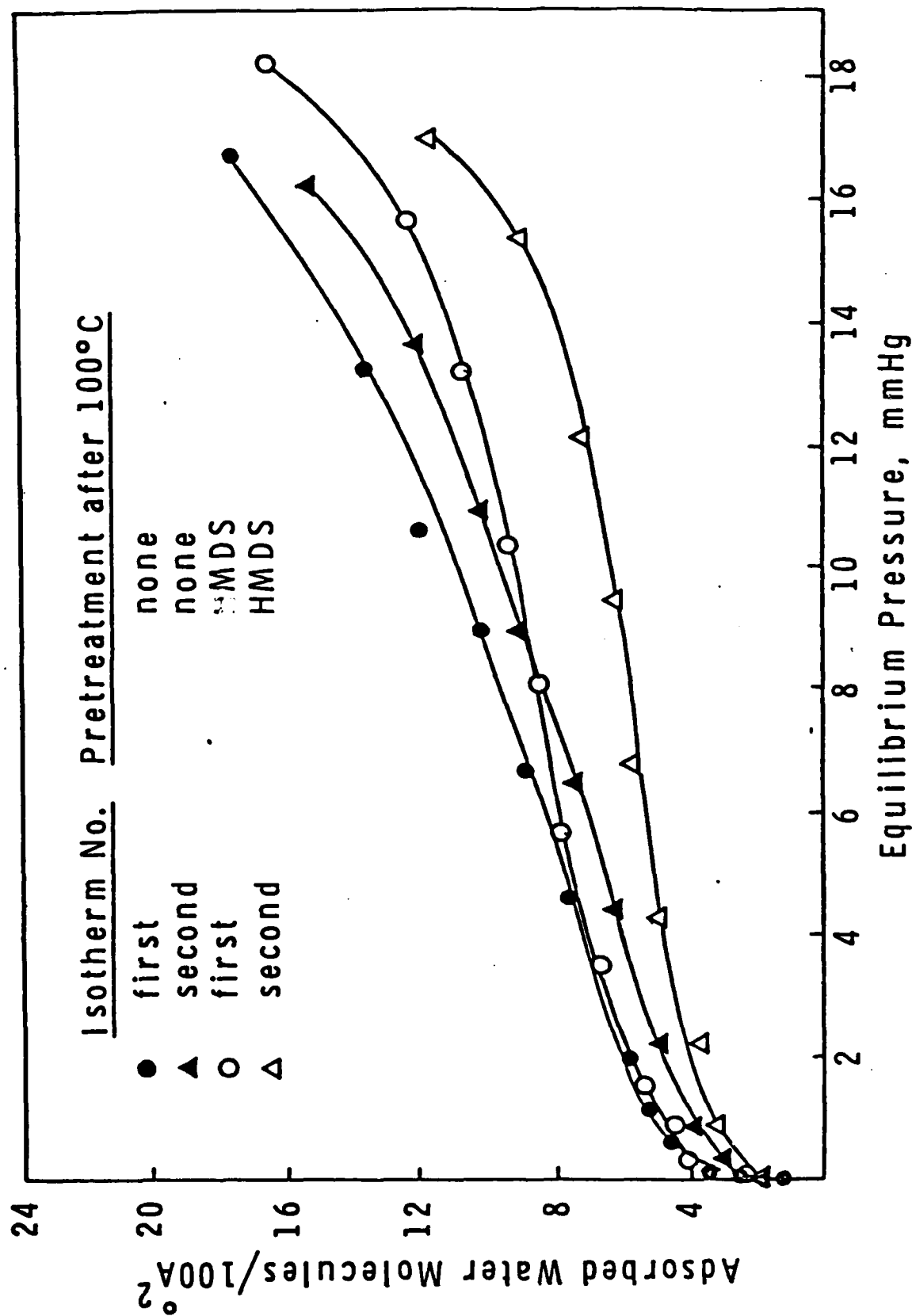


Figure 3. Water adsorption isotherm on $\alpha\text{-Fe}_2\text{O}_3$ after activation at 100°C and with and without pretreated HMDS.

the multilayer region for the HMDS treated samples. Figure 4 presents the water adsorption isotherms for the HMDS-treated and untreated α -Fe₂O₃ activated at 400°C. The irreversibly, or chemically, adsorbed water is reduced by 2.0 molecules/100 Å², which is in good agreement with the irreversibly adsorbed HMDS results. It is also significant to note from the water adsorption results in Figure 4 that the amount adsorbed is much less for the HMDS-treated sample in the multilayer region. It should be noted here that the difference in the monolayer value of the first and second isotherm is larger for HMDS-treated samples than untreated sample. The indication may be that the umbrella shape of the -O-Si(CH₃)₃ groups do not completely sterically hinder first layer water adsorption to surface hydroxyls where 2/3 of the original adsorption sites remain. They do, however, interfere with the multilayer water adsorption, primarily the second and third physisorbed layers as indicated by a decrease in adsorption at high relative pressures (Figs. 3 and 4).

The water adsorption results for HMDS-treated and untreated Fe₃O₄ activated at 100°C are presented in Figure 5. The monolayer results, Table II, show that there is a decrease of 4.16 molecules/100 Å² in the first isotherm monolayer values and a 4.17 molecules/100 Å² decrease in the second isotherm monolayer values for irreversibly adsorbed HMDS value of 1.80 -Si(CH₃)₃ groups/100 Å², which is in good agreement with the concept of one -Si(CH₃)₃ blocking two sites. There is a significant decrease in adsorption in the multilayer region for HMDS-treated samples. Figure 6 presents the water adsorption isotherms for HMDS-treated and untreated Fe₃O₄ activated at 400°C. The irreversibly adsorbed HMDS is less for this sample, 1.55 -Si(CH₃)₃ groups/100 Å², and the result is a smaller reduction in the first water monolayer value of 2.21 molecules/100 Å² and in the second water monolayer value of 2.43 molecules/100 Å². It is also significant to note that the amount of water in the multilayer region for the HMDS-treated sample is decreased as compared to the untreated sample.

Water adsorption isotherms were measured on α -FeOOH, which was prepared in this laboratory, as a function of activation temperature in the range of 25° to 400°C. The results, summarized in Table III, show that the specific surface area of 56 M²/g remains constant up to 200°C where it increases to a maximum of 134 M²/g followed by a decrease to 40 M²/g at 400°C activation. A color change from yellow to red was observed at 200°C indicating a change in crystal structure to α -Fe₂O₃. The water monolayer values at 25°C for the first isotherm as a function of activation temperature show that the surface is 100% hydrophilic up to and including 200°C and becomes relatively hydrophobic at higher temperatures. The cumulative weight loss, third column of Table III, as a function of activation temperature, is much greater than can be accounted for by the irreversibly adsorbed water at activation temperatures of 200°C and higher. These results, however, are consistent with the dehydration conversion of FeOOH to Fe₂O₃.

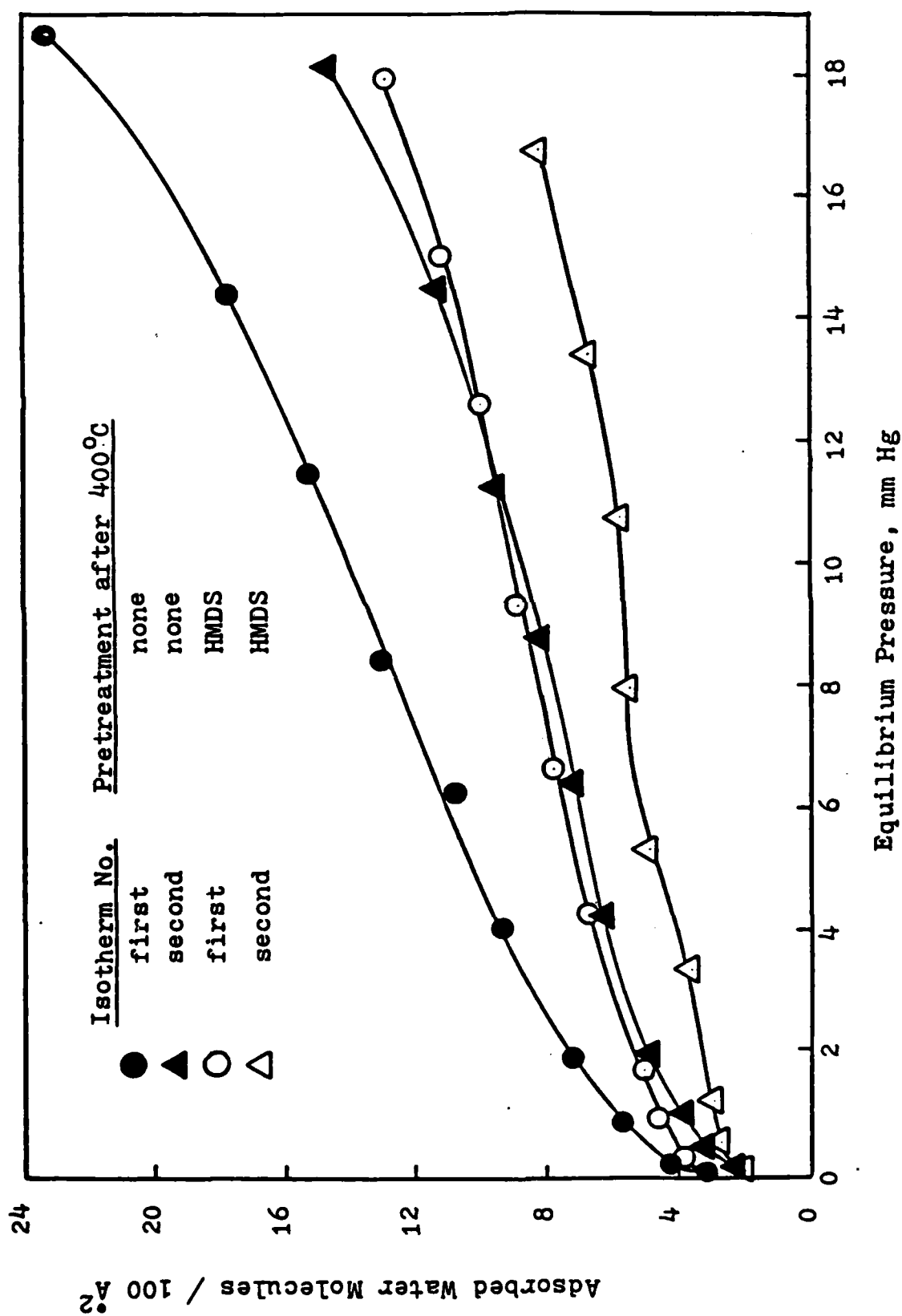


Figure 4. Water adsorption isotherm on $\alpha\text{-Fe}_2\text{O}_3$ after activation at 400°C and with and without pretreated HMDS.

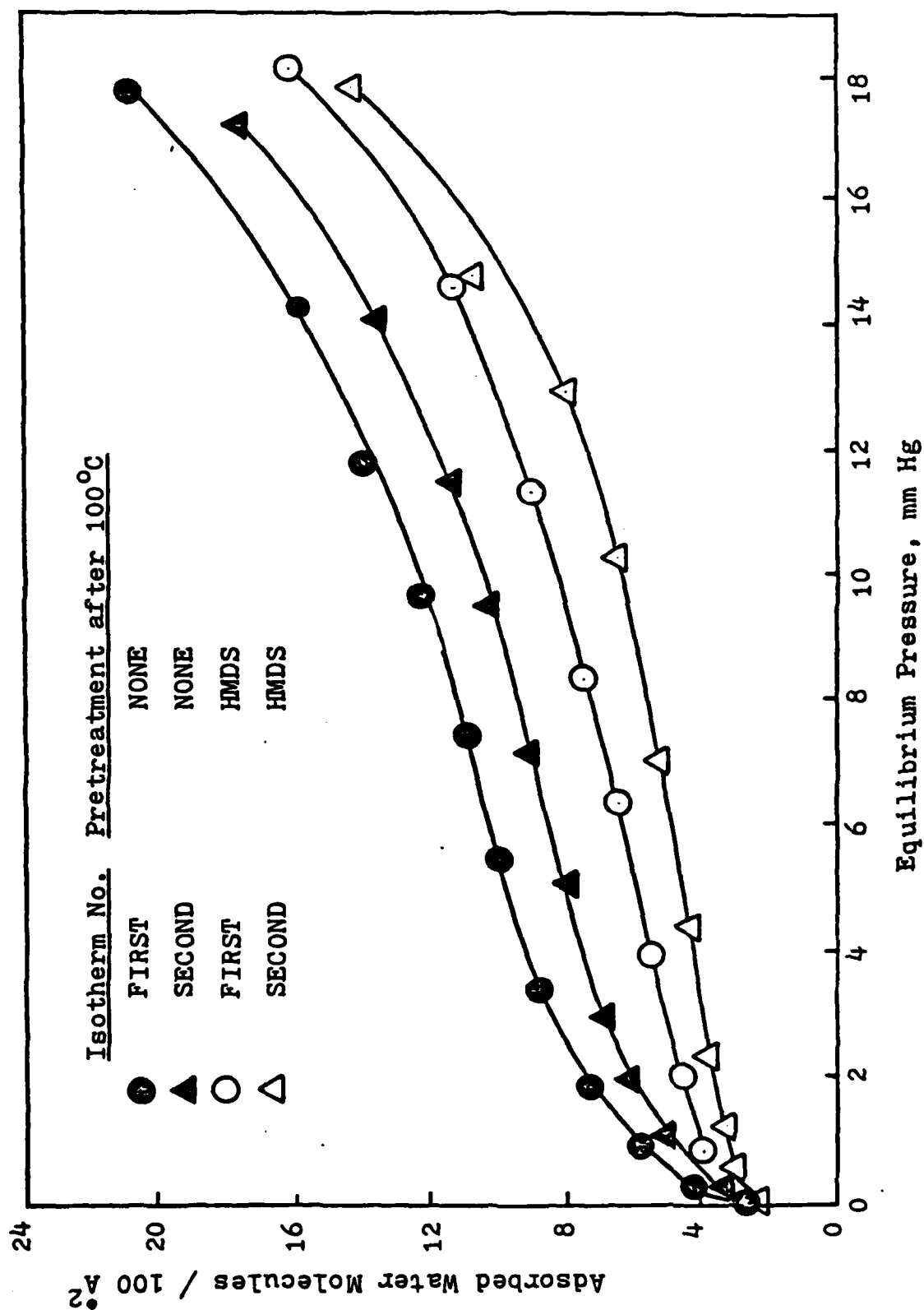


Figure 5. Water adsorption isotherm of Fe_3O_4 after activation at 100°C and with and without pretreated HMDS.

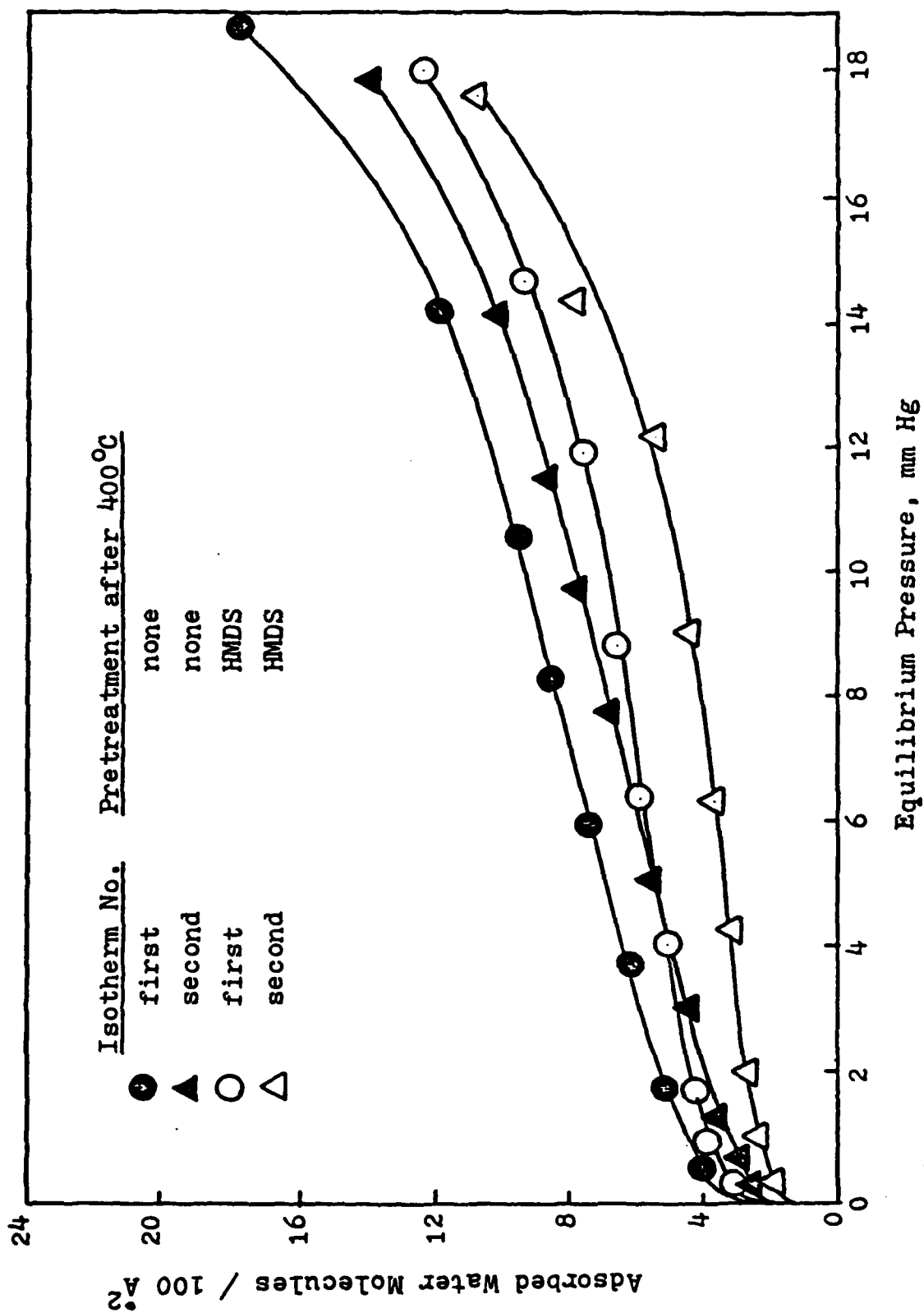


Figure 6. Water adsorption isotherm on Fe_3O_4 after activation at 400°C and with and without pretreatment HMDS.

Table III
Gas Adsorption Results on α -FeOOH and HMDS Treated α -FeOOH

α -FeOOH										
Activation Temp., °C	Specific Surface Area (m ² /g)	Wt. Loss mg/g	W _{ml} *		W _{m2} **		W _{ml} -W		Irreversibly Adsorbed Water	
			mg/g	molecules/100 Å ²	mg/g	molecules/100 Å ²	mg/g	molecules/100 Å ²	mg/g	mg/g
25	56	--	18.0	10.0	--	--	--	--	--	1.6
100	60	8.1	18.0	9.5	12.2	7.8	5.8	1.7	--	5.1
200	134	90.6	44.0	11.5	34.0	8.8	10.0	2.7	--	8.0
300	117	133.9	5.0	2.0	5.0	2.0	0	0	--	2.3
400	40	161.4	1.8	1.5	1.8	1.5	0	0	--	1.9

HMDS Treated α -FeOOH after 100°C Activation										
25	60	--	10.2	5.8	11.0	6.0	0	0	--	0.9
100	60	4.7	14.0	7.8	9.2	4.2	5.2	3.6	--	7.5
200	134	78.4	35.0	8.0	17.2	3.2	17.8	4.8	--	17.1
300	117	105.7	13.8	3.6	9.4	2.0	4.4	1.6	--	9.5
400	40	123.1	7.8	5.6	5.8	4.0	3.0	1.6	--	5.7

*First water adsorption isotherm monolayer at 25°C after indicated activation temperature.

**Second water adsorption isotherm monolayer at 25°C after activation at 25°C.

An adsorption isotherm of HMDS was measured on α -FeOOH after activation at 100°C. The results, Figure 7, plotted in units of adsorbed trimethyl silicon groups/100 Å², show that a monolayer value is reached at two groups/100 Å². Desorption of the sample showed that 1.5 trimethyl silicon groups/100 Å² were irreversibly adsorbed. Water adsorption isotherms were subsequently measured at 25°C on this HMDS pretreated sample as a function of activation temperature. The water adsorption isotherms for the untreated and HMDS pretreated α -FeOOH are presented in Figures 8-12 for the activation temperatures of 25°, 100°, 200°, 300°, and 400°C, respectively. The results, summarized in Table III, show that the HMDS treatment has a definite effect on hydrophobing the α -FeOOH surface in the activation temperature range of 25° to 200°C. At temperatures above 200°C the HMDS treatment appears to render the surface more hydrophilic. The weight loss results as a function of activation temperature, however, show that the HMDS-treated sample loses much less weight with increasing temperature than the untreated sample. The interpretation of these results is that the dehydration of the surface hydroxyls, via adjacent hydroxyl groups, is hindered in the presence of the chemically bound trimethyl silicon groups. It should also be noted that the irreversibly adsorbed water on the HMDS-treated α -FeOOH at activation temperatures above 200°C is much greater than the untreated sample indicating that the strong physically adsorbed water which desorbs at the higher temperatures is not readily desorbed at 25°C in the presence of trimethyl silicon groups due to steric hindrance.

Water adsorption isotherm measurements have been initiated on β -FeOOH. The amount of water was found to increase with increasing activation temperature probably due to an increase in specific surface area, which measurements have yet to be completed. This work will continue with the HMDS treatment in order to determine the degree of similarity in surface properties of the β -FeOOH with the other iron oxide samples which have been investigated.

Heats of Immersion

Heats of immersion in water were measured on α -Fe₂O₃ activated at 100° and 400°C, and on HMDS treated α -Fe₂O₃ after 400°C activation. The heats of immersion results as a function of concentration of preadsorbed water are presented in Figure 13. The results at zero water coverage show that the 400°C activated sample exhibits a higher heat of wetting than the 100°C activated and HMDS-treated samples. The 100°C activated sample, furthermore, remains below the 400°C sample, while the HMDS activated sample acquires a higher heat of wetting value up to the indicated monolayer value after which it undergoes a decrease. The interpretation of these results is that strong physically adsorbed water is desorbed at 100°C and then readsorbed at 25°C, which is the temperature of the heats of immersion measurement, and that chemically adsorbed water, which is in the form of hydroxyls, are desorbed at 400°C and low

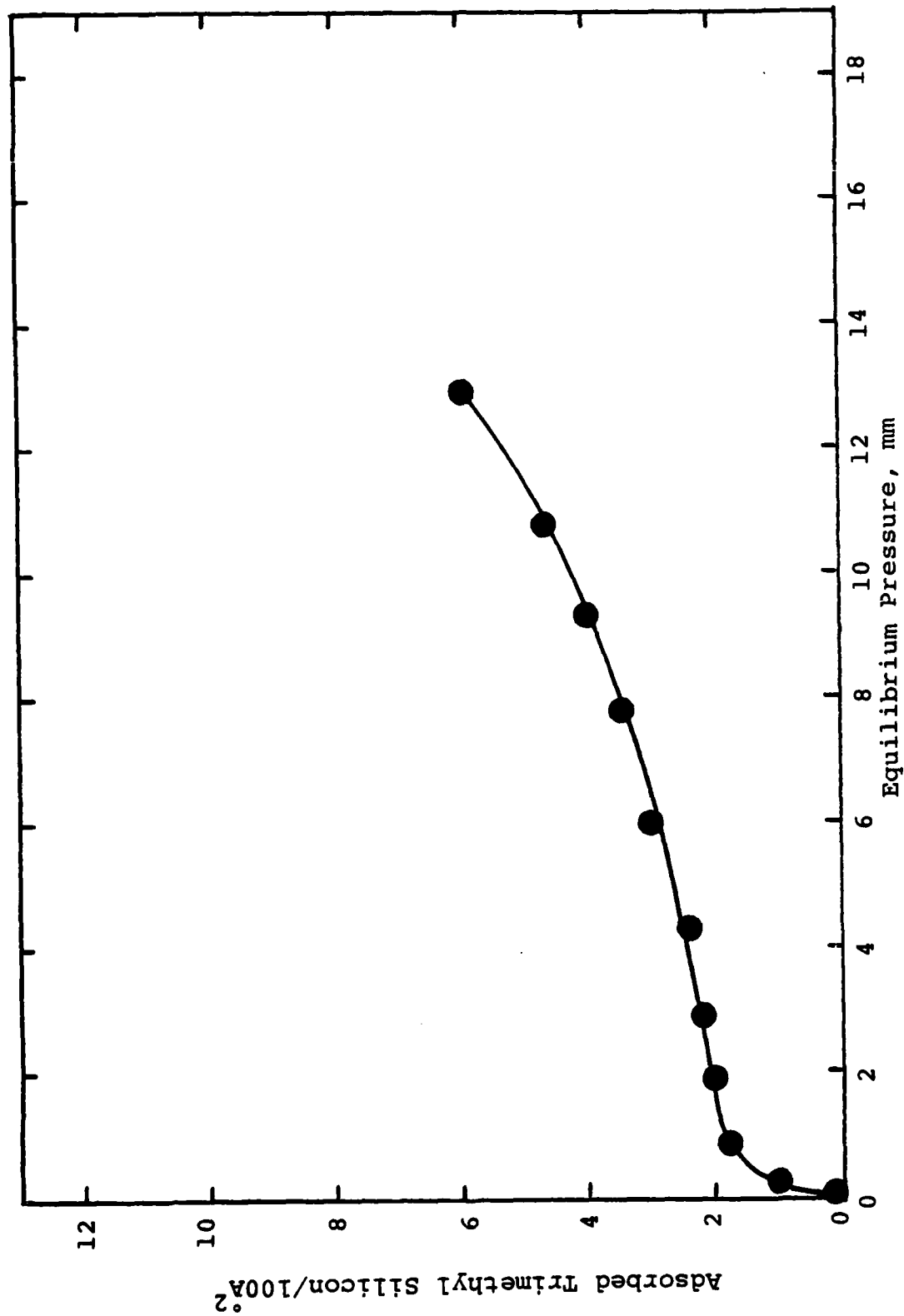


Figure 7. Adsorption Isotherm of HMDS on α -FeOOH after Activation at 100°C.

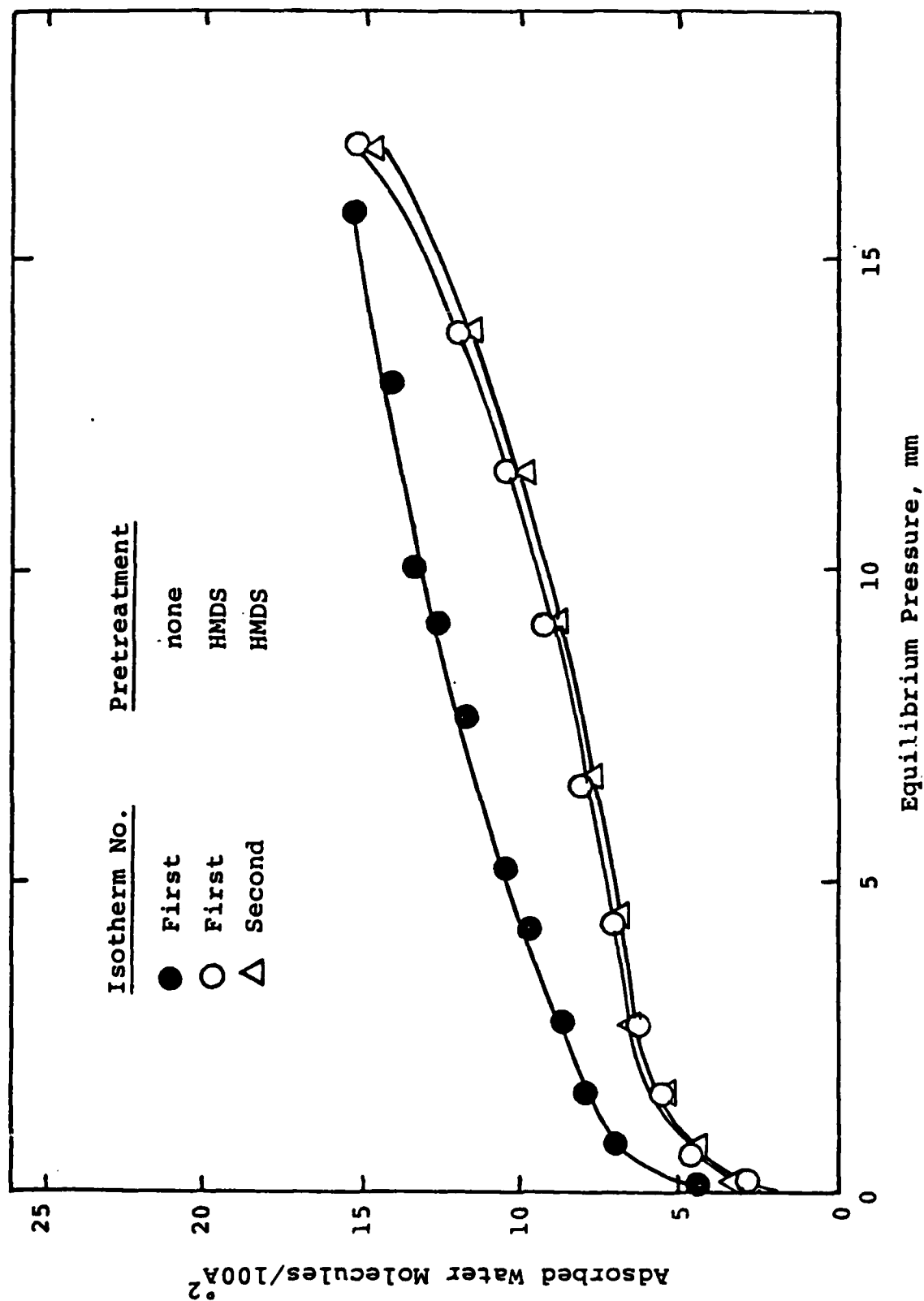


Figure 8. Water adsorption isotherms at 25°C after 25°C activation on α -FeOOH with and without pretreatment of HMDS.

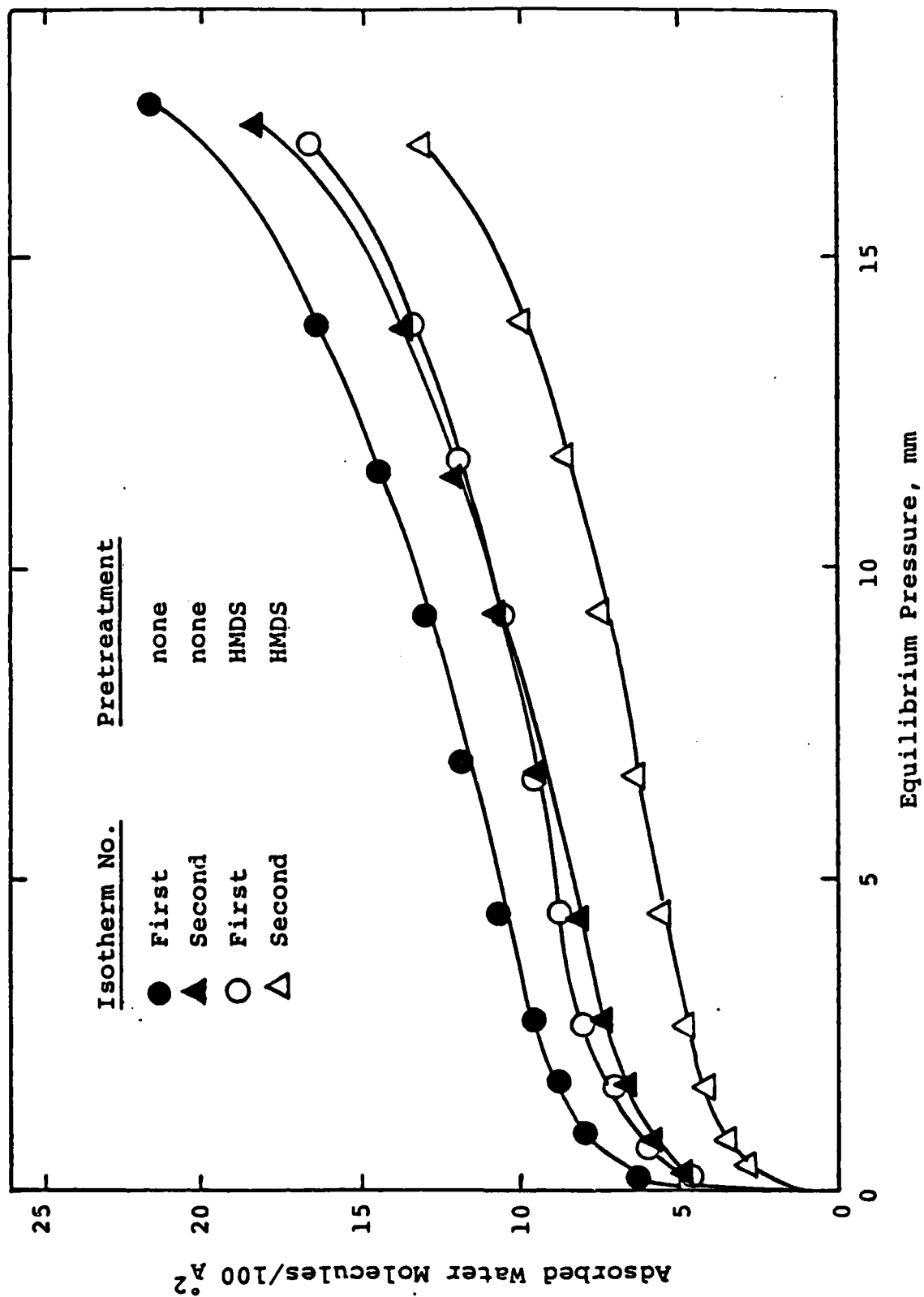


Figure 9. Water adsorption isotherms at 25°C after 100°C activation on α -FeOOH with and without pretreatment of HMDS.

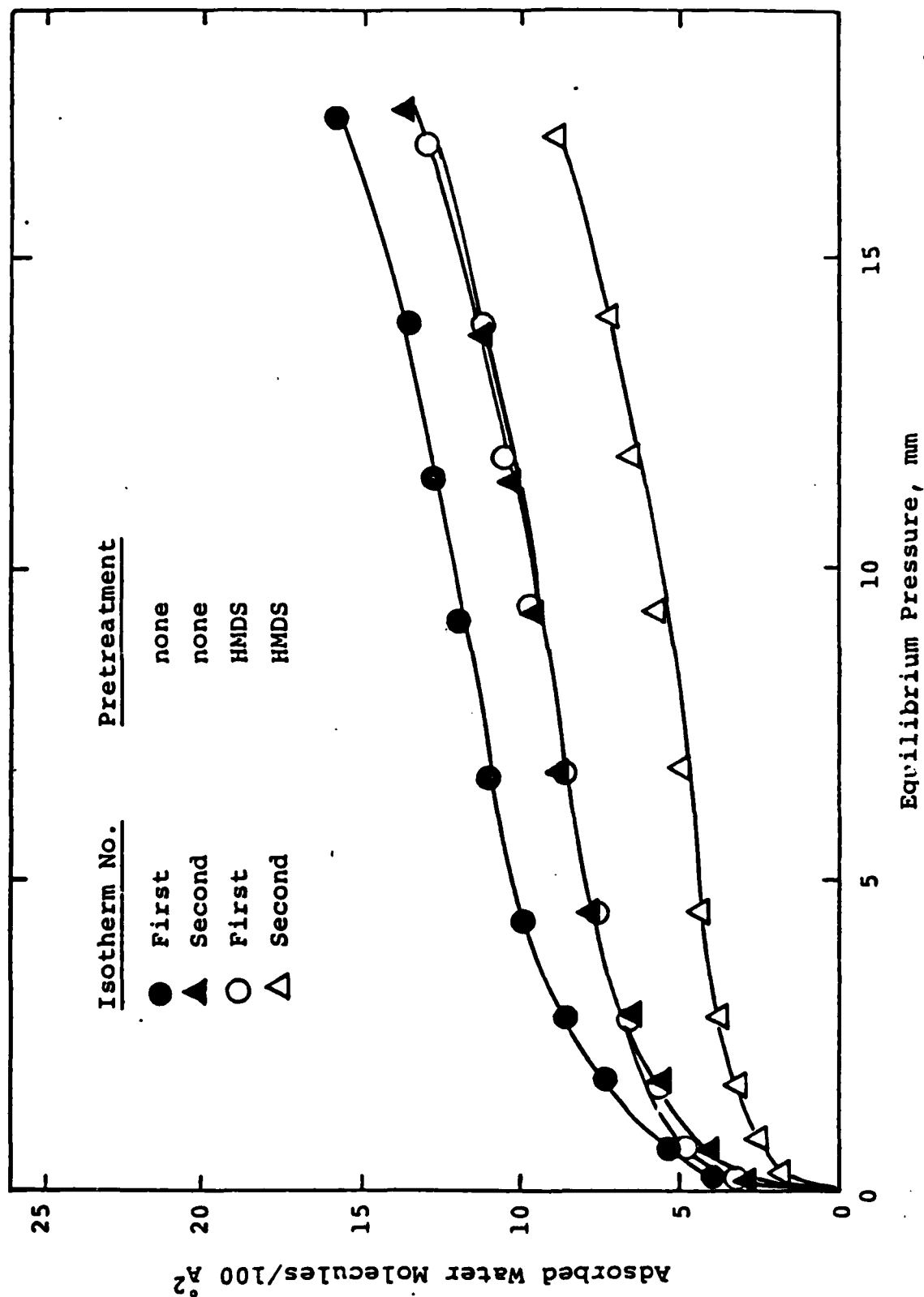


Figure 10. Water adsorption isotherms at 25°C after 200°C activation on α -FeOOH with and without pretreatment of HMDS.

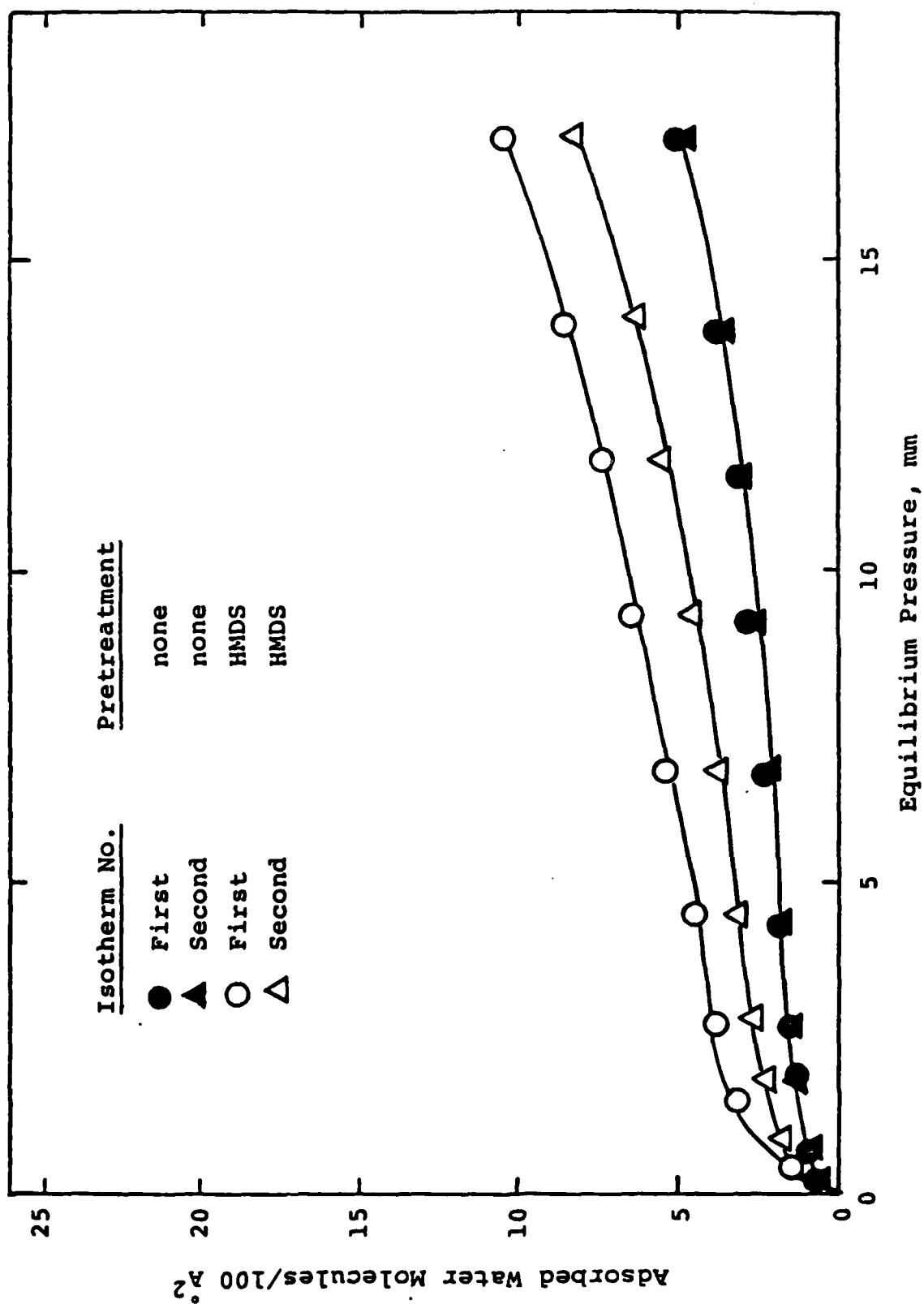


Figure 11. Water adsorption isotherms at 25°C after 300°C activation on α -FeOOH with and without pretreatment of HMDS.

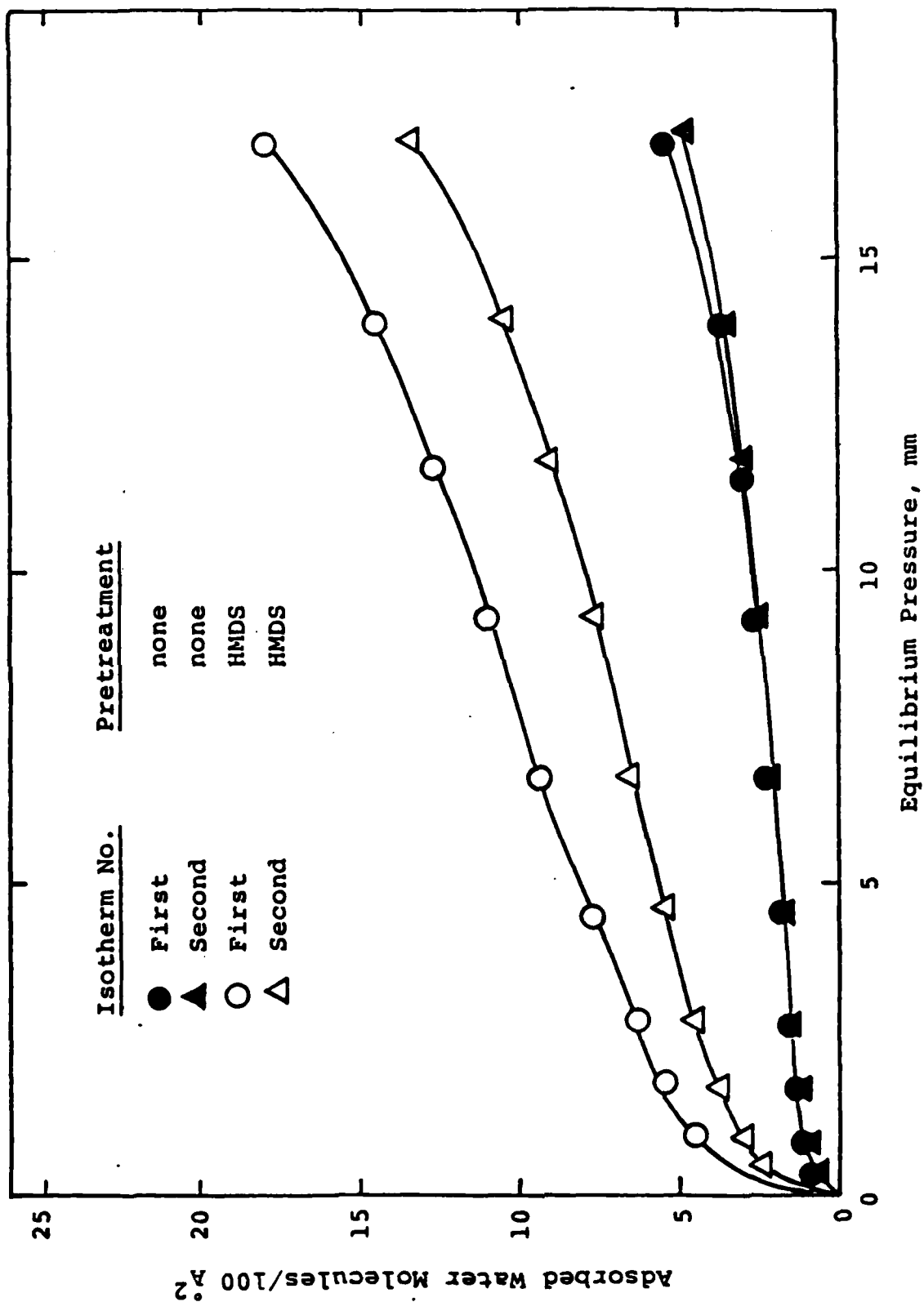


Figure 12. Water adsorption isotherms at 25°C after 400°C activation on α -FeOOH with and without pretreatment of HMDS.

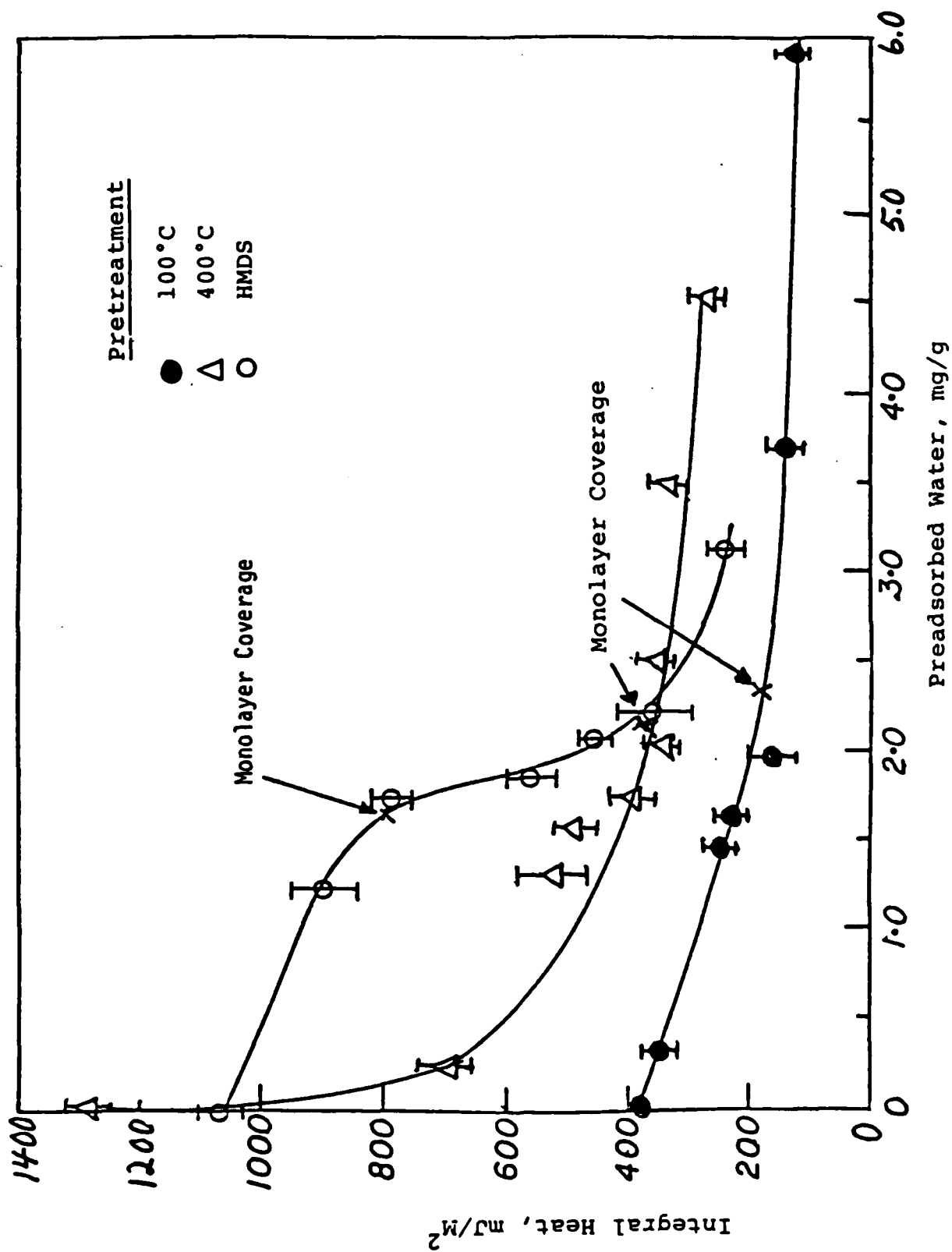


Figure 13. Heats of immersion as a function of water coverage of heat treated and HMDS treated α -Fe₂O₃.

concentrations are readsorbed at 25°C. Although chemically bound water may also be involved in the HMDS-treated sample, the primary heat contribution may be due to steric hindrance brought about by the presence of chemically bound trimethyl silicon. A clarification of the interpretation of these results requires further experiments, especially with the FeOOH samples as a function of pretreatment conditions. These experiments are specially significant because of the purity of the iron oxide samples prepared in this laboratory.

CONCLUSIONS

The HMDS treatment has a pronounced effect on decreasing the surface hydrophilicity of both α -Fe₂O₃ and Fe₃O₄, and probably by replacing the proton of surface hydroxyl with a trimethyl/silicon group. For α -Fe₂O₃, this effect is more pronounced for the sample activated at 400°C than 100°C due to the fact that the surface hydroxyl concentration is higher for the 400°C activated sample than the 100°C activated sample. The results for Fe₃O₄, by contrast, show that the effect of increasing surface hydrophobicity is more pronounced for the sample activated at 100°C than 400°C which is in good agreement with higher surface hydroxyl concentration for the 100°C activated sample. There appears to be a close one-to-two and one-to-three correlation between the concentration of irreversibly adsorbed trimethyl/silicon and the surface hydroxyl concentration for α -Fe₂O₃ and Fe₃O₄, respectively. The departure from one-to-one correlation is due to the steric effect and unequally spaced surface hydroxyls.

The surface of α -FeOOH is strongly hydrophilic and this degree of hydrophilicity is maintained at activation temperatures up to 200°C. Higher activation temperatures render the surface hydrophobic by the proposed mechanism of dehydroxylation of the surface, and subsequent exposure of the surface to water vapor indicates that the surface does not rehydroxylate. Exposure of the α -FeOOH surface to HMDS after 100°C activation reduces the degree of surface hydrophilicity by 40% with a trimethyl silicon to hydroxyl site ratio of one to two. The adsorption of HMDS, furthermore, has the effect of reducing dehydroxylation of the surface at activation temperatures above 200°C.

Heats of immersion of α -Fe₂O₃ in water as a function of activation temperature and HMDS treatment indicate that physically bound water is removed at 100°C and that limited dehydroxylation occurs at 400°C, but that the surface is rehydroxylated upon exposure to water vapor at room temperature. The HMDS treatment of α -Fe₂O₃ after 100°C activation has a small effect on reducing surface hydrophilicity, but does increase the energy of water

adsorption. The different surface properties exhibited by α -FeOOH and α -Fe₂O₃ and Fe₃O₄ may be due to surface-modifying agents present on the latter two samples which were obtained from Pfizer Inc. The verification of this concept is being pursued by investigating the same iron oxides prepared in this laboratory.

Further studies of the surface properties of iron oxide corrosion products will continue with samples prepared in this laboratory. Heats of immersion will continue and diffuse infrared spectroscopy will be employed to verify the proposed hypothesis and to define the conditions necessary for effectively hydrophobing iron oxide surfaces. The chemical treatment of the surface, furthermore, will not necessarily be limited to HMDS, but will be extended to other molecules such as silanes with different and smaller functional groups.

REFERENCES

- [1] T. A. Banfield, Progress in Organic Coatings 7, 253 (1979).
- [2] M. J. Graham and M. Cohen, Corrosion 32, 432 (1976).
- [3] E. McCafferty and A. C. Zettlemoyer, J. Colloid Interface Sci. 34, 452 (1970).
- [4] A. C. Zettlemoyer and E. McCafferty, Z. Phys. Chem. N. F. 64, 41 (1969).
- [5] E. McCafferty and A. C. Zettlemoyer, Trans. Faraday Soc. 66, 1720 (1970).
- [6] E. McCafferty and A. C. Zettlemoyer, Trans. Faraday Soc. 66, 1732 (1970).
- [7] E. McCafferty and A. C. Zettlemoyer, Disc. Faraday Soc. 52, 239 (1971).
- [8] G. Blyholder and E. A. Richardson, J. Phys. Chem. 66, 2597 (1962).
- [9] J. J. Jurinak, J. Colloid Sci. 19, 477 (1964).
- [10] T. Morimoto, M. Nagao, and F. Tokuda, J. Phys. Chem. 73, 243 (1968).
- [11] F. O. Stark, O. K. Johannson, G. E. Vogel, R. G. Chaffee, and R. M. Lacefield, J. Phys. Chem. 72, 2750 (1968).

- [12] W. Hertal and M. L. Hair, J. Phys. Chem. 75, 181 (1971).
- [13] M. L. Hair, J. Colloid Interface Sci. 60, 154 (1977).
- [14] V. Y. Davydov, A. V. Kiselev, and L. T. Zhuravlev, Trans. Faraday Soc. 60, 2254 (1964).
- [15] M. L. Hair and W. Hertl, J. Phys. Chem. 73, 2372 (1969).
- [16] A. C. Zettlemoyer and H. H. Hsing, J. Colloid Interface Sci. 55, 637 (1976).
- [17] A. C. Zettlemoyer and H. H. Hsing, J. Colloid Interface Sci. 58, 263 (1977).
- [18] A. V. Kiselev, B. V. Kuzhetsov, and S. N. Lanin, J. Colloid Interface Sci. 69, 148 (1979).

Program #14. An Understanding of the Principles Related
to the Application of Paints to Rusted Steel Surfaces
with Little or No Surface Preparation

INTRODUCTION

The purpose of this work is to develop a fundamental understanding of the adhesion of polymer coatings to the various iron corrosion products and to investigate the coating of rusted steel surfaces after removal of only the loose surface rust. An effective coating must wet and penetrate through the porous rusted layer and bind firmly to the underlying solid substrate so as to prevent further corrosion. Wetting and adsorption studies require significant surface areas for accurate measurements. To give the requisite large surface areas, iron corrosion products were prepared in the form of colloidal sols by: (i) aqueous precipitation reactions followed by transfer of the colloidal particles to organic media; (ii) dispersion of commercial iron corrosion products in organic media. In both cases, the colloidal form gives the large surface areas needed for accurate determination of polymer adsorption isotherms. From the thermodynamic point of view, the adsorption interaction at the interface is determined by the work of adhesion of the polymer to the solid surface. The work of adhesion comprises contributions from several types of interactions, especially acid-base interactions. Therefore, the adsorption results were interpreted according to the Fowkes-Manson acid-base interaction scheme [1,2], which characterizes all compounds as Lewis acids or bases and allows selection of coating vehicle and solvents on the same bases.

Eight compounds have been identified as corrosion products of iron: Fe_3O_4 , $\alpha\text{-Fe}_2\text{O}_3$, $\gamma\text{-Fe}_2\text{O}_3$, $\alpha\text{-FeOOH}$, $\beta\text{-FeOOH}$, $\gamma\text{-FeOOH}$, $\delta\text{-FeOOH}$, and FeCO_3 . All eight were prepared in the form of colloidal sols, and their preparation was reported earlier [3,4] or herein. Sols of $\alpha\text{-Fe}_2\text{O}_3$, $\beta\text{-FeOOH}$, and Fe_3O_4 were prepared by aqueous precipitation reactions in closed systems at high temperatures using adaptations of classical methods [3]. These preparations gave only small concentrations of particles: 0.14% for $\alpha\text{-Fe}_2\text{O}_3$, 0.23% for $\beta\text{-FeOOH}$, and 0.27% for Fe_3O_4 . These low solids contents meant that large volumes of the colloidal sols would have to be prepared to give sufficient quantities for characterization, let alone polymer adsorption studies. Therefore, laboratory preparations adapted from industrial processes were used to give sols of 4-10% weight concentration, high enough to give significant weights of particles. Sols of $\alpha\text{-Fe}_2\text{O}_3$, $\alpha\text{-FeOOH}$, and $\gamma\text{-FeOOH}$ were prepared earlier in concentrations of 9.60, 5.38, and 3.97 gm/100 ml,

respectively [4,5]. Their compositions were confirmed by Mössbauer spectroscopy and titration methods.

This report describes the adaptation of these industrial processes to prepare colloidal sols of the remaining five iron corrosion products, Fe_3O_4 , $\gamma\text{-Fe}_2\text{O}_3$, $\beta\text{-FeOOH}$, $\delta\text{-FeOOH}$, and FeCO_3 , in concentrations of 3.18, 2.91, 2.74, 2.95, and 6.27 gm/100 ml, respectively. These sols were cleaned by centrifugation-decantation, their compositions were confirmed by Mössbauer spectroscopy and X-ray diffraction, their specific surface areas were determined by argon gas adsorption, their particle morphology by electron microscopy, and the acid-base character of their surfaces by adsorption of standard acidic and basic polymers as well as Epon 1001F epoxy resin and Emerez 1511 curing agent.

In addition, four commercial iron corrosion products, $\alpha\text{-Fe}_2\text{O}_3$, $\gamma\text{-Fe}_2\text{O}_3$, Fe_3O_4 , and $\alpha\text{-FeOOH}$, were characterized and dispersed in organic media as described earlier [3,4,6], and their acid-base surface characteristics were determined.

Experimental Details - Preparation by Aqueous Precipitation Reactions

The preparation of all the iron corrosion products in the form of colloidal sols reported herein used adaptations of industrial processes to laboratory-size equipment. Stirred 4-liter glass beakers were used as reactors.

Precipitated magnetite, black magnetic iron oxide, Fe_3O_4 , was prepared by reacting equimolar amounts of ferrous and ferric hydroxide in hot ($90+^\circ\text{C}$) aqueous, slightly alkaline media. Two-thirds of the required amount of $\text{FeSO}_4\cdot 7\text{H}_2\text{O}$ (Matheson, Coleman and Bell) was dissolved in dilute sulfuric acid solution at 90°C and oxidized by sodium chlorate (Fisher). The remaining one-third was then added together with sodium hydroxide solution to the former solution. The ferrous sulfate solution was precipitated by a slight stoichiometric excess of sodium hydroxide. The mixture was heated to boiling for a period of time to complete the reaction. The black magnetic oxide was washed by decantation prior to centrifugation-decantation cleaning and further testing.

Gamma ferric oxide, $\gamma\text{-Fe}_2\text{O}_3$, brown magnetic iron oxide, sometimes referred to as maghemite, was prepared by filtering and drying the foregoing washed magnetite slurry, followed by heating in air at $250\text{--}300^\circ\text{C}$ in an electric muffle furnace for a sufficient period of time. The product was ball-milled wet for redispersing prior to subsequent tests. Chemical titration analysis showed this brown magnetic $\gamma\text{-Fe}_2\text{O}_3$ contained only a trace amount (0.25%) of the former magnetite particles.

Delta hydrated ferric oxide, $\delta\text{-FeOOH}$, a brown constituent of iron rust, was prepared by rapid, vigorous oxidation of ferrous

hydroxide precipitated from ferrous sulfate solution by sodium hydroxide solution, followed by addition of strong oxidants such as excess of 30% aqueous hydrogen peroxide (Fisher) or ammonium persulfate (Fisher) at the appropriate temperatures. The medium-brown final precipitate was of large enough particle size and therefore was not subjected to the crystal growth treatment which was necessary for the alpha and gamma iron hydrates.

Beta hydrated ferric oxide, β -FeOOH, brown, non-magnetic akaganeite, was prepared by hydrolysis of hot aqueous ferric chloride solution. $\text{FeCl}_3 \cdot 6\text{H}_2\text{O}$ (J. T. Baker Chemical) was dissolved in deionized water and then heated to boiling for one hr. After continuous heating of the slurry at 90°C for five more hr, a light tan-yellow precipitate of β -FeOOH formed. The pH of this slurry was 1.1 owing to the free hydrochloric acid formed by hydrolysis. Immediate washing by decantation was necessary until no greenish-yellow color was observed in the solution.

Ferrous carbonate, FeCO_3 , a minor rust constituent generally referred to as siderite, was prepared as a white precipitate by mixing and reacting air-free aqueous ferrous sulfate solution (free of ferric sulfate) and sodium carbonate solution in a nitrogen atmosphere. The deaerated water was prepared by boiling deionized water in a stoppered 4-liter flask equipped with a Bunsen valve and then cooling under nitrogen. The ferrous sulfate (Matheson, Coleman and Bell) and sodium carbonate (Fisher) solutions were prepared separately using the deaerated water under nitrogen atmosphere and then mixed together. The white precipitate of FeCO_3 formed immediately after mixing.

Serum replacement, the best method to clean latexes, proved to be suitable for cleaning low-solids-content sols, but was difficult to apply to the high-solids-content sols of these iron corrosion products [4]. Therefore, the foregoing colloidal sols were cleaned by repeated redispersion-centrifugation-decantation before characterization and polymer adsorption studies. Initially, the electrolyte concentrations remaining in the supernatant layer were high, and at least twelve volumes of deionized water were required to clean one volume of the initial sol. The cleaning was continued until the final conductance of the supernatant layer reached a constant value. The final conductances of the sols were $1.5 \times 10^{-5} \text{ ohm}^{-1}\text{cm}^{-1}$ for Fe_3O_4 , $2.6 \times 10^{-6} \text{ ohm}^{-1}\text{cm}^{-1}$ for γ - Fe_2O_3 , $1.2 \times 10^{-5} \text{ ohm}^{-1}\text{cm}^{-1}$ for δ -FeOOH, and $1.1 \times 10^{-5} \text{ ohm}^{-1}\text{cm}^{-1}$ for β -FeOOH, where the conductance of deionized water was $7.5 \times 10^{-7} \text{ ohm}^{-1}\text{cm}^{-1}$.

The cleaned sols were filtered through a Büchner funnel and dried in a circulating air oven at 50°C for 24 hr followed by another 24 hr in a vacuum oven at 40°C . The low drying temperatures were used to avoid dehydration and crystal structure change of the iron corrosion products. The dried products were ground in a mortar and pestle and analyzed by X-ray diffraction, Mössbauer spectroscopy, and argon gas adsorption.

The X-ray diffractograms were taken using the APD-3600 automatic X-ray powder diffractometer. The CuK lines (45 KV, 40 mA) were used for all the samples. The diffractograms were run from 10° to 75° of the 2-theta value range (8.8375 \AA to 1.2663 \AA in d-spacings), which was an adequate range for comparing the results with the Joint Committee of Powder Diffraction Standards.

The Mössbauer spectra were recorded at room temperature [7], and the Mössbauer parameters were compared with literature values to confirm the compositions of the prepared iron corrosion products.

A classical BET volumetric vacuum rig was used to determine the specific surface areas of these iron corrosion products. The argon gas adsorption isotherms obtained at liquid nitrogen temperature were used to calculate the specific surface areas according to the BET equation. Transmission electron micrographs were taken of the grids containing the diluted cleaned sols.

Since the white FeCO_3 precipitate was oxidized rapidly to reddish-brown Fe(OH)_3 by atmospheric oxygen, great difficulty was encountered in attempting to wash or filter this material; however, it was assumed that the cleaned and dried product might resist oxidation. Therefore, the sol was cleaned to $5.0 \times 10^{-4} \text{ ohm}^{-1}\text{cm}^{-1}$ conductance of the supernatant layer and then freeze-dried in liquid nitrogen while under a nitrogen atmosphere. The dried product was oxidized after ten min exposure in air. Obviously, such an unstable compound as FeCO_3 does not exist in iron surface rust, but may be present in deep thick rust, especially in a damp environment containing carbonate ions.

To obtain good dispersions of the iron corrosion products in organic media, each of the foregoing cleaned aqueous sols was flushed directly into toluene, 1,4-dioxane, and diethylene glycol monobutyl ether, respectively. The solvents were chosen according to the following factors: (i) a high solubility of the polymer in the solvent; (ii) adequate acidity-basicity; (iii) low volatility; (iv) the possibility of removal by azeotropic distillation. The azeotropic distillations were carried out in a Büchler flash-evaporator at 40°C and 50-100 torr. For the water-miscible solvents, the azeotropes were distilled out with periodic additions of solvent to the sol. Ethanol was added to the mixture of water-immiscible solvent and water to make them compatible, and the periodic addition of both solvent and ethanol to the sol was required to maintain good dispersion. The distillations were monitored by measuring the volume of distillate, and were continued until all of the ethanol and water were removed.

Stock solutions of polymethyl methacrylate (Lucite 4F; E. I. duPont de Nemours; $\bar{M}_n 3.1 \times 10^5$; $\bar{M}_w 9.8 \times 10^5$) in toluene, post-chlorinated polyvinyl chloride (Geon 627x563; BF Goodrich; $\bar{M}_n 5.6 \times 10^4$; $\bar{M}_w 1.2 \times 10^5$) in 1,4-dioxane, Epon 1001F (Shell Chemical; epoxide equivalent weight 450-550) in diethylene glycol monobutyl ether, and Emerez 1511 (General Mills; amine equivalent weight 230-246) also in diethylene glycol monobutyl ether were

prepared in 5% concentrations. The polymer solutions were filtered through a Büchner funnel to remove any particulate contamination and were then used for adsorption studies.

In the earlier study [4], the adsorption of polymethyl methacrylate and post-chlorinated polyvinyl chloride on the laboratory-prepared α -Fe₂O₃, α -FeOOH, and γ -FeOOH particles reached equilibrium in 12 hr and that of the Epon 1001F and Emerez 1511 oligomers, in 2 hr. To ensure that these times are also applicable to the other iron corrosion products, the same experiments were carried out for the Fe₃O₄ particles. From the earlier results, the equilibrium concentrations of the polymer solutions on the plateau regions were less than 3 gm/100 ml. Therefore, initial polymer concentrations of ca. 4 gm/100 ml were used to ascertain if the equilibrium times were adequate for the Fe₃O₄ as adsorbent. To get a greater change in polymer concentration, the polymer-to-particle ratio was adjusted to 3:1. The polymer solution mixed with the Fe₃O₄ organosol in an 8-oz glass bottle was roller-milled, and the polymer concentration was monitored periodically by centrifuging 25 ml of the mixture and drying 10 ml of the supernatant layer to constant weight; 24 hr in an air oven at 100°-110°C followed by 48 hr in a vacuum oven at 120°C was sufficient to dry all of the polymer solutions. Eventually, it was found that the equilibrium times determined previously were adequate for the Fe₃O₄ particles.

Polymer solutions of 0.5-3.5 gm/100 ml concentrations were used to determine the adsorption isotherm by tumbling them with the Fe₃O₄ particles for the foregoing equilibrium times. The weight of Fe₃O₄ particles per unit volume of sol pipetted was not constant owing to the difficulty in pipetting the settling sol. Ten samples were used to obtain an average solids content based on the weight of the sol, and the Fe₃O₄ organosol pipetted for adsorption was weighed to determine the weight of the particles. Thus far, the adsorption isotherms for Fe₃O₄ are complete, and the isotherms for the other iron corrosion products are being measured.

Results and Discussion — Preparation by Aqueous Precipitation Reactions

Figures 1, 2, 3, and 4 show the X-ray diffractograms of the Fe₃O₄, γ -Fe₂O₃, δ -FeOOH, and β -FeOOH particles, respectively. The 2-theta values and the corresponding d-spacings are compared with the literature results [8] in Tables I, II, III, and IV. These diffractograms and the computer analysis confirmed the compositions and the crystalline structures of these iron corrosion products. Although the particle sizes of Fe₃O₄ and γ -Fe₂O₃ were as small as 0.01 μ m, not-too-broad peaks were still obtained as shown in Figures 1 and 2, owing to the perfect crystallinity and symmetry of these crystals.

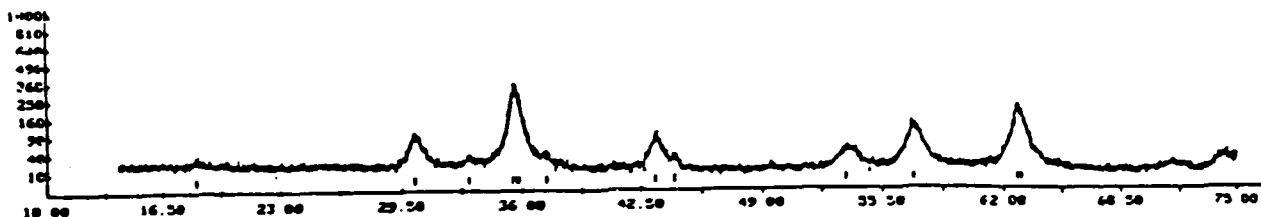


Figure 1. X-ray diffractogram of Fe_3O_4 particles.

Table I

Comparison of the d-Spacings of the Prepared Fe_3O_4 Sample to the Literature Standard

<u>Fe_3O_4 Sample</u>		<u>Literature Standard</u>	
<u>2-Theta</u>	<u>d (Å)</u>	<u>d (Å)</u>	<u>Intensity</u>
18.37	4.830	4.850	8
30.16	2.963	2.967	30
35.43	2.534	2.532	100
37.25	2.414	2.424	8
43.22	2.093	2.099	20
53.54	1.712	1.715	10
57.16	1.612	1.616	30
62.72	1.481	1.485	40

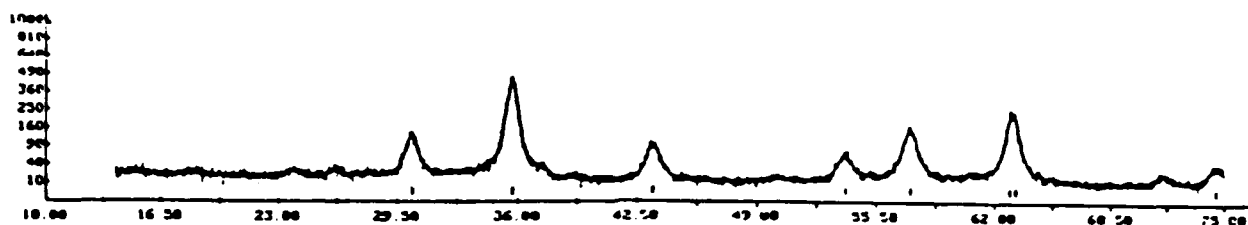


Figure 2. X-ray diffractogram of $\gamma\text{-Fe}_2\text{O}_3$ particles.

Table II

Comparison of the d-Spacings of the Prepared $\gamma\text{-Fe}_2\text{O}_3$ Sample to the Literature Standard

$\gamma\text{-Fe}_2\text{O}_3$ Sample		Literature Standard	
2-Theta	d (Å)	d (Å)	Intensity
30.31	2.95	2.95	34
35.68	2.52	2.52	100
43.35	2.08	2.08	24
53.82	1.70	1.70	12
57.37	1.61	1.61	33
62.85	1.48	1.48	53
74.50	1.27	1.27	11

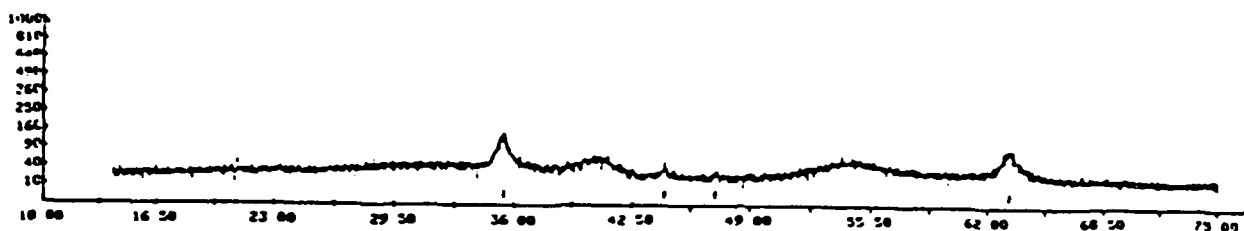


Figure 3. X-ray diffractogram of δ -FeOOH particles.

Table III

Comparison of the d-Spacings of the Prepared δ -FeOOH Sample to the Literature Standard

<u>δ-FeOOH Sample</u>		<u>Literature Standard</u>	
<u>2-Theta</u>	<u>d (Å)</u>	<u>d (Å)</u>	<u>Intensity</u>
35.33	2.540	2.545	100
63.21	1.471	1.471	100

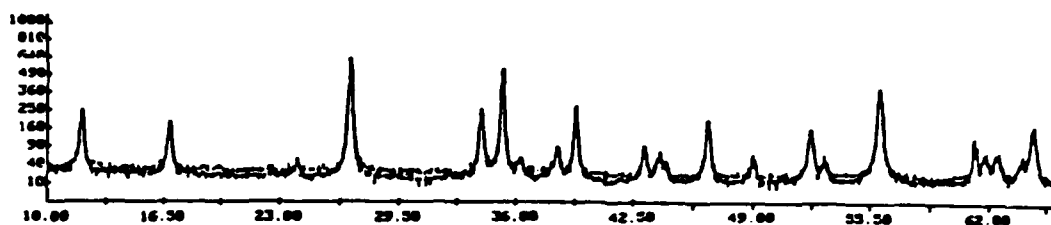


Figure 4. X-ray diffractogram of β -FeOOH particles.

Table IV

Comparison of the d-Spacings of the Prepared β -FeOOH Sample to the Literature Standard

<u>β-FeOOH Sample</u>		<u>Literature Standard</u>	
<u>2-Theta</u>	<u>d (\AA)</u>	<u>d (\AA)</u>	<u>Intensity</u>
11.91	7.424	7.40	100
16.85	5.259	5.25	40
23.93	3.715	3.70	10
26.80	3.324	3.311	100
34.08	2.629	2.616	40
35.24	2.545	2.543	80
38.24	2.351	2.343	20
39.29	2.291	2.285	40
43.04	2.100	2.097	20
43.90	2.061	2.064	20
46.54	1.950	1.944	60
49.00	1.857	1.854	10
52.18	1.752	1.746	40
52.99	1.727	1.719	10
56.03	1.640	1.635	100
61.11	1.515	1.515	40
61.74	1.501	1.497	20
62.48	1.485	1.480	20
63.83	1.457	1.459	10
64.51	1.443	1.438	80
67.91	1.379	1.374	40

In Figure 5, the Mössbauer spectrum of Fe_3O_4 particles is compared to the spectrum of $\alpha\text{-Fe}$, the effective magnetic field at Fe^{3+} position, H value, was 494 ± 1 kOe, in good agreement with the literature value of 493 kOe [9]. The spectrum of $\gamma\text{-Fe}_2\text{O}_3$ in Figure 6 shows that the H value 490 ± 1 kOe, which is in reasonable agreement with the literature value of 502 kOe [10]. The deviation is attributed to the small particle size of the $\gamma\text{-Fe}_2\text{O}_3$. From Figure 7(a), the quadrupole splitting value, Q.S., of $\delta\text{-FeOOH}$ was 0.63 ± 0.03 mm/s. There are as yet no literature references to confirm this value; Loseva and Murashko [11] found that the quadrupole splitting of $\delta\text{-FeOOH}$ was 0.40 ± 0.06 mm/s, and Bhat et al. [12] found it was 0.80 mm/s. Although this discrepancy has not been resolved, the composition of the prepared $\delta\text{-FeOOH}$ particles was confirmed by the X-ray diffraction analysis. Magnetic splitting was observed at room temperature for $\delta\text{-FeOOH}$ [13], but the $0.03 \mu\text{m}$ particle size of our $\delta\text{-FeOOH}$ sample might be too small to get magnetic splitting at room temperature. The quadrupole splitting of $\beta\text{-FeOOH}$ is 0.61 ± 0.03 mm/s by comparing the spectra of $\beta\text{-FeOOH}$ and $\alpha\text{-Fe}$ in Figure 7. This value is in good agreement with the literature value of 0.62 mm/s [14]. Combining the results from X-ray diffraction and Mössbauer spectroscopy, the compositions of the prepared Fe_3O_4 , $\gamma\text{-Fe}_2\text{O}_3$, $\delta\text{-FeOOH}$, and $\beta\text{-FeOOH}$ samples were confirmed.

The specific surface areas of these samples are summarized in Table V, along with the spherical particle sizes calculated from these areas. All of these particles have high specific surface areas. Although the surface areas of the particles accessible to the polymer segments and argon molecules might be different, the adsorption of polymers from solution should increase with increasing specific surface area of the particles. Figures 8-11 show the transmission electron micrographs of these particles. The Fe_3O_4 and $\gamma\text{-Fe}_2\text{O}_3$ particles are cubic, the $\delta\text{-FeOOH}$ particles needlelike, and the $\beta\text{-FeOOH}$ particles spindles. The particle shapes and sizes based on these micrographs are listed in Table V. The particle sizes of Fe_3O_4 and $\gamma\text{-Fe}_2\text{O}_3$ calculated from specific surface areas are in good agreement with the values obtained from the electron micrographs.

Table V
Morphology and Size of the Prepared Particles

Particle	Particle Shape	Particle Size (μm)	Specific Surface Area (m^2/g)	Particle Diameter Based on S.S.A. (μm)
Fe_3O_4	cubic	0.01	82.5	0.01
$\gamma\text{-Fe}_2\text{O}_3$	cubic	0.01	68.9	0.02
$\delta\text{-FeOOH}$	needlelike	0.03	206.0	--
$\beta\text{-FeOOH}$	spindle	0.60	16.5	--

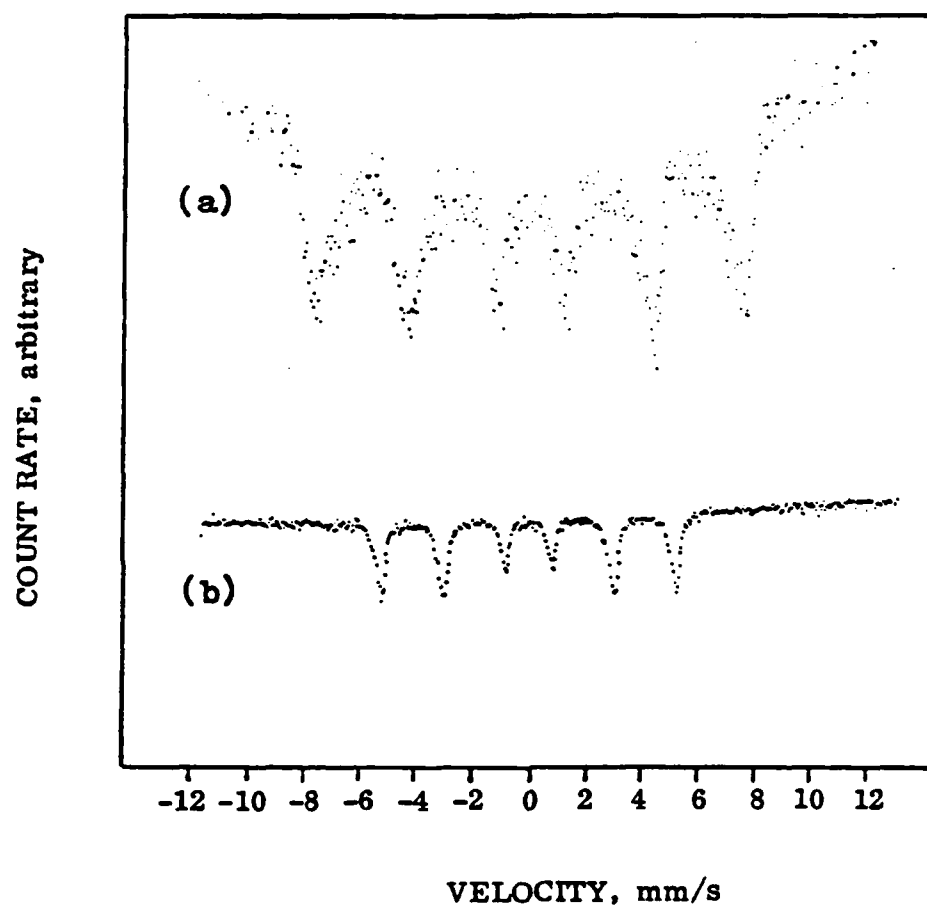


Figure 5. Mössbauer spectra (room temperature) of
(a) prepared Fe_3O_4 particles; (b) $\alpha\text{-Fe}$
as standard.

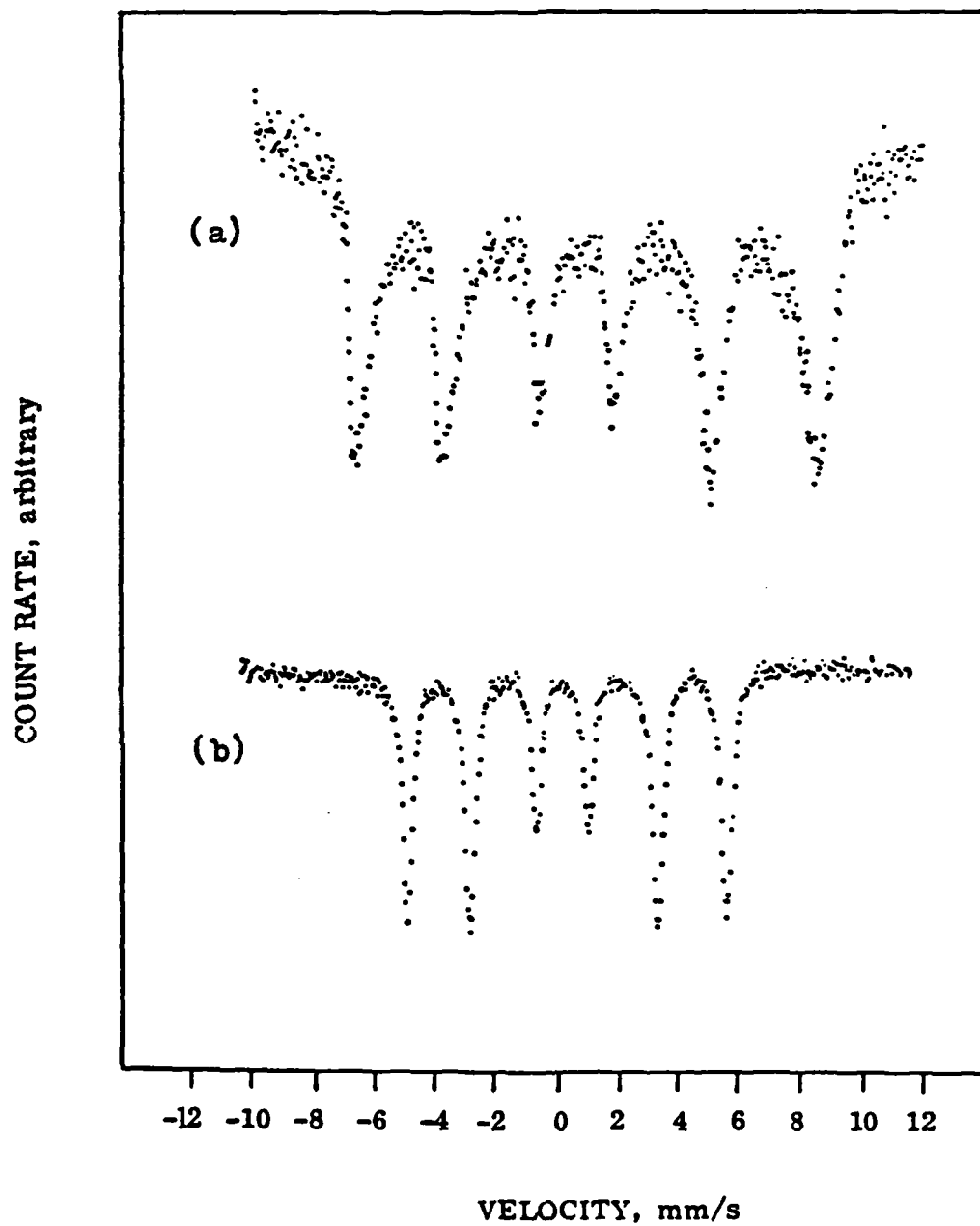


Figure 6. Mössbauer spectra (room temperature) of
(a) prepared $\gamma\text{-Fe}_2\text{O}_3$ particles; (b) $\alpha\text{-Fe}$
as standard.

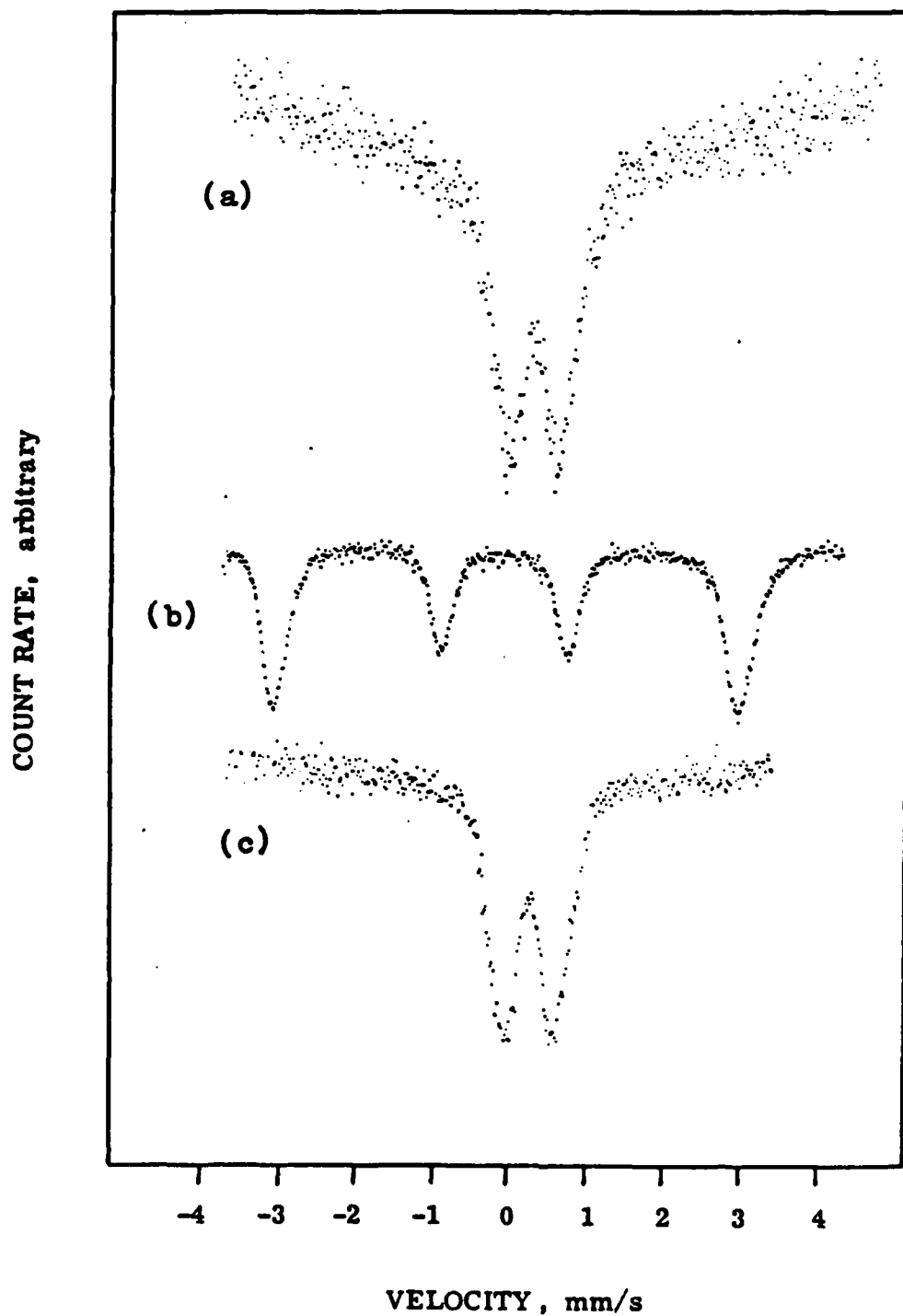


Figure 7. Mössbauer spectra (room temperature) of
(a) prepared δ -FeOOH particles; (b) α -Fe as
standard; (c) prepared β -FeOOH particles.



Figure 8. Transmission electron micrograph of Fe_3O_4 particles.



Figure 9. Transmission electron micrograph of $\gamma\text{-Fe}_2\text{O}_3$ particles.

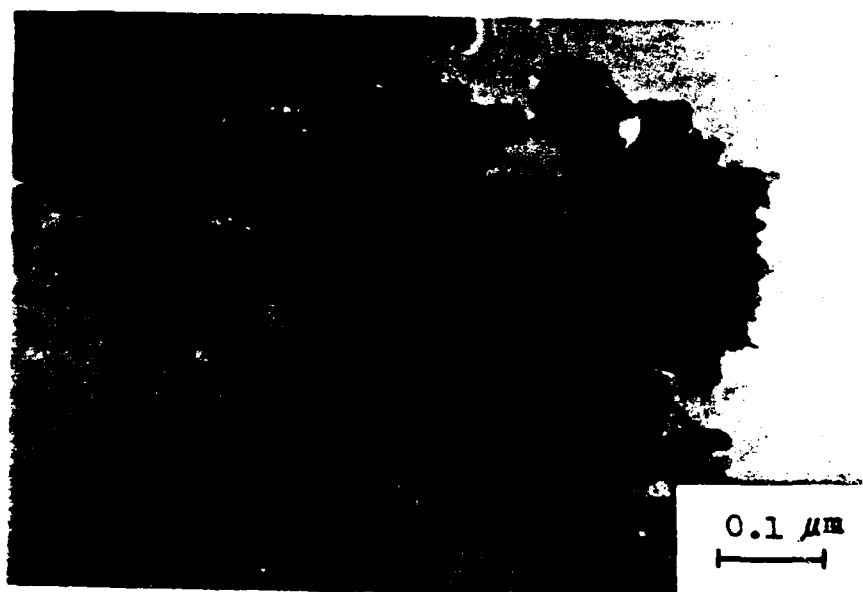


Figure 10. Transmission electron micrograph of δ -FeOOH particles.



Figure 11. Transmission electron micrograph of β -FeOOH particles.

The rate at which the adsorption of polymer on the particle surface reaches equilibrium depends upon the molecular weight of the polymer. It was suggested that the rate of adsorption decreases with increasing molecular weight [13]. Probably, the adsorption rate depends upon the diffusion rate of polymer onto the surface of the adsorbent. It is not surprising that the equilibrium times for polymethyl methacrylate and post-chlorinated polyvinyl chloride are six times longer than those for the Epon 1001F and Emerez 1511 oligomers.

Figure 12 shows the adsorption isotherms of these polymers on the Fe_3O_4 sample. The critical polymer solution concentrations to reach the plateau regions are ca. 1.0 gm/100 ml. The number of polymer segments adsorbed per 100 \AA^2 were 72.3 for polymethyl methacrylate (12.0 mg/m^2), 47.8 for post-chlorinated polyvinyl chloride (6.4 mg/m^2), 6.9 for Epon 1001F (5.7 mg/m^2), and 22.5 for Emerez 1511 (8.9 mg/m^2). These values are about the same order of magnitude as the adsorption on the commercial $\alpha\text{-Fe}_2\text{O}_3$, $\alpha\text{-FeOOH}$, and $\gamma\text{-FeOOH}$ samples. These results showed that the Fe_3O_4 surface is amphoteric, and the ratio of the acidic sites to the basic sites is about 1.5. The thinner adsorbed layers for the oligomers is attributed to their greater tendency to form more compact surface layers than the high-molecular-weight polymers.

Experimental Details - Preparation by Dispersion

Table VI lists the four commercial iron corrosion products (Pfizer Pigment and Metals Division).

Table VI
Commercial Iron Oxides

<u>Iron Oxide</u>	<u>Sample Designation</u>	<u>Lot Number</u>
$\alpha\text{-Fe}_2\text{O}_3$	R-2199	E9036
$\gamma\text{-Fe}_2\text{O}_3$	MO-2228	E9460
Fe_3O_4	BK-5000	E9516
$\alpha\text{-FeOOH}$	YLO-2288-D	F9006

These iron oxides were characterized and used in polymer adsorption studies earlier [3,4,6]. In these studies, the commercial iron oxides adsorbed significantly less polymer than the corresponding iron oxides prepared in the laboratory. This difference

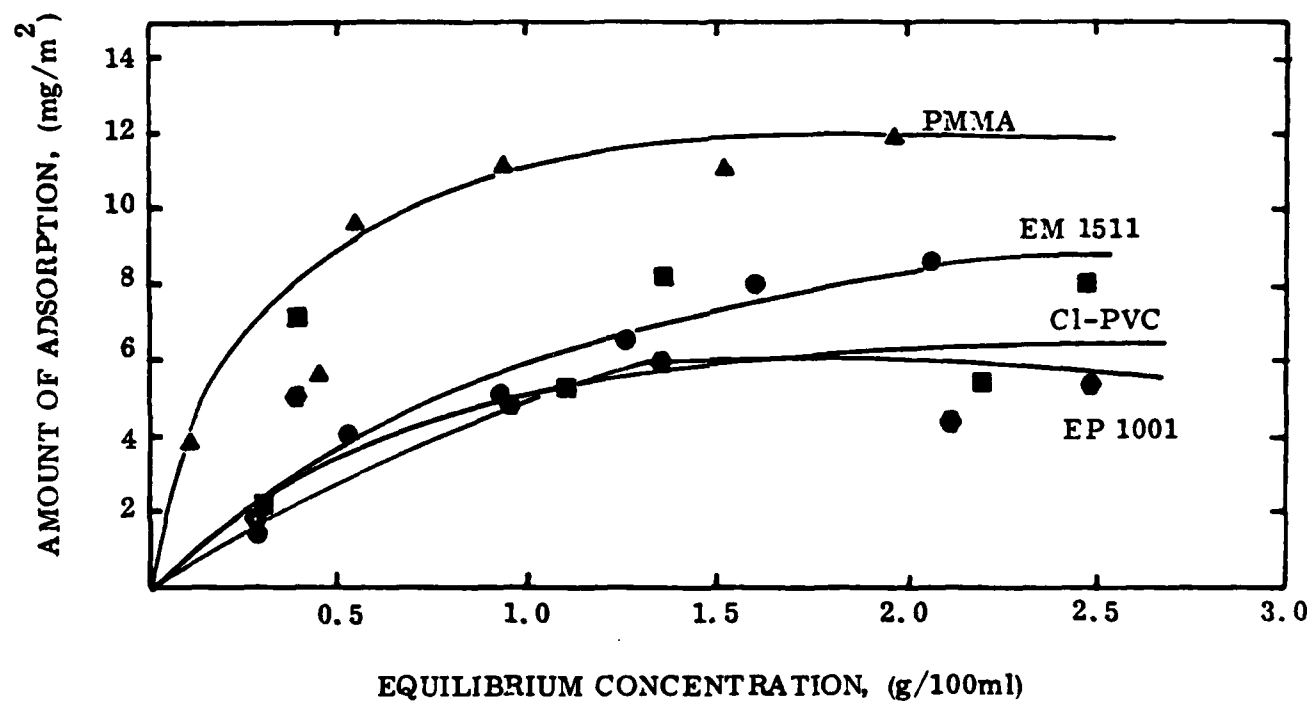


Figure 12. Adsorption isotherms of different polymers on Fe_3O_4 .

was attributed to the finer particle size of the laboratory iron oxides.

In the present work, the iron oxides were washed in a Büchner funnel using deionized water. The packed oxide cake was flooded with water and allowed to settle; then the water was decanted. This washing was continued until the conductance of the effluent water reached a constant value. Typically, ten liters of water were used to wash 100 gm oxide. Table VII gives the initial and final conductances of the wash water.

Table VII
Conductance of Wash Water from Iron Oxides

Iron Oxide	Conductance, $\text{ohm}^{-1}\text{cm}^{-1}$		Final/Initial Ratio, $\times 10^3$
	Initial, $\times 10^3$	Final, $\times 10^6$	
$\alpha\text{-Fe}_2\text{O}_3$	0.13	9.0	69
$\gamma\text{-Fe}_2\text{O}_3$	4.8	31.	6.5
Fe_3O_4	1.6	45.	0.28
$\alpha\text{-FeOOH}$	1.5	35.	0.23

Conductance of deionized water $0.75 \times 10^{-6} \text{ ohm}^{-1}\text{cm}^{-1}$.			

After washing, the iron oxides were dried in a circulating air oven for 24 hr at 50° followed by at least 48 hr in a vacuum desiccator over phosphorus pentoxide. The dried oxides were then ball-milled for 24 hr in 8-oz Nalgene polypropylene bottles using Burundum grinding media. After milling, a small portion of the dispersion was centrifuged, and its refractive index was compared with that of the pure solvent to ensure that the dispersions were not contaminated by material leached or abraded from the polypropylene bottles.

Colloidal sols of these iron oxides were prepared by dispersion. The major differences in the sol preparation compared with the methods used earlier [3,4,6] were: (i) the means of transferring the oxides to the organic phase; (ii) the method of monitoring the cleaning of the oxides; (iii) the solvents used to disperse the oxides for the polymer adsorption experiments. These factors were not investigated extensively; instead, the experience gained in this and other projects was used to select experimental procedures that would minimize the blocking of acidic and basic adsorption sites on the oxide particles. Therefore, the oxides were cleaned to constant conductance rather than to constant pH

because the conductance is more sensitive than the pH to very small concentrations of ions. The oxides were transferred to organic media by drying and ball-milling rather than by serum replacement or azeotropic distillation to remove the adsorbed water more completely. More neutral solvents were also used: carbon tetrachloride rather than toluene for the polymethyl methacrylate; benzene rather than 1,4-dioxane for the chlorinated polyvinyl chloride.

Scanning electron micrographs were prepared of the oxide dispersions in the carbon tetrachloride, methylene chloride, and diethylene glycol monobutyl ether solvents used for the adsorption studies to characterize the particle size and shape, and to determine the effect of the dispersion medium on the degree of dispersion.

The stability of the oxide dispersions was determined by measuring the time required for the oxide to settle completely after the dispersion had been completely mixed to a uniform state.

The polymers used in the adsorption studies were the same as those used earlier: basic polymethyl methacrylate; acidic chlorinated polyvinyl chloride; Epon 1001F epoxy resin; Emerez 1511 curing agent. The solvents selected for the basic and polymethyl methacrylate and acidic chlorinated polyvinyl chloride were those which were neither more basic nor acidic than the polymer according to the Fowkes-Manson acid-base interaction scheme [1,2]: carbon tetrachloride for the basic polymethyl methacrylate; methylene chloride for the acidic chlorinated polyvinyl chloride. The high volatility of the methylene chloride was responsible for the poor reproducibility, however, so the slightly basic benzene was substituted for it. Diethylene glycol monobutyl ether was used as the solvent for the Epon 1001F epoxy resin and Emerez 1511 curing agent.

The polymer adsorption isotherms were determined gravimetrically using polymer solutions of up to 5% concentration. Exactly 10.00 ml iron oxide dispersion in solvent and 90.00 ml polymer solution in the same solvent were pipetted into 8-oz glass bottles with aluminum foil-lined caps. The mixtures were subjected to ultrasonic irradiation for 2 min and were then stirred with a magnetic stirrer to maintain a uniform dispersion while the 10.00 ml samples were removed by pipetting. The bottles were rolled on the roller-mill until the amount of adsorbed polymer reached its equilibrium value; 12 hr were required for the samples containing polymethyl methacrylate and chlorinated polyvinyl chloride, and two hr for the Epon 1001F epoxy resin and Emerez 1511 curing agent. Then the samples were centrifuged at high speed for 20 min to sediment the particles. Ten-ml aliquots of the supernatant polymer solution were dried to determine the concentration of unadsorbed polymer: the solutions containing polymethyl methacrylate and chlorinated polyvinyl chloride in an air oven at 100° for 24 hr and in a vacuum oven at 120° for 48 hr; those containing Epon 1001F epoxy resin and Emerez 1511 curing agent were dried in an

air oven for 24 hr at 100°. The concentrations of iron oxide particles in the oxide dispersions were measured by pipetting 10.00 ml dispersion into a tared aluminum dish and evaporating the solvent in an air oven for 48 hr at 100°.

Experimental Results and Discussion - Preparation by Dispersion

Figure 13 shows scanning electron micrographs at two magnifications of the γ -Fe₂O₃ dispersion in methylene chloride, Figures 14-17 the dispersions of α -Fe₂O₃, γ -Fe₂O₃, Fe₃O₄, and α -FeOOH in carbon tetrachloride, respectively, and Figure 18 the γ -Fe₂O₃ dispersion in diethylene glycol monobutyl ether. All of the dispersions show relatively uniform primary particle sizes with a moderate degree of aggregation. The dispersion in diethylene glycol monobutyl ether shows clearly the characteristic crystal structure, particularly at the higher magnification. The oxide dispersions in diethylene glycol monobutyl ether were stable (i.e., did not settle) for 4 hr and those in methylene chloride, carbon tetrachloride, and benzene were stable for 1 hr.

The adsorption isotherms were measured, and the values of the plateau region are given in Table VIII in mg polymer/m² of oxide surface area and the number of polymer segments adsorbed/100 Å² of oxide surface area; the values for polymethyl methacrylate and chlorinated polyvinyl chloride were calculated using the molecular weight of one segment, and those for Epon 1001F and Emerez 1511 using the epoxide and amine equivalent values, respectively.

Table VIII
Polymer Adsorption on Oxide Dispersions Prepared
by Dispersion

<u>Iron Oxide</u>	<u>Polymer Adsorption, mg Polymer/m² Surface Area</u>			
	<u>PMMA</u>	<u>Cl-PVC</u>	<u>Epon 1001F</u>	<u>Emerez 1511</u>
α -Fe ₂ O ₃	90.	22.	20.5	17.0
γ -Fe ₂ O ₃	315.	1.6	8.8	13.0
Fe ₃ O ₄	140	14.8	1.95	10.8
α -FeOOH	590.	4.5	19.0	11.5



Figure 13. Scanning electron micrographs of γ -Fe₂O₃ dispersions in methylene chloride.

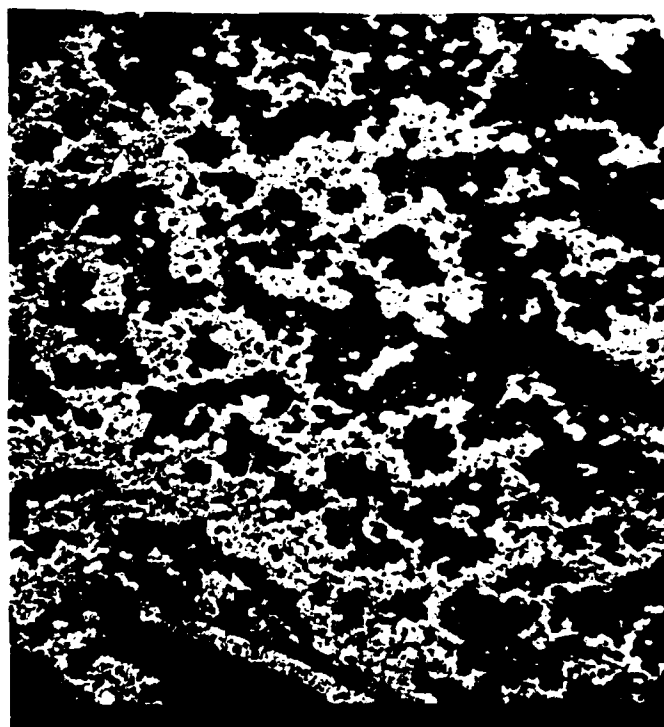
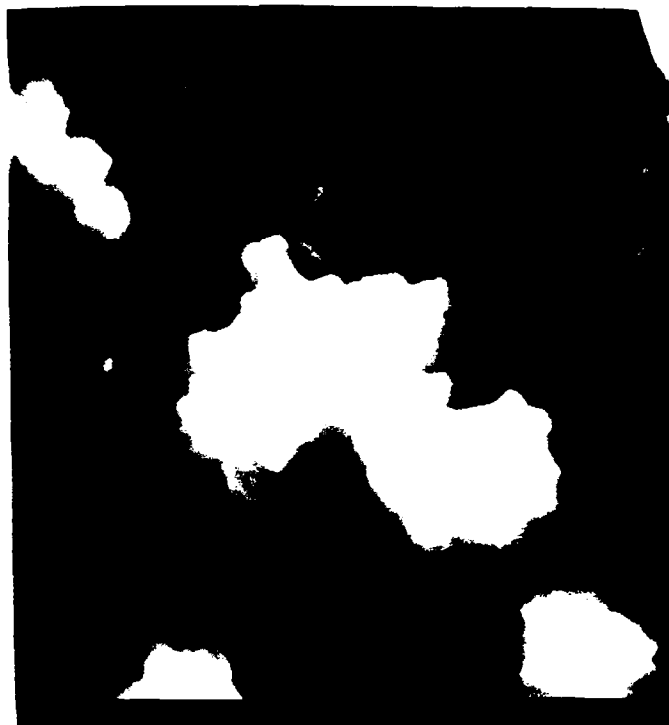


Figure 14. Scanning electron micrographs of α -Fe₂O₃ dispersions in carbon tetrachloride.

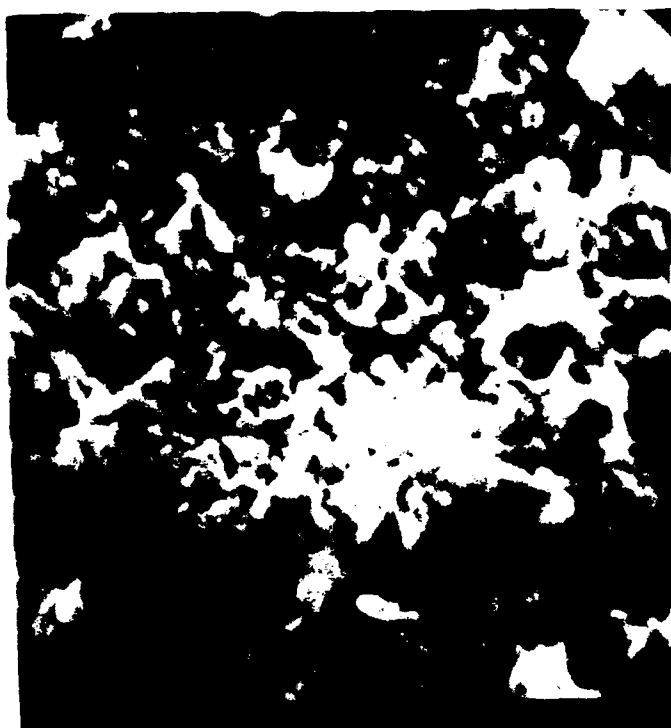


Figure 15. Scanning electron micrographs of γ -Fe₂O₃ dispersions in carbon tetrachloride.



Figure 16. Scanning electron micrographs of Fe_3O_4 dispersions in carbon tetrachloride.

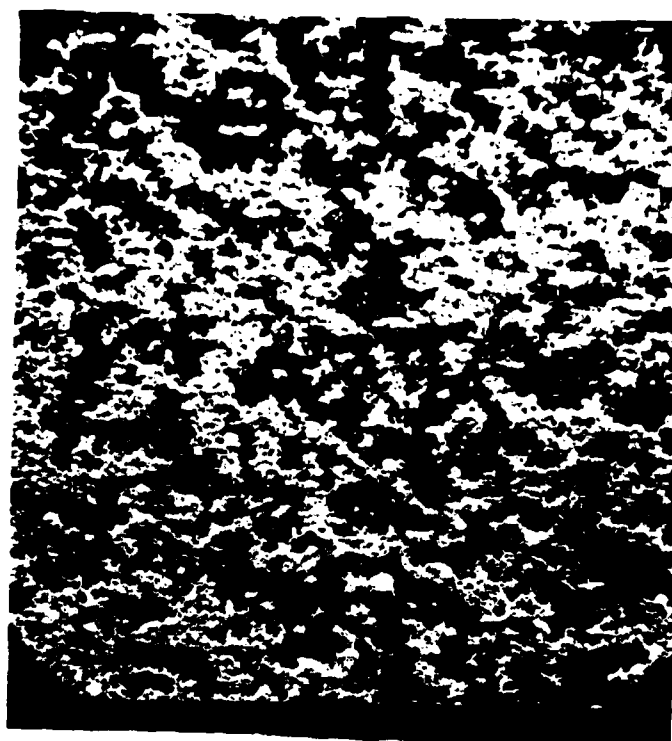


Figure 17. Scanning electron micrographs of α -FeOOH dispersions in carbon tetrachloride.



Figure 18. Scanning electron micrographs of γ -Fe₂O₃ dispersions in diethylene glycol monobutyl ether.

Table VIII (Cont'd.)

Iron Oxide	Polymer Adsorption, Polymer Segments/100 Å ²			
	PMMA	Cl-PVC	Epon 1001F	Emerez 1511
α-Fe ₂ O ₃	541.	165.	24.7	43.4
γ-Fe ₂ O ₃	1900.	12.0	10.6	33.2
Fe ₃ O ₄	843.	111.	2.35	27.6
α-FeOOH	3550.	33.8	22.9	29.4

The number of polymer segments adsorbed/100 Å² of oxide surface area is great relative to the maximum number of 10 water molecules adsorbed/100 Å² oxide surface area. The determination of the number of water molecules adsorbed/100 Å² has been used as a measure of the number of polar sites where the number is 10/100 Å² or smaller. All of these experiments except the Epon 1001F on Fe₃O₄ show values of 10 or greater; some values for polymethyl methacrylate and chlorinated polyvinyl chloride are much greater. These high values suggest that the polymer chains are adsorbed with one segment at a given adsorption site with the chains forming loops that extend far out into the continuous phase.

All four oxides are amphoteric, i.e., they adsorb both the basic polymethyl methacrylate and the acidic chlorinated polyvinyl chloride; however, the acidic character of the γ-Fe₂O₃ appears to be greater than its basic character from the disparity in the amounts of polymer adsorbed. For the Epon 1001F, the only oxide which adsorbed less than 10 segments/100 Å² was Fe₃O₄, which adsorbed only 2.35 segments/100 Å². Similarly, γ-Fe₂O₃ adsorbed 10.6 segments/100 Å². The other values for Epon 1001F, as well as those for Emerez 1511, were greater, which suggests multi-layer adsorption.

Table IX compares the values given in Table VIII with those obtained for the same samples but using the method of sample preparation used earlier [4,6]: (i) cleaning by washing with water to constant pH; (ii) particle size reduction by ball-milling in water; (iii) transfer to organic media by serum replacement with toluene followed by vacuum drying. This earlier procedure is denoted as Method A and the method described in this report as Method B. In this table, the oxides are listed in order of increasing specific surface area. For the basic polymethyl methacrylate, the amounts of polymer adsorbed were much greater for Method B than for Method A. For the acidic chlorinated polyvinyl chloride, the amounts adsorbed, although still large, were smaller than for the basic polymethyl methacrylate; moreover, the amount adsorbed for Method B was greater in only one case (α-Fe₂O₃); for the other oxides, the amount adsorbed was smaller for Method B than for Method A. For Epon 1001F, the amounts adsorbed were much

Table IX

Polymer Adsorption on Oxide Dispersions Prepared by Dispersion

Iron Oxide	Specific Surface Area, m ² /gm	Method	Polymer Adsorption, Segments/100 Å ²			
			PMMA	Cl-PVC	Epon 1001F	Emarez 1511
Fe ₃ O ₄	5.72	A	57.8	174.	8.95	12.5
		B	843.	111.	2.35	27.6
α-Fe ₂ O ₃	9.90	A	66.2	90.0	13.0	15.3
		B	541.	165.	24.7	43.4
α-FeOOH	10.66	A	57.8	90.1	4.34	7.41
		B	3550.	33.8	22.9	29.4
γ-Fe ₃ O ₄	19.80	A	18.1	52.6	5.96	2.50
		B	1900.	12.0	10.6	33.2

smaller than for the high-molecular-weight polymers, and were larger for Method B than for Method A, except for Fe₃O₄, for which the opposite was the case. For Emarez 1511, the amounts adsorbed for Method B were greater than for Method A.

The results of the adsorption experiments varied strongly with the method used to prepare the dispersions. This result is consistent with the dependence of the degree of dispersion on the method used to make the dispersion. Different dispersion methods would be expected to give differing degrees of breakdown, particularly of the hard aggregates, during the dispersion process. Generally, it appears that Method B gives smaller average particle sizes than Method A. Both methods give values far in excess of those expected for adsorption of less than one monolayer.

Comparison of Laboratory and Commercial Iron Oxides

Table IX gives the number of polymer segments adsorbed/100 Å² of oxide surface area for the commercial iron oxide samples dispersed in two different ways. Table X gives the corresponding results determined thus far for the laboratory iron oxide samples prepared earlier [5] and described in this report. In this case, too, the oxides are arranged in order of increasing specific surface area.

Table X

Polymer Adsorption of Oxide Dispersions Prepared by
Aqueous Precipitation Reactions

Iron Oxide	Specific Surface Area, m ² /gm	Polymer Adsorption, Segments/100 Å ²			
		PMMA	Cl-PVC	Epon 1001F	Emerez 1511
α-Fe ₂ O ₃	3.4	499.	774.	216.	1003.
γ-FeOOH	18.3	70.0	80.8	57.0	86.8
α-FeOOH	56.3	50.2	19.0	18.2	24.2
Fe ₃ O ₄	82.5	72.3	47.8	6.9	22.5

Comparison of the foregoing results with those of Table IX shows that the surface areas of the laboratory samples are greater for α-FeOOH and Fe₃O₄ but smaller for α-Fe₂O₃. Such differences are expected because the size of the laboratory samples is determined by the details of preparation while that of the commercial oxides is determined by the degree to which the aggregates and agglomerates are broken down by the respective milling processes; indeed, in the latter process, some particles may be cleaved during the milling. In contrast, the primary particle sizes of the laboratory samples are relatively uniform, while those of the commercial samples are not.

The number of polymer segments adsorbed/100 Å² varies widely, and there are no obvious correlations between the laboratory and commercial samples. Generally, the amount of polymer adsorbed is greater for the laboratory samples than for the commercial samples prepared by Method A but is lesser than for the commercial samples prepared by Method B; however, there are exceptions to this generality.

All of the iron oxides, both laboratory and commercial, are amphoteric, i.e., they adsorb significant amounts of both the basic polymethyl methacrylate and acidic chlorinated polyvinyl chloride. There are some differences in the amounts adsorbed, but generally all values are so high that the adsorption can be explained only by multilayer adsorption or loops of the polymer chains extending out into the continuous medium.

It was shown earlier [16] that the number of polymer segments adsorbed/100 Å² of oxide surface area increased with decreasing specific area. This correlation was attributed to a smaller adsorption of polymer on particles with a smaller radii of curvature, the presence of pores too small to be covered by an adsorbed

layer of polymer chains, or the entrainment of polymer from solution by the descending iron oxide particles during centrifugation. Figures 19-22 show the variation of the number of polymer segments adsorbed/100 Å² or oxide surface area independent of the iron oxide and its method of preparation, with the reciprocal specific surface area for chlorinated polyvinyl chloride, polymethyl methacrylate, Epon 1001F, and Emerez 1511, respectively. It can be seen that the amount of polymer adsorbed/100 Å² increases exponentially with reciprocal specific surface area for the chlorinated polyvinyl chloride and polymethyl methacrylate; however, the corresponding relationships for Epon 1001F and Emerez 1511 show a much poorer correlation.

It is difficult to develop a satisfactory physical explanation for this correlation observed for the high-molecular-weight polymers. The foregoing reasons----different radii of curvature of the particles, the variation of surface pore size, entrainment of polymer by sedimenting oxide particles----are all reasonable explanations for the observations. There is another explanation, however: the classical method of determining polymer adsorption on colloidal particles is strongly dependent upon the degree of dispersion and the experimental conditions as well as the character of the particle surfaces. Indeed, until these results are reconciled, the classical method of determining polymer adsorption must be considered of doubtful validity.

Future Work

At this point, the first of the original goals, i.e., the preparation of the eight iron corrosion products in the form of colloidal sols, has been completed. The adsorption isotherms of four of these products have been measured, and the measurement of the remaining three (FeCO₃ is too unstable to measure) is in progress.

The future work will comprise: (i) completion of the development of methods to measure polymer adsorption on a single or a small number of particles to check the results of the classical polymer adsorption experiments.

There are three approaches to the measurement of polymer adsorption on a single or small number of polymer particles: (i) sedimentation; (ii) chromatography; (iii) laser-Doppler anemometry. All three approaches measure the hydrodynamic diameter so that all three are applicable to a comparison of the diameters with and without an adsorbed layer of polymer.

Sedimentation has the advantage that it can be used with a relatively broad distribution of particle sizes; however, the accuracy of determination decreases with the increasing breadth of particle size distribution. Lehigh has the Joyce-Loebl disk centrifuge and the Beckman Spinco Model E ultracentrifuge

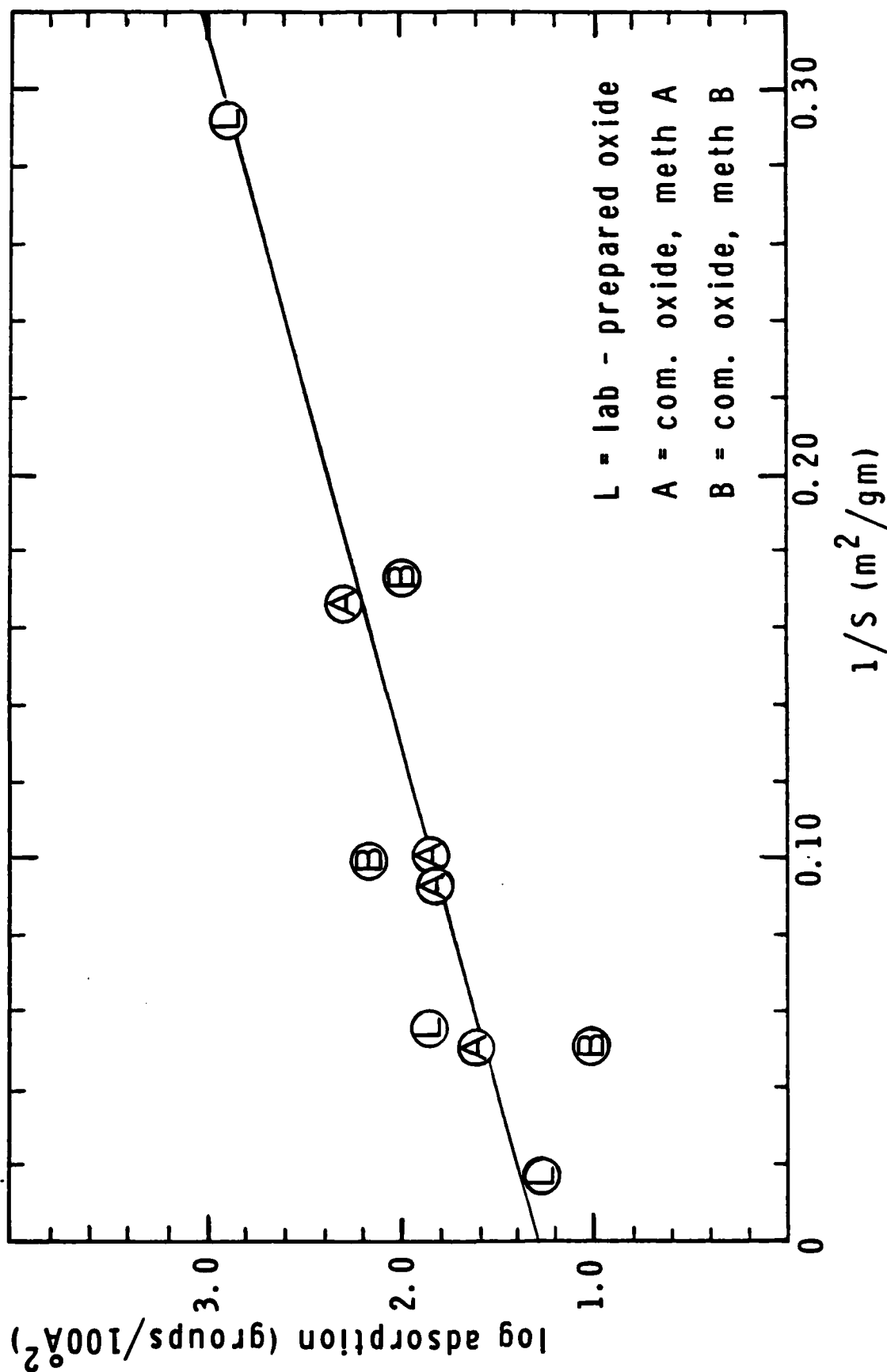


Figure 19. Variation of log polymer segments adsorbed/100 Å² oxide surface area with reciprocal specific surface area for chlorinated polyvinyl chloride.

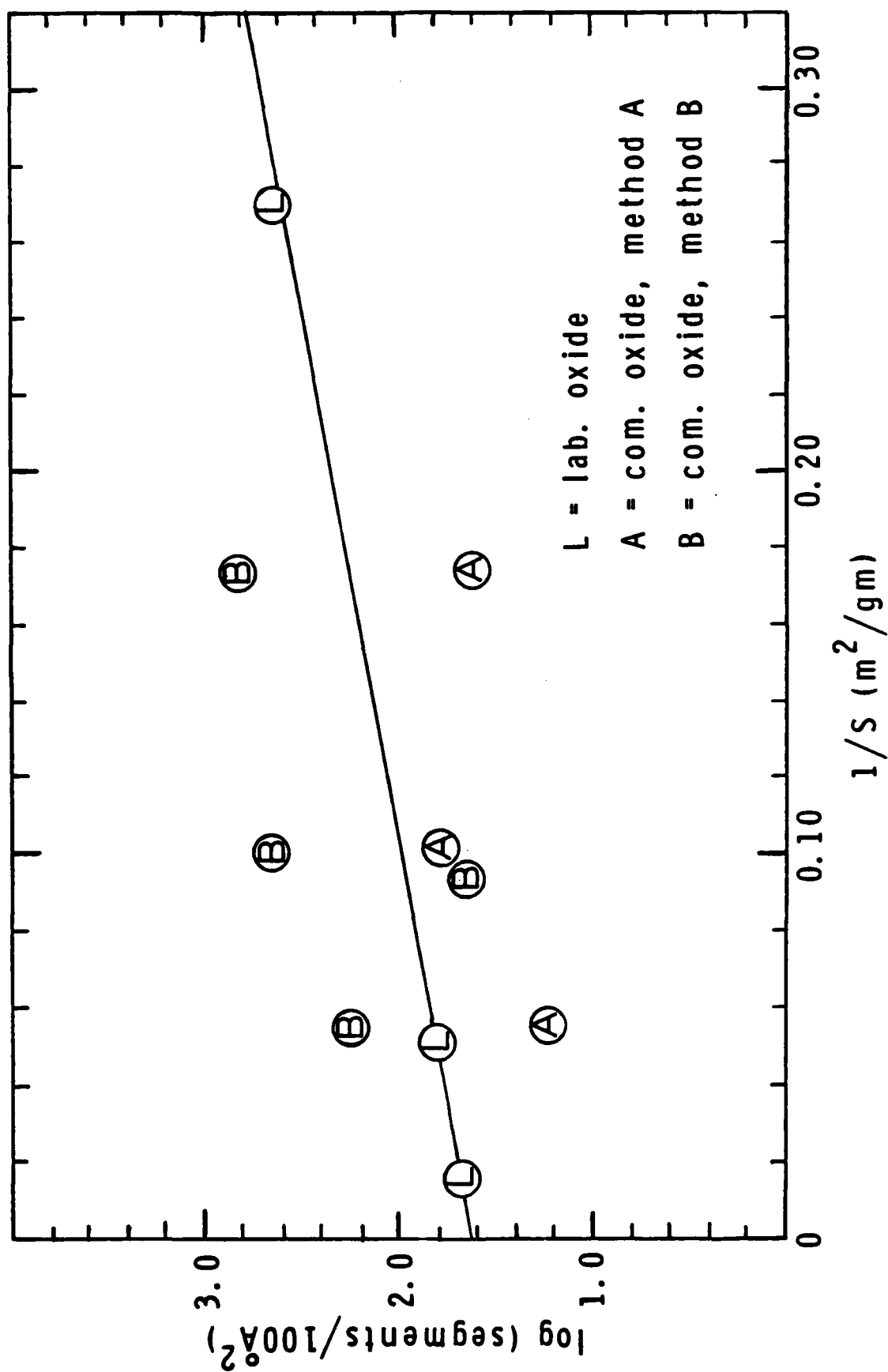


Figure 20. Variation of log polymer segments adsorbed/100 Å² oxide surface area with reciprocal surface area for polymethyl methacrylate.

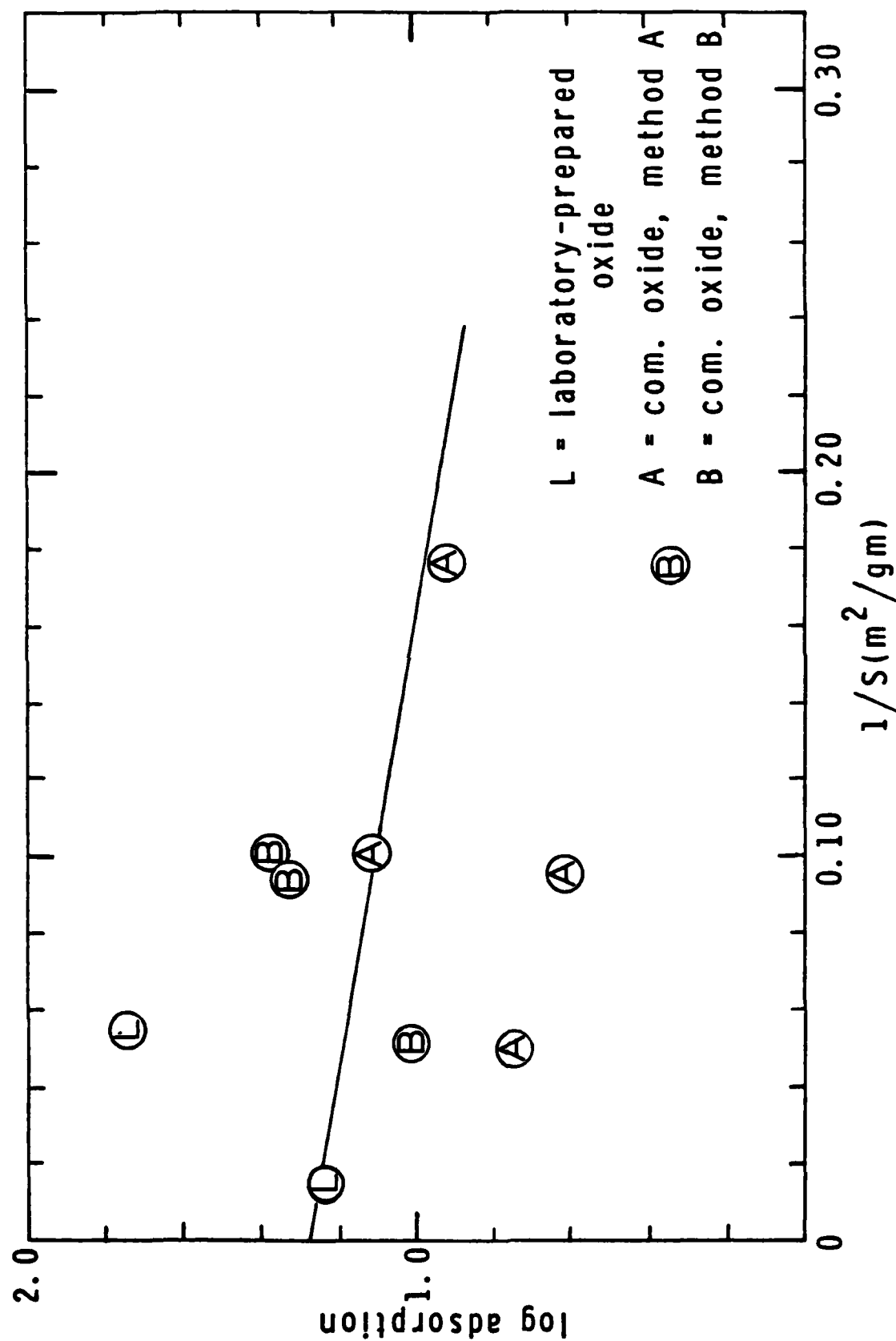


Figure 21. Variation of log polymer segments adsorbed/100 Å² oxide surface area with reciprocal specific surface area for Epon 1001F epoxy resin.

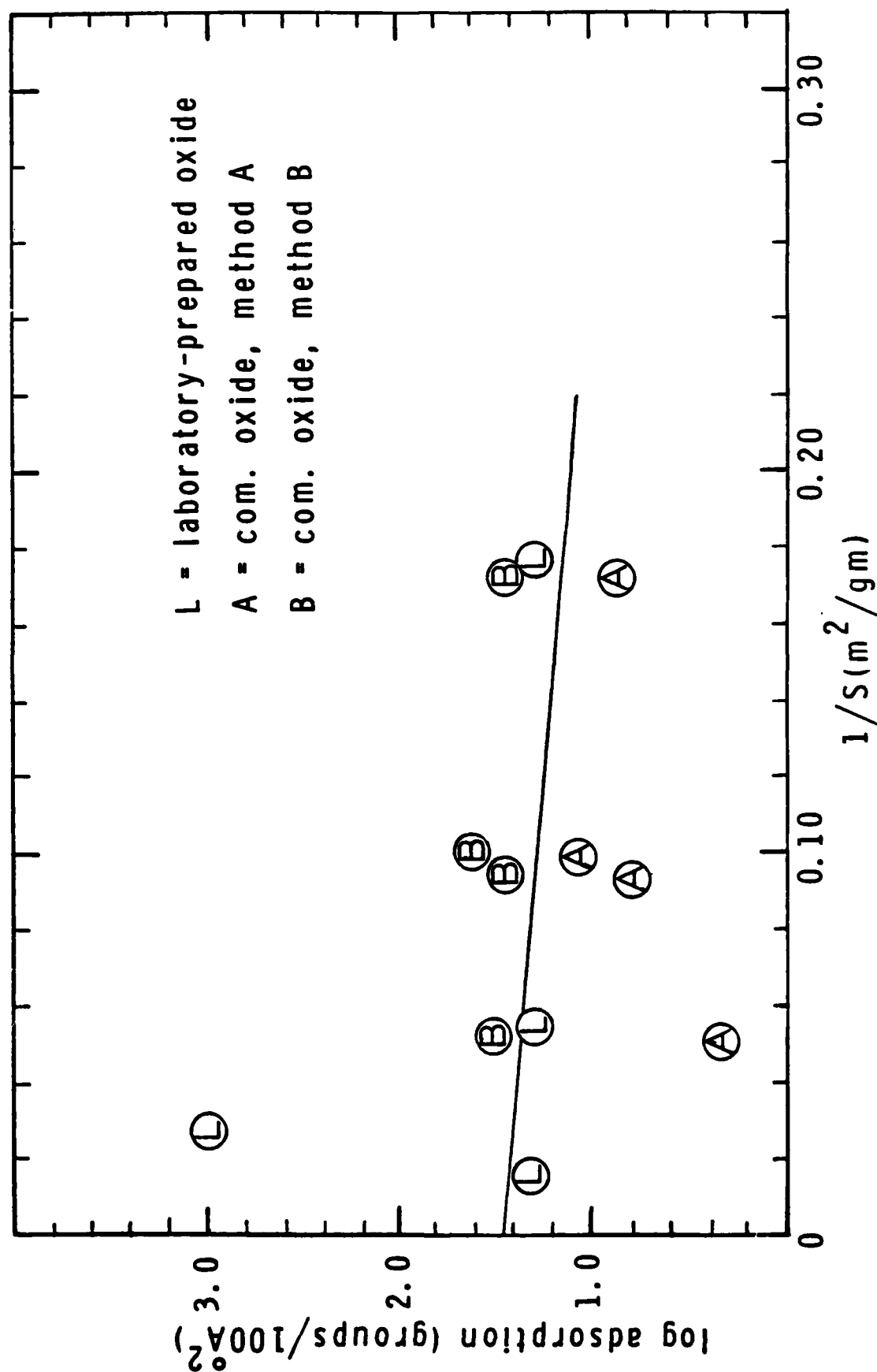


Figure 22. Variation of log polymer segments adsorbed/100 Å² oxide surface area with reciprocal specific surface area for Emerez 1511 curing agent.

available for these experiments. The cells of both centrifuges must be altered to accommodate organic media.

Chromatography can be carried out by capillary chromatography or hydrodynamic chromatography. This method also has the advantage that it can be used with a broad distribution of particle sizes, but the accuracy also decreases with increasing breadth of distribution. Capillary chromatography can accommodate particles up to the diameter of the capillary (usually 100-250 μm); however, the accuracy of this method diminishes at sizes smaller than 0.2 μm [17,18], so that many of the laboratory iron oxides could not be measured accurately using this method. Hydrodynamic chromatography gives good accuracy for particles as small as 0.03 μm but is limited to particles smaller than 0.5 μm . Thus this method would work well, but a filter column must be installed before the measuring columns to remove any particles larger than 0.5 μm . Moreover, the usual styrene-divinylbenzene copolymer bead packing would have to be replaced by glass bead packing.

Laser-Doppler anemometry can be used to measure the thickness of an adsorbed polymer layer on a colloidal particle, e.g. the thickness of an adsorbed methylcellulose layer on monodisperse polystyrene particles has been measured in a preliminary way using the Pen Kem 3000 [19]. However, this method is limited to narrow size distributions; increasing breadth of the distribution gives decreasing resolution of the signal. Moreover, the instrument must be altered to accommodate the organic solvent medium of the present samples.

At present, preparations are in progress to make preliminary measurements using hydrodynamic chromatography, laser-Doppler anemometry in the Pen Kem 3000, and centrifugation in the Joyce-Loebl disk centrifuge. If successful, these measurements could give a measure of adsorbed polymer layer thickness on individual particles so that experiments could be run with a very small amount of iron oxide sample.

REFERENCES

- [1] M. J. Marmo, M. A. Mostafa, H. Jinnai, F. M. Fowkes, and J. A. Manson, I&EC Prod. Res. Dev. 15 (3), 206 (1976).
- [2] F. M. Fowkes and M. A. Mostafa, I&EC Prod. Res. Dev. 17 (1), 3 (1978).
- [3] First Annual Report "Corrosion Control through a Better Understanding of the Metallic Substrate/Organic Coating/Interface," Sept. 1, 1979 to August 31, 1980, Agreement No. N00014-79-C-0731, Dec. 1, 1980, p.9.

- [4] Second Annual Report "Corrosion Control Through a Better Understanding of the Metallic Substrate/Organic Coating/Interface," Sept. 1, 1980 to Aug. 31, 1981, Agreement No. N00014-79-C-0731, Nov. 1, 1981, p.161.
- [5] J. M. Kang, "Preparation and Polymer Interaction of Colloidal Iron Corrosion Products," M.S. Thesis, Lehigh University, 1981.
- [6] D. W. Timmons, "An Understanding of the Principles Related to the Application of Paints to Corroded Steel Surfaces with Little or No Surface Preparation," M.S. Thesis, Lehigh University, 1981.
- [7] Mössbauer spectra were taken by A. Vértes and S. Music.
- [8] Card file numbers 19-629 (Fe_3O_4), 4-0755 ($\gamma\text{-Fe}_2\text{O}_3$), 13-87 ($\delta\text{-FeOOH}$), and 13-157 ($\beta\text{-FeOOH}$); Joint Committee of Powder Diffraction Standards (1972).
- [9] B. J. Evans and S. S. Hafner, J. Appl. Phys. 40, 1411 (1969).
- [10] D. Khalafalla and A. H. Morrish, J. Appl. Phys. 43, 624 (1972).
- [11] G. V. Loseva and N. V. Murashko, Inorg. Mater. (USSR) 7, 1306 (1971).
- [12] P. C. Bhat, M. P. Sathyavathiamma, N. G. Puttaswamy, and R. M. Mallya, "A Comparative Study of Corrosion of Different Types of Iron Using Mössbauer Spectroscopy," International Conference on the Application of Mössbauer Spectroscopy at Jaipur, India, Dec. 1981.
- [13] I. Dezsi, L. Keszthelyi, D. Kulgawczuk, B. Moinar, and N. A. Elissa, Phys. Status Solidi 22, 617 (1967).
- [14] P. O. Voznyuk and V. N. Dubiniu, Sov. Phys.-Solid State 15, 1265 (1973).
- [15] G. S. Bindord and E. M. Gessler, J. Phys. Chem. 63, 1376 (1959).
- [16] J. W. Vanderhoff, L. M. Bennetch, M. J. Cantow, K. A. Earhart, M. S. El-Aasser, T. C. Huang, M. H. Kang, F. J. Micale, O. L. Shaffer, D. W. Timmons, and J. A. Manson, Org. Coatings Plastics Chem. 46, 12 (1982).
- [17] P. Huwart, "Measurement of the Degree of Dispersion of Pigments in Water-Based Flexographic Inks using Chromatographic Methods," M. S. Thesis, Lehigh University, 1980.

- [18] P. Huwart and J. W. Vanderhoff, Double Liaison Chim. Peint.
314, 482-94 (1981).
- [19] R. V. Mann, F. J. Micale and J. W. Vanderhoff, Emulsion Poly-
mers Institute Graduate Research Progress Reports No. 18,
July 1982, p.97.